University of Reading

Synthesis of Novel Metal Selective Ligand Systems

Doctor of Philosophy

Department of Chemistry

Zoe Selfe

June 2023

Declaration

I confirm that this is my own work and the use of all material from other sources has been properly and fully acknowledged.

Zoe Selfe

June 2023

Acknowledgements

Firstly, I would like to thank Professor Laurence Harwood for giving me the opportunity to be his last PhD student and to work in his research group. I am very grateful for all your advice, suggestions and being so approachable, as well as all your bad jokes.

Thank you to Dr Ashfaq Afsar for all your help and letting me ask you lots of questions and listening to all my ideas, you potato! I also want to thank Dr Chris Smith for all your help and knowledge. Thank you to Dr Joe Cowell for teaching me lab stuff and giving me confidence in the lab during my MChem.

I would also like to thank all the members of the Harwood group for making it a fun and welcoming environment; James Westwood, Iain Hopkins and Jasraj Singh Babra and all of the hilarious MChems. Thank you Jasraj for all our chats and laughs throughout the years.

I would like to acknowledge the Chemical Analysis Facility for letting me use their machines. Thank you to Andy Dodson for helping me run the ICP-MS machine and always being there for it. Thank you to Amanpreet Kaur for running SEM and TEM for me.

Thank you to everyone in the office for all your jokes and strange chats; Adam O'Donnell, Alex Gavriel, Charlotte Edwards-Gayle, Dan Skelson, Hannah Bowden, Iain Hopkins, Jack Cheeseman, James Westwood, Jasraj Singh Babra, Jessi Godleman, Jessica Hutchinson, Kaan Alkan, Lewis Hart, Matt Hyder, Oli Balmford, Sam Burholt, Sara Salimi and Tahkur Singh Babra.

Thank you to all my friends outside of PhD land, especially; Amy Penfold, Jack Poulter, Jay Sackwild, Sara Iannaccone and Saskia Mitchell.

Special thanks to my parents; Yvonne and Andy, for keeping me fed and watered, and for all of your support and encouragement. Thank you.

Abstract

The Rare Earth Elements (REEs) are becoming increasingly vital in today's modern society, with uses in mobile phones, televisions, wind turbines, light bulbs and medical equipment. Despite the fact they are used so regularly, only 1% of all REEs are recycled from end-of-life products. REEs are currently some of the most critical elements on the critical elements list and with their demand so high, strategies must be put in place to keep up with this increasing demand.

Chapter 1 This work summarizes the occurrence of these elements in the Earth's crust and their uses and demands in modern life. The mining and processing of REEs involves multiple stages including leaching, benefaction, pyrometallurgy and hydrometallurgy; either ion exchange or solvent exchange to afford pure REEs. The reprocessing of REEs from end-of-life products is also discussed.

Chapter 2 Neocuproine immobilized silica gel (NC-Si) contains an N-donor phenanthroline substituent able to bind to REEs and provide a way to separate REEs from each other providing a potential method for the reprocessing of REEs. This study explores the adsorption and desorption of REEs from a fixed-bed column of NC-Si. Thermogravimetric analysis (TGA) confirmed that approximately 5% w/w of neocuproine content was present on the NC-Si, resulting in a molarity of 0.1466 mmol per gram of adsorbent. The adsorption capacities of NC-Si for all REEs (including Sc and Y) ranged from 0.0005 to 0.0012 mg g^{-1}, with a preference for the late REEs (Ho-Lu), with an overall adsorption capacity of 0.0153 mg g^{-1}. Breakthrough times (t_b) were used to classify the REEs series into three groups; early (Y, La-Pr) (<3 mins), mid (Sc, Nd-Dy) (3.5 - 15 mins), and late (Ho-Lu) (>44 mins), indicating the potential of NC-Si for REE separations. Different models; Adams-Bohart, Thomas, Yoon Nelson, Modified Dose Response (MDR), and Lagergren's pseudo first and second order rate kinetics were applied to describe the adsorption of the multicomponent solution. The Yoon-Nelson model had the highest correlation coefficient ($R^2 \approx 0.95$) and effectively fit the mid and later REEs (Nd-Lu) among all the models tested. The MDR and Thomas models showed good fitting for early ($R^2 \approx 0.95$) and early/mid ($R^2 \approx 0.93$) REEs, respectively. The Adams-Bohart model provided the lowest correlation coefficient ($R^2 \approx 0.81$) but was able to describe all ions.

Chapter 3 Similarly to NC-Si, $CyMe_4$-BTPhen also contains a phenanthroline functional group and is able to bind to REEs, however separation of REE is not as efficient. $CyMe_4$-BTPhen was immobilised onto silica (BTPhen-Si) and fixed-bed column techniques were carried out. BTPhen-Si had an overall adsorption capacity of 0.048 mg g^{-1} with adsorption capacities ranging from 0.0016 to 0.0038 mg g^{-1} for Y and Sc, respectively. Based on the breakthrough times (t_b) the series could be separated into two groups, mid REE ions (Pr-Eu) (>3 mins) and late REE ions (Gd-Lu) (<1.5 mins), however Sc and Ce would elute with the mid REE ions, whereas Y and La elute with the late REEs. Adams-Bohart and Thomas models were able to

describe all ions (Sc, Y and all REEs), however they gave the lowest correlation coefficients at R^2 = ~0.86 and 0.9, respectively. Yoon-Nelson and MDR were not able to describe Sc, Pr, Nd, Sm and Eu. BTPhen-Si shows potential as a material for extracting REE ions, but further improvements are needed to enhance separation and adsorption capacities.

Chapter 4 Four ligand systems were developed to investigate extraction and partition capabilities of REEs in a fixed-bed column system which allowed comparison with NC-Si and BTPhen-Si. All ligands contained the phenanthroline functional group but all had different linkages to the silica gel. ANC-Si, BNC-Si, HANC-Si and TBTPhen-Si were successfully synthesized, characterised and measured for REE extraction. The models; Adams-Bohart, Thomas, Yoon Nelson and Modified Dose Response (MDR) were applied to the breakthrough curves of each of the ligand systems. HANC-Si could not be described by any model, however BNC-Si and TBTPhen-Si were best described by MDR and ANC-Si described by Adams-Bohart and Thomas. Adsorption capacities of the four ligand systems were as followed for ANC-Si, BNC-Si, HANC-Si and TBTPhen-Si; 0.0106, 0.0157, 0.0101 and 0.00484 mg g^{-1}. Cost, REE separation, w/w% and adsorption capacities were compared to for all four ligands as well as with NC-Si and BTPhen-Si. Overall, NC-Si was the most efficient at separating the REEs from each other into small sub-groups of REEs. BTPhen-Si had the highest adsorption capacity out of the six ligands (0.0484 mg g^{-1}).

Notes on the Thesis Structure

Chapter 1	A general introduction to Rare Earth Elements (REEs) including their importance and uses along with current reprocessing and recycling methods. Rare Earth metals are of very high economic value, with applications in almost every high-tech product. REEs have been on the EU critical materials list since 2011 and currently only 1% of all REEs are recycled. A potential technique to recycle REEs would be to use solid phase extraction to separate and partition the REEs into smaller sub-groups or separate single ion fractions. Various solid phase extractant materials are discussed and compared.
Chapter 2	The first paper explores ion exchange techniques and adsorbents for the separation of REEs. The application of neocuproine functionalised SiO_2 gel (NC-Si) to REE separations is explored using a dynamic fixed-bed column is presented in this work. A variety of models are applied to describe the adsorption mechanism of the REEs onto the column and parameters determined. The contraction of REEs ionic radii across the series is advantageous for the portioning into smaller groups and a separation across the series is observed as NC-Si prefers the later REEs.
Chapter 3	This second paper explores the synthesis and application of $CyMe_4$-BTPhen immobilised silica (BTPhen-Si) for REE separation. BTPhen-Si was tested in fixed-bed dynamic experiments alongside NC-Si and gave a 4-fold increase in the extraction of all REE ions (0.048 mg g^{-1}) compared to NC-Si (0.015 mg g^{-1}), however no appreciable selectivity was observed. Breakthrough models along with the desorption kinetics were modelled and an effective comparison between sorbent materials, and the literature was made.
Chapter 4	The final paper looks at creating sustainable REE absorbents. The synthesis of NC-Si and BTPhen-Si both require a Suzuki-Miyuara cross coupling reaction. The catalyst used is palladium based which is also identified as a critical material by the EU and has been, along with the REEs since 2011. Alternatives to this reaction are studied and three alternative ligand systems were synthesized. Extraction studies were carried out on these novel systems and compared to NC-Si and BTPhen-Si for the partitioning of REE ions. The silica absorbents synthesized and tested are a benzimidazole-fused neocuproine functionalised silica gel (BNC-Si), hydroxyaminopropylneocuproine-functionalised silica gel (HANC-Si), tetra(4-hydroxyphenyl)BTPhen-functionalised silica gel (TBTPhen-Si), and an aminopropyl neocuproine silica gel (ANC-Si).

Chapter 5	This chapter summarizes the key findings of this project providing critical evaluation of the research carried out and suggests potential avenues for future work. The future of technology is dependent on the recycling and reuse of rare earth metals. NC-Si would provide a brilliant material to recover and separate the REE ions into individual pure fractions of each Rare Earth ion.

Table of Contents

Chapter 1 – Introduction

1.1 Importance of Rare Earth Elements (REEs)

The Rare Earth Elements (REEs), otherwise known as the lanthanide metals, are comprised of 14 elements with atomic numbers spanning from 57 to 71. Scandium and Yttrium are considered lanthanide-like because they have very similar physical and chemical properties to the rest of the group. They are all naturally found in the Earth's crust with promethium being the rarest due to the absence of long-lived stable isotopes. Contradictory to their name; "Rare Earth Elements", these elements are actually relatively abundant, although availability is limited as their concentration in their ores is very low, Table 1.1 displays the abundance of the REEs in the Earth's crust. Light Rare Earth Elements (LREEs) (lanthanum to europium) are more abundant than Heavy Rare Earth Elements (HREEs) (gadolinium to lutetium) and even numbered REEs are more abundant than odd numbered REEs. Thus, Cerium is ranked the 28th most abundant element with thulium ranked 63rd. Overall the REEs are found in greater occurrence than silver and copper [1, 2].

Their name arises from their limited availability, as the concentration of REEs in even the richest ore is only 5% [1]. The REEs are found in over 200 types of minerals, with 95% of the REEs occurring in bastnasite ($CeFCO_3$), monazite ($(Ce, La, Th, Y) PO_4$) and xenotime (YPO_4). Bastnasite is found in hard rock deposits, whereas xenotime and monazite are found in both hard rock and placer deposits[1] [1,2]. It is estimated that 93.4 million metric tons of rare earth oxides (REOs) are available in the Earth's crust, with 52% of the world's resources being located in China, followed by Namibia (22%), United States (15%) and Australia (3%). Bayan Obo, China, contains approximately 48 million metric tons comprised of basanite (70%) and monazite (30%) [3].

1.2 Properties

The REEs have many distinguishing features in their chemistry, they can all occur in the +3 oxidation state and whilst in the +3 oxidation state they exhibit a phenomenon known as "lanthanide contraction" across the series, left to right (Table 1.1). This phenomenon occurs as a result of the poor shielding from the 4*f* electrons that penetrate the 5*s* and 5*p* orbitals, resulting in less shielding from the increased nuclear charge. The electron cloud decreases and therefore the ionic radius decreases too. Across the series the 4*f* electrons behave more like core electrons causing their ability to form bonds more difficult due to their small ligand field stabilisation energies. Some of the REEs, such as Ce^{4+}, Eu^{2+} and Yb^{2+}, are also able to adopt the +2 and +4 oxidation states as they exhibit empty, half occupied or full 4*f* electron shells (Ce^{4+} ($4f^0$), Eu^{2+} ($4f^7$) and Yb^{2+} ($4f^{14}$)). REE ions are hard Lewis acids and co-ordinate

[1] Surficial mineral deposits formed by the mechanical concentration of mineral particles from weather debris [2].

readily with hard bases, such as oxygen and nitrogen group atoms. The most common coordination numbers for REEs are 8 and 6, but they can range from 3 to 12. The large ionic radii of the REE series allows the accommodation of a high coordination number as well as the bonds being more electrostatic in nature.

Table 1.1 shows various properties of the REE including electron configurations, density and abundance as well as the ionic radii of the most commonly occurring coordination numbers (CN) of the ions. The earlier REEs (La-Nd) and Y and Sc are the most abundant REEs out of the series, as well as having the highest ionic radii and density compared to the later REEs. Europium has a half full 4*f* orbital which increases the ionic radii and thus decreases the density, which also leads to a lower enthalpy of atomizaton (Δ_{at}). The Δ_{at} shows that most REEs have a relatively high Δ_{at} compared to other elements of the periodic table. REEs tend to exist as trivalent cations, held together by metallic bonds, requiring large amounts of energy to break into gaseous atom. In general there is a correlation between the melting point and Δ_{at}, where elements with higher Δ_{at} tend to have higher melting points due to the increase in bond strength [4]

Table 1.1. Table of Rare Earth Elements and selected properties compiled from the literature [5–9].

Name	Atomic # & Symbol	Electron config.	M^{3+} electron config.	Ionic Radius (M^{3+}, Å)		Density	Abundance	Melting point	$\Delta_{at} H^b$
				CN = 6	CN = 8	($g \cdot cm^{-3}$)	($mg \cdot kg^{-1}$)	(°C)	($kJ \cdot mol^{-1}$)
Scandium	^{21}Sc	[Ar] $3d^1\ 4s^2$	[Ar]	0.887	1.010	2.985	26.0	1541	378
Yttrium	^{39}Y	[Kr] $4d^1\ 5s^2$	[Kr]	1.040	1.159	4.472	29.0	1526	425
Lanthanum	^{57}La	[Xe] $5d^1\ 6s^2$	[Xe]	1.172	1.300	6.146	34.0	920	431
Cerium	^{58}Ce	[Xe] $4f^1\ 5d^1\ 6s^2$	$4f^1$	1.15	1.283	6.689	60.0	795	423
Praseodymium	^{59}Pr	[Xe] $4f^3\ 6s^2$	$4f^2$	1.13	1.266	6.640	8.70	935	356
Neodymium	^{60}Nd	[Xe] $4f^4\ 6s^2$	$4f^3$	1.123	1.249	6.800	33.0	1024	328
Promethium	^{61}Pm	[Xe] $4f^5\ 6s^2$	$4f^4$	1.11	1.233	7.264	N.A.[c]	1100	~350
Samarium	^{62}Sm	[Xe] $4f^6\ 6s^2$	$4f^5$	1.098	1.219	7.353	6.00	1072	207
Europium	^{63}Eu	[Xe] $4f^7\ 6s^2$	$4f^6$	1.31	1.206	5.244	1.80	826	175
Gadolinium	^{64}Gd	[Xe] $4f^7\ 5d^1\ 6s^2$	$4f^7$	1.078	1.193	7.901	5.20	1312	398
Terbium	^{65}Tb	[Xe] $4f^9\ 6s^2$	$4f^8$	1.063	1.180	8.219	0.940	1356	389
Dysprosium	^{66}Dy	[Xe] $4f^{10}\ 6s^2$	$4f^9$	1.052	1.167	8.551	6.20	1407	290
Holmium	^{67}Ho	[Xe] $4f^{11}\ 6s^2$	$4f^{10}$	1.041	1.155	8.795	1.20	1461	301
Erbium	^{68}Er	[Xe] $4f^{12}\ 6s^2$	$4f^{11}$	1.030	1.144	9.066	3.00	1529	317
Thulium	^{69}Tm	[Xe] $4f^{13}\ 6s^2$	$4f^{12}$	1.020	1.134	9.321	0.450	1545	232
Ytterbium	^{70}Yb	[Xe] $4f^{14}\ 6s^2$	$4f^{13}$	1.008	1.125	6.570	2.80	824	152
Lutetium	^{71}Lu	[Xe] $4f^{14}\ 5d^1\ 6s^2$	$4f^{14}$	1.001	1.117	9.841	0.560	1652	428

[a]In the earth's crust, [b]Enthalpy of atomization is the amount of enthalpy change when an elemental solid is broken into component mono-atoms, which is the same as the enthalpy of sublimation if the gas produced is mono-atomic, [c]All isotopes of Promethium are radioactive with the longest-lived isotope is Pm-145 which has a half-life of 17.7 years. For this reason, it is not abundant on Earth

1.3 Demands and Uses

Today's world is heavily reliant on REEs, with uses in magnets (21%), catalysts (19%) and ceramics (6%) (Table 1.2), they occur in just about every piece of technology, with a net market worth of 1.5 billion pounds in 2014 [10]. 210,000 metric tons of rare earth oxides (REOs) were mined in the year of 2020 where it is expected to rise to 315,000 tons by 2030 and 650,000 tons by 2040 (Figure 1.1) [11–13]. The annual consumption of rare earth metals is more than 100,000 tons per year, fortunately the current demand is being met with China producing the most (105,000 metric tons in 2014) followed by Australia (20,000 mt) and Russia (5,000 mt) [14].

Table 1.2. Uses of REEs [15–18]

Rare Earth Element	Application	Rare Earths uses by volume [6]
Scandium	Electron beam tubes, high strength Al-Sc alloys	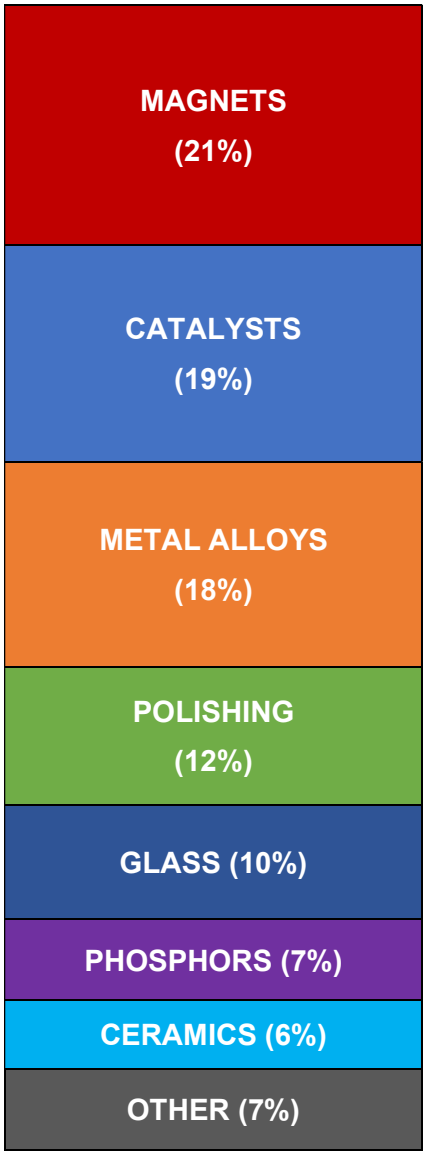
Yttrium	Capacitors, phosphors, glasses, oxygen sensors, radars, lasers, superconductors	
Lanthanum	Glasses, ceramics, car catalysts, phosphors, pigments, misch metal, UV filters	
Cerium	Ceramics, glasses, pigments	
Praseodymium	Permanent magnets, catalysts, IR filters, pigments for glasses, lasers	
Promethium	Miniature nuclear batteries and research	
Samarium	Nuclear industry, microwave e filters, permeant magnets	
Europium	Phosphors	
Gadolinium	Visualization of images in medicine optical and magnetic detectors, ceramics, glasses, crystal scintillator	
Terbium	Phosphors	
Dysprosium	Phosphors, ceramics, nuclear industry	
Holmium	Ceramics, lasers, nuclear industry	
Erbium	Ceramics, dye for glass, optical fibres, nuclear industry	
Thulium	Electron beam tubes, visualization of images in medicine	
Ytterbium	Metallurgy, chemical industry	
Lutecium	Single crystal scintillator	

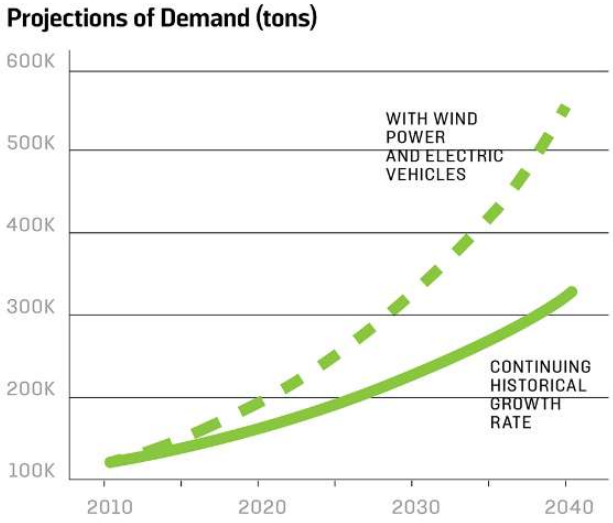

Figure 1.1. Future prediction of REE demands [12]

A major use for rare earth metals is in the catalyst industry, accounting for 19% of the total volume, although only 5% by value of the total value of the rare earth market. Cerium carbonate and cerium oxide are used in catalytic converters in vehicles, converting the polluting compounds in car exhausts into non-toxic compounds [19]. They are also used in fluid cracking converters (FCC) for refining crude oil for the conversion of heavy molecules into lighter compounds to produce light petroleum, gas, jet fuel and diesel [20,21].

Due to the unpaired electrons in the 4*f* shell, rare earth metals find themselves being used in the magnet industry, accounting for 22% by volume of the uses for rare earths and 38% by value of the rare earth market. Neodymium-iron-boron species have a very high magnetic energy with a 84.4% iron content, making it a relatively cheap alternative to cobalt-containing magnets. Its use in everyday objects such as earphones, speakers, DVD drives, hard drives, MRI scanners, hybrid cars, wind turbines and air conditioning systems show just how important neodymium is [22]. The incorporation of REEs in nickel metal-hydride batteries allows for efficient hydrogen storage. $LaNi_5$ is capable of absorbing vast quantities of hydrogen gas as it forms the hydride $LaNi_5H_6$ where one cubic meter of liquid hydrogen weighs 71 kg whereas one cubic meter of $LaNi_5H_6$ contains 88 kg of hydrogen [23]. Fluorescent lamps contain various rare earth complexes, lasting four times longer than incandescent lamps with a much higher efficiency. Their use in fluorescent lamps (phosphors) accounts for 7% of the global volume of rare earths in 2014 with 32% by value [10].

Recycling of REEs is imperative as the main demand for REE is for Nd, Pr and Dy for use in magnets and batteries. La and Ce are the main metals being produced, and so the issue of specific REEs shortage must be overcome by recycling. Due to the complexity of separating the REEs from each other means that only 1% of today's REE is actually recycled [24–26].

1.4 Rare Earth Trade Dispute

In 2006 China decreased its export quota by 40% in 2010 to protect the environment, this caused the prices outside of China to increase dramatically which triggered supply shortages in countries that are depending on the supplies from China, such as the electronics trade in Japan and the defence trade in United Sates. Following these concerns, the US and Japan filed two complaints to the World Trade Organisation (WTO) in 2009 and 2012 as it was claimed that China was breaching trade rules. Since 1990 China has increased its rare earth supplies from 27% in 2009 to 97% of all world trade in REEs in 2012 maintaining its monopoly of REEs. The price of REEs is currently very high outside of China, and many companies have been forced to move to China or find alternatives in their products.

From 1965 to 1984 the U.S had been the main supplier of REEs with most of its sources coming from the Mountain Pass mine in California, owned by Molycorp. In 1984 China suddenly took the lead and in 2015 the Mountain Pass mine filled bankruptcy and had to close [27]. A report was issued in 2018 by the U.S Secretary of Defence where it recommends the U.S “create an industrial policy in support of national security efforts” and to “diversify away from complete dependency on sources of supply in politically unstable countries who may cut off U.S. access.” In the 116th Congress, Senator Manchin's proposed that the US Department of Energy's Office of Fossil Energy should create innovative separation technologies to extract and reclaim REEs and minerals from coal and coal by-products [28].

In 2022 the Department of Energy in the U.S announced a $30 million initiative that will go towards researching and gaining a U.S domestic supply chain for REEs and other metals for battery production [29]. In 2017 a company called MP Materials based in Las Vegas restarted production and now produces a concentrate that contains 15% of the REE content consumed annually [30]. Currently 60% comes from China, with the three other sources being Myanmar, Australia and Mountain Pass [31].

1.4.1 Environmental Concerns

In 1991 the United States Environmental Protection Agency (EPA) identified four waste streams that were of cause for environmental concern when mining and reprocessing REEs was: (1) ignitability concerns of waste solvent, (2) toxicity of spent lead filter cake, (3) toxicity of waste zinc contaminated with mercury and (4) ignitability of solvent extraction crud. The main cause for concern was the risk of the treatment and disposal of the tailings [32,33]. The tailings contain high surface-area particles, wastewater and chemicals which remain in the area until rainwater washes away these tailings into surrounding areas, thus contaminating soils and bodies of water. These tailings include radioactive materials, fluorides, sulphides, acids and heavy metals (aluminium, arsenic, barium, beryllium, cadmium, lead and copper). Fugitive dust from the tailings is also an issue as it pollutes the air and soil which can be inhaled by workers and nearby residents. This dust particles can be toxic, irritating, or carcinogenic.

Radioactivity is also another issue, as REEs and yttrium are recovered from primary ores that also contain naturally occurring uranium and thorium. The waste sludges will therefore contain high levels of radionuclides that would give rise to unacceptable radiation levels. Surface run off and dust causes the unwanted transportation of these radioactive waste materials [33].

1.5 The Extractive Metallurgy Processes

Overall, the extraction of metals from their ores is a reduction process, wherein energy is required to release the metal present in a compound and collect it in it's elemental (metallic) form [34]. The outline of the unit operations involved in a theoretical extractive metallurgy process is given in Figure 1.2. The ores mentioned in this section is Bastnasite and Monazite. Bastnasite is a rare earth flurorocarbonate compound, $RE(CO_3)F$, mainly containing the earlier REEs. Monazite is mainly comprised of the earlier REEs and some of the later REEs such as Nd, Pr and Sm. In order to extract pure rare earth metal out of the ores, many different processes must be carried out which involves multiple stages and types of processing. These steps include crushing, milling, physical beneficiation (froth floatation), chemical beneficiation, and leaching. Once the REE is separated from its ore, further processes are required to separate the individual REEs from each other. Fractionation-crystallisation, fractionation-precipitation, adsorption, ion exchange, solvent extraction, membrane separation, and liquid-liquid chromatography.

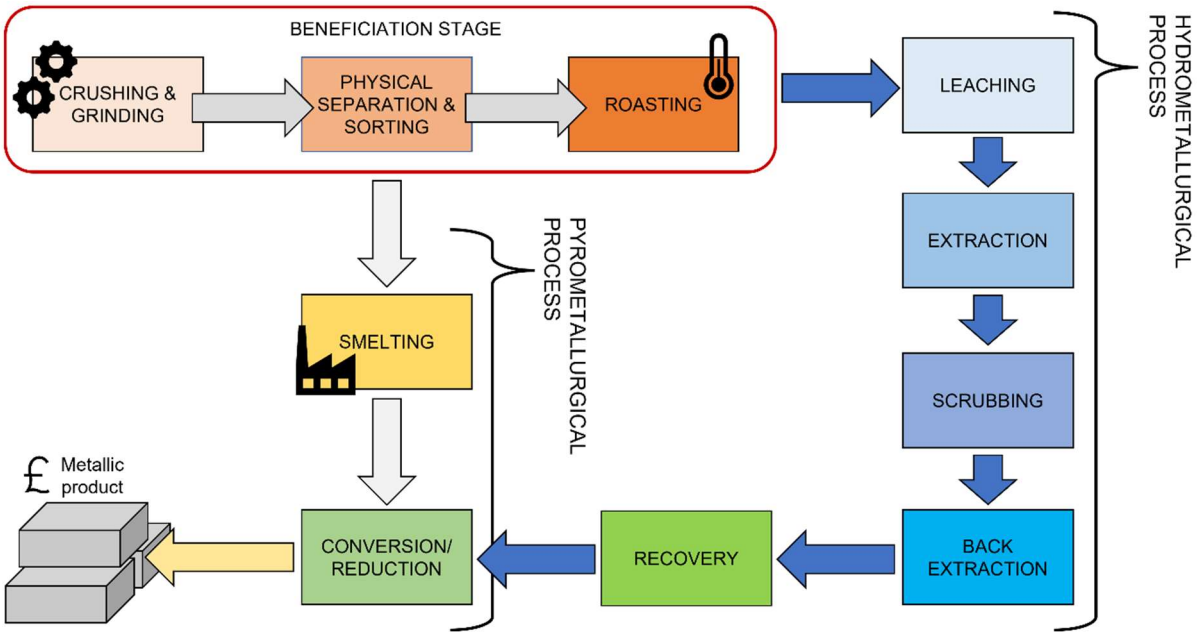

Figure 1.2. Outline of the extractive metallurgy process

1.5.1 Mining

Rare Earth mining can either be open pit, leached in-situ or underground mining. The typical type of mining is open pit mining where the removal of soil by explosives to blast away the surface of the ground then digging the ores and removing them by truck. This method is safer than underground mining as it is caried out closer to the surface of (<100 meters). Most of the

ores are extracted as a by-product from mining other sources such as titanium, zircon or tin. Hard rock deposits such as Bastnäsite are extracted using underground mining and/or open pit mining [35]. After mining the raw materials milling, crushing and grinding occurs. The product is then concentrated to contain about 30-70% of REE bearing ore. If the soil is of the soft sand monazite ore then wet dredging is used where a floating dredge digs through the bottom of a large pond and pumps the ore slurry into a container above the water [36].

1.5.1 Beneficiation Stage

In the industry of extractive metallurgy, beneficiation is used as a term to any process that improves the economic value of the ore by removing the gangue minerals and increasing particle surface area, which ultimately results in a higher recovery. Beneficiation can include the unit operations of scrubbing (to remove slime, clay and any surface oxidation), crushing, and physical separation based upon particle size, gravity, magnetism, radioactivity and flotation methods. The application of these unit operations will be dependent on the concentration and speciation of the target metal in the ore, the gangue material present, and how this correlates to the density and the hardness of the target mineral phase. Roasting of an ore may be conducted as part of the beneficiation stage. Roasting involves changing the oxidation state of the Rare Earth metal so it can be more easily dissolved, leaving iron and other waste materials as solids in the waste streams.

1.5.2 Pyrometallurgical Process

After beneficiation, pyrometallurgy is the process which involves the high temperature processing of ore to chemically convert REEs into another phase to allow the separation from the main non-REE components. Pyrometallurgy is an efficient but intensive method which can process large quantities of material relatively quickly. High purity REEs from pyrometallurgy methods can be obtained. The downsides to pyrometallurgy include the high environmental concerns from the production of toxic gases, as well as high energy consumption [37].

There are two types of pyrometallurgical processes for processing REE from their ores; REE reduction and calcium reduction. REE reduction involves high temperature (1200°C) and high vacuum to reduce REOs to metal vapor using lanthanum [38]. This vapor subsequently cools and deposits as pure solid metal on a cool surface. Lanthanum is used as the reducing agent because it has a low vapor pressure and is a strong reductant. The second method that can be used in pyrometallurgy is calcium reduction which uses high temperature (1470°C) calcium to reduce rare earth fluorides into molten metal. A plant in Japan is currently using this method for the processing of REE ore, where materials from America get shipped to [39].

1.5.3 Hydrometallurgical Process

An alternative method to pyrometallurgy for the recovery of REEs is hydrometallurgy which involves strong acid or basic solutions to selectively dissolve and precipitate specific metals of interest. Four common techniques involved are leaching, solvent extraction, ion exchange and precipitation.

1.5.3.1 Leaching

After the ore is ground into a fine powder a chemical leaching agent, such as hydrochloric acid, sulfuric acid or sodium hydroxide selectively dissolves the REEs from their ores. This mixture is stirred over time and the desired rare earth metal is dissolved away from the rest of the ore and can be taken into further reprocessing steps.

Current techniques for the leaching of bastnasite involve an alkaline conversion of REF_3 to $RE(OH)_3$, followed by a HCl to extract REE carbonates before alkaline conversion. Sulfuric acid can also be used to roast the bastnasite and then follows with a NaCl solution to leach the REE chlorides as Na double sulphates. Current leaching techniques for monazite are similar to Bastnasite where the ore is converted to $RE(OH)_3$ using hot 60-70% NaOH [40]. A hot water wash follows to produce a high yielding metal. Alternatively heating with $CaCl_2$ and $CaCO_3$ whilst reducing and sulphidizing to form REE oxysulphides (RE_2O_2S) and oxychlorides (REOCl) can be carried out. From this mixture the rare earth metal can then be selectively obtained with 3% HCl [40].

Biological leaching provides a safer and less wasteful way of leaching REE ores compared to chemical leaching. The idea of using bacteria to bioleach rare earth metals from their ores is rather novel. Researchers have explored the use of *Acidithiobacillus ferrooxidans* bacteria to bioleach REEs from low-grade Gibbsite ore, which found to obtain a leaching efficiency of 55% for REEs and 49% for uranium [41]. A study in Japan also managed to bioleach REEs from a Vietnamese ore using blue-green algae named '*phormidium*' in combination with $(NH_4)_2SO_4$ for the extraction of REE from ion adsorbed clays [42].

1.5.4. Separation and Purification Stage

After the removal of the REE metals from their ore, the next stage is the purification and partitioning the rare earths from each other to afford the individual metals of high purity. Common techniques include solvent extraction, ion exchange resins and extraction chromatography.

1.5.4.1 Solvent Extraction

To separate the REEs from each other, a liquid-liquid solvent extraction technique is commonly used. This involves transferring the REE ions from an aqueous solvent to an organic medium by mass transfer into solutions such as kerosene or aromatic solvents, through the use of a ligand. There are three classes of ligands; cation exchangers (or acidic extractants), and anion

exchangers (or basic extractants). In the 1960s ion exchange was the most common method and could purify solutions of small quantities, nowadays the use of solvent extraction allows large quantities of materials to be processed (~180 g REO/L) [43]. Following on from the extraction stages, the stripping and recovery of rare earths involves the addition of an acid, such as HNO_3 to strip the REE from the ligand.

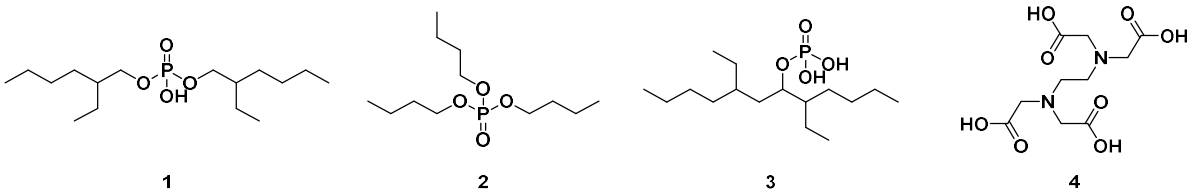

Figure 1.3. Chemical structures of HDEHP **1**, TBP **2**, HEHEHPA **3** and EDTA **4**

Di-2-ethyl-hexylphosphoric acid (HDEHP) **1** is a commercially used extractant for RE chlorides and sulfates, while tri-n-butyl phosphate (TBP) **2** is used for RE nitrates. Other ligands, such as 2-ethyl-hexyl-2-ethyl-hexyl-phosphoric acid (HEHEHPA) **3** (Figure 1.3). Versatic acid 10 46, versatic acid, Cyanex® 572, and Aliquat 336, are also used. These ligands typically contain hard O-atom donors that chelate to the metal cations and are fed into the organic phase. Cation exchangers (weak acids) such as HDEPA or TBP work as typical cation exchange extractants that involve the displacement of a hydrogen ion forming a neutral organic soluble complex as shown below where the acid actually appears in dimers or larger oligomers [44].

$$[RE^{3+}]_{aq} + [3(HA)_2]_{org} \rightarrow [RE(HA_2)_3]_{org} + 2[H^+]_{aq} \quad (1)$$

Anion exchangers extract metals as anionic complexes and the ligands used are mainly ammonium containing ligands [44]. Equation (2) depicts the reaction between tri-octyl methylammonium nitrate (Aliquat 336) [45]. The chelation with ethylenediaminetetraacetic acid (EDTA) **4** improved extraction and separation of REE pairs. Contrary to cation exchange, ammonium salts provide a way to extract the light REEs from solution [46].

$$RE^{3+} + 3NO_3^- + x(R_4N^+NO_3^-)_n \rightarrow RENO_3 \cdot xnR_4N^+NO_3^- \quad (2)$$

Two main terms are used to describe the efficiency of solvent extraction; distribution factor and separation factor, as seen below in equations (3) and (4), respectively. To determine the extraction efficiency of a ligand in a liquid-liquid extraction technique, the distribution ratio (D) for each element is calculated as the ratio between the concentration of extracted metal present in the organic phase and the concentration of that same metal remaining in the aqueous phase. Where [M] is the molar concentration of a certain metal.

$$D_M = \frac{[M]_{org}}{[M]_{Aq}} \quad (3)$$

When separating a particular metal from another metal in liquid-liquid extraction techniques, the separation factor is calculated to measure the relative extraction of one metal compared to

another. To determine the selectivity of one metal compared to another metal, the ratio between their distribution ratios is calculated using equation (4).

$$SF_{M_1/M_2} = \frac{D_{M_1}}{D_{M_2}} \quad (4)$$

The extraction of REEs using HDEPA is more efficient as the radius of the REE decreases, due to the increase in electrostatic charge between the element and the organophosphoric acid. The distribution factor increases upon atomic number with an average separation factor of ~2.5 between adjacent REEs, resulting in a high separation factor between the earliest REE (La) and the latest REE (Lu) of $SF_{Lu/La}$ = ~6800. The system can also work in the presence of chlorates, nitrates, sulfates and perchlorates and is typically carried out in kerosene. Phase transfer catalysts can be added to the system to increase the extraction efficiency.

In 1965, Molycorp used HDEPA **1** on a feed of bastnasite containing 0.1% Eu_2O_3, managing to concentrate to 15% [44]. In 1996 it was demonstrated that HDEPA (0.4 M in xylene) could concentrate a Europium from a chloride solution containing 0.22 ± 0.01 M total rare earths (%: Eu 93, Sm 3, Nd 2, Ce 1, Pr 0.5, and Gd 0.5). 99.98% Eu was obtained in a single extraction stage at pH 2.7 [47]. HDEPA **1** can also be used to separate a 99.8% La_2O_3 product from a chloride solution that contains; 45% La_2O_3, 35% Nd_2O_3, 10% Pr_6O_{11} and 5% Sm_2O_3. A 26-stage counter current extraction circuits were carried out to obtain a La recovery of 60% [48].

The process Molycorp used when processing bastnasite ore from Mountain pass followed multiple stages to obtain 99.99% Eu_2O_3. Leaching with HCl generated a chloride solution of La, Ce, Pr, Nd, Sm, Eu and Fe where 10% HDEPA (10%v/v) was added. Sm, Eu and Fe were extracted into the organic HDEPA layer, leaving the earlier REEs (La, Pr, Ce and Nd) behind in the aqueous solution which was precipitated with ammonium and sodium hydrogen sulfide and further processed using larger scale equipment. Sm and Eu were then stripped from HDEPA using HCl and the iron was precipitated out leaving just Sm and Eu in the organic layer. This solution as passed through a column of zinc amalgam to reduce Eu(III) to Eu(II). Sulfuric acid was then added to precipitate europium sulfate, and after calcination produced 99.99% Eu_2O_3 [40].

1.5.4.2 Solid Phase Extraction

Much effort has been expended on developing solvent-solvent extraction processes, but a number of drawbacks arise from such protocols, such as the need for a large amount of solvent that results in secondary organic waste. Third phase formation is also a problem, requiring the need for phase modifiers. Due to these problems, a solid-solvent extraction system has been considered more recently including ion exchange resins, extraction chromatography and biosorption, to name a few.

Ion exchange is the most commonly used solid phase for the extraction of REE which involves the separation of ions from a solution using solid inorganic oxides or organic ion exchange

resins with negative or positive charges. Examples of inorganic matrices include silica gel, alumina, zirconia, bentonite and zeolites whereas organic matrices include polymeric resins, cellulose, dendrimers, polyethyleneimine, polyacrylamide and chitosan. Both inorganic and organic resins can be functionalised with ligands containing carboxylic acids, phosphonic acids, amines and iminodiacetic acids to increase the selectivity and efficiency of REE separation. The ion exchange resins are capable of changing stoichiometry and reversibility by exchanging the ions it carries (A) with other ions coming from a solution (B) surrounding the resin. Equation (5) represents the reversible reaction between the resin (R) and the ions (A/B).

$$B(aq) + R - A(s) \rightleftharpoons A(aq) + R - B(s) \quad (5)$$

The most common functional groups of commercial ions exchange resins for REE separation are; phosphonic acids, sulfonic acids, quaternary ammoniums, phosphinic acids, phosphoric acids and primary amines. Static (batch) studies can be conducted on resins where a solution of REE ions is mixed with the resin and shaken. The distribution ratios (D) and Separation Factors (SF) can then be determined using equations (6) and (7). Equation (6) represents the distribution ratio between the molar concentration ([M]) of a certain metal absorbed on the resin and the [M] of that metal still remaining the solution. These can then be compared to the distribution ratio obtained from solvent extraction techniques and other ion exchange resins. From this the separation factor can then be determined from the ratio between the distribution ratios of two different REEs (equation (2)).

$$D_M = \frac{[M]_{resin}}{[M]_{sol}} \quad (6)$$

$$SF_{M_1/M_2} = \frac{D_{M_1}}{D_{M_2}} \quad (7)$$

For column-based experiments, a leach solution containing a mixture of REEs is fed through the resin matrix which absorbs the ions, separating them from the leach solution. The absorbed ions are then exchanged back into a different eluent in a purer form. To separate the ions into individual fractions of REEs, selective elution must take place. Selective elution involves a complexing agent to desorb the ions from the resin in order of selectively, usually based on stability constants of the ions and the complexing agent. EDTA **4** is an example of a complexing agent where REEs are eluted in reverse order of atomic number because the stability of the complexes increase from early to late REEs [49].

1.6 Adsorption

Adsorption is another method of separation whereby the rare earth adsorbate ions collect on the surface of a material, forming a film. The ability to adsorb a metal is based on the pore size and the adsorption mechanism. Many parameters can be changed to optimise separation and achieve highly selective separations. Many different adsorbents are available, such as zeolite, silica, graphene, activated carbon, polymers and chitosan. Discussed later in this thesis are

some of the main adsorbents used in the separation of REEs today. The adsorbent must fulfil several criteria in order to be used in industrial applications, including; high rates of adsorption/desorption, stability in low pH environments, high adsorption capacities, reusability, low cost and high mechanical resistance [50].

1.6.1 Zeolites and Clay

Zeolites can be natural or synthetic materials comprising of aluminosilicate (SiO_4^- and AlO_4^-) tetrahedra to give a crystalline structure with a negatively charged surface. There are many different structures of zeolites that adsorb REEs according to the zeolite's pore size [51,52]. A Na-X synthesized faujasite zeolite was shown to adsorb Y^{3+} two times more than Nd^{3+} showing potential to separate individual REEs [53]. Another zeolite structure, clinoptilolite was able to separate Nd and Gd from each other with maximum adsorption capacities of 1.81 and 6.5 mg g^{-1} for Nd(III) and Gd (III) ions, respectively. Bentonite is a naturally occurring aluminium phyllosilicate clay, which can be synthesized by co-precipitation with iron oxide to form magnetic bentonite [54]. Upon the application of the Langmuir isotherm model, the maximum adsorption capacity for Yb (III), Eu (III) and La (III) was 71.4, 26.1 and 18.4 mg g^{-1} respectively, proving that selectivity amongst the REEs is feasible with bentonite [54].

1.6.2 Decorated Silica

Silica is a common adsorbent matrix providing a stable material with a high surface area and a high porosity. It is also eco-friendly and reusable. Impregnating the silica gel with ligands increases the number of available binding sites, leading to an increased adsorptive capacity. Ligands such as HDEHP **1** can be functionalised onto silica gel for the adsorption of Gd at high temperatures with an adsorption capacity of 49.5 mg g^{-1}, reported by Shu *et al* (Figure 1.4) [55]. Another silica/ligand support studied for the extraction of rare earth ions was polyacrylamide grafted gum Arabic (GA-g-PAM/SiO_2) where the adsorption capacities reported for Eu, La, Nd and Sc were 10.11, 7.90, 12.24 and 11.05 mg g^{-1}, respectively, providing a decent material for the adsorption of REEs [56]. (SBA-15) N-propylsalicylaldimine **5** is a common ligand that can be functionalised with silica gel. SBA-15 silica gel bares oxygen and nitrogen donor atoms giving adsorption capacities of 4.7 and 18.5 mg g^{-1} for Eu and Th, respectively [57]. Further functionalisation of SBA-15 silica gel with N,N'-bis(salicylidene)ethylenediamine **6** (SBA/EnSA) improved the adsorption of Eu and Th with adsorption capacities of 15 and 81 mg g^{-1}, respectively. Finally, Lysine **7** is another molecule capable of functionalising SBA-15 giving good selective adsorption capabilities for Sc from a mixture of REEs, with an adsorption capacity of 35.29 mg g^{-1} [58].

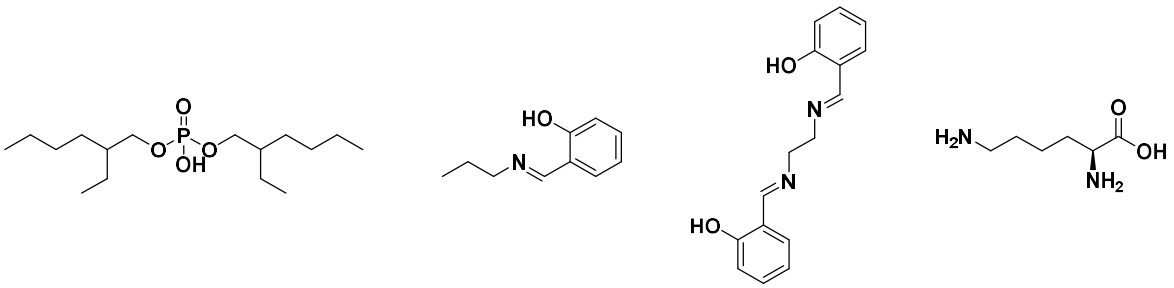

1 5 6 7

Figure 1.4. Structures of HDEHP **1**, N-propylsalicylaldimine **5**, N,N'-bis(salicylidene)ethylenediamine **6** and lysine **7**

The synthesis of EDASiDGA **8** has also been carried out and adsorption capabilities have been found, EDASiDGA **8** consists of a 3-(ethylenediamino)propyl silica gel where each amine group is functionalised with digylcolic acid, to give two diglycolic acid groups in total (Figure 1.5). Good adsorption capacities were found from a mixture of rare earth ions with a concentration of 0.2–5 mmol L^{-1} for each rare earth ion at pH 1. The adsorption capacities were as followed for La, Ce, Pr, Nd, Sm, Eu, Gd, Tb, Dy, Ho, Er, Tm, Yb, Lu; 10.41, 14.57, 12.72, 16.15, 18.80, 22.03, 21.3, 22.73, 23.72, 24.401, 24.42, 24.49, 23.02, 21.17 mg g^{-1} respectively [59].

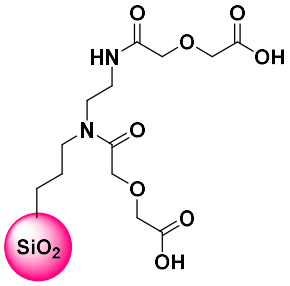

8

Figure 1.5. Structure of EDASiDGA **8**

KIT-6 is a mesoporous silica material where Ravi *et al* grafted EDTA **4** onto the surface which resulted in a high adsorption capacity for Nd(III) at 109.8 mg g^{-1}. Other ligands have been immobilised onto KIT-6 silica, altering the bite angle. 1,2-phthaloyl diamido-propyltriethoxysilane (KIT-1,2-PA-APTS) **9**, 1,3-phthaloyl diamido-propyltriethoxysilane (KIT-1,3-PA-APTS) **10** and 1,4-phthaloyl diamido-propyltriethoxysilane (KIT-1,4-PA-APTS) **11** have been synthesized and shown in Figure 1.6. All three ligands showed a significantly higher extraction capacity compared to KIT-6 itself. KIT-1,2-PA-APTS **9** has the smallest bite angle and showed an affinity for the late REE; Ho, Er, Tm, Yb and Lu. KIT-1,3-PA-APTS **10** has a larger bit angle and a preference for the earlier REE. Interestingly, KIT-1,4-PA-APTS **11** didn't show any selectively for any REE ions, possibly due to the two carbonyl groups para to each other [60].

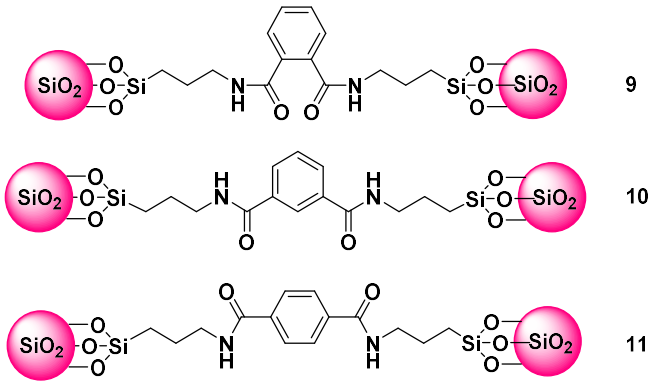

Figure 1.6. Structures of KIT-1,2-PA-APTS **9** (top), KIT-1,3-PA-APTS **10** (middle) and KIT-1,4-PA-APTS **11** (bottom)

1.6.3 Activated Carbon

Carbon based materials, produced from agricultural biomass waste, provide a natural alternative for synthetic adsorbents [61]. Carbon has many different oxidation states and coordination numbers, resulting in many different types of materials to be formed, such as graphite, graphene oxide (GO), carbon nanotubes and carbon nanofibers. Activated carbon (AC) (also known as charcoal) is a type of carbon-based material that has been heated to increase adsorptive properties whilst keeping it's large surface area (500 to 1500 m^2 g^{-1}) and has already been seen to remove pollutants from waste water [62,63]. Their highly porous structure and easily modifiable surface chemistry is advantageous, however native activated carbon is a poor adsorbent of REEs and so the surface must be functionalised. The strong oxidizing power of $KMnO_4$ and H_2SO_4 or H_3PO_4 activates the carbon surface by the addition of more oxygen groups to improve rare earth adsorption efficiency [64]. Studies by Kano *et al* show that treatment with $KMnO_4$ increased the adsorption capacity for La from 48 to 71 mg g^{-1}. Surprisingly, decreasing the pore size and pore volume improved the adsorption efficiency of REEs, however there was no correlation between size of the REEs and the adsorption capacity [65].

Ligands can also be used to functionalise the surface of activated carbon/ Ethylenediaminetetraacetic acid (EDTA)-functionalised activated carbon **12** was found to have a maximum adsorption capacity of 71.4 mg g^{-1} for Nd (III) (Figure 1.7) [66]. Pentaethylenehexamine (PEHA) **13** is also a good ligand to functionalise the surface of activated carbon giving a maximum adsorption capacity of 107 mg g^{-1} compared to 76.5 mg g^{-1} for non-functionalised activated carbon for La (III) (Figure 1.7) [67]. Using rice husk derived activated carbon modified with phosphoric acid obtained a good adsorption capacity of 175.4 mg g^{-1} for La whilst also adding value to waste and tackling waste issues [68].

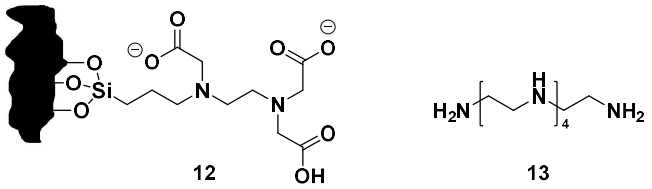

Figure 1.7. Structures of EDTA-functionalised activated carbon **12** (left) and PEHA **13** (right)

Graphene oxide (GO) **14** is another example of a carbon-based adsorbent, it is composed of sp^2 hybridized C atoms which allows for a material to stable in high temperatures and high mechanical strength as well as possessing high surface areas (Scheme 1). Graphene oxide is prepared by oxidizing graphene **15** with $KMnO_4$ with H_3PO_4 or H_2SO_4 (Scheme 1.1). Many different studies have been performed on graphene-based structures for the extraction and separation of REEs. One study used graphene oxide colloids to partition REEs from each other from a solution of 5000 µg L^{-1} in a pH of 6 (using NaOH or HNO_3 to adjust the pH). The adsorption capacities (q) obtained for La, Nd, Gd and Y were 85.6, 189, 226 and 136 mg g^{-1}, respectively [69]. Another study functionalised GO with polyaniline (PANI) and tested its extraction capabilities on a multicomponent solution of REEs gave the highest maximum adsorption capacity of 250 mg g^{-1} for Eu [70].

Another example of carbon-based materials involve Multiwalled Carbon Nanotubes Oxidized (MWCNTs-oxidized), these are single walled cylindrical tubes consisting of 6-membered carbon rings (as in graphite) nested inside one another with large diameters of 30 nm. The adsorption behavior of MWCNTs-oxidized in nitric acid observed adsorption capacities of 99.01 mg g^{-1} for La(III) and 78.12 mg g^{-1} for Dy(III) [71]. Graphene oxide nanosheets provide an suitable material for rare earth ion adsorption with adsorption capacities of 12.0, 14.8, 16.4 and 12.8 mg g^{-1} for La (III), Nd (III), Gd (III) and Y(III), respectively [69].

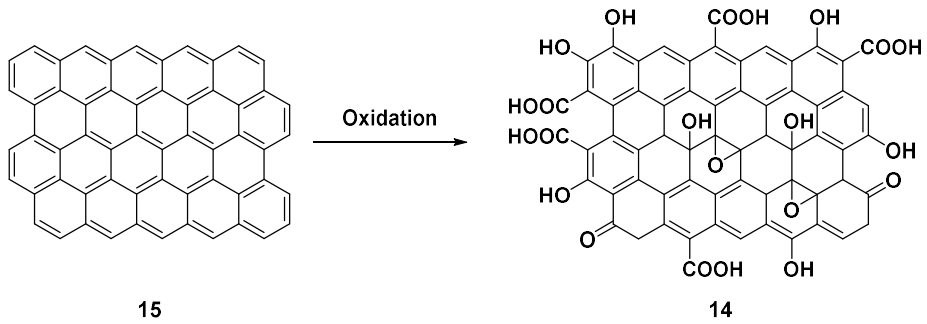

Scheme 1.1. Synthesis of graphene oxide **15**

1.6.4 Hydrogel Adsorbents

Hydrogels provide a good alternative to activated carbon, they are three-dimensional cross-linked polymers with a high water uptake capacity. They possess a highly porous structure with -COOH and -OH functional groups allowing physical adsorption of heavy metal ions. Most

hydrogels are polysaccharides made from chitosan, cellulose, pectin and starch, rendering them cost effective and eco-friendly as they are bioavailable.

Chitosan **16** is a promising low-cost bio-absorbent with a structure consisting of a linear polysaccharide composed of randomly distributed β-(1,4)-linked D-glucosamine (deacetylated unit) and *N*-acetyl-D-glucosamine (acetylated unit) (Figure 1.8). The chitosan structure is very easy to functionalise as it bears a high number of amino groups. EDTA **4** and diethylenetriaminepentaacetic acid (DPTA)-functionalised chitosan-silica hybrid particles have been compared for the adsorption of rare earth ions (the structure of DPTA **17** is shown in Figure 1.9). High absorption capacities for Nd were obtained for EDTA **4** and DPTA-functionalised chitosan silica at 60.6 and 106.7 mg g^{-1} respectively [72]. Chitosan can also be immobilised onto a magnetite Fe_2O_3 core via a co-precipitation method to produce a magnetic material. Adsorption capacities obtained for the adsorption of Gd (III) onto magnetite chitosan nanoparticles were relatively high at 89.6 mg g^{-1} [73].

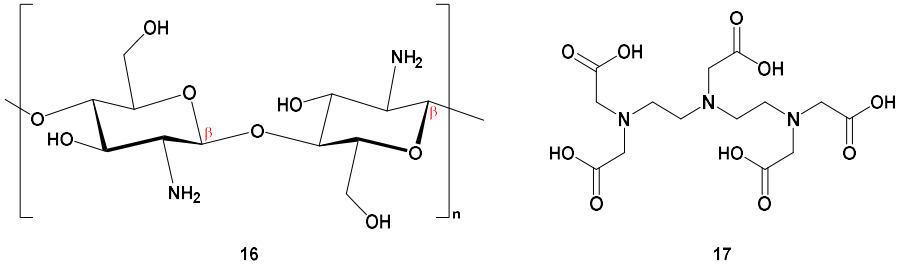

Figure 1.8. Chemical structures of Chitosan **16** (left) and DPTA **17** (right)

Another example of hydrogel adsorbent for the recovery of REEs is the use of highly abundant cellulose. It can be engineered to produce a anionic hairy nanocellulose (AHNC) for the removal of Nd(III). AHNC comprises of solubilized dicarboxylated cellulose (DCC) chains and cellulose nanocrystals (CNC) decorated with DCC (hairs) with a 264 mg g^{-1} adsorption capacity for Nd (III) [74]. Another method of adapting cellulose is the grafting of acrylic acid (AA) onto hydroxypropyl cellulose (HPC) to give a three-dimensional polymeric structure with a high surface area. Adsorption capacities for La(III) and Ce(III) were 264.2 and 199.3 mg g^{-1} respectively [75].

1.6.5 Polymeric Resins

Another method for the extraction of rare earths from an aqueous solution is the application of ion exchange resin technology. Strong acid (SA) cation exchange resins have been seen to have good extraction capabilities as they have a high selection for REEs. Trials on mining waste waters for REE proved a success, as well as REE recycling of rare earth oxide phosphors from technological waste streams [76,77]. A comparative study on various resins has been carried out with different functional groups including sulfonic (SA) **21**; mixed sulfonic/phosphonic (SP) **22**; aminophosphonic (AP) **23** and iminodiacetic (IDA) acid **24** (Figure 1.9). La adsorption was tested at pH 1.5 which found the adsorption capacities to be

64, 52, 39 and 49 g L^{-1} for SA, SP, AP and IDA, respectively, indicating sulfonic acid groups have a higher affinity for rare earths [78].

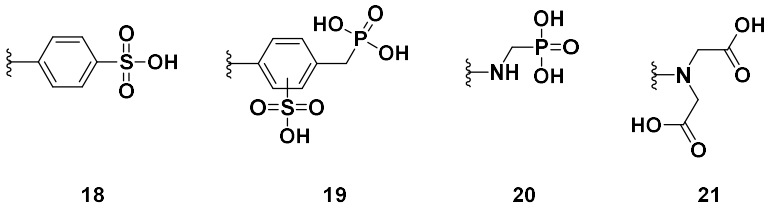

Figure 1.9. Structures of strong acid (SA) **18**, sulfonic/phosphonic acid (SP) **19**, aminophosphonic acid (AP) **20** and iminodiacetic acid (IDA) **21**

1.6.6 Selective Precipitation

Selective precipitation involves removing some of the rare earths from a solution by adding a reagent to form a less soluble compound. The remaining rare earths can be recovered by further precipitation steps. Common compounds for selective precipitation are hydroxides and double sulfates. To separate Y from the rest of the rare earths, the formation of a double chromate precipitate is carried out [40]. Hydrolysis of all rare earth ions occurs readily except for La, which remains in the solution. The formation of double sulfates ($RE_2(SO_4)_3 \cdot Na_2SO_4 \cdot nH_2O$) of La, Ce, Pr, Nd and Sm allows selective precipitation because they are sparingly soluble compared to Ho, Er, Tm, Yb, Lu and Y, whereas Eu, Gd, Dy are of intermediate solubility. Another method of precipitation is the addition of a ligand (EDTA **4** or sodium sulfate) to form complexes to some of the REEs leaving behind the rest of the REEs which can be precipitated out with oxalic acid or nitrilotriacetic acid. Selective precipitation methods are insufficient and tedious and were discontinued in the 1950s when ion exchange and solvent extraction became the most common techniques [40].

1.6.7 Fractional Crystallisation

Much like selective precipitation, fractional crystallisation is based on each REE complex having different solubilities to enable separation from each other. However, this method is inefficient due to the lengthy time and high number of steps whilst giving poor purity and was discontinued in 1950. It works on the basis that all rare earth metals except La, Ce, Pr, Nd form insoluble sulfates upon the addition of Na_2SO_4 and therefore can be filtered off.

1.7 Recovery of REE From Waste Materials

Due to the spike in REE prices and finite resources, a balance between mining and recycling has to occur in order to meet the high demands for REEs. Discussed below are some potential ways in which technological waste can be reprocessed. The REE content of mobile phones, hard disc drives (HDD) is unfortunately so low that it is difficult to separate the REEs from other metals; Al, Fe, Cu, Sn, Ni, AG, Au and Pd [79]. The larger sized products such as wind turbines and electric vehicle motors can more easily be recycled.

1.7.1. Catalysts

A major use for REEs is in the catalyst industry, accounting for 19% of the total volume, although only 5% by value of the value of the rare earth market. Cerium carbonate and cerium oxide are used in catalytic converters in vehicles, converting the polluting compounds in car exhausts into non-toxic compounds [19]. They are also used in fluid cracking converters (FCC) for refining crude oil for the conversion of heavy molecules into lighter compounds to produce light petroleum, gas, jet fuel and diesel [21,80]. Mainly lanthanum and small amounts of cerium are used in FCC catalysts. 50% of all REEs produced goes towards the production of these catalysts however there is little development in the way of recycling the rare earth metals from the FCC catalysts. Research has been carried out where acidic conditions to leach the metals could provide a means to recycle REEs [81].

1.7.2 Magnets

The majority of the REEs have unpaired electrons due to the incomplete 4*f* shell; therefore, most of the REEs are paramagnetic, apart from La^{3+}, Lu^{3+}, Yb^{2+} and Ce^{4+} which are diamagnetic. Their uses as magnets account for 22% by volume of the uses for REEs and 38% by value of the REE market. Neodymium-iron-boron species have a very high magnetic energy with a 84.4% iron content, making it a relatively cheap alternative to cobalt-containing magnets. Its use in everyday objects such as earphones, speakers, DVD drives, hard drives, MRI scanners, hybrid cars and air conditioning systems show just how important neodymium is [82].

Most REE recycling comes from magnets where they can be melted down and recycled into other metals via hydrometallurgical methods. The most common magnet form is a neodymium-iron-boron (NdFeB) alloy, comprised of a $Nd_2Fe_{14}B$ matrix encased in a neodymium phase, containing various other metals such as dysprosium, gadolinium, praseodymium [83]. These magnets are found in wind turbines and electric motors, as well as computer hard drives and small electronics. Various techniques can be employed to separate and recycle the REEs from NdFeB magnets. One such method category is hydrometallurgical which consists of three steps;

1. Leaching of the magnet; the complete leaching in H_2SO_4 at room temperature has been developed by Layman and Palmer in 1993 where all the components in NdFeB magnets are dissolved [84]. The Nd is then precipitated out as a double sulfate salt and converted into NdF_3 or Nd_2O_3. Banadara has also demonstrated that leaching with 4 M HCl selectively dissolves NdFeB leaving steel and copper particles completely untouched, oxalic acid is then added to precipitate with oxalic acid to give a 82% recovery of the REEs with a 99% purity [85].
2. Separation of individual REEs by solvent extraction where di-(2-ethylhexyl)phosphoric acid (DEHPA) **1** is used to extract the REEs with a separation factor of approximately 2.5.

Bis (2,4,4-trimethylpentyl) phosphinic acid (Cyanex 272) **22** and 2-ethylhexyl phosphonic mono-2-ethyl-hexyl ester (PC88A) **23** are also good extractants (Figure 1.10) [86–88]. Ionic liquids provide a safer alternative to solvent extractant molecules as they are ions that are volatile and non-flammable. Common ionic liquids that are used in this process are 1-methyl-3-octyl imidazolium bis(trifluoromethylsulfonyl)imide **24** in combination with (N,N'-dioctyldiglycolamic acid) DODGAA **25** and 1-alkyl-3-methylimidazolium hexafluorophosphate **25** (Figure 1.11) in combination with DEHPA **1** [89,90].

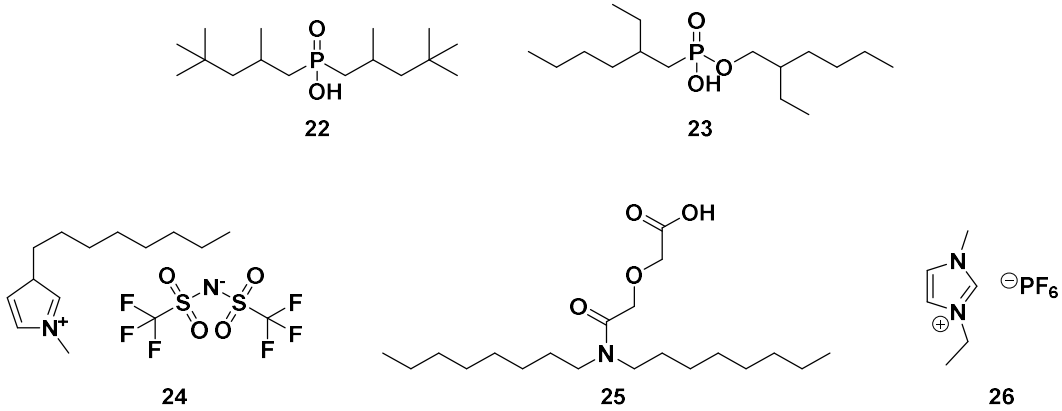

Figure 1.10: Cyanex 272 **22** (top left), PC88A (top right) **23**, 1-methyl-3-octyl imidazolium bis(trifluoromethylsulfonyl)imide **24** (bottom left), DODGAA (bottom middle) **25** and 1-alkyl-3-methylimidazolium hexafluorophosphate **25** (bottom right)

3. The precipitation follows steps 1 and 2, where the REE are precipitated out of the solution using oxalic acid or hydrogen fluoride. It is preferable to precipitate out the REEs via a calciothermic reduction reaction of the fluoride to produce high quality material, however removal of other dissolved species is an issue.

Pyrometallurgical methods provide an alternative to hydrometallurgical methods. Pyrometallurgical involves the high temperature processing of NdFeB magnet scraps to convert the REEs into another phase to allow the separation from the main non-REE components [23,91,92]. Pyrometallurgical extraction methods involve; (1) roasting, (2) liquid metal extraction, (3) molten salt extraction, (4) molten slag extraction, and (5) electrochemical processing [93].

1. Roasting: the aim of roasting is to change the state of the REEs in the NdFeB magnets at high temperatures so that the product can be more selectively dissolved. leaving iron and other waste materials as solids in the waste streams. Chlorination roasting involves the selective chlorination of the REEs in the magnetics by use of chlorination agents such as $MgCl_2$ which converts the REEs into molten $NdCl_3$ and $MgCl_3$ at 1000 ℃, $FeCl_2$ is also used at 800°C as well as NH_4Cl, Cl_2 gas and $AlCl_3$.[94,95] $NdCl_3$ and $DyCl_3$ can be distilled off at high temperature to leave the iron residue. Sulfonation roasting is an alternative process to chlorination roasting, whereby all the components of the magnet are converted to water soluble sulfates. The sulfates are subjected to high temperatures where only the RE

sulfates are thermally stable leaving the iron sulfates to decompose iron oxide which is insoluble in water [96].

2. Liquid metal extraction treatment with magnesium; the Ames Laboratory (USA) found that neodymium can be extracted from magnet scraps using liquid magnesium at 1000°C, before distilling the magnesium away from the melt to leave pure Nd. The same process can be carried out with molten silver, where the silver extracts the Nd away from the scraps. The silver is then removed by oxidation of the Nd to form Nd_2O_3 [97,98].
3. Molten salt techniques have been carried out at Anhui university of technology (China) where a molten chloride salt (MgCl and KCl) selectively dissolved Nd and other REEs at temperatures between 700-1000°C to form $NdCl_3$ with a yield of 90% [99].Tanaka *et al* discovered that molten fluoride will react with REOs to form REO-fluorides to be used in salt electrolysis [100].
4. Molten slag extraction involves molten B_2O_3 to selectively oxidise the REEs from the NdFeB alloys to form Nd_2O_3-B_2O_3 slag. This slag is then leached with acid to dissolve the Nd and recovered from the leachate by precipitation to form $Nd(OH)_3$ [101].

1.7.3 Hard Drives

In 2018 there was 20-50 million tons of Waste Electrical and Electronic Equipment (WEEE) being produced worldwide each year where only 12% of the electronic waste is being recycled for any metal (Au, Ag, Pt, Pd and Rh) [36,102]. This large volume of waste production contributes to make WEEE a challenge to manage [102]. The composition of REE in products such as speakers and electronics is extremely low (g to <mg), making it very difficult to extract and recycle the metals. Less than 1% of all REEs are recycled and, while much research has been carried out, nothing has moved past the laboratory scale [103].

Recycling electronic waste requires pyrometallurgical treatments, which produces a large amount of harmful waste. The economic and safety issues of such processes would have to be weighed up against the economic value of the small quantities of the recoverable rare earth metals. As the quantity of REEs in electronics are so small, they are present as fine particles attached to larger steel waste streams which makes it difficult to recover. Research by Abrahami *et al* demonstrated that Nd could be recovered from computer hard disc drives [104]. This process involved the mechanical shredding of the hard drives, taking advantage of the brittle nature of the NdFeB magnets which would form fine particles for ease of reprocessing. Thermal demagnetisation at temperatures above 312°C was carried out followed by grinding and screening. Two pyrometallurgical slag systems were investigated; (1) 40% CaO – 40% SiO_2 – 20% Al_2O_3 (in wt-%) and (2) 35% CaO– 65% CaF_2 (in wt-%) to extract rare earths from the scrap into the slag. After which the rare earths were dissolved in 2 M H_2SO_4 followed by 2 M sodium hydroxide to convert the REEs into double salts which can be converted to RF_3 and R_2O_3 with a purity of 98.4% and a yield of 99%.

1.7.4 Metallurgical Alloys

The Mische metal is a pyrophoric material, used in lighters and flint ignition devices and is comprised of an alloy containing a similar rare earth ratio as the naturally occurring bastnasite (50% cerium and 25% lanthanum and other elements). Lanthanum is also used as the anode in nickel metal hydride (NiMH) rechargeable batteries found mainly in hybrid cars [105].

1.7.5 Ni-MH Batteries

The incorporation of REEs in nickel metal-hydride batteries allows for efficient hydrogen storage. $LaNi_5$ is capable of absorbing vast quantities of hydrogen gas as it forms the hydride $LaNi_5H_6$. One cubic meter of liquid hydrogen weighs 71 kg whereas one cubic meter of $LaNi_5H_6$ contains 88 kg of hydrogen [23]. The price of the batteries is high because of the need for pure lanthanum. To lower the prices, mischmetal is used which contains a mixture of light REEs (La, Ce, Pr, Nd). Every Toyota Prius contains 2.5 kg of REEs in its battery pack [105]. The composition of nickel metal hydride batteries contain; 36%-42% nickel, 3-4% cobalt and 8-10% mischmetal containing lanthanum, cerium and praseodymium and neodymium. In 2007 Umicore developed an ultra-high temperature smelting technology which has a capacity of 7000 tons, corresponding to 150,000 electric vehicle batteries or 250 million mobile phone batteries [106]. The details are not revealed but the batteries are fed into a furnace where an oxygen rich source is injected into the furnace. Little external energy input is required because the combustion of the plastic casing of the batteries releases a large amount of energy. All the components in the furnace are converted into oxides where they are processed to be fed into a rare earth separation plant in La Rochelle (France).

Up until recently, Ni-MH would be recycled by incorporating it into stainless steel production as a cheap nickel source. Various research groups have developed hydrometallurgical methods to recover the REEs. Lyman and Parker discovered that the leaching NiMH scrap with 4 M HCl would bring the REEs into solution [107]. Yoshida developed a method to dissolve REEs in a chloride solution and precipitate them out of solution using phosphoric acid [108,109]. Zhang reported dissolving the metals in 2 M H_2SO_4 before extracting the rare earth metals with 25% DEHPA **1** in kerosene [110]. After which oxalic acid was added to precipitate the REEs from the organic solution. The rare earth metal oxalates were then converted into oxides.

1.7.6 Fluorescent Lamps (Phosphors)

Fluorescent lamps last four times longer than incandescent lamps with a much higher efficiency. Fluorescent lamps produce 63 lumens of light per watt of electricity consumed (lmW^{-1}) compared to 15 lmW^{-1} in incandescent lamps. Fluorescent lamps emit light when voltage is applied to mercury gas which emits UV light. As the UV light enters the phosphor powder coating of the lamp, a white light is produced [111].

Phosphors accounted for 7% of the global volume of REEs in 2014, with 32% by value [112]. Their importance is seen in plasma displays where they are activated by photons and emit luminescence. The colours produced are from different types of REEs. Five rare earth phosphors comprise a fluorescent lamp; phosphor $Y_2O_3:Eu^{3+}$ (YOX), the green phosphors $LaPO_4:Ce^{3+}$, Tb^{3+} (LAP), $(Gd,Mg)B_5O_{12}:Ce^{3+},Tb^{3+}$ (CBT), (Ce,Tb) $MgAl_{11}O_{19}$ (CAT) and the blue phosphor $BaMgAl_{10}O_{17}:Eu^{2+}$ (BAM). Halophosphate phosphors containing $(Sr,Ca)_{10}(PO_4)(Cl,F)_2:Sb^{3+},Mn^{2+}$ emit only white light and are often mixed with YOX to produce a better colour. The halophosphate has little value for recycling but can make up 50 wt%. The fluorescent lamps also contain significant amounts of alumina (Al_2O_3) and SiO_2 which acts as a barrier layer between the phosphor layer and the glass tube.

The waste produced from fluorescence lamps contain around 20% REEs by weight, making it difficult to recycle the phosphors as they are comprised of many different elements. They are a rich source of REEs, especially heavy elements such as Eu, Tb and Y and Ce.

Separation techniques are first employed, where a centrifugal pneumatic separator with an RPM of 5000 and a 0.053 m^3s^{-1} air flow rate is the optimum condition for achieving a 70% recovery of the rare earth phosphor. Wet separation processes have also been carried out using diiodomethane, where the REEs are less dense than the other components, causing them to float allowing for their recovery

Current techniques involve bringing the REEs into solution and recovering by precipitating out or using solvent extraction. The resistance to various acids varies; the halophosphate phosphors and $Y_2O_3:Eu^{3+}$ can be dissolved in dilute HCl at temperatures below 30°C. Whereas the phosphate phosphor; $LaPO_4:Ce^{3+}/Tb^{3+}$ can be dissolved in concentrated sulfuric acid at temperatures between 120 and 230°C. (Ce,Tb)$MgAl_{11}O_{19}$ and $BaMgAl_{10}O_{17}:Eu^{2+}$ all require strong conditions such as dissolution using hydrochloric acid (4 M) and precipitating out with hydrogen peroxide or heating to 1000°C in molten sodium carbonate. Work has also been carried out using supercritical carbon dioxide, TBP **2**, nitric acid and water where it showed a recovery of 99% Y and Eu can be extracted under a pressure of 15 MPa at 60°C.

1.7.7 Optical Lenses

Lanthanum can be used in the manufacturing of optical lenses as it has a high refractive index and a low dispersion. The lenses in cameras, microscopes and binoculars contain more than 40% of pure transition metal-free La_2O_3 and Gd_2O_3 contained in the borosilicate glass. In 2013 the total world annual production of optical lenses was 20,000 tons per year and recycling of the lenses would yield roughly 1600 tons of REOs per year [82]. Recycling of optical lenses currently consists of hydrometallurgical processes where hot sodium hydroxide solution converts the REEs to insoluble rare earth hydroxides at 140°C. Leaching of the rare earths with hot 6 M hydrochloric acid to yield rare earth chlorides which can be processed in a separation plant giving a recovery of 99.4% for La, 100% for Y and 100% for Gd [23,81,113].

1.8 Pyridine Based Extractants

Suzuki. T *et al* studied the ability of pyridine **26**, an N-donor molecule, for the extraction and separation of REEs (Figure 1.11). Pyridine was functionalised using 4-vinylpyridine and *m/p*-divinylbenzene embedded in silica beads and packed into a column. An eluent of separate REE lithium chloride and hydrochloride eluent solutions were added to the column where it was found that the earlier REEs eluted before the later REEs, the opposite true for the hydrochloride solution [114–117].

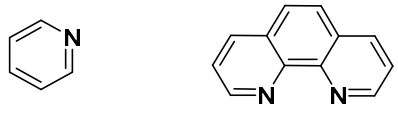

26 27

Figure 1.11. Chemical structures of pyridine **26** and 1,10-phenanthroline **27**

The successful ability of pyridine to act as a soft donor ligand for REE extraction led to the testing of 1,10-phenanthroline **27** (Figure 1.11). 1,10-phenanthroline was capable of forming 1,10-phenanthroline REE chloride and 1,10-phenanthroline REE tritthiocyanate complexes for all REEs [118]. The functionality of 1,10-phenanthroline was also altered to give N-octyl-N-tolyl-1,10-phenanthroline-2-carboxamide (OcTolPTA) where successful complexes with all REEs was achieved [119]. 1,10-phenanthroline was also functionalised with silica gel for the removal of trace transition metals from dilute acid solutions [120].

1.9 Column Behaviour

Continuous moving-bed, continuous fixed-bed and pulsed-bed are some of the various techniques used in adsorption column techniques. The fixed-bed column is the most common and the most efficient technique to use to achieve maximum adsorption. The fixed-bed column technique involves a solid adsorbent packed in a column where the eluent is introduced at the top of the column and the eluate is collected at the bottom, however the reverse of this is used too.

The performance of a fixed-bed column is evaluated through the use of breakthrough curves showing the concentration of ions in the eluent. The mechanism of this system is based on axial dispersion, film diffusion and intraparticle diffusion resistance, as well as sorption equilibrium with the sorbent. There are different zones throughout the sorption process, the first stage is the mass transfer zone (MTZ) where the inlet solution is fed into the column and adsorption occurs rapidly [121]. Initially the concentration of ions in the eluate (C) is zero as all of the ions from the solution are adsorbed by the column. A breakthrough curve is plotted as the bed volume against C/C_0 where C_0 is the concentration of ions in the eluent (Figure 1.12). At this stage there is no release of ions from the column and the C/C_0 ratio is zero showing a relatively flat curve on the breakthrough curve. After saturation of the column has occurred,

the concentration of ions in the eluate starts to increase along with C/C_0 and the breakthrough curve starts to rise. The breakthrough point zone is when C/C_0 is 0.05, where ions are just starting to be release from the column. The exhaustion point refers to another zone when C/C_0 is equal to 1. Here the concentration of eluate and the concentration of the eluent are equal to each other, and the adsorbent cannot hold any more ions so the curve becomes flat.

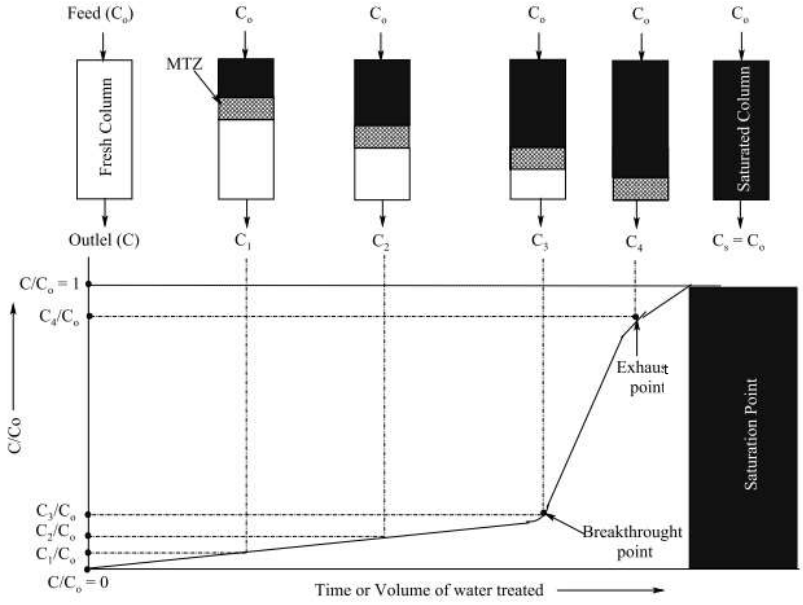

Figure 1.12. Representation of breakthrough curve [121]

By applying models to these breakthrough curves the mechanisms and behaviours of adsorption can be predicted. Rates can also be determined allowing quantitative analysis to fine tune their parameters to afford the most efficient adsorption. Commonly used models include; Adams-Bohart, Thomas model, Yoon-Nelson model, Modified Dose Response model (MDR), Clark, Wolborska and Bed Depth Service Time (BDST).

The Thomas model is the most widely used model and is based upon the assumption of Langmuir kinetics where adsorption and desorption follow a second order reaction kinetics with no axial dispersion [122,123]. The limitations from this model state that the adsorption is governed by mass transfer and not chemical processes and occurs as a monolayer. The MDR model is very similar to Thomas, however it is simpler and negates any error that arises at low or high time periods [124]. Adams-Bohart states that the rate of adsorption is dependent upon the concentration of ions in the eluent as well as the residual capacity of adsorption [125]. This model describes the process in two stages however is only limited to the initial stage. It describes the process as having minimal dispersion and little mass transfer and similarly to Thomas model, the adsorption occurs in a monolayer type fashion [126]. The Yoon-Nelson model does not focus on the properties of the adsorbent, such as the type and dimensions of the column bed. It assumes that the decreasing rate of adsorption is directly proportional to the concentration of ions in the eluent. The Clark model is based around the Freundlich model

where the dispersion phenomenon is disregarded, it also states that adsorption behaviours similarly to a piston motion [121].

A fixed-bed adsorption study using common exchange resins have been conducted and the models described above were applied to their breakthrough curves. The exchange resins studied which had a closer fit to Thomas and Yoon-Nelson models were; Purolite S957, Purolite S950, Lewatit SP112, Lewatit M600, Lewatit MP500, Amberlite IRA 958, and Amberlite IRA 67 ion exchangers. The models that had a closer fit to Adams-Bohart and Wolborska were; Lewatit M500, Amberjet 4200, Amberjet 4400, Amberjet 4600 and Amberlite IRA 458 ion exchangers [127]. Naturally occurring alginate based adsorbents have been functionalised and their adsorption properties were measured according to the models discussed above. Alginate is a polysaccharide formed of anionic repeating units of D-mannuronic acid and gluronic acid. And is a naturally occurring polymer from seaweed and algae. The alginate units were functionalised with biochar, lignin and cellulose and separate column studies were carried out for the adsorption of La(III). It was found that the alginate-based adsorbents followed the Thomas and Yoon-Nelson models better when compared to the Adams-Bohart and Wolborska models [128].

1.10 Conclusions

This thesis covers various important aspects of REEs, including their demand, usage, and supply issues. REEs have magnetic properties and, therefore, are very useful in a number of different applications, such as phosphor lamps, glass, medical devices, and mobile phones. With the increasing demand for these elements due to the rise of technological industries, the mining of REEs is expected to triple by 2040. As resources are finite, recycling is a must if we want to keep up with modern-day advances. The Rare Earth trade dispute saw the prices of REEs increase drastically, and many mining companies were forced to declare bankruptcy, which is another contributing reason to recycle REEs.

The processing of REEs after mining is a lengthy process involving multiple steps. Beneficiation includes crushing of the ore into fine powders or separating the components by size or properties. These first steps facilitate the dissolution of the ores in later stages. Following on from beneficiation we see pyrometallurgical methods which convert REEs into another phase under high temperatures to allow the separation from the main non-REE components. Hydrometallurgy is safer and less intensive achieving the same outcome as pyrometallurgy. Hydrometallurgical techniques involve leaching, solvent extraction and ion exchange. For REE processing leaching techniques require the use of acids and bases at high temperatures. Solvent extraction requires the mixing of an aqueous phase of REE ore and a ligand capable of binding to REEs which draw the REE from the aqueous phase into the organic phase and then stripped accordingly. Most ligands used in solvent extraction possess O-donor groups as seen in phosphoric acids, carboxylic acids. Amines are also seen in

extractant ligands bearing nitrogen donor groups. Ion exchange provides an alternative to solvent exchange where a charged ligand resin exchanges its ions with REE ions from the eluent. The REEs can subsequently be stripped from the resin using another ligand. A similar mechanism occurs with adsorbents (clay, zeolites, carbon, and silica, which can be functionalized with organic ligands) where the REE will be adsorbed onto the surface of the adsorbent and a ligand or acid will then strip it separating ions from each other based on their differing affinity for REEs.

Recycling of REEs is a challenging process due to their similar physical and chemical properties. The decrease in atomic radii across the series provides a way to separate REE from each other. The reprocessing of end-of-life products involves very similar techniques to processing of the ores for individual REEs. Small electronics are more difficult to recycle compared to wind turbines and engines as they are difficult to separate from the rest of the components, and so multiple steps are required with little yield. The main products discussed in this work are HDDs, catalysts, alloys, batteries and magnets. Most reprocesses require crushing and milling into smaller particles followed by the use of high temperatures and strong acids.

Pyridine **26** and 1,10-phenanthroline **27**, which contain N-donor groups, have demonstrated the ability to bind to REEs. 1,10-phenanthroline can be functionalised on the phenanthroline backbone and also used to form REE complexes. The focus of this thesis is to explore the hypothesis of ***"whether REEs can be recovered using sustainable nitrogen donor functionalized silica solid phase extractants."*** Neocuproine **28** is very similar in chemical structure to 1,10-phenanthroline however, neocuproine possesses two methyl groups (Figure 1.13). Containing two N-donor atoms, this molecule is functionalised with silica and its REE extraction capabilities are demonstrated in this thesis. The 1,10-phenanthroline moiety is seen a lot throughout this thesis as it is used to form a number of ligand functionalised silica systems for the extraction of REEs.

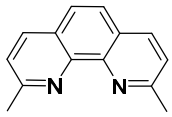

28

Figure 1.13. Chemical structure of neocuproine **28**

1.11 References

1. Gupta, C.K.; KrishnamurthyN. *Extractive Metallurgy of Rare Earths*; CRC Press LLC: Boca Raton, 2005;
2. Roonwal, G.S. Placer Deposits. In: The Indian Ocean: Exploitable Mineral and Petroleum Resources. In *Placer Deposits. In: The Indian Ocean: Exploitable Mineral and Petroleum Resources*; 1986; pp. 51–52.
3. Gambogi, J. Rare Earths, 2015. *Min. Eng.* **2016**, *68*, 30.
4. Cotton, S. Lanthanide and Actinide Chemistry. *Lanthan. Actin. Chem.* 2006, 1–263.
5. James, A.M.; Lord, M.P. *Macmillan's Chemical and Physical Data*; Macmillan: London, 1992; ISBN 0333511670; 9780333511671.
6. Lide, B.D.R. *Chemical Rubber Company Hanbook of Chemistry and Physics*; 77th ed.; CRC Press: Boca Raton, Florida, USA, 1996.
7. Dean, C.J.A. *Lange's Handbook of Chemistry*; 14th ed.; McGraw-Hill: New York, USA, 1992.
8. Kaye, D.G.W..; Laby, T.. *Tables of Physical and Chemical Constants*; 15th ed.; Longman: London, UK, 1993.
9. Nuclear Data Center at KAERI - Table of Nuclides Available online: https://atom.kaeri.re.kr/nuchart/ (accessed May 2023).
10. Kingsnorth, D.J. Meeting the Challenges of Supply This Decade.; Washington DC, 2011.
11. Alonso, E.; Sherman, A.M.; Wallington, T.J.; Everson, M.P.; Field, F.R.; Roth, R.; Kirchain, R.E. Evaluating Rare Earth Element Availability: A Case with Revolutionary Demand from Clean Technologies. *Environ. Sci. Technol.* **2012**, 3406–3414.
12. Lee Simmons Foreign Policy - Rare Earth Market Available online: https://foreignpolicy.com/2016/07/12/decoder-rare-earth-market-tech-defense-clean-energy-china-trade/ (accessed May 2023).
13. USGS Rare Earths Data Sheet. *U.S. Geol. Surv. Miner. Commod. Summ.* **2020**, 132–133.
14. Weng, Z.; Jowitt, S.M.; Mudd, G.M.; Haque, N. A Detailed Assessment of Global Rare Earth Element Resources: Opportunities and Challenges. *Econ. Geol.* **2015**, *110*, 1925–1952.
15. Charalampides, G.; Vatalis, K.I.; Apostoplos, B.; Ploutarch-Nikolas, B. Rare Earth Elements: Industrial Applications and Economic Dependency of Europe. *Procedia Econ. Financ.* **2015**, *24*, 126–135.

16. Christmanna, P. A Forward Look into Rare Earth Supply and Demand: A Role for Sedimentary Phosphate Deposits. *Procedia Eng.* **2014**, *83*, 19–26.

17. Talens Peiró, L.; Villalba Méndez, G. Material and Energy Requirement for Rare Earth Production. *Jom.* **2013**, *65*, 1 327–1340.

18. Haque, N.; Hughes, A.; Lim, S.; Vernon, C. Rare Earth Elements: Overview of Mining, Mineralogy, Uses, Sustainability and Environmental Impact. *Resources.* **2014**, *3,* 614-635

19. Kogel, J.E.; Trivedi, N.C.; Barker, J.M.; Krukowski, S.T. *Industrial Minerals and Rocks - Commodities, Markets, and Uses (7th Edition)*; 7th ed.; Society for Mining, Metallurgy, and Exploration, Inc. (SME): Colorado, 2009.

20. Bartlett, N.J. *Critical Materials Strategy for Clean Energy Technologies*; U.S. Department of Energy, Washington DC, 2011.

21. Zhan, W.; Guo, Y.; Gong, X.; Guo, Y.; Wang, Y.; Lu, G. Current Status and Perspectives of Rare Earth Catalytic Materials and Catalysis. *Chinese J. Catal.* **2014**, *35*, 1238–1250.

22. British Geological Society, Rare Earth Elements, https://www.geolsoc.org.uk (accessed Jul 2021).

23. Binnemans, K.; Jones, P.T.; Blanpain, B.; Van Gerven, T.; Yang, Y.; Walton, A.; Buchert, M. Recycling of Rare Earths: A Critical Review. *J. Clean. Prod.* **2013**, *51*, 1–22.

24. Eggert, R.; Wadia, C.; Anderson, C.; Bauer, D.; Fields, F.; Meinert, L.; Taylor, P. Rare Earths: Market Disruption, Innovation, and Global Supply Chains. *Annu. Rev. Environ. Resour.* **2016**, *41*, 199–222.

25. Ober, J.A. *Mineral Commodity Summaries 2016*; U.S. Geological Survey, Reston VA, **2016**.

26. Ober, J.A. *Mineral Commodity Summaries 2018*; U.S. Geological Survey, Reston VA, **2018**.

27. Survey, U.S.G. Rare Earth Elements — Critical Resources for High Technology. **2002**, 1–11.

28. Sutter, K.M. Trade Dispute with China and Rare Earth Elements. *Congr. Res. Serv.* **2019**, *IF11259*, 2–3.

29. CNBC The New U.S. Plan to Rival China and End Cornering of Market in Rare Earth Metals Available online: https://www.cnbc.com/2021/04/17/the-new-us-plan-to-rival-chinas-dominance-in-rare-earth-metals.html (accessed May 2023).

30. MP Materials - What Are Rare Earth Elements: https://mpmaterials.com/what-we-do/

(accessed May 2023).

31. Khan, Y. The U.S. Wants a Rare-Earths Supply Chain. Here's Why It Won't Come Easily. Available online: https://www.wsj.com/articles/the-u-s-wants-a-rare-earths-supply-chain-heres-why-it-wont-come-easily-dfc3b632 (accessed May 2023).

32. Walter, P. Rhodia Recovers Rare Earths. *Chem. Ind.* **2011**, *49*, 30–40.

33. EPA Rare Earth Elements : A Review of Production , Processing , Recycling, and Associated Environmental Issues. *United States Environ. Prot. Agency* **2012**, 135.

34. Habashi, F. Principles of Extractive Metallurgy. *Princ. Extr. Metall.* **1970**, *3*, 1–479.

35. Christiansen, G.; Jackson, W.D. *International Strategic Minerals Inventory Summary Report-Rare-Earth Oxides*; U.S. Dept. of the Interior, Geological Survey, **1993**.

36. Haque, N.; Hughes, A.; Lim, S.; Vernon, C. Rare Earth Elements: Overview of Mining, Mineralogy, Uses, Sustainability and Environmental Impact. *Resources.* **2014**, *3*, 614–635.

37. Faraji, F.; Khanlarian, M.; Roshanfar, M.; Alvial-Hein, G.; Mahandra, H. 27 - Recyclability and Recycling Technologies for Lithium–Sulfur Batteries. In; Gupta, R.K., Nguyen, T.A., Song, H., Yasin, G.B.T.-L.-S.B., Eds.; Elsevier, 2022; pp. 627–651.

38. Rafique, M.M.A. Pyrometallurgy and Electrometallurgy of Rare Earths–Part A: Analysis of Metallothermic Reduction and Its Variants. *Miner. Process. Extr. Metall. Rev.* **2023**, 1–14.

39. Tabuki, H. Japan Recycles Minerals from Used Electronics Available online: http://www.nytimes.com/2010/10/05/business/global/05recycle.html (accessed May 2023).

40. Gupta, C.K.; Krishnamurthy, N. Extractive Metallurgy of Rare Earths. *Int. Mater. Rev.* **1992**, *37*, 197–248.

41. Hewedy, M.A.; Rushdy, A.A.; Kamal, N.M. Bioleaching of Rare Earth Elements and Uranium from Sinai Soil , Egypt Using Actinomycetes. *Egypt. J. Hosp. Med.* **2013**, *53*, 909–917.

42. Kim, J.A.; Dodbiba, G.; Tanimura, Y.; Mitsuhashi, K.; Fukuda, N.; Okaya, K.; Matsuo, S.; Fujita, T. Leaching of Rare-Earth Elements and Their Adsorption by Using Blue-Green Algae. *Mater. Trans.* **2011**, *52*, 1799–1806.

43. McGill, I. *Rare Earth Elements*; 2000.

44. Xie, F.; Zhang, T.A.; Dreisinger, D.; Doyle, F. A Critical Review on Solvent Extraction of Rare Earths from Aqueous Solutions. *Miner. Eng.* **2014**, *56*, 10–28.

45. Hsu, K.H.; Huang, C.H.; King, T.C.; Li, P.K. Separation of Praseodymium and

Neodymium in High Purity (99.9%) by Counter-Current Exchange Extraction and Its Mechanism. In Proceedings of the Proceedings of International Solvent Extraction Conference; 1980; Vol. 80, pp. 80–82.

46. Černá, M.; Volaufová, E.; Rod, V. Extraction of Light Rare Earth Elements by Amines at High Inorganic Nitrate Concentration. *Hydrometallurgy* **1992**, *28*, 339–352.

47. Preston, J.S.; Du Preez, A.C. The Separation of Europium from a Middle Rare Earth Concentrate by Combined Chemical Reduction, Precipitation and Solvent-Extraction Methods. *J. Chem. Technol. Biotechnol.* **1996**, *65*, 93–101.

48. Nair, S.G.K.; Smutz, M. Recovery of Lanthanum from Didymium Chloride with Di(2-Ethylhexyl)-Phosphoric Acid as Solvent. *J. Inorg. Nucl. Chem.* **1967**, *29*, 1787–1797.

49. Wilfong, W.C.; Ji, T.; Duan, Y.; Shi, F.; Wang, Q.; Gray, M.L. Critical Review of Functionalized Silica Sorbent Strategies for Selective Extraction of Rare Earth Elements from Acid Mine Drainage. *J. Hazard. Mater.* **2022**, *424*, 127625-127673.

50. Costa, T.B. da; Silva, M.G.C. da; Vieira, M.G.A. Recovery of Rare-Earth Metals from Aqueous Solutions by Bio/Adsorption Using Non-Conventional Materials: A Review with Recent Studies and Promising Approaches in Column Applications. *J. Rare Earths* **2020**, *38*, 339-355.

51. Mosai, A.K.; Chimuka, L. The Recovery of Rare Earth Elements (REEs) from Aqueous Solutions Using Natural Zeolite and Bentonite. **2019**. 230, 188-206.

52. Asadollahzadeh, M.; Torkaman, R.; Torab-mostaedi, M. Extraction and Separation of Rare Earth Elements by Adsorption Approaches : Current Status and Future Trends Extraction and Separation of Rare Earth Elements by Adsorption Approaches : Current. *Sep. Purif. Rev.* **2021**, *50*, 417-444.

53. Guzzinati, R.; Sarti, E.; Catani, M.; Costa, V.; Pagnoni, A.; Martucci, A.; Rodeghero, E.; Capitani, D.; Pietrantonio, M.; Cavazzini, A.; et al. Formation of Supramolecular Clusters at the Interface of Zeolite X Following the Adsorption of Rare-Earth Cations and Their Impact on the Macroscopic Properties of the Zeolite. *Chemphyschem* **2018**, *19 17*, 2208–2217.

54. Wu, D.; Zhu, C.; Chen, Y.; Zhu, B.; Yang, Y. Preparation , Characterization and Adsorptive Study of Rare Earth Ions Using Magnetic GMZ Bentonite Applied Clay Science Preparation , Characterization and Adsorptive Study of Rare Earth Ions Using Magnetic GMZ Bentonite. *Appl. Clay Sci.* **2012**, *62–63*.

55. Shu, Q.; Khayambashi, A.; Wang, X.; Wei, Y. Studies on Adsorption of Rare Earth Elements from Nitric Acid Solution with Macroporous Silica-Based Bis(2-Ethylhexyl)Phosphoric Acid Impregnated Polymeric Adsorbent. *Adsorpt. Sci. Technol.* **2018**, *36*, 1049–1065.

56. Iftekhar, S.; Srivastava, V.; Casas, A.; Sillanpää, M. Synthesis of Novel GA-g-PAM/SiO2 Nanocomposite for the Recovery of Rare Earth Elements (REE) Ions from Aqueous Solution. *J. Clean. Prod.* **2018**, *170*, 251–259.

57. Dolatyari, L.; Yaftian, M.R.; Rostamnia, S. Fixed-Bed Column Dynamic Studies and Breakthrough Curve Analysis of Eu(III) Ion Adsorption onto Chemically Modified SBA-15 Silica Materials. *Sep. Sci. Technol.* **2017**, *52*, 393–403.

58. Ma, J.; Wang, Z.; Shi, Y.; Li, Q. Synthesis and Characterization of Lysine-Modified SBA-15 and Its Selective Adsorption of Scandium from a Solution of Rare Earth Elements. *RSC Adv.* **2014**, *40*, 41597–41604.

59. Ogata, T.; Narita, H.; Tanaka, M. Adsorption Behavior of Rare Earth Elements on Silica Gel Modified with Diglycol Amic Acid. *Hydrometallurgy* **2015**, *152*, 178–182.

60. Hu, Y.; Drouin, E.; Larivière, D.; Kleitz, F.; Fontaine, F.G. Highly Efficient and Selective Recovery of Rare Earth Elements Using Mesoporous Silica Functionalized by Preorganized Chelating Ligands. *ACS Appl. Mater. Interfaces* **2017**, *9*, 44, 38584-38593.

61. Gan, Y.X. Activated Carbon from Biomass Sustainable Sources. **2021**, 7,39.

62. Yin, C.Y.; Aroua, M.K.; Daud, W.M.A.W. Review of Modifications of Activated Carbon for Enhancing Contaminant Uptakes from Aqueous Solutions. *Sep. Purif. Technol.* **2007**, *52*, 403–415.

63. Barakat, M.A. New Trends in Removing Heavy Metals from Industrial Wastewater. *Arab. J. Chem.* **2011**, *4*, 361–377.

64. Cardoso, C.E.D.; Almeida, J.C.; Lopes, C.B.; Trindade, T.; Vale, C.; Pereira, E. Recovery of Rare Earth Elements by Carbon-Based Nanomaterials—a Review. *Nanomaterials* **2019**, *9*, 1–35.

65. Kano, N.; Pang, M.; Deng, Y.; Imaizumi, H. Adsorption of Rare Earth Elements (REEs) onto Activated Carbon Modified with Potassium Permanganate ($KMnO_4$). **2017**, 51–61.

66. Babu, C.M.; Binnemans, K.; Roosen, J. EDTA-Functionalized Activated Carbon for the Adsorption of Rare Earths from Aqueous Solutions EDTA-Functionalized Activated Carbon for the Adsorption of Rare Earths from Aqueous Solutions. **2018**. 57, 1487–1497.

67. Iannicelli-zubiani, E.M.; Stampino, P.G.; Cristiani, C.; Dotelli, G. Enhanced Lanthanum Adsorption by Amine Modified Activated Carbon. **2018**. 341, 75-82.

68. Awwad, N.S.; Gad, H.M.H.; Ahmad, M.I.; Aly, H.F. Sorption of Lanthanum and Erbium from Aqueous Solution by Activated Carbon Prepared from Rice Husk. *Colloids*

Surfaces B Biointerfaces **2010**, *81*, 593–599.

69. Ashour, R.M.; Abdelhamid, H.N.; Abdel-Magied, A.F.; Abdel-Khalek, A.A.; Ali, M.M.; Uheida, A.; Muhammed, M.; Zou, X.; Dutta, J. Rare Earth Ions Adsorption onto Graphene Oxide Nanosheets. *Solvent Extr. Ion Exch.* **2017**, *35*, 91–103.

70. Sun, Y.; Shao, D.; Chen, C.; Yang, S.; Wang, X. Highly Efficient Enrichment of Radionuclides on Graphene Oxide-Supported Polyaniline. *Environ. Sci. Technol.* **2013**, *47*, 9904–9910.

71. Koochaki-Mohammadpour, S.M.A.; Torab-Mostaedi, M.; Talebizadeh-Rafsanjani, A.; Naderi-Behdani, F. Adsorption Isotherm, Kinetic, Thermodynamic, and Desorption Studies of Lanthanum and Dysprosium on Oxidized Multiwalled Carbon Nanotubes. *J. Dispers. Sci. Technol.* **2014**, *35*, 244–254.

72. Roosen, J.; Spooren, J.; Binnemans, K. Adsorption Performance of Functionalized Chitosan – Silica Hybrid Materials toward Rare. **2014**, *45*,19415–19426.

73. Pylypchuk, I. V.; Kołodyńska, D.; Kozioł, M.; Gorbyk, P.P. Gd-DTPA Adsorption on Chitosan/Magnetite Nanocomposites. *Nanoscale Res. Lett.* **2016**, *11*. 168-178.

74. Wamea, P.; Pitcher, M.L.; Muthami, J.; Sheikhi, A. Nanoengineering Cellulose for the Selective Removal of Neodymium: Towards Sustainable Rare Earth Element Recovery. *Chem. Eng. J.* **2022**, *428*, 131086-131097.

75. Zhu, Y.; Zheng, Y.; Wang, A. A Simple Approach to Fabricate Granular Adsorbent for Adsorption of Rare Elements. *Int. J. Biol. Macromol.* **2015**, *72*, 410–420.

76. Shokobayev, N.M.; Bouffier, C.; Dauletbakov, T.S. Rare Earth Metals Sorption Recovery from Uranium in Situ Leaching Process Solutions. *Rare Met.* **2015**, *34*, 195–201.

77. Pateli, I.M.; Abbott, A.P.; Binnemans, K.; Rodriguez Rodriguez, N. Recovery of Yttrium and Europium from Spent Fluorescent Lamps Using Pure Levulinic Acid and the Deep Eutectic Solvent Levulinic Acid-Choline Chloride. *RSC Adv.* **2020**, *10*, 28879–28890.

78. Page, M.J.; Soldenhoff, K.; Ogden, M.D. Comparative Study of the Application of Chelating Resins for Rare Earth Recovery. *Hydrometallurgy.* **2017**, *169*, 275–281.

79. Nguyen, R.T.; Diaz, L.A.; Imholte, D.D.; Lister, T.E. Economic Assessment for Recycling Critical Metals From Hard Disk Drives Using a Comprehensive Recovery Process. *Jom.* **2017**, *69*, 1546–1552.

80. Bartlett, N.J. Critical Materials Strategy for Clean Energy Technologies. **2011**, 1–170.

81. Hagelüken, C. Recycling the Platinum Group Metals. *Platin. Met. Rev.* **2012**, *56*, 29–35.

82. British Geological Society, Rare Earth Elements, Www.Geolsoc.Org.Uk (Accessed Jul

2021).

83. Binnemans, K.; Jones, P.T. Perspectives for the Recovery of Rare Earths from End-of-Life Fluorescent Lamps. *J. Rare Earths* **2014**, *32*, 195–200.

84. J.W. Lyman; G.R. Palmer Recycling of Rare Earths and Iron from NdFeB Magnet Scrap. *High Temp. Mater. Process. (London, U. K.)* **1993**, *11*, 175–188.

85. Dhammika Bandara, H.M.; Field, K.D.; Emmert, M.H. Rare Earth Recovery from End-of-Life Motors Employing Green Chemistry Design Principles. *Green Chem.* **2016**, *18*, 753–759.

86. Choppin, G.R. Separation Processes for Actinide Elements. *Sep. Sci. Technol.* **1984**, *19*, 911–925.

87. Kraikaew, J.; Srinuttrakul, W.; Chayavadhanakur, C. Solvent Extraction Study of Rare Earth from Nitrate Medium by the Mixtures of TBP and D2EHPA in Kerosene. *J. Met. Mater. Miner.* **2005**, *15*, 89–95.

88. Mohammadi, M.; Forsberg, K.; Kloo, L.; Martinez De La Cruz, J.; Rasmuson, Å. Separation of ND(III), DY(III) and Y(III) by Solvent Extraction Using D2EHPA and EHEHPA. *Hydrometallurgy* **2015**, *156*, 215–224.

89. Yoon, S.J.; Lee, J.G.; Tajima, H.; Yamasaki, A.; Kiyono, F.; Nakazato, T.; Tao, H. Extraction of Lanthanide Ions from Aqueous Solution by Bis(2-Ethylhexyl)Phosphoric Acid with Room-Temperature Ionic Liquids. *J. Ind. Eng. Chem.* **2010**, *16*, 350–354.

90. Baba, Y.; Kubota, F.; Kamiya, N.; Goto, M. Recent Advances in Extraction and Separation of Rare-Earth Metals Using Ionic Liquids. *J. Chem. Eng. Jpn.* **2011**, *44*, 679–685.

91. Firdaus, M.; Rhamdhani, M.A.; Durandet, Y.; Rankin, W.J.; McGregor, K. Review of High-Temperature Recovery of Rare Earth (Nd/Dy) from Magnet Waste. *J. Sustain. Metall.* **2016**, *2*, 276–295.

92. Takeda, O.; Okabe, T.H. Current Status on Resource and Recycling Technology for Rare Earths. *Met. Mater. Trans. E.* **2014**, *1*, 160–173.

93. Gutfleisch, O. Controlling the Properties of High Energy Density Permanent Magnetic Materials by Different Processing Routes. *J. Phys. D Appl. Phys.* **2000**, *33*, 157–172.

94. Okabe, T.H.; Shirayama, S. 2011 - Okabe & Shirayama - Patent - Method and Apparatus for Recovery of Rare Earth Elements 2011.

95. Uda, T. Recovery of Rare Earths from Magnet Sludge by FeCl2. *Mater. Trans.* **2002**, *43*, 55–62.

96. Önal, M.A.R.; Borra, C.R.; Guo, M.; Blanpain, B.; Van Gerven, T. Recycling of NdFeB

Magnets Using Sulfation, Selective Roasting, and Water Leaching. *J. Sustain. Metall.* **2015**, *1*, 199–215.

97. Xu, Y.; Chumbley, L.S.; Laabs, F.C. Liquid Metal Extraction of Nd from NdFeB Magnet Scrap. *Int. J. Mater. Res.* **2000**, *15*, 2296–2304.

98. Takeda, O.; Okabe, T.H.; Umetsu, Y. Recovery of Neodymium from a Mixture of Magnet Scrap and Other Scrap. *J. Alloy. Compd.* **2006**, *165*, *408–412*..

99. Hua, Z.; Wang, J.; Wang, L.; Zhao, Z.; Li, X.; Xiao, Y.; Yang, Y. Selective Extraction of Rare Earth Elements from NdFeB Scrap by Molten Chlorides. *ACS Sustain. Chem. Eng.* **2014**, *2*, 2536–2543.

100. Tanaka, M.; Oki, T.; Koyama, K.; Narita, H.; Oishi, T. Recycling of Rare Earths from Scrap. *Handb. Phys. Chem. Rare Earths* **2013**, *43*, 159–211.

101. Saito, T.; Sato, H.; Ozawa, S.; Yu, J.; Motegi, T. The Extraction of Nd from Waste Nd–Fe–B Alloys by the Glass Slag Method. *J. Alloy. Compd.* **2003**, *353*, 189–193.

102. Marra, A.; Cesaro, A.; Belgiorno, V. Separation Efficiency of Valuable and Critical Metals in WEEE Mechanical Treatments. *J. Clean. Prod.* **2018**, *186*, 490–498.

103. A. Tsamis and M. Coyne *Recovery of Rare Earths from Electronic Wastes: An Opportunity for High-Tech SMEs*; 2015;

104. Abrahami, S.T.; Xiao, Y.; Yang, Y. Rare-Earth Elements Recovery from Post-Consumer Hard-Disc Drives. *Miner. Process. Extr. Metall.* **2015**, *124*, 106–115.

105. Buchert, M. Life Cycle Assessment (LCA) of Nickel Metal Hydride Batteries for HEV Application.; Presentation at IARC, Basel (Switzerland), 2010.

106. Cheret, D.; Santen, S. 7169206B2 Battery Recycling 2007.

107. Lyman, J W; Palmer, G.R. Hydrometallurgical Treatment of Nickel-Metal Hydride Battery Electrodes. In Proceedings of the Hydrometallurgical Treatment of Nickel-metal Hydride Battery Eectrodes; United States, 1995.

108. Larouche, F.; Tedjar, F.; Amouzegar, K.; Houlachi, G.; Bouchard, P.; Demopoulos, G.P.; Zaghib, K. Progress and Status of Hydrometallurgical and Direct Recycling of Li-Ion Batteries and Beyond. *Mater. (Basel, Switzerland)* **2020**, *13.*

109. Yoshida, T; Ono, H; Shirai, R. *Preceedings of Recycling of Used Ni-MH Rechargeable Batteries*; United States, 1995;

110. Zhang, P.; Yokoyama, T.; Itabashi, O.; Wakui, Y.; Suzuki, T.M.; Inoue, K. Hydrometallurgical Process for Recovery of Metal Values from Spent Nickel-Metal Hydride Secondary Batteries. *Hydrometallurgy* 1998, *50*, 61–75.

111. Machacek, E.; Richter, J.L.; Habib, K.; Klossek, P. Recycling of Rare Earths from

Fluorescent Lamps: Value Analysis of Closing-the-Loop under Demand and Supply Uncertainties. *Resour. Conserv. Recycl.* **2015**, *104*, 76–93.

112. Kingsnorth, D. Meeting the Challenges of Supply This Decade. *Present. to Environ. Energy Study,* **2011**.

113. Jiang, Y.; Shibayama, A.; Liu, K.; Fujita, T. Recovery Of Rare Earths From The Spent Optical Glass By Hydrometallurgical Process. *Can. Met. Q. Can Met. Q* **2004**, *43*, 431–438.

114. Suzuki, T.; Tanaka, M.; Ikeda, Y.; Koyama, S.I. Adsorption Behaviors of Trivalent Actinides and Lanthanides on Pyridine Resin in Lithium Chloride Aqueous Solution. *J. Radioanal. Nucl. Chem.* **2013**, *296*, 289–292.

115. Sreedhar, B.; Suzuki, T.; Hobbs, D.T.; Kawajiri, Y. Evaluation of Tertiary Pyridine Resin for the Separation of Lanthanides by Simulated Moving-Bed Chromatography. *J. Sep. Sci.* **2014**, *37*, 2892–2899.

116. Suzuki, T.; Aida, M.; Ban, Y.; Fujii, Y.; Hara, M.; Mitsugashira, T. Group Separation of Trivalent Actinides and Lanthanides by Tertiary Pyridine-Type Anion-Exchange Resin Embedded in Silica Beads. *J. Radioanal. Nucl. Chem.* **2003**, *255*, 581–583.

117. Ikeda, A.; Itoh, K.; Suzuki, T.; Aida, M.; Fujii, Y.; Mitsugashira, T.; Hara, M.; Ozawa, M. Effect of Counter-Anions on the Adsorption of Trivalent Actinides and Lanthanides on Tertiary Pyridine Resin in Alcoholic Chloride and Nitrate Solutions. *J. Alloys Compd.* **2006**, *408–412*, 1052–1055.

118. Ogden, M.D.; Hoch, C.L.; Sinkov, S.I.; Meier, G.P.; Lumetta, G.J.; Nash, K.L. Complexation Studies of Bidentate Heterocyclic N-Donor Ligands with Nd(III) and Am(III). *J. Solution Chem.* **2011**, *40*, 1874–1888.

119. Simonnet, M.; Suzuki, S.; Miyazaki, Y.; Kobayashi, T.; Yokoyama, K.; Yaita, T. Lanthanide Intra-Series Separation by a 1,10-Phenanthroline Derivative: Counterion Effect. *Solvent Extr. Ion Exch.* **2020**, *38*, 430–440.

120. Simonzadeh, N.; Schilt, A.A. Chelation Properties of Silica-Bound 1,10-Phenanthroline. *J. Coord. Chem.* **1989**, *20*, 117–120.

121. Patel, H. Fixed-Bed Column Adsorption Study: A Comprehensive Review. *Appl. Water Sci.* **2019**, *9*, 1–17.

122. Solgi, M.; Tabil, L.G.; Wilson, L.D. Modified Biopolymer Adsorbents for Column Treatment of Sulfate Species in Saline Aquifers. *Materials (Basel).* **2020**, *13*.

123. Basu, M.; Guha, A.K.; Ray, L. Adsorption of Lead on Lentil Husk in Fixed-bed Column Bioreactor. *Bioresour. Technol.* **2019**, *283*, 86–95.

124. Biswas, S.; Mishra, U. Continuous Fixed-Bed Column Study and Adsorption Modelling: Removal of Lead Ion from Aqueous Solution by Charcoal Originated from Chemical Carbonization of Rubber Wood Sawdust. *J. Chem.* **2015**, 1-9.

125. Dorado, A.D.; Gamisans, X.; Valderrama, C.; Solé, M.; Lao, C. Cr(III) Removal from Aqueous Solutions: A Straightforward Model Approaching of the Adsorption in a Fixed-Bed Column. *J. Environ. Sci. Heal. - Part A Toxic/Hazardous Subst. Environ. Eng.* **2014**, *49*, 179–186.

126. Bohart, G.S.; Adams, E.Q. Some Aspects of the Behavior of Charcoal with Respect to Chlorine. *J. Am. Chem. Soc.* **1920**, *42*, 523–544.

127. Burdzy, K.; Aurich, A.; Hunger, S.; Jastrząb, R.; Zabiszak, M.; Kołodyńska, D. Green Citric Acid in the Sorption Process of Rare Earth Elements. *Chem. Eng. J.* **2022**, *437*, 135366-135386.

128. Fila, D.; Kołodyńska, D. Fixed-Bed Column Adsorption Studies: Comparison of Alginate-Based Adsorbents for La(III) Ions Recovery. *Materials (Basel).* **2023**, *16,* 1058-1080.

Chapter 2 – Application of Phenanthroline Functionalised Silica to the Separation of Rare Earth Elements (REEs)

2.1 Advantages of Ion Exchange Over Solvent Exchange

Liquid-liquid extraction is an efficient method for the extraction and partitioning of REEs, however there are several drawbacks that arise from this process. Large amounts of highly flammable toxic solvents are required leading to the formation of large amounts of waste products. The high quantity of waste produced raises safety and environmental concerns and requires proper handling and disposal. Inefficiency of extraction caused by third phase formation can occur and thus requires the need for another ligand to increase the contact time between the organic and aqueous layers, this need adds to the cost and waste products being produced.

2.2 Pyridine and Phenanthroline

Pyridine, a N-donor molecule, can bind to REEs. REE extraction/separation ability of pyridine-functionalized resin materials has been studied using 80 wt% of 4-vinylpyridine and 20 wt% *m/p*-divinylbenzene embedded in silica beads by Suzuki et al. A comparison was made between lithium chloride and hydrochloride eluent solutions for use in a resin-packed column. The column using a hydrochloride solution had more apparent protonation of the resin, allowing complexation of the REEs with the pyridine, as pyridine acts as a soft donor [1–4].

An alternative to pyridine is 1,10-phenanthroline **27**, a precursor of neocuproine **28** (1,10-phenanthroline 2,9 dimethyl), containing two N-donor atoms capable of binding to various elements. Complexation studies have shown that 1,10-phenanthroline can bind to Nd (III) and Am (III) with binding constants ($\log_{10}K_{101}$) of 1.61 ± 0.03 and 3.03 ± 0.09, respectively [5]. F. Hart and F. Laming have isolated 1,10-phenanthroline REE chlorides and 1,10-phenanthroline REE tritthiocyanates for all REEs (La-Lu) [6]. Complexes with other ligands have also been studied, where three β-diketonate units (DBM) surround the REEs to give [Sm(DBM)$_3$(Phen)] **29**, [Sm(DBM)$_3$(NH$_2$Phen)] **30**, [Eu(DBM)$_3$(NH$_2$Phen)] **31** and [Tb(DBM)$_3$(NH$_2$Phen)] **32** (Figure 2.1) [7]. The functionality of 1,10-phenanthroline was also altered to give N-octyl-N-tolyl-1,10-phenanthroline-2-carboxamide (OcTolPTA) where successful complexes with all REEs was achieved [8].

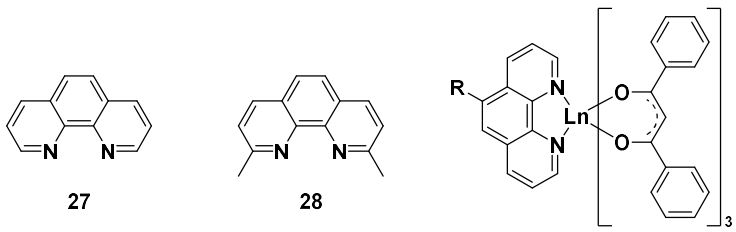

Ln = Sm; R = H ; [Sm(DBM)$_3$Phen] **29**
Ln = Sm; R = NH$_2$; [Sm(DBM)$_3$(NH$_2$Phen)] **30**
Ln = Eu; R = NH$_2$; [Sm(DBM)$_3$(NH$_2$Phen)] **31**
Ln = Tb; R = NH$_2$; [Sm(DBM)$_3$(NH$_2$Phen)] **32**

Figure 2.1. Structures of phenanthroline **27**, neocuproine **28** [Sm(DBM)$_3$(Phen)] **29**, [Sm(DBM)$_3$(NH$_2$Phen)] **30**, [Eu(DBM)$_3$(NH$_2$Phen)] **31** and [Tb(DBM)$_3$(NH$_2$Phen)] **32**

The functionalisation of 1,10-phenanthroline with silica gel was achieved by N. Simonzadeh *et al.* and was able to remove trace levels of transition metal ions from dilute acid solutions, however back extraction was impossible [9]. Functionalisation of the phenanthroline backbone in 1,10-phenanthroline was reported by G. M. Kloster where a (triethoxysilyl)propyl isocyanate was attached to phenanthroline to form a matrix to trap iron (II) and used to form complexes with Eu (III) ions **33** (Figure 2.2) [10,11]. 1,10-phenanthroline can also be functionalised with Merrifield resin (cross-linked chloromethylated polystyrene) and complexes with Nd, Sm, Eu, Gd, Tb, Er and Yb were formed [12].

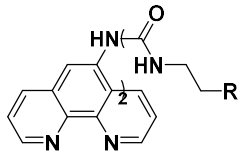

33

Figure 2.2. Structure of modified phenanthroline ligand **33** where R = -Si(OCH_2CH_3)$_3$

2.3 Extraction of Metals Using Neocuproine Functionalised SiO_2 Gel (NC-Si)

Neocuproine holds two extra methyl groups on 1,10-phenanthroline to give the chemical structure 2,9-dimethyl-1,10-phenanthroline **28**. These two methyl groups change the electronics and affect the extraction capabilities for metals. In this work the phenanthroline backbone of neocuproine was modified by a mono bromination at the 5-position using bromine (0.6 equivalents) and H_2SO_4 (20% SO_3). Bromo neocuproine **34** was then used in a Suzuki-Miyaura reaction with 4-hydroxyphenylboronic acid to synthesize 4-(hydroxyphenyl) neocuproine. This ligand was then immobilized onto 3-chloropropyl-functionalised silica gel with NaH in DMF to create neocuproine-functionalised silica gel (NC-Si) **36** shown in Scheme 2.1.

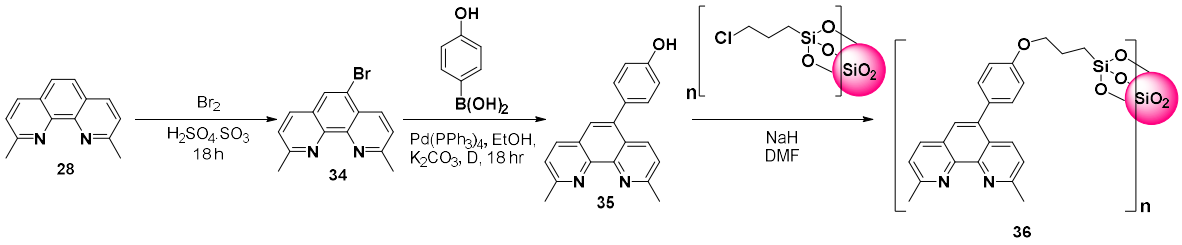

Scheme 2.1. Synthesis of NC-Si **36**

In this work, the synthesis and characterisation of NC-Si will be carried out and fixed-bed dynamic column experiments will determine the extraction capabilities. Isotherm models will be applied to determine the mechanism of extraction.

2.4 References

1. Suzuki, T.; Tanaka, M.; Ikeda, Y.; Koyama, S.I. Adsorption Behaviors of Trivalent Actinides and Lanthanides on Pyridine Resin in Lithium Chloride Aqueous Solution. *J.*

Radioanal. Nucl. Chem. **2013**, *296*, 289–292.

2. Sreedhar, B.; Suzuki, T.; Hobbs, D.T.; Kawajiri, Y. Evaluation of Tertiary Pyridine Resin for the Separation of Lanthanides by Simulated Moving-Bed Chromatography. *J. Sep. Sci.* **2014**, *37*, 2892–2899.

3. Suzuki, T.; Aida, M.; Ban, Y.; Fujii, Y.; Hara, M.; Mitsugashira, T. Group Separation of Trivalent Actinides and Lanthanides by Tertiary Pyridine-Type Anion-Exchange Resin Embedded in Silica Beads. *J. Radioanal. Nucl. Chem.* **2003**, *255*, 581–583.

4. Ikeda, A.; Itoh, K.; Suzuki, T.; Aida, M.; Fujii, Y.; Mitsugashira, T.; Hara, M.; Ozawa, M. Effect of Counter-Anions on the Adsorption of Trivalent Actinides and Lanthanides on Tertiary Pyridine Resin in Alcoholic Chloride and Nitrate Solutions. *J. Alloys Compd.* **2006**, *408–412*, 1052–1055.

5. Ogden, M.D.; Hoch, C.L.; Sinkov, S.I.; Meier, G.P.; Lumetta, G.J.; Nash, K.L. Complexation Studies of Bidentate Heterocyclic N-Donor Ligands with Nd(III) and Am(III). *J. Solution Chem.* **2011**, *40*, 1874–1888.

6. Hart, F.A.; Laming, F.P. Complexes of 1,10-Phenanthroline with Lanthanide Chlorides and Thiocyanates. *J. Inorg. Nucl. Chem.* **1964**, *26*, 579–585.

7. Cabral Campello, M.P.; Palma, E.; Correia, I.; Paulo, P.M.R.; Matos, A.; Rino, J.; Coimbra, J.; Pessoa, J.C.; Gambino, D.; Paulo, A.; et al. Lanthanide Complexes with Phenanthroline-Based Ligands: Insights into Cell Death Mechanisms Obtained by Microscopy Techniques. *Dalt. Trans.* **2019**, *48*, 4611–4624.

8. Simonnet, M.; Suzuki, S.; Miyazaki, Y.; Kobayashi, T.; Yokoyama, K.; Yaita, T. Lanthanide Intra-Series Separation by a 1,10-Phenanthroline Derivative: Counterion Effect. *Solvent Extr. Ion Exch.* **2020**, *38*, 430–440.

9. Simonzadeh, N.; Schilt, A.A. Chelation Properties of Silica-Bound 1,10-Phenanthroline. *J. Coord. Chem.* **1989**, *20*, 117–120.

10. Li, H.R.; Lin, J.; Fu, L.S.; Guo, J.F.; Meng, Q.G.; Liu, F.Y.; Zhang, H.J. Phenanthroline-Functionalized MCM-41 Doped with Europium Ions. *Microporous Mesoporous Mater.* **2002**, *55*, 103–107.

11. Kloster, G.M.; Watton, S.P. Oxidation of Immobilized Iron(II)-1,10-Phenanthroline Complexes by Cerium(IV): A Probe into the Site Accessibility of Metal Complexes Covalently Attached to Silica Sol-Gels. *Inorganica Chim. Acta* **2000**, *297*, 156–161.

12. Lenaerts, P.; Driesen, K.; Van Deun, R.; Binnemans, K. Covalent Coupling of Luminescent Tris(2-Thenoyltrifluoroacetonato) Lanthanide(III) Complexes on a Merrifield Resin. *Chem. Mater.* **2005**, *17*, 2148–2154.

Application of a Phenanthroline Functionalized Silica to the Separation of Rare Earth Elements (REEs)

[1]Zoe Y. Selfe, [1]Laurence M. Harwood, [2]Mark D. Ogden

[1]Department Of Chemistry, University of Reading, Whiteknights, Reading RG6 6AD, UK

[2]Department of Chemical and Biological Engineering, University of Sheffield, Sir Robert Hadfield Building, Sheffield, S1 3JD, United Kingdom

Corresponding author: Zoe.Selfe@pgr.reading.ac.uk

ABSTRACT

Rare Earth Elements (REEs) are essential for the manufacturing of high technological products and are critical to green technology deployment. This work is focused on the application of functionalised silica to the separation of REEs in nitric acid. This research sits in the nexus between advanced nuclear fuel cycle separations and the clash between modern technology and the sustainability of green energy. This application of "taking nuclear to market" investigates the continuous adsorption and separation of the REEs (except Pm), Sc and Y using a fixed-bed of neocuproine-functionalised silica gel (NC-Si). The functionalisation of silica gel with neocuproine involves a three-step synthesis with yields of 71% and 75% for the first and second step. 1 g of neocuproine starting material will produce 3.84 g of NC-Si with 57% of the available sites on the SiO_2 gel functionalised with neocuproine. Functionality of the silica gel was determined using thermogravimetric analysis (TGA), infrared spectroscopy (FT-IR) and energy dispersive X-ray analysis to confirm immobilisation of neocuproine onto silica gel. TGA analysis confirmed *ca*. 5% w/w of neocuproine content was present on the NC-Si giving a molarity of 0.1466 mmol per g of adsorbent. Overall, NC-Si had adsorption capacities ranging from 0.0005 to 0.0012 mg g^{-1} for all REEs (including Sc and Y) with a preference for the later REEs (Ho-Lu) and an overall adsorption capacity of 0.0153 mg g^{-1}. Based on breakthrough times (t_b) the REEs series can be separated into three groups; early (Y, La – Pr) (<3 mins), mid (Sc, Nd - Dy) (3.5 – 15 mins) and late (Ho – Lu) (>44 mins) showing NC-Si has the potential for REE separations. Simple models successfully described breakthrough curves (i.e., Adams-Bohart, Thomas, Yoon Nelson, Modified Dose Response (MDR) and Lagergren's pseudo first and second order rate kinetics) for the adsorption of the multicomponent solution. Adams-Bohart model was able to describe all ions (Sc, Y and all REEs), however it gave the lowest correlation coefficient (R^2 = ~0.81). The MDR and Thomas models were able to fit the early (R^2 = ~0.95) and early/mid (R^2 = ~0.93) REE ions respectively. Yoon-Nelson model was able to fit the mid and later REEs (Nd-Lu) (R^2 = ~0.95) to give the highest correlation coefficient out of all models.

Keywords: synthesis, ion exchange, rare earth elements, rare earth separations, functionalized silica

1 INTRODUCTION

The Rare Earth Elements (REEs) are vital to modern living due to their magnetic and conductive properties. The addition of REEs to the makeup of modern life's hardware makes them stronger, faster, and lighter [1]. The REEs are a group of seventeen chemical elements including scandium (Sc), yttrium (Y) and the lanthanide series (lanthanum (La) to lutetium (Lu)) [2]. Contrary to the name "Rare Earth" the metals are actually quite abundant in the Earth's crust, however they are given their name as they are difficult to separate from each other and other elements. The most abundant REE is Ce with a concentration of 66 ppm in the Earth's crust, similar to that of Cu (68 ppm) [3]. The later REEs are less abundant with Tm and Lu being the least abundant elements with concentrations of 0.3 and 0.31 ppm respectively [3].

REEs have a broad range of applications in many different important high-tech fields in both consumer products and industry including; catalysts (74%), ceramics and glass (10%), metallurgical applications and alloys (6%), polishing (4%) and others (6%) [4]. In the 1960s the majority of applications that required REEs were in the petroleum industry. Today, REEs are used in medical systems, fluorescent lamps, catalysts and clean energy technologies such as wind turbines and electric cars. The main uses that dominate the consumption of REEs are catalysts where cerium carbonate and cerium oxide are used in catalytic converters in vehicles and fluid cracking converters (FCC) for refining crude oil [5]. Neodymium-iron-boron alloys are used in the field of metallurgy as they have strong magnetic fields with uses in computer hard drives, electric vehicles, mobile phones and wind turbines. Currently 7,300 tonnes of Nd and 24,000 tonnes of Ce are being produced worldwide per year [6].

REEs have been present on the EU critical materials list since 2011 due to their high import dependency rate (100%), low recycle rates (1%), and the fact that the bulk of their supply came from the China (90%) [7,8]. The main parameters for identifying the critical nature of a material are the economic importance and supply risk [9]. The economic importance aims at providing insight in terms of end-use applications and the value added for manufacturing sectors corrected by a substitution index parameter [7]. Supply risk is based upon the concentration of primary supply, global suppliers, and the source countries. Supply risk is measured at the 'bottleneck' stage of extraction or processing [9]. Substitution and recycling are considered risk-reducing measures.

In 2020 the global consumption of REEs reached 167,000 tonnes and is forecasted to reach 280,000 tonnes by 2030 [10,11]. The global consumption of NdFeB magnets rose by 18.1% from 2020 to 2021 and will be expected to increase by 8.6% per year until 2035. In 2035 40% of the demand for NdFeB magnets will be used in electric vehicles to keep up with the demand for clean energy [12,13].

Due to the spike in REE prices and finite resources, a balance between mining and recycling has to occur in order to meet the high demands for REEs. Retired wind turbines and electric vehicle motors are rather large and subsequently provide a source of recyclable REEs without too much difficulty. Nissan have developed a method to recover REEs from their electric vehicles by subjecting the motors to 1400 °C with the addition of iron oxide to the molten mixture. Borate-based flux is added to dissolve the REE allowing separation from the iron-carbon slag materials [14].

Unfortunately, infrastructure to recycle smaller products containing REEs, such as hard disk drives (HDD) and mobile phones, is underdeveloped and costly as they contain low concentrations of REEs. In an average hard disc drive (HDD) there are 2.5-4.6 g of NdFeB in amongst other metals such as Al, Fe, Cu, Sn, Ni, AG, Au and Pd [15]. Hitachi have developed a method to recycle the rare earth magnets in hard drives and air conditioners by employing large drums to vibrate the HDDs to allow detachment of the metals from the casing. The metals surface and can be collected via visual screening and X-Ray [8,16]. The traditional route of recovery of Nd from NdFeB permanent magnets in small electronics is hydrometallurgy where

Nd is precipitated out as a double sulfate with H_2SO_4 at room temperature. Conversion to NdF_3 or Nd_2O_3 follows to separate from the steel and copper particles. [8,17]. An issue with hydrometallurgy techniques is the large quantity of harmful chemicals required, the Ames laboratory in Iowa have implemented a route of recovering REEs from scrap NdFeB by dissolution in Cu (II) solutions under 100 °C. Ammonium oxalate is added to precipitate the REEs and calcinated at 800 °C to afford RE_2O_3 which is currently implemented commercially [18].

Phosphor lamps contain the REEs; La, Ce, Gd, Tb, Eu and Y and can last four times longer than incandescent lamps with much higher lumens of light per Watt of electricity consumed, 63 LmW^{-1} compared to 13 LmW^{-1}. Phosphors accounted for 7% of the global volume of rare earths in 2014, with 32% by value [19]. The waste produced from fluorescence lamps contains around 28% REE by weight, making it difficult to recycle as they are comprised of many different elements. Dry separation techniques are first employed where a centrifugal pneumatic separator is first employed to recover 70% of the REEs. Diiodomethane is then added to separate the REEs as they have a higher density than the halophosphates and so will sink [8].

The processing of REEs from mines is a lengthy process involving multiple steps. After mining for REEs, physical beneficiation is required to crush the minerals to particle sizes of 0.1 nm, after which water and fatty acids are added to separate the REE from the low economic minerals. Chemicals beneficiation using HCl and calcination is added to remove strontium/calcium carbonates to give a 85-90% Rare Earth oxide (REO) purity.

Intra-rare earth separation is the most challenging step as they have very similar properties to each other. They most commonly occur in the 3+ oxidation state, however some REEs can be found in other stable oxidation states such as Ce^{4+}, Yb^{2+}, Sm^{2+} and Eu^{2+} [20,21]. The valence 4f-orbitals are diffuse and rather core-like in nature providing minimal shielding for the outer electrons. This causes a decrease in the ionic radii to be observed across the REE series (“Lanthanide Contraction”) and an increase in the Lewis acidity due to increasing nuclear charge [22,23]. Selective oxidation/reduction of some of the REEs is useful for separations as Ce, Pr and Tb can occur in the tetravalent state and trivalent state whereas Sm, Eu and Tb can occur in the divalent state. Fractional distillation is a discontinued technique were hundreds of dissolution and crystallization steps of REE nitrates/hydroxides are required to separate out based on the varying solubilities of the REE [24].

Nowadays, the separation of REEs from each other is typically performed using a counter current liquid-liquid solvent extraction techniques, where the REE ion will transfer from an aqueous solvent to the organic medium (kerosene or aromatic solvents) via the use of a ligand. Commercially used extractants are di-2-ethyl-hexylphosphoric acid (HDEHP) for RE chlorides and sulfates, and tri-n-butyl phosphate (TBP) for RE nitrates. Other examples that are used are 2-ethyl-hexyl-2- ethyl-hexyl-phosphoric acid (HEHEHPA), versatic acid 10 46, versatic acid, Cyanex ® 572 and Aliquat 336 [25]. Most of these ligands contain hard O-atom donors which chelate to the metal cations and fed into the organic phase. DEPHA gives an inter-separation factor of $SP_{RE1/RE2}$ = 2.5, which increases between later REEs. The chemical company Rhône-Poulec can produce all REEs with purities >99.999% using 1,000 separation units requiring ~7.2 tonnes of TBP to yield 1 tonne of Rare Earth metal [26,27].

Another effective method is chromatography, a highly effective method already used in the separation of actinides and REEs from each other. Examples include extraction chromatography, cation-exchange chromatography and displacement chromatography. Spedding *et al* managed to separate REEs from each other using Amberlite IR-100 resin, a strong acid cation exchanger, packed into a column using hydrochloric acid as the eluent [28]. Other work by Strewlow and Victor used a column packed with AG 50W-X4 resin as a cation exchanger to extract REE ions. Hydroxyethylenediaminetriacetate (HEDTA) is added as the eluent to displace the REE ions from the resin and elute them from the column. This allows a separation of Nd and Y to occur from the heavier REEs [29].

Pyridine is a N-donor molecule with the ability to bind to REEs, Suzuki. T *et al* has studied REE extraction/separation ability of pyridine functionalised resin materials using 4-vinylpyridine and *m/p*-divinylbenzene embedded in silica beads. A comparison between lithium chloride and hydrochloride eluent solutions for use in a column packed with the resin material were made. The column using lithium chloride solution had the earlier REEs eluting before the later REEs, the opposite true for the hydrochloride solution. Protonation of the resin in hydrochloride acid is more apparent than in lithium chloride which allows complexation of the REEs with the pyridine, as pyridine acts as a soft donor [30–33].

An alternative to pyridine is 1,10-phenanthroline, a precursor of neocuproine **1** (1,10-phenanthroline 2,9 dimethyl), containing two N-donor atoms capable of binding to various elements. Complexation studies have shown that 1,10-phenanthroline can bind to Nd (III) and Am (III) with binding constants ($\log_{10}K_{101}$) of 1.61 ± 0.03 and 3.03 ± 0.09, respectively [34]. F. Hart and F. Laming have isolated 1,10-phenanthroline REE chlorides and 1,10-phenanthroline REE tritthiocyanates for all REEs (La-Lu) [35]. Complexes with other ligands have also been studied, where three β-diketonate units (DBM) surround the REE to give [Sm(DBM)$_3$(Phen)], [Sm(DBM)$_3$(NH_2Phen)], [Eu(DBM)$_3$(NH_2Phen)] and [Tb(DBM)$_3$(NH_2Phen)] [36]. The functionality of 1,10-phenanthroline was also altered to give N-octyl-N-tolyl-1,10-phenanthroline-2-carboxamide (OcTolPTA) where successful complexes with all REEs was achieved [37].

The functionalisation of 1,10-phenanthroline with silica gel was achieved by N. Simonzadeh and used to remove trace levels of transition metal ions from dilute acid solutions, however back extraction was unachievable due to too strong a bonds formed between the transition metals and 1,10-phenanthroline [38]. Functionalisation of the phenanthroline backbone in 1,10-phenanthroline was reported by G. M. Kloster where a (triethoxysilyl)propyl isocyanate was attached to form a matrix to trap iron (II) [39] and used to form complexes with Eu (III) ions [40]. REE (III) complexes (Ln = Nd, Sm, Eu, Gd, Tb, Er and Yb) have also been formed with 1,10-phenanthroline functionalised Merrifield resin (cross-linked chloromethylated polystyrene) and their luminescence was observed.

This work investigates the functionalisation of neocuproine onto silica, resulting in a novel material called neocuproine functionalised silica (NC-Si). The ability of NC-Si for the adsorption and desorption of REEs will be demonstrated through a fixed-bed column technique. This technique involves an aqueous solution of REEs to be passed through a column of NC-Si where nitric acid will be added as the eluent to elute the REEs into individual fractions of REEs. Ultimately, the findings of this research could have significant implications for industries that rely heavily on REEs, such as electronics, renewable energy, and transportation. The structure and details for this material are given in Figure 1. Neocuproine is a known extractant of copper, iron and cobalt forming 2:1 ligand to metal complexes [41–44]. The methyl groups and the phenanthroline backbone can also easily be modified to form variations of neocuproine [45–48]. As neocuproine is a moiety of 1,10-phenanthroline containing two N-donors with a similar bite size and angle, it is thought that neocuproine will also be able to bind to REEs. If NC-Si is packed into a column and fed with a solution of REEs, the extraction of REEs would occur and preferences for certain REEs would be observed due to the slight differences in properties between REEs.

Functionality	Characteristic	
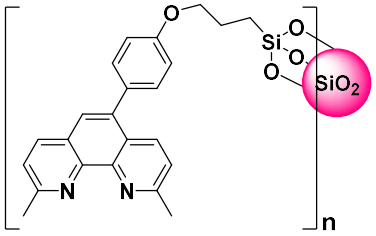	Name:	2,9-dimethyl-1,10-phenanthroline on silica gel
	Acronym:	NC-Si
	Particle size:	40-63 μm*
	Pore size:	60 Å*
	H^+ capacity:	0.628 ± 0.001 mmol g^{-1}

Figure 1. Functionality and characteristics of neocuproine functionalized silica gel (NC-Si). *taken from silica gel precursor material [49]

2. MATERIALS AND METHODS

2.1. Materials

All reagents were purchased from AlfarAesar, Fisher, Fluorochem or Sigma-Aldrich. All chemicals were of analytical grade and used as received without further purification. 3-Chloropropyl-functionalized silica gel (**4** in Figure 2) was purchased from Sigma Aldrich, particle size 230-400 mesh and a pore size of 60 Å) and used as supplied [49]. The extent of chloropropyl labelling of the purchased substrate was ~ 2.5 % loading and the matrix active group was ~ 8 % functionalised.

2.2. Synthesis of NC-Si

In order to introduce functionality onto the phenanthroline backbone of neocuproine 1, mono bromination at the 5-position was carried out using bromine (0.6 equivalents) in the presence of H_2SO_4 (20% SO_3). 4-(Hydroxyphenyl) neocuproine 3 was synthesized by a Suzuki-Miyaura reaction using bromo neocuproine 2 and 4-hydroxyphenylboronic acid. This phenol functionalised ligand could then be immobilised onto 3-chloropropyl-functionalised silica gel using NaH in DMF to afford neocuproine-functionalised silica gel (NC-Si) as shown in Figure 2.

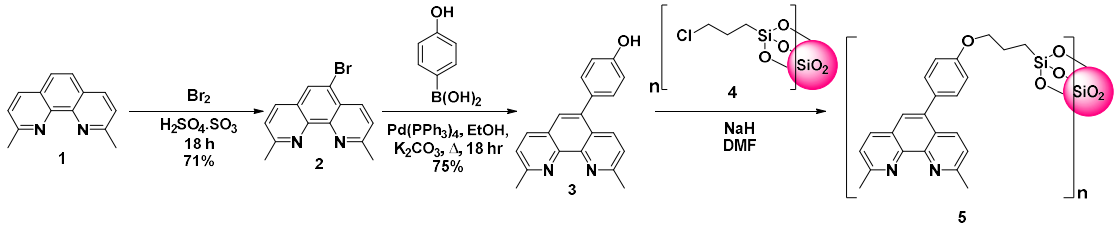

Figure 2. Synthesis of NC-Si solid phase extractant

2.3 Characterisation of NC-Si

Confirmation of the synthesis of 4-(hydroxyphenyl) neocuproine was achieved using NMR analysis using either a Bruker AMX400 or an Advance DFX400 instrument. The immobilisation of neocuproine on the silica surface was estimated by elemental analysis using Energy Dispersive X-ray Spectroscopy (EDX) in conjunction with SEM. Thermogravimetric analysis (TGA) to determine the percentage organic content was performed using a TGA-Q50 thermogravimetric analyser.

For adsorption studies ICP-MS analysis was carried out using a Thermo-Fisher iCAP Q ICP-MS with Rh as the internal standard. A stock solution of 2% HNO_3 spiked with 5 ppb Rh was prepared using ultra-pure water and HNO_3 (70%, purified by redistillation, ≥ 99.999% trace metals basis). All standard solutions were prepared using a stock solution of 2% HNO_3 spiked with 5 ppb Rh. Standards were prepared using metal mixes purchased from Sigma-Aldrich as TraceCERT (Traceable Certified Reference Materials). Standards used to calibrate the ICP-MS were at concentrations of 5, 10, 25, 50 and 100 ppb. All extraction samples were

normalised to 2% HNO_3 and spiked with 5 ppb Rh before testing. Samples (5 mL) were taken before and after extractions to provide true initial and end concentrations. An average of three readings was taken with all samples.

2.4 Adsorption Studies – Dynamic Method

Neocuproine-functionalized SiO_2 gel (1 g) was loaded into a column (D=1.4 cm, H=4.1 cm). A sample of REE solution (containing Sc, Y, La, Ce, Pr, Nd, Sm, Eu, Gd, Tb, Dy, Ho, Er, Tm, Yb, Lu) (~0.12 mg L^{-1}) (10 mL) in 2% nitric acid (HNO_3) was passed through the column with a flow rate of 0.5 mL min-1. The eluate was collected from the column and subjected to Inductively coupled plasma mass spectroscopy analysis (ICP-MS) analysis. Desorption of REE (III) ions was performed by passing samples of nitric acid with various concentrations (0.01 M, 0.1 M, 0.15 M, 0.2 M, 0.3 M, 0.4 M, 0.5 M, 0.6 M, 0.75 M, 1 M) (3 mL) through the column with a flow rate of 0.5 cm^3min^{-1}. The effluent solution was collected in 3 mL fractions and subjected to ICP-MS analysis. A graph of C_0/C_t against time was plotted to obtain the breakthrough curve where C_0 is the initial REE (III) ions concentration (mg L^{-1}), C_t is the outlet concentration (mg L^{-1}). An experimental repetition was conducted using 3-chloropropyl functionalized silica gel and no adsorption of rare earth metals was observed, confirming that the neocuproine ligand itself was responsible for the adsorption of rare earth metals.

2.4.1 Column Kinetics

In order to investigate the adsorption rates of the rare earth ions on neocuproine-functionalised SiO_2 (Figure 1) the adsorption process was determined using pseudo-first order (PFO) and pseudo second-order (PSO) kinetic models. The kinetics are determined by the adsorption sites on the solid extractant, as well as the quantity of rare earth ions (III) in the liquid phase. The linear equation for pseudo-first order model, based on Lagregren's model is given in equation (1) and the linear pseudo second-order expression is given in equation (2) [50–57].

$$ln(q_e - q_t) = ln(k_1 q_e) - k_1 t \quad (1)$$

$$\frac{t}{q_t} = \frac{1}{k_2 q_e^2} + \frac{t}{q_e} \quad (2)$$

Where k_1 (min^{-1}) is the pseudo-first order rate constant, k_2 (min^{-1}) is the second-order rate constant, q_e (mg g^{-1}) is the adsorption capacity at equilibrium. q_t (mg g^{-1}) is the adsorption capacity at any time t (min) which is calculated using equation (3) where C_0 is the initial REE (III) ions concentration (mg L^{-1}), C_t is the outlet concentration (mg L^{-1}), W is the mass of the material used and V is the solution volume (L).

$$q_t = (C_0 - C_t)\left(\frac{V}{W}\right) \quad (3)$$

2.4.2 Breakthrough Modelling

In order to compare the adsorption capabilities of NC-Si **5** between the rare earth elements, a breakthrough curve was plotted. The variation of C_t/C_0 as a function of time for the adsorption of rare earth metals allows models to be applied to the data to find predicted uptake capacity and model suitability. Several mathematical models have been developed to predict the dynamic behaviour of the column. The following models were used to determine the breakthrough performance as well as to calculate the rate constants and adsorption capacities. In this study; Adams-Bohart, Yoon Nelson, Thomas and Modified Dose Response models were applied to the data obtained from the adsorption study [50,54,58,59]. All the models used to fit the breakthrough data are given in SI.2.

2.4.3 Gibbs Free Energy

To determine the spontaneity of the adsorption reaction, the change in Gibbs free energy (∆G°) was determined using equations (4) and (5).

$$K_C = \frac{q_e}{C_e} \quad (4)$$

$$\Delta G^{\circ} = -RTlnK_c \quad (5)$$

Where K_c is the equilibrium constant (calculated from equation (4)), q_e is the amount of ion (mg) absorbed onto **5** from 1 L of solution at equilibrium, C_e is the equilibrium concentration (mg L^{-1}) of the ion in the eluted solution, T is the temperature in Kelvin and R is the gas constant (j mol^{-1} K^{-1}) to give ΔG (kJ mol^{-1} K^{-1}) [50].

3 RESULTS

3.1 Characterisation of Adsorbent

Full characterization data is shown in supplemental information (SI) section. FT-IR showed both NC-Si (**5** Figure. 2) and chloropropyl-functionalised SiO_2 (CP-Si) gel (**4** Figure. 2) have strong Si-O-Si stretches at 1052 cm^{-1}. However only NC-Si **5** possessed weak absorptions corresponding to C=C aromatic vibrations from the ligand between 1500-1600 cm^{-1} (SI.1.1). CP-Si and NC-Si were both analysed using energy dispersive X-ray spectroscopy (SI.1.2) to measure the decrease in Cl content when functionalising CP-Si with neocuproine. Over half of the chlorine was found to have been lost which equates to ~57% immobilisation of neocuproine onto the available sites on the SiO_2 gel. TGA analysis showed a mass loss around 90 °C, corresponding to evolution of absorbed water. The subsequent mass loss between 100-475 °C relates to the decomposition of organic matter, indicating circa 5% w/w of 4-hydroxypropyl neocuproine content is in NC-Si as depicted in SI 2.3. 5% w/w of 4-hydroxypropyl neocuproine (0.146 mmol present in 1 g of NC-Si **5**).

3.2 Adsorption Studies – Dynamic Method

Column parameters determined from the dynamic data are presented for all the rare earths, apart from Pm, in Table 1. The breakthrough curves, $C_t/C_0 = f(t)$, for the rare earth metals (III) (La-Lu) and Sc (III) and Y(III) are displayed in Figure 3.

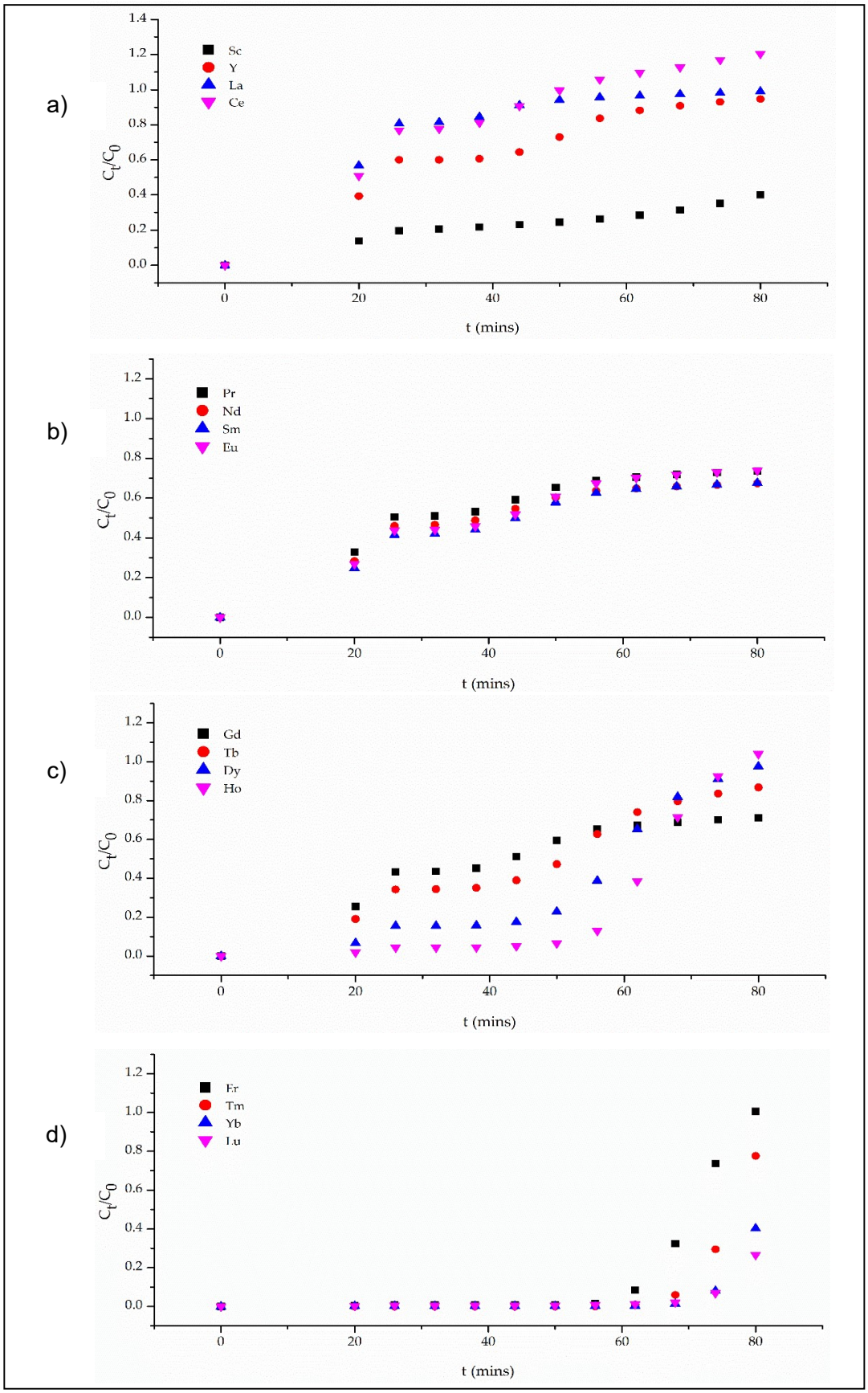

Figure 3. Breakthrough curves for the adsorption of first quarter of the REE series (a), second quarter of the REE series (b), third quarter of the REE series (c) and the last quarter of the REE series (d) rare earth metals by NC-Si flow rate 0.5 mL min^{-1} .

By analyzing the breakthrough curves in a dynamic adsorption process, the performance of a fixed-bed adsorption can be evaluated based on the breakthrough time (t_b) and exhaustion time (t_s) [60,61]. The t_b is the point where the effluent concentration (C_t) from the column is *ca.* 5% of the initial concentration (C_t/C_0 = 0.05) and the t_s is the point where the concentration of the effluent reaches *ca.* 95% of the initial concentration (C_t/C_0 = 0.95). The time it takes for 50% of the ions to elute (C_t/C_0 = 0.5) (τ) is also a key characteristic in the analysis of breakthrough curves. The total adsorption capacity for all REEs extracted from the aqueous inlet solution is 0.0153 mg g^{-1} which is rather low compared to other materials from literature and improvements can be made into increase extraction efficiency. TGA analysis and elemental analysis shows that hydroxyphenyl-neocuproine **3** only makes up ~0.05 g of 1 g of NC-Si **5** (section 3.1, SI.1.2 and SI.1.3). If 20 g of NC-S **5** was employed, this would equate to 1 g of the active binding functional group, neocuproine, which would allow a total adsorption capacity of 0.31 mg of all REE ions. Comparing the mass of the neocuproine content (~0.05 g per 1 g of NC-Si as described in sections 3.1, SI.1.2 and SI.1.3) to the overall adsorption capacity (0.0153 mg g^{-1}) gives a metal to ligand molar ratio of 1:1450 using the average molecular weight of all REEs (excluding Promethium), Y and Sc (139.23).

The breakthrough curves of the rare earth series demonstrate significant differences in the kinetics of adsorption/desorption between each ion. Based on the time to breakthrough (t_b), the series can be partitioned into three groups: early, mid, and late rare earth ions (III), as shown in Table 1 and Figure 4. As the ionic radii of the REE ions decrease across the series, the charge density increases, leading to stronger bonds formed with neocuproine. This ultimately results in longer elution and t_b times.

Table 1. Column parameters determined for breakthrough behavior upon increasing nitric acid concentration 0.01 – 1 M. Flow rate; 0.5 mL min^{-1}, pH; 5, temperature; 24°C.

REE	Breakthrough		Exhaustion		50% Capacity	
	conc. (units)	time (mins)	conc. (units)	time (mins)	conc. (units)	time (mins)
Sc	0.0036	7.3				
Y	0.0015	2.6			0.0008	23.1
La	0.0024	1.8	0.00013	53.4	0.0013	17.6
Ce	0.0034	2.0	0.00018	46.9	0.0018	19.7
Pr	0.0036	3.0			0.0019	25.9
Nd	0.0036	3.6			0.0019	39.3
Sm	0.0035	4.1			0.0019	44.1
Eu	0.0034	3.7			0.0018	42.2
Gd	0.0022	3.9			0.0011	42.9
Tb	0.0024	5.3			0.0013	51.1
Dy	0.0027	15.2	0.00014	77.6	0.0014	58.6
Ho	0.0026	44.0	0.00015	75.3	0.0014	64.1
Er	0.0027	59.1	0.00014	78.8	0.0014	70.6
Tm	0.0027	66.9			0.0014	76.6
Yb	0.0028	71.3				
Lu	0.0027	71.6				

Some of the rare earth ions did not reach 50% breakthrough time (τ) (Sc, Yb and Lu) or exhaustion point (t_s) (Sc, Y, Pr-Tb and Tm-Lu), indicating that a larger volume and/or a higher concentration of nitric acid would be required to elute those ions (Table 1 and Figure 4). The largest difference of breakthrough times between two adjacent rare earth ions occurred between Dy (II) and Ho (III), as well as between Ho (III) and Er (III). The large differences in t_b between various rare earth ions across the series could provide a means to separate the rare earth ions from each other into pure fractions or smaller groups of similar rare earth ions, potentially only requiring just a few steps.

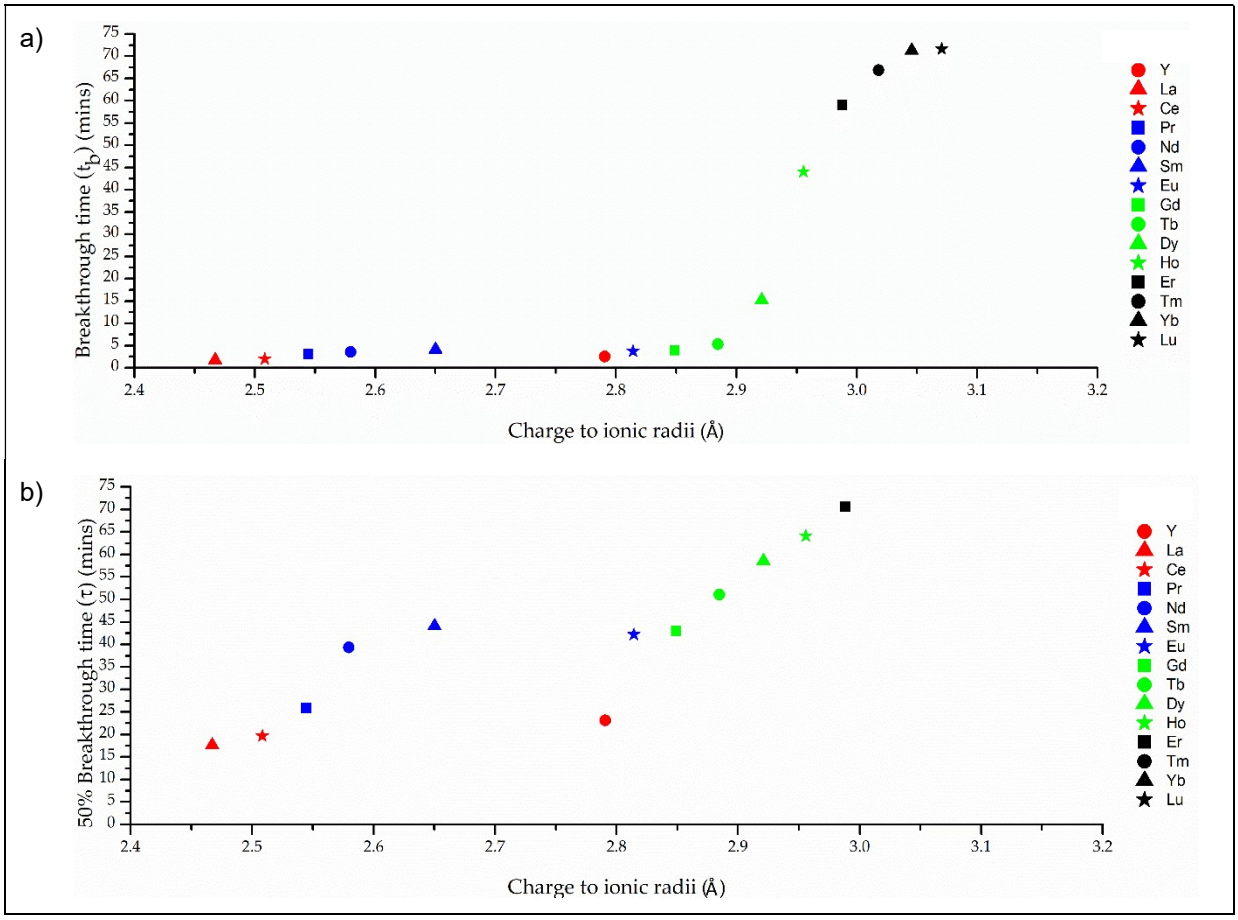

Figure 4. Breakthrough times a) for t_b and b) for τ upon increasing nitric acid concentration 0.01 – 1 M. Flow rate; 0.5 mL min^{-1}, pH; 5, temperature; 24°C.

Y has a similar z/r ratio to Sm and Eu, however it elutes a lot sooner from the column in relation to elution times of Sm and Eu. Y has a similar τ time to Pr, La, and Ce at 15-22 mins, as displayed in Figure 2. similarly, the t_b time of Y is also a lot less than its neighbouring ions; Sm and Eu and elutes around similar times to Y, La and Ce (~4 mins), showing that z/r isn't the only factor involved in the desorption process.

3.2.1 Column Kinetics

A graph of $\ln(q_e - q_t)$ was plot against t using Lagregren's expression (1), linear regression was applied and the pseudo first-order rate constant (k_1) and q_e was found from the slope and intercept for each of the rare earth ions respectively and displayed in table 2 [62]. Similarly, a linear regression plot was applied to a graph of q_t/t against t and the pseudo second-order rate constant (k_2) and q_e was found from the intercept and the slope respectively using expression (2) (Table 2). The pseudo-second order model determines the q_e values to be much closer to the experimental q_e with higher correlation coefficients (R^2) than the pseudo first-order model. Pseudo second-order dynamic model assumes that two reactions are occurring; the first one is fast and reaches equilibrium quickly and the second reaction is much slower. The negative values for k_2 and k_2 reiterated the fact that the process studied in this model is desorption of the ions from neocuproine-functionalised SiO_2 gel whereas the Lagergren equation describes adsorption.

Table 2. REE uptake by NC-Si **5** in 2 M nitric acid subsequentially increasing nitric acid concentration 0.01 – 1 M. Flow rate; 0.5 mL min^{-1}, pH; 5, temperature; 24°C.

REE	Experimental	PFO			PSO		
	q_e (mg g^{-1}) (x 10^{-3})	q_e (mg g^{-1})	k_1 (min^{-1})	R^2	q_e (mg g^{-1}) (x 10^{-3})	k_2 (min^{-1})	R^2
Sc	1.103	8.13E-04	-0.027	0.997	1.011	-1240	0.999
Y	0.743	3.10E-03	-0.022	0.915	0.531	-809	0.994
La	0.541	8.46E-03	-0.011	0.842	0.378	-1920	0.999
Ce	0.606	4.80E-03	-0.020	0.930	0.347	-829	0.988
Pr	0.824	3.77E-03	-0.018	0.882	0.666	-1300	0.999
Nd	0.878	4.09E-03	-0.017	0.873	0.727	-1420	0.999
Sm	0.913	3.14E-03	-0.020	0.880	0.747	-1140	0.999
Eu	0.886	2.70E-03	-0.023	0.890	0.704	-962	0.998
Gd	0.860	2.97E-03	-0.021	0.888	0.694	-1090	0.999
Tb	0.971	1.37E-03	-0.034	0.928	0.719	-528	0.992
Dy	1.111	4.14E-04	-0.053	0.918	0.788	-343	0.978
Ho	1.165	5.50E-05	-0.083	0.899	0.828	-283	0.961
Er	1.165	3.43E-06	-0.119	0.852	0.885	-289	0.948
Tm	1.167	1.49E-10	-0.300	0.952	0.994	-394	0.964
Yb	1.189	8.30E-07	-0.102	0.662	1.110	-778	0.990
Lu	1.165	2.61E-06	-0.088	0.803	1.113	-1170	0.996

3.2.2. Adsorption Modelling

Several mathematical models have been proposed for predicting the efficiency of lab scale column studies for industrial applications. Model constants for selected REE uptake by NC-Si are presented in Figure 5. In this present study, Adams-Bohart, Yoon Nelson, Thomas and MDR models were employed to find the best fitting model to predict the behavior of the dynamic column. The key parameters obtained from modelling are presented in table 2.

The values of $\ln(C_0/C_t)$ were plotted against t and the slope (k_{AB}) and intercept (N_0) were calculated using the linear Adams-Bohart equation (S1). The values of k_{AB} and N_0 are represented in table 3 along with the correlation coefficients for each rare earth ion. The correlation coefficients obtained are found to have relatively low values (between 0.592 and 0.938) suggesting that the Adams-Bohart model is not the most suitable to describe the rare earth adsorption mechanism on neocuproine-functionalised SiO_2 gel **5** in a dynamic regime. Adams-Bohart was the only model able to describe the adsorption process of Sc (III) on NC-Si **5**. Figure 5 a) shows that the K_{AB} is directly proportional to the charge density of the ion until 3 Å, where we see a decrease in K_{AB} after Tm.

The Yoon-Nelson model determines the values of τ and k_{YN} to obtained from a graph of C_t/C_0 against t by plotting a non-linear curve fit using equation (3), these constants and correlation coefficients for all rare earth ions (III) are represented in Table 3. The k_{Yn} is the rate constant that explains the diffusion characteristics of the mass transfer zone. The Yoon-Nelson isotherm was not applicable to the early rare earth ions (III) (Sc-Pr) and so no constants were obtained. For the remaining rare earth ions (III), high correlation coefficient values were obtained (between 0.856 and 1) proving that the Yoon-Nelson model provides a good description of the mechanism of adsorption of the mid/late rare earth ions onto neocuproine-functionalised SiO_2 gel **5**. The lowest k_{YN} values are for the mid rare earth ions (III) (Nd-Tb), with values between 0.024 and 0.033 $mins^{-1}$, indicating they have a better mass transfer by diffusion rate compared to the later rare earths. It is desirable to have a high τ-value as it shows the absorbent is able to absorb more of the absorbate metal ion. It appears that τ increases as the size of the ion

decreases, showing the absorbent has bound to a high quantity of small ions. The k_{YN} constant remains very similar for Nd, Sm, Eu, Gd and Tb, whom have a charge to ion radii <2.9. After which, the k_{YN} increases till Tm (3.05 Å) and then decreases again as shown in Figure 5 b).

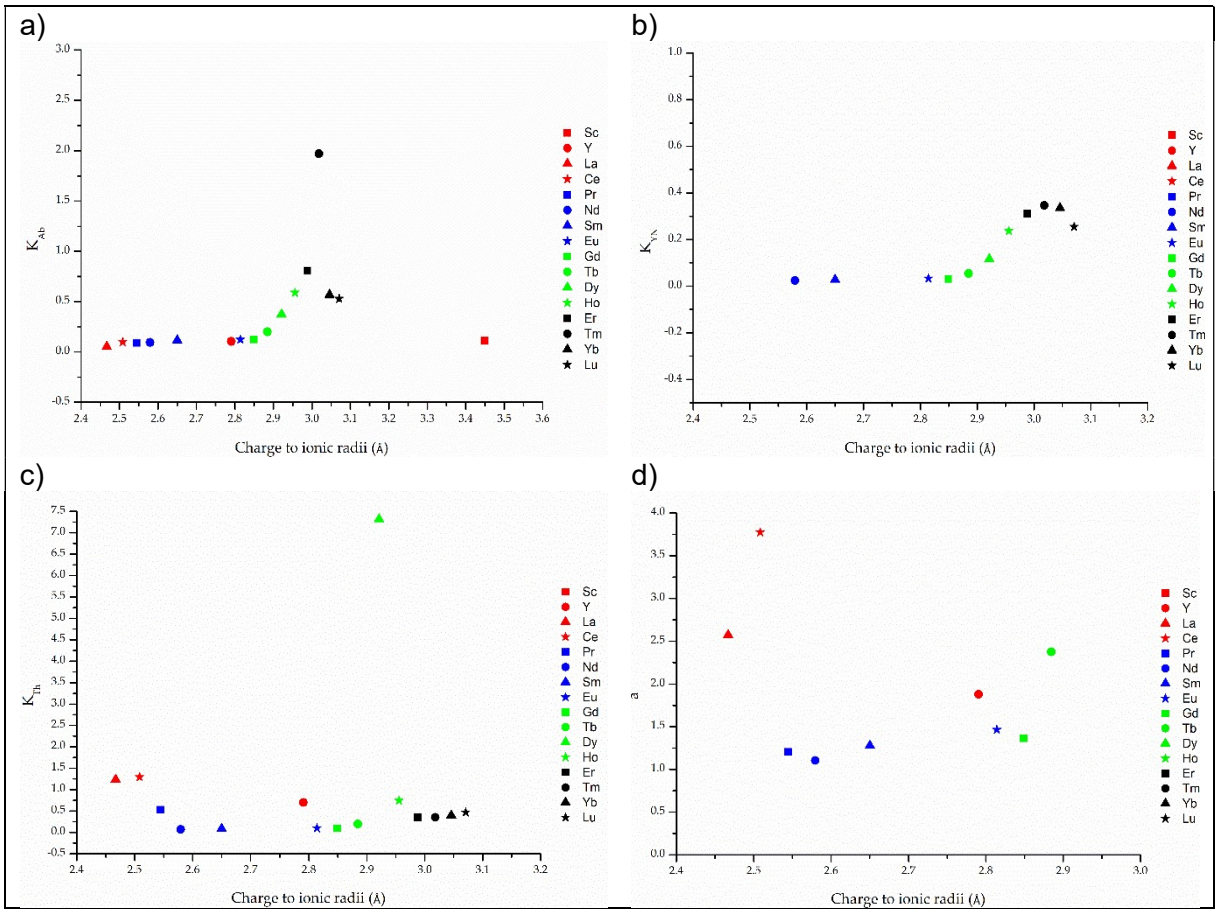

Figure 5. Model parameters for breakthrough models plotted versus charge density indicator (Z/IR) of REE – a) Adams-Bohart constant (k_{AB}), b) Yoon-Nelson constant (k_{YN}), c) Thomas constnant (k_{Th}) and d) MDR constant (a) - upon increasing nitric acid concentration 0.01 – 1 M. Flow rate; 0.5 mL min^{-1}, pH; 5, temperature; 24°C.

Overall, the Thomas model provided an excellent fit to the experimental data, with a higher overall R^2 value than the Adams-Bohart model for every rare earth ion, except for Sc(III) which could not be fit due to the fact that minimal adsorption had occurred. The well-fitting of the experimental data with the Thomas model indicated that the external and internal diffusion is not the limiting step. The k_{Th} and q_0 was found by plotting a non-linear curve using equation (5) to a graph of C_t/C_0 against t. The q_0 values are higher for the late rare earth ions (III) compared to the early/mid rare earth ions. Figure 5 c) displays the relationship between k_{Th} and the charge to ionic radii, there isn't much of a trend, however Dy has the highest k_{Th}.

Table 3. Breakthrough modelling parameters for REE on NC-Si

REE	Adams-Bohart			Yoon-Nelson		
	k_{AB} (L mg^{-1} min^{-1})	N_0 (mg L^{-1})	R^2	k_{YN} (min^{-1})	τ (min)	R^2
Sc	0.114	1.476	0.938			
Y	0.104	0.743	0.864			
La	0.054	0.690	0.634			
Ce	0.097	0.555	0.841			
Pr	0.090	0.946	0.778			
Nd	0.094	1.002	0.742	0.024	39.766	0.856
Sm	0.116	0.935	0.794	0.028	44.499	0.898
Eu	0.121	0.871	0.837	0.033	40.163	0.932
Gd	0.124	0.859	0.807	0.031	41.970	0.913
Tb	0.198	0.762	0.923	0.054	46.635	0.949
Dy	0.372	0.727	0.931	0.117	57.328	0.953
Ho	0.586	0.746	0.907	0.237	63.899	0.991
Er	0.807	0.797	0.829	0.312	70.377	0.997
Tm	1.969	0.720	0.870	0.347	76.462	1.000
Yb	0.567	1.158	0.592	0.336	81.189	0.999
Lu	0.526	1.144	0.741	0.255	84.009	0.995

REE	Thomas			Dose-Response		
	k_{Th} (L mg^{-1} min^{-1})	q_0 (mg g^{-1})	R^2	q_m (mg g^{-1})	a	R^2
Sc						
Y	0.700	1.209	0.919	0.0016	1.879	0.955
La	1.236	0.947	0.959	0.0011	2.574	0.991
Ce	1.292	0.996	0.876	0.0012	3.773	0.885
Pr	0.527	1.303	0.822	0.0019	1.203	0.984
Nd	0.070	6.841	0.838	0.0023	1.103	0.937
Sm	0.087	7.182	0.885	0.0025	1.276	0.951
Eu	0.099	6.793	0.923	0.0023	1.461	0.952
Gd	0.092	6.949	0.902	0.0022	1.364	0.951
Tb	0.195	6.465	0.943	0.0026	2.375	0.887
Dy	7.320	0.439	0.947			
Ho	0.742	10.146	0.990			
Er	0.349	31.523	0.996			
Tm	0.350	37.835	1.000			
Yb	0.396	34.132	0.999			
Lu	0.468	22.494	0.993			

A non-linear curve was plot using equation (7) to a graph of C_t/C_0 against t to determine whether the Modified Dose Response model (MDR) gave a good description of the mechanics of the adsorption of the rare earth ions (III) by neocuproine-functionalised SiO_2 gel **5**. Good correlation coefficients were obtained (0.8865 to 0.9914) for the early to mid-rare earth ions (III) (La to Tb) as well as Y(III), however Sc (III) could not be described by MDR as little Sc (III) was desorbed by neocuproine-functionalised SiO_2 gel **5**. The late rare earth ions (III), however, could not be described by the MDR model as no fitting could be achieved. Higher q_m values were found for the mid rare earth ions (III) compared to the early ions. As the charge to ionic radii increases, a trend with the MDR constant (*a*) was not observed (Figure 3 d)

Overall, the Adams-Bohart model could be used to describe all rare earth ions, however the R^2 values were the lowest compared to Yoon-Nelson, Thomas and MDR models. Out of the ions that were able to have models fit, Yoon Nelson had the highest average value of R^2 and therefore could be used to describe the adsorption process of the late and mid REE ions.

3.2.3. Gibbs Free Energy

The Gibbs free energy (ΔG°) was calculated for each of the rare earth ions to understand how favourable the adsorption of rare earths are onto **5** are at room temperature (Figure 6). The positive values for rare earth ions, except La and Ce, indicate a spontaneous nature of adsorption at room temperature [63]. A negative ΔG° for La and Ce indicates an unfavourable reaction where energy input is required for absorption onto **5**. Overall, the later rare earth ions (Dy-Lu) have a much more negative ΔG° value than the early and mid-rare earth ions, with Tm having the lowest value at -76 kJ mol^{-1}. The trend in Gibbs free energy change compared to charge to ionic radii is observed in figure 6.

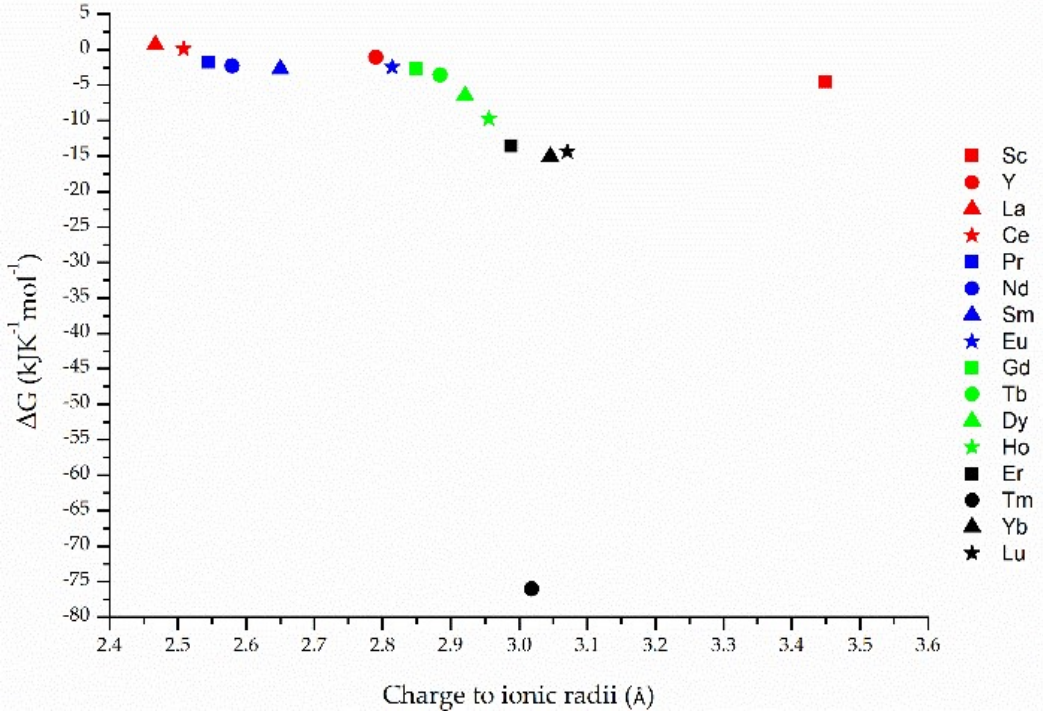

Figure 6. Gibbs free energy change (ΔG°) for the adsorption of rare earth ions onto NC-Si

4. Discussion

The method described separates the REE series into three groups; early, mid and later REE ions. The late REEs are more strongly sorbed than the early and mid REEs and have longer breakthrough times and longer exhaustion times, requiring larger volumes and/or higher concentrations of nitric acid. These ions have a higher charge to ionic radii ratio which may account for their longer elution times from the column as they form stronger bonds to the neocuproine core. Elution studies using CP-Si **4** showed no extraction of REEs occurred, proving that absorption is purely down to neocuproine itself and not getting “lost” in the silica matrix. Y was an anomaly to the trend as it has similar z/r ratios to Sm and Eu, however it elutes around a similar time to the earlier ions; Pr, La and Ce. Unlike the rest of the REE ions, Y has a unique electronic structure, while the other REE ions have partially filled 4*f* orbitals, Y has a full 4*f* orbital and partially filled 5*s* and 4*d* orbitals. Weaker bonds with NC-Si are formed and Y is eluted sooner. Sc has the smallest ionic radii and therefore has the highest charge to

ionic radii density, allowing it to form strong covalent bonds with atoms of high electronegativity, such as nitrogen.

Fitting data to isothermal and kinetic data is a useful tool for quantifying adsorbent capacities, rates and breakthrough times as well as determining competitive behavior between ions. Data can then be compared to other absorbents and suitability can be assessed. The model parameters here may not be transferable to real life REE waste sludges as concentrations will vary and other components in the aqueous media system may be present. This data gives a preliminary account of the absorption behaviour of NC-Si. All successful fittings are provided in supplementary information.

From the data it is noted that the Adams-Bohart model manages to describe all REE ions with reasonable fit to the data (average R^2 = 0.814). Showing that, for all REE ions, the assumption that the experimental data follows a linear equilibrium isotherm and that the rate of adsorption is proportional to the difference between the concentration of the solute in the bulk fluid and the concentration of the solute on the adsorbent surface.

The mid and the later REE ions (Nd-Lu) can be described by the Yoon-Nelson model (average R^2 = 0.953) which is an extension of the Adams-Bohart model. For the REEs, Nd to Lu, it can be assumed, according to the Yoon-Nelson model, that the pore diffusion is the rate-limiting step and that the concentration of the solute at the adsorption sites is proportional to the concentration of the solute in the pores. The Yoon-Nelson also gives an accurate measure of the τ when compared to experimental data where the τ increases upon increasing z/r ratio.

All REE ions, except for Sc, can be described by the Thomas model, with a good fitting (average R^2 = 0.932). The Thomas model states that the driving force of the adsorption is the difference between the concentration of the adsorbate in the bulk phase and the concentration at the surface of NC-Si and that the adsorption process is reversible. The Thomas model also shows an increase in the adsorption capacities upon increasing z/r ratio.

The Modified Dose Response (MDR) model can be used to describe the adsorption behavior for the early and mid REEs, except for Sc. The MDR model takes into account the flow rate, initial concentration of adsorbate and the characteristics of the adsorbent which can all be varied in to improve the performance of the fixed-bed column system. The MDR model states that the adsorption capacity is related to the concentration of ions in the bulk fluid. If there is a high concentration of REE ions in the bulk fluid, then the adsorption capacity will be lower than if it was a low concentration as the solid state will get saturated quicker.

Silica provides a good material for extraction of metals into high acidic solutions as it is chemically stable. The synthesis of NC-Si was reliable and gave good yields with the potential to be scaled up if implemented in industry.

Previously, solid supports made of various materials have been used to extract REE ions from aqueous media. Table 4 provides a comparison of the adsorption capacities of solid supports from multi-element mixtures of REEs. [64]. Among the various solid supports, phosphinic acid, sulfonic acid, diglycolamides, and carbon-based materials have been the most extensively studied. The adsorption capacities of diglycolamides and hydroxamic acids are found to be the highest, with values exceeding 15 and 190 mg g^{-1}, respectively. On the other hand, sulfonic acid resins exhibit a relatively lower adsorption capacity of around 10 mg g^{-1} for all REE ions with no various across the series [65]. Among the various materials, silica-supported poly-diglycolamide has been observed to provide the best separation, as it exhibits the greatest difference in adsorption capacities between the early and late REE [66]. In general, an increase in the z/r ratio results in an increase in the adsorption capacity of the solid supports, with a few exceptions. For instance, kenaf cellulose-based poly(hydroxamic acid) ligand, graphene oxide-

corn zein composites, and poly(acrylamino phosphonic dithiocarbamate) fibers exhibit a decrease in adsorption capacity upon increasing the z/r ratio [64,67,68]. NC-Si **5** appears to have low *q* in comparison to the other adsorbents due to the low concentration of neocuproine onto the silica gel if this concentration of ligand onto the solid supports were to be increased then NC-Si **5** would stand in better stead to be used in industry for the extraction and recycling of REE ions.

Table 4. Comparison of solid supports for the extraction of REE ions

Solid support	Functional Group	Analyte	Adsorption Capacity ($mg\ g^{-1}$)	Ref.
Modified Activated Carbon with 0.01 mol^{-1} $KMnO_4$	-	Y, Sc, La, Yb, Lu, Eu,	0.048, 0.051, 0.05, 0.06, 0.051, 0.051	[69]
Fe_3O_4@mSiO_2–DODGA	Diglycolamide	Y, Sc, Nd, Sm, Eu, Ho, Yb, Lu,	16.29, 14.28, 60.80, 27.54, 36.86, 17.16, 34.36, 42.15,	[70]
Silica gel modified with diglycol amic acid	Diglycolamide	La, Ce, Pr, Nd, Sm, Eu, Gd, Tb, Dy, Ho, Er, Tm, Yb and Lu	10.3, 14.7, 12.8, 16.2, 18.9, 20.9, 21.6, 22.8, 25.9, 27.2, 28.0, 28.6, 25.7, 21.2	[71]
Silica-supported poly-diglycolamide	Diglycolamide	La, Ce, Pr, Nd, Sm, Ey, Gd, Tb, Yd, Ho, Er, Tm, Yb, Lu	29, 32, 33, 35, 39, 42,51, 48, 51, 52, 50, 48, 49	[66]
Fluorinated b-diketone group on solid support styrene divinyl benzene	Diketone	La, Ce, Nd, Sm, Eu, Gd, Dy, Er, Yb, Lu	9.91, 9.82, 8.37, 9.20, 8.49, 9.95, 10.53, 9.18, 9.33, 9.63	[72]
Alkyl phosphinic acid resin (APAR)	Phosphinic acid	Y, La, Ce, Pr, Nd, Sm, Eu, Gd, Tb, Dy, Ho, Er, Tm, Yb, Lu	1.40,1.99, 1.96, 1.98, 2.03, 2.14, 2.14, 2.18, 2.18, 2.22, 2.21, 2.22, 2.26, 2.32, 2.36	[73]
Kenaf cellulose-based poly(hydroxamic acid) ligand	Hydroxamic acid	La, Ce, Pr, Gd, Nd, Eu, Sm	260, 245, 235, 220, 210, 195, 192	[64]
Graphene oxide-corn zein composites	-	Y, La, Er, Yb, Nd	14.2, 17.3, 11.7, 10.1, 9.7	[67]
DOWEX 50WX8	Sulfonic acid	Y, La, Ce, Nd, Dy, Gd	11.2, 25.4, 23.3, 21.2, 16.9, 17.7	[65]
Lewatit MDS 200H	Sulfonic acid	Y, La, Ce, Nd, Dy, Gd	10.6, 26.8, 24.9, 20.9, 16.2, 17.9	[65]
Purolite C160	Sulfonic acid	Y, La, Ce, Nd, Dy, Gd	10.0, 28.7, 26.4, 25.5, 13.0, 13.8	[65]

Poly(acrylamino phosphonic dithiocarbamate) fibres	Phosphonic acid	Y, La, Ce, Pr, Nd, Sm, Eu, Gd, Tb, Dy, Ho, Er, Tm, Yb, and Lu	62.59, 28.60, 30.29, 30.95, 31.70, 32.68, 32.68, 31.79, 32.16, 31.51, 31.36, 30.32, 30.98, 31.69, 31.15	[68]
NC-Si **5**	Phenanthroline	Y, Sc, La, Ce, Pr, Nd, Sm, Eu, Gd, Tb, Dy, Ho, Er, Tm, Yb, Lu	0.0016, 0.0038, 0.0026, 0.0036, 0.0038, 0.0038, 0.0037, 0.0036, 0.0023, 0.0026, 0.0028, 0.0028, 0.0028, 0.0028, 0.003, 0.0029	This study

5. CONCLUSIONS

The REE adsorption performance of NC-Si **5** was evaluated through a continuous-flow, fixed-bed adsorption experiment. The Adams-Bohart model could be used to describe all rare earth ions, however the R^2 values were the lowest compared to Yoon-Nelson, Thomas and MDR. Out of the ions that were able to have models fit, Yoon Nelson had the highest average value of R^2 and therefore described adsorption of REE ions onto **5**. Lagergren's pseudo second-order reaction kinetics provided a better fit to the data with higher R^2 values than pseudo first-order reaction kinetics. Pseudo second-order reaction kinetics gave closer theoretical q_e values for all rare earth ions than pseudo first-order reaction kinetics. Gibbs free energy change (ΔG) showed the adsorption of all REEs (except for La and Ce) onto **5** was a spontaneous process, with Tm having the larger negative ΔG. Overall the adsorption capacities were rather low. In order to increase the adsorption capacities, further studies would be required to optimise conditions, including pH, acid type, temperature. An increase in the concentration of neocuproine on the silica could also be carried out to see if an improvement in the adsorption capacities occurs.

5. REFERENCES

1. Klinger, J.M. Rare Earth Elements: Development, Sustainability and Policy Issues. *Extr. Ind. Soc.* **2018**, *5*, 1–7, doi:10.1016/j.exis.2017.12.016.
2. Gschneidner, Karl A. , Jr., and Pecharsky, V.K. “rare-Earth Element”. Encyclopedia Britannica, Available online: https://www.britannica.com/science/rare-earth-element (accessed on 9 January 2023).
3. Rudnick, R.L.; Gao, S. Rudnick_Gao_Treatise. *Treatise on geochemistry* **2003**, *3*, 1–64.
4. *Mineral Commodity Summaries 2021*; Reston, VA, 2021;
5. Xu, L.; Guo, G.; Uy, D.; O’Neill, A.E.; Weber, W.H.; Rokosz, M.J.; McCabe, R.W. Cerium Phosphate in Automotive Exhaust Catalyst Poisoning. *Appl. Catal. B Environ.* **2004**, *50*, 113–125, doi:10.1016/j.apcatb.2004.01.017.
6. Humphries, M. Rare Earth Elements: The Global Supply Chain. *Rare Earth Miner. Policies Issues* **2011**, 1–20.
7. European Commission *Tackling the Challenges in Commodity Markets and on Raw Materials*; Brussels, 2012;
8. Binnemans, K.; Jones, P.T.; Blanpain, B.; Van Gerven, T.; Yang, Y.; Walton, A.; Buchert, M. Recycling of Rare Earths: A Critical Review. *J. Clean. Prod.* **2013**, *51*, 1–22, doi:10.1016/j.jclepro.2012.12.037.
9. European Commission Methodology for Establishing the EU List of Critical Raw Materials. *Publ. Off. Eur. Union* **2017**, 1–25, doi:10.2873/769526.
10. Wang, J.; Guo, M.; Liu, M.; Wei, X. Long-Term Outlook for Global Rare Earth Production. *Resour. Policy* **2020**, *65*, 101569, doi:10.1016/j.resourpol.2019.101569.
11. Watari, T.; Nansai, K.; Nakajima, K. Review of Critical Metal Dynamics to 2050 for 48 Elements. *Resour. Conserv. Recycl.* **2020**, *155*, 104669, doi:10.1016/j.resconrec.2019.104669.
12. Adamas Intelligence, Rare Earth Magnet Market Outlook to 2035 Available online: https://www.adamasintel.com/report/rare-earth-magnet-market-outlook-to-2035/ (accessed on 7 January 2023).
13. Roskill *Rare Earths, Outlook to 2030*; 2021;
14. Nissan and Waseda University in Japan Testing Jointly Developed Recycling Process for Electrified Vehicle Motors Available online: https://global.nissannews.com/en/releases/nissan-waseda-university-in-japan-testing-jointly-developed-recycling-process-for-ev-motors (accessed on 7 January 2023).
15. Nguyen, R.T.; Diaz, L.A.; Imholte, D.D.; Lister, T.E. Economic Assessment for Recycling Critical Metals From Hard Disk Drives Using a Comprehensive Recovery Process. *Jom* **2017**, *69*, 1546–1552, doi:10.1007/s11837-017-2399-2.
16. Release, F.O.R.I. Hitachi News Release December 6, 2010 : Hitachi Develops Recycling Technologies for Rare Earth Metals. **2010**, *c*, 6–9.
17. J.W. Lyman; G.R. Palmer Recycling of Rare Earths and Iron from NdFeB Magnet Scrap. *High Temp. Mater. Process. (London, U. K.)* **1993**, *11*, 175–188, doi:doi:10.1515/HTMP.1993.11.1-4.175.
18. Mudring, A.-V.; Prodius, D.; Nlebedium, C.I. Dissolution and Separation of Rare Earth Metals 2020.
19. Chegwidden, J. and Kingsnorth, D.J. Rare Earths: Facing the Uncertainties of Supply. Proceedings of the Sixth International Rare Earths Conference.; Hong Kong, 2010.
20. Nash, K.L.; Jensen, M.P. Analytical-Scale Separations Of The Lanthanides: A Review Of Techniques And Fundamentals. *Sep. Sci. Technol.* **1999**, *36*, 1257–1282.

21. Cotton, S. Lanthanide and Actinide Chemistry. *Lanthan. Actin. Chem.* 2006, 1–263.

22. Choppin, G.R. Comparative Solution Chemistry of the 4f and 5f Elements. *J. Alloy. Compd.* **1995**, *223*, 174–179, doi:10.1016/0925-8388(94)09002-5.

23. Cotton, S.A.; Raithby, P.R. Systematics and Surprises in Lanthanide Coordination Chemistry. *Coord. Chem. Rev.* **2017**, *340*, 220–231, doi:10.1016/j.ccr.2017.01.011.

24. Gupta, C.K.; Krishnamurthy, N. Extractive Metallurgy of Rare Earths. *Int. Mater. Rev.* **1992**, *37*, 197–248, doi:10.1179/imr.1992.37.1.197.

25. Talens Peiró, L.; Villalba Méndez, G. Material and Energy Requirement for Rare Earth Production. *Jom* **2013**, *65*, 1327–1340, doi:10.1007/s11837-013-0719-8.

26. McGill, I. *Rare Earth Elements*; 2000;

27. Perry, R.H.; Chilton, C.H. *Chemical Engineer's Handbook*; 5th ed.; McGraw-Hill: New York, 2009;

28. Spedding, F.H.; Fulmer, E.I.; Butler, T.A.; Powell, J.E. The Separation of Rare Earths by Ion Exchange.1 IV. Further Investigations Concerning Variables Involved in the Separation of Samarium, Neodymium and Praseodymium. *J. Am. Chem. Soc.* **1950**, *72*, 2349–2354, doi:10.1021/ja01162a003.

29. Strelow, F.W.E.; Victor, A.H. Separation of Yttrium and Neodymium from Samarium and the Heavier Lanthanides by Cation-Exchange Chromatography with Hydroxyethylenediaminetriacetate in Monochloroacetate Buffer. *Talanta* **1990**, *37*, 1155–1161, doi:10.1016/0039-9140(90)80185-I.

30. Suzuki, T.; Tanaka, M.; Ikeda, Y.; Koyama, S.I. Adsorption Behaviors of Trivalent Actinides and Lanthanides on Pyridine Resin in Lithium Chloride Aqueous Solution. *J. Radioanal. Nucl. Chem.* **2013**, *296*, 289–292, doi:10.1007/s10967-012-2011-8.

31. Sreedhar, B.; Suzuki, T.; Hobbs, D.T.; Kawajiri, Y. Evaluation of Tertiary Pyridine Resin for the Separation of Lanthanides by Simulated Moving-Bed Chromatography. *J. Sep. Sci.* **2014**, *37*, 2892–2899, doi:10.1002/jssc.201400516.

32. Suzuki, T.; Aida, M.; Ban, Y.; Fujii, Y.; Hara, M.; Mitsugashira, T. Group Separation of Trivalent Actinides and Lanthanides by Tertiary Pyridine-Type Anion-Exchange Resin Embedded in Silica Beads. *J. Radioanal. Nucl. Chem.* **2003**, *255*, 581–583, doi:10.1023/A:1022509205421.

33. Ikeda, A.; Itoh, K.; Suzuki, T.; Aida, M.; Fujii, Y.; Mitsugashira, T.; Hara, M.; Ozawa, M. Effect of Counter-Anions on the Adsorption of Trivalent Actinides and Lanthanides on Tertiary Pyridine Resin in Alcoholic Chloride and Nitrate Solutions. *J. Alloys Compd.* **2006**, *408–412*, 1052–1055, doi:10.1016/j.jallcom.2004.11.096.

34. Ogden, M.D.; Hoch, C.L.; Sinkov, S.I.; Meier, G.P.; Lumetta, G.J.; Nash, K.L. Complexation Studies of Bidentate Heterocyclic N-Donor Ligands with Nd(III) and Am(III). *J. Solution Chem.* **2011**, *40*, 1874–1888, doi:10.1007/s10953-011-9762-7.

35. Hart, F.A.; Laming, F.P. Complexes of 1,10-Phenanthroline with Lanthanide Chlorides and Thiocyanates. *J. Inorg. Nucl. Chem.* **1964**, *26*, 579–585, doi:10.1016/0022-1902(64)80291-8.

36. Cabral Campello, M.P.; Palma, E.; Correia, I.; Paulo, P.M.R.; Matos, A.; Rino, J.; Coimbra, J.; Pessoa, J.C.; Gambino, D.; Paulo, A.; et al. Lanthanide Complexes with Phenanthroline-Based Ligands: Insights into Cell Death Mechanisms Obtained by Microscopy Techniques. *Dalt. Trans.* **2019**, *48*, 4611–4624, doi:10.1039/c9dt00640k.

37. Simonnet, M.; Suzuki, S.; Miyazaki, Y.; Kobayashi, T.; Yokoyama, K.; Yaita, T. Lanthanide Intra-Series Separation by a 1,10-Phenanthroline Derivative: Counterion Effect. *Solvent Extr. Ion Exch.* **2020**, *38*, 430–440, doi:10.1080/07366299.2020.1744806.

38. Simonzadeh, N.; Schilt, A.A. Chelation Properties of Silica-Bound 1,10-Phenanthroline. *J. Coord. Chem.* **1989**, *20*, 117–120, doi:10.1080/00958978909408856.

39. Kloster, G.M.; Watton, S.P. Oxidation of Immobilized Iron(II)-1,10-Phenanthroline Complexes by Cerium(IV): A Probe into the Site Accessibility of Metal Complexes Covalently Attached to Silica Sol-Gels. *Inorganica Chim. Acta* **2000**, *297*, 156–161, doi:10.1016/S0020-1693(99)00412-0.

40. Li, H.R.; Lin, J.; Fu, L.S.; Guo, J.F.; Meng, Q.G.; Liu, F.Y.; Zhang, H.J. Phenanthroline-Functionalized MCM-41 Doped with Europium Ions. *Microporous Mesoporous Mater.* **2002**, *55*, 103–107, doi:10.1016/S1387-1811(02)00410-9.

41. Frederick Smith, G.; McCurdy, W.H. 2,9-Dimethyl-1,10-Phenanthroline, New Specific in Spectrophotometric Determination of Copper. *Anal. Chem.* **1952**, *24*, 371–373.

42. O'Reilly, E.J.; Plowman, R.A. Coordination Compounds of Substituted 1, 10-Phenanthrolines and Related Dipyridyls: I. Synthesis of 2, 9-Dimethpl-1, 10-Phenanthroline. *Aust. J. Chem.* **1960**, *13*, 145–149, doi:10.1071/CH9600145.

43. Lalia-Kantouri, M.; Gdaniec, M.; Czapik, A.; Chrissafis, K.; Ferenc, W.; Sarzynski, J.; Papadopoulos, C.D. Neocuproine as a Redox-Active Ligand Platform on Iron and Cobalt. *J. Therm. Anal. Calorim.* **2012**, *109*, 131–139, doi:10.1007/s10973-011-1692-5.

44. Jesse, K.A.; Filatov, A.S.; Xie, J.; Anderson, J.S. Neocuproine as a Redox-Active Ligand Platform on Iron and Cobalt. *Inorg. Chem.* **2019**, *58*, 9057–9066, doi:10.1021/acs.inorgchem.9b00531.

45. Newkome, G.R.; Theriot, K.J.; Gupta, V.K.; Fronczek, F.R.; Baker, G.R. Chemistry of Heterocyclic Compounds. 124. Mono-.Alpha.-Functionalization of 2,9-Dimethyl-1,10-Phenanthroline. *J. Org. Chem.* **1989**, *54*, 1766–1769, doi:10.1021/jo00268a055.

46. Eggert, J.P.W.; Lüning, U.; Näther, C. Synthesis and Functionalisation of 5-Substituted Neocuproine Derivatives. *European J. Org. Chem.* **2005**, 1107–1112, doi:10.1002/ejoc.200400635.

47. Chandler, C.J.; Deady, L.W.; Reiss, J.A. Synthesis of Some 2,9-disubstituted-1,10-phenanthrolines. *J. Heterocycl. Chem. 18*, 599–601.

48. Lewis, F.W.; Harwood, L.M.; Hudson, M.J.; Drew, M.G.B.; Wilden, A.; Sypula, M.; Modolo, G.; Vu, T.-H.; Simonin, J.-P.; Vidick, G.; et al. From BTBPs to BTPhens: The Effect of Ligand Pre-Organization on the Extraction Properties of Quadridentate Bis-Triazine Ligands. *Procedia Chem.* **2012**, *7*, 231–238, doi:10.1016/j.proche.2012.10.038.

49. Sigma-Aldrich - 3-Chloropropyl-Functionalized Silica Gel Available online: https://www.sigmaaldrich.com/GB/en/product/aldrich/364266 (accessed on 11 January 2023).

50. Costa, T.B. da; Silva, M.G.C. da; Vieira, M.G.A. Recovery of Rare-Earth Metals from Aqueous Solutions by Bio/Adsorption Using Non-Conventional Materials: A Review with Recent Studies and Promising Approaches in Column Applications. *J. Rare Earths* **2020**, *38*, 339–355, doi:10.1016/j.jre.2019.06.001.

51. Mosai, A.K.; Chimuka, L.; Cukrowska, E.M.; Kotzé, I.A.; Tutu, H. The Recovery of Rare Earth Elements (REEs) from Aqueous Solutions Using Natural Zeolite and Bentonite. *Water. Air. Soil Pollut.* **2019**, *230*, doi:10.1007/s11270-019-4236-4.

52. Laventine, D.M.; Afsar, A.; Hudson, M.J.; Harwood, L.M. Tuning the Solubilities of Bis-Triazinylphenanthroline Ligands (Btphens) and Their Complexes. *Heterocycles* **2012**, *86*, 1419–1429, doi:10.3987/COM-12-S(N)102.

53. Qiu, H.; Lv, L.; Pan, B.C.; Zhang, Q.J.; Zhang, W.M.; Zhang, Q.X. Critical Review in Adsorption Kinetic Models. *J. Zhejiang Univ. Sci. A* **2009**, *10*, 716–724, doi:10.1631/jzus.A0820524.

54. Lakshmipathy, R.; Sarada, N.C. A Fixed-bed Column Study for the Removal of Pb2+ Ions by Watermelon Rind. *Environ. Sci. Water Res. Technol.* **2015**, *1*, 244–250, doi:10.1039/c4ew00027g.

55. Mahdi, Z.; Yu, Q.J.; El Hanandeh, A. Removal of Lead(II) from Aqueous Solution Using Date Seed-Derived Biochar: Batch and Column Studies. *Appl. Water Sci.* **2018**, *8*, 1–13, doi:10.1007/s13201-018-0829-0.

56. Rusdiarso, B.; Basuki, R.; Santosa, S.J. Evaluation of Lagergren Kinetics Equation by Using Novel Kinetics Expression of Sorption of Zn2+ onto Horse Dung Humic Acid (HD-HA). *Indones. J. Chem.* **2016**, *16*, 338–346, doi:10.22146/ijc.1158.

57. Ho, Y.S. Second-Order Kinetic Model for the Sorption of Cadmium onto Tree Fern: A Comparison of Linear and Non-Linear Methods. *Water Res.* **2006**, *40*, 119–125, doi:10.1016/j.watres.2005.10.040.

58. Park, D.; Yun, Y.S.; Park, J.M. The Past, Present, and Future Trends of Biosorption. *Biotechnol. Bioprocess Eng.* **2010**, *15*, 86–102, doi:10.1007/s12257-009-0199-4.

59. Solgi, M.; Tabil, L.G.; Wilson, L.D. Modified Biopolymer Adsorbents for Column Treatment of Sulfate Species in Saline Aquifers. *Materials (Basel).* **2020**, *13*, doi:10.3390/ma13102408.

60. Patel, H. Fixed-Bed Column Adsorption Study: A Comprehensive Review. *Appl. Water Sci.* **2019**, *9*, 1–17, doi:10.1007/s13201-019-0927-7.

61. Dolatyari, L.; Yaftian, M.R.; Rostamnia, S. Fixed-Bed Column Dynamic Studies and Breakthrough Curve Analysis of Eu(III) Ion Adsorption onto Chemically Modified SBA-15 Silica Materials. *Sep. Sci. Technol.* **2017**, *52*, 393–403, doi:10.1080/01496395.2016.1250781.

62. Basuki, R.; Ngatijo; Santosa, S.J.; Rusdiarso, B. Comparison the New Kinetics Equation of Noncompetitive Sorption Cd(II) and Zn(II) onto Green Sorbent Horse Dung Humic Acid (HD-HA). *Bull. Chem. React. Eng. & Catal.* **2018**, *13*, 475–488, doi:10.9767/bcrec.13.3.1774.475-488.

63. Xu, S.; Wang, Z.; Gao, Y.; Zhang, S.; Wu, K. Adsorption of Rare Earths(III) Using an Efficient Sodium Alginate Hydrogel Cross-Linked with Poly-γ-Glutamate. *PLoS One* **2015**, *10*, 1–12, doi:10.1371/journal.pone.0124826.

64. Rahman, M.L.; Biswas, T.K.; Sarkar, S.M.; Yusoff, M.M.; Sarjadi, M.S.; Arshad, S.E.; Musta, B. Adsorption of Rare Earth Metals from Water Using a Kenaf Cellulose-Based Poly(Hydroxamic Acid) Ligand. *J. Mol. Liq.* **2017**, *243*, 616–623, doi:10.1016/j.molliq.2017.08.096.

65. Felipe, E.C.B.; Batista, K.A.; Ladeira, A.C.Q. Recovery of Rare Earth Elements from Acid Mine Drainage by Ion Exchange. *Environ. Technol. (United Kingdom)* **2021**, *42*, 2721–2732, doi:10.1080/09593330.2020.1713219.

66. Liu, Z.; Liu, Y.; Gong, A. Preparation of Diglycolamide Polymer Modified Silica and Its Application as Adsorbent for Rare Earth Ions. *Des. Monomers Polym.* **2019**, *22*, 1–7, doi:10.1080/15685551.2018.1564425.

67. Xu, X.; Jiang, X.Y.; Jiao, F.P.; Chen, X.Q.; Yu, J.G. Tunable Assembly of Porous Three-Dimensional Graphene Oxide-Corn Zein Composites with Strong Mechanical Properties for Adsorption of Rare Earth Elements. *J. Taiwan Inst. Chem. Eng.* **2018**, *85*, 106–114, doi:10.1016/j.jtice.2017.12.024.

68. Zhang, T.H.; Shan, X.Q.; Liu, R.X.; Tang, H.X.; Zhang, S.Z. Preconcentration of Rare Earth Elements in Seawater with Poly(Acrylaminophosphonic Dithiocarbamate) Chelating Fiber Prior to Determination by Inductively Coupled Plasma Mass Spectrometry. *Anal. Chem.* **1998**, *70*, 3964–3968, doi:10.1021/ac980321h.

69. Kano, N.; Pang, M.; Deng, Y.; Imaizumi, H. Adsorption of Rare Earth Elements (REEs) onto Activated Carbon Modified with Potassium Permanganate (KMnO 4). **2017**, 51–61.

70. Li, J.; Gong, A.; Li, F.; Qiu, L.; Zhang, W.; Gao, G.; Liu, Y.; Li, J. Synthesis and Characterization of Magnetic Mesoporous Fe3O4@mSiO2-DODGA Nanoparticles for Adsorption of 16 Rare Earth Elements. *RSC Adv.* **2018**, *8*, 39149–39161,

doi:10.1039/c8ra07762b.

71. Ogata, T.; Narita, H.; Tanaka, M. Adsorption Behavior of Rare Earth Elements on Silica Gel Modified with Diglycol Amic Acid. *Hydrometallurgy* **2015**, *152*, 178–182, doi:10.1016/j.hydromet.2015.01.005.

72. Waqar, F.; Jan, S.; Mohammad, B.; Hakim, M.; Alam, S.; Yawar, W. Preconcentration of Rare Earth Elements in Seawater with Chelating Resin Having Fluorinated β-Diketone Immobilized on Styrene Divinyl Benzene for Their Determination by ICP-OES. *J. Chinese Chem. Soc.* **2009**, *56*, 335–340, doi:10.1002/jccs.200900049.

73. Fu, Q.; Yang, L.; Wang, Q. On-Line Preconcentration with a Novel Alkyl Phosphinic Acid Extraction Resin Coupled with Inductively Coupled Plasma Mass Spectrometry for Determination of Trace Rare Earth Elements in Seawater. *Talanta* **2007**, *72*, 1248–1254, doi:10.1016/j.talanta.2007.01.015.

74. Bohart, G.S.; Adams, E.Q. Some Aspects of the Behavior of Charcoal with Respect to Chlorine. *J. Am. Chem. Soc.* **1920**, *42*, 523–544, doi:10.1021/ja01448a018.

75. Yoon, Y.H.E.E.; Nelson, J.H. Application of Gas Adsorption Kinetics I. A Theoretical Model for Respirator Cartridge Service Life. *Am. Ind. Hyg. Assoc. J.* **1984**, *45*, 509–516, doi:10.1080/15298668491400197.

76. Thomas, H.C. Heterogeneous Ion Exchange in a Flowing System. *J. Am. Chem. Soc.* **1944**, *66*, 1664–1666, doi:10.1021/ja01238a017.

77. Thomas, H.C. Chromatography: A Problem In Kinetics. *Ann. N. Y. Acad. Sci.* **1948**, *49*, 161–182, doi:https://doi.org/10.1111/j.1749-6632.1948.tb35248.x.

78. Yan, G.; Viraraghavan, T.; Chen, M. A New Model for Heavy Metal Removal in a Biosorption Column. *Adsorpt. Sci. Technol.* **2001**, *19*, 25–43, doi:10.1260/0263617011493953.

79. Xu, Z.; Cai, J.G.; Pan, B.C. Mathematically Modelling Fixed-Bed Adsorption in Aqueous Systems. *J. Zhejiang Univ. Sci. A* **2013**, *14*, 155–176, doi:10.1631/jzus.A1300029.

Supplementary Information

SI.1 Characterisation of Neocuproine Functionalised Silica (NC-Si)

SI.1.1. FT-IR analysis of NC-Si **5**

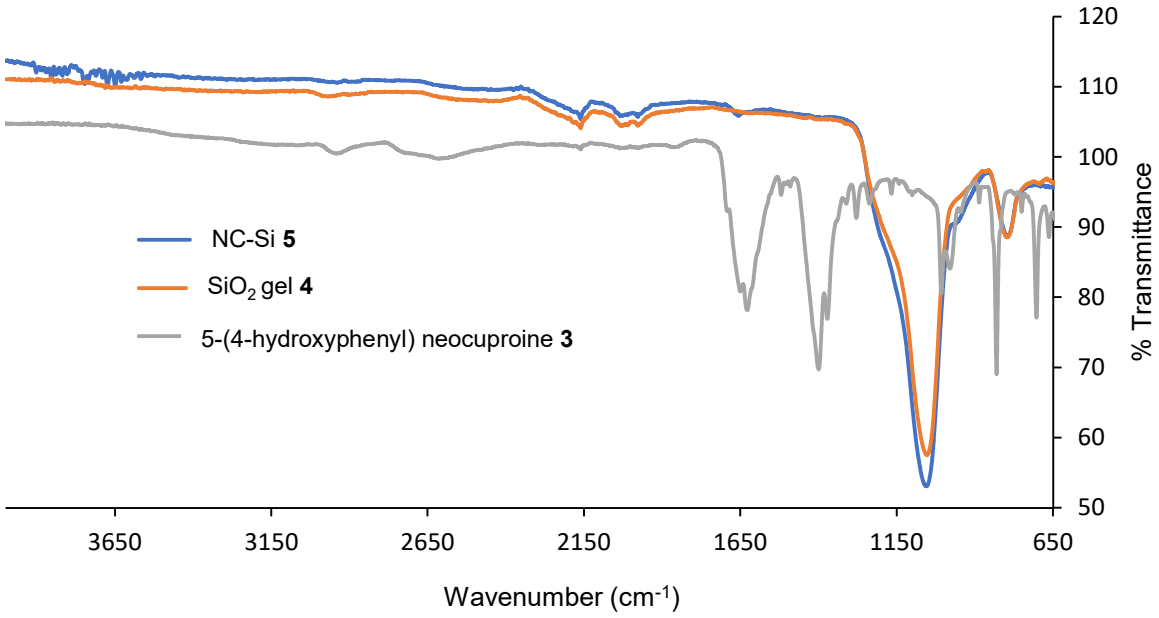

SI Figure **1.** FT-IR spectra

SI Table **1.** FT-IR assignment

Wavelength (cm^{-1})	Assignment	Reference
1052	Si-O-Si	5, 4
1500-1600	C=C	5, 3
823	C-Cl	5

SI.1.2 EDX Analysis of NC-Si **5**

SI Table 2. EDX analysis of NC-Si **5**

Element	CP-Si **4**	NC-Si **5**
Carbon (%)	16.86	53.88
Oxygen (%)	44.11	28.53
Silicon (%)	34.27	15.74
Chlorine (%)	1.04	0.43

SI 1.3 TGA Analysis of NC-Si

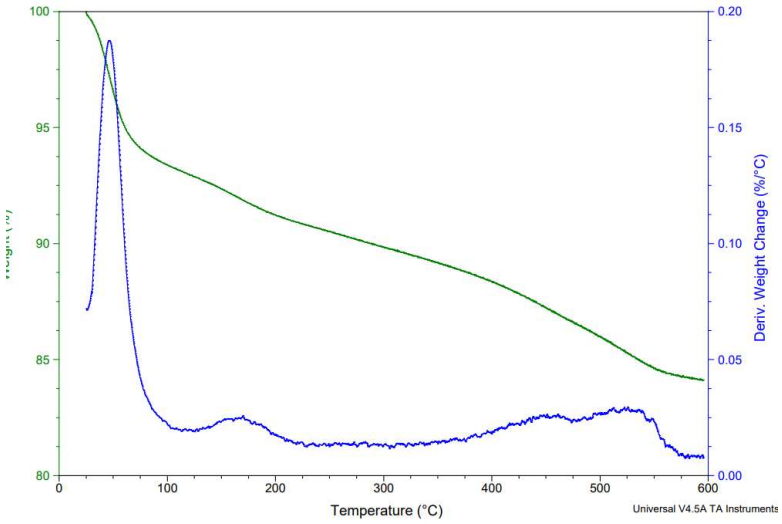

SI Figure 2. TGA analysis of NC-Si **5**

SI.2 Breakthrough Modelling of REE Column Behaviour

SI.2.1. Adams-Bohart model

The Adams-Bohart model is a widely used model for the prediction of breakthrough curves. It assumes that the rate of adsorption is proportional to the concentration of the adsorbing species and the residual capacity of the adsorbent and only focuses on the initial part of the breakthrough curve [74]. It is expressed as equation (S1) as its non-linear form and equation (S2) as it's linear form:

$$\frac{C_t}{C_0} = exp(k_{AB}C_0 t - k_{AB}q\frac{H}{v}) \quad \text{(S1)}$$

$$\ln\left(\frac{C_t}{C_0}\right) = k_{AB}C_0 t - k_{AB}q\frac{H}{v} \quad \text{(S2)}$$

Where C_0 is the initial REE (III) ions concentration (mg L^{-1}), C_t is the outlet concentration (mg·L^{-1}), k_{AB} is the Adams-Bohart rate constant (L·mg^{-1}·min^{-1}), q is the adsorption capacity (mg·L), H is the bed depth of the fixed-bed column (cm), v is the linear velocity calculated by dividing the flow rate by the column sectional area (cm·min^{-1}).

a)

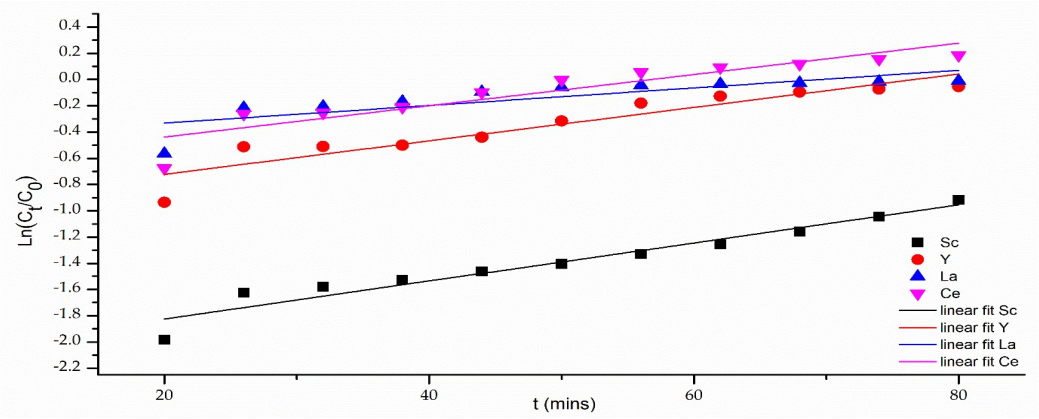

b)

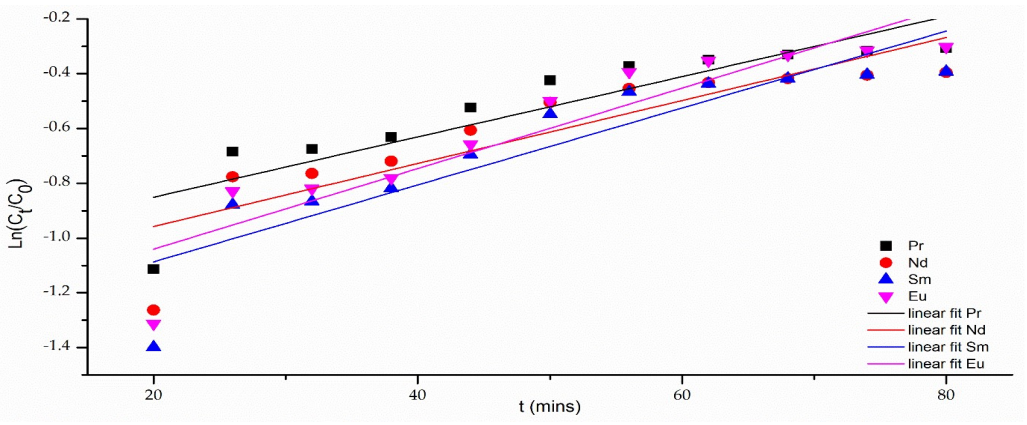

c)

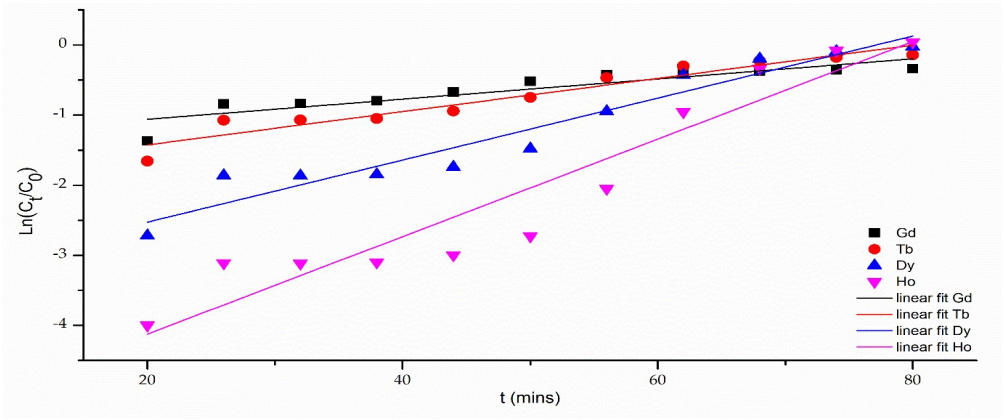

d)

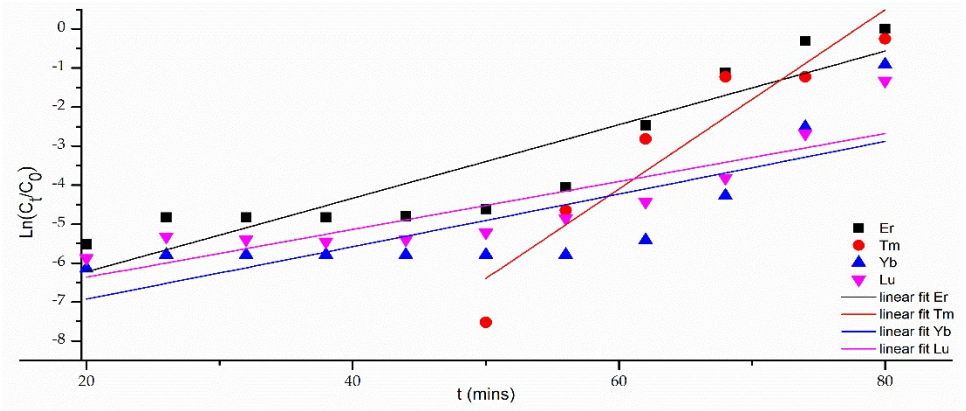

SI Figure 3. Fitting of the Adams-Bohart model to a) Sc-Ce, b) Pr-Eu, c) Gd-Ho and d) Er-Lu

SI.2.2 Yoon-Nelson model

This model is a simple model compared to other models and doesn't require any information on the characteristics of the system, such as the physical properties of the adsorption bed or the type of adsorbent [75]. It assumes that probability of adsorption is proportional to the probability of sorbate sorption and the probability of sorbate breakthrough on the sorbent. The equation for the non-linear Yoon-Nelson model and linear model are expressed as equation (S3) and (S4) respectively, where k_{YN} is the Yoon-Nelson rate constant (min^{-1}) and τ is the time required for 50% adsorbate breakthrough (min).

$$\frac{C_t}{C_0} = \frac{1}{1+e^{k_{YN}(\tau - t)}} \qquad \text{(S3)}$$

$$\ln\left(\frac{C_t}{C_0 - C_t}\right) = k_{YN}t - k_{YN}\tau \qquad \text{(S4)}$$

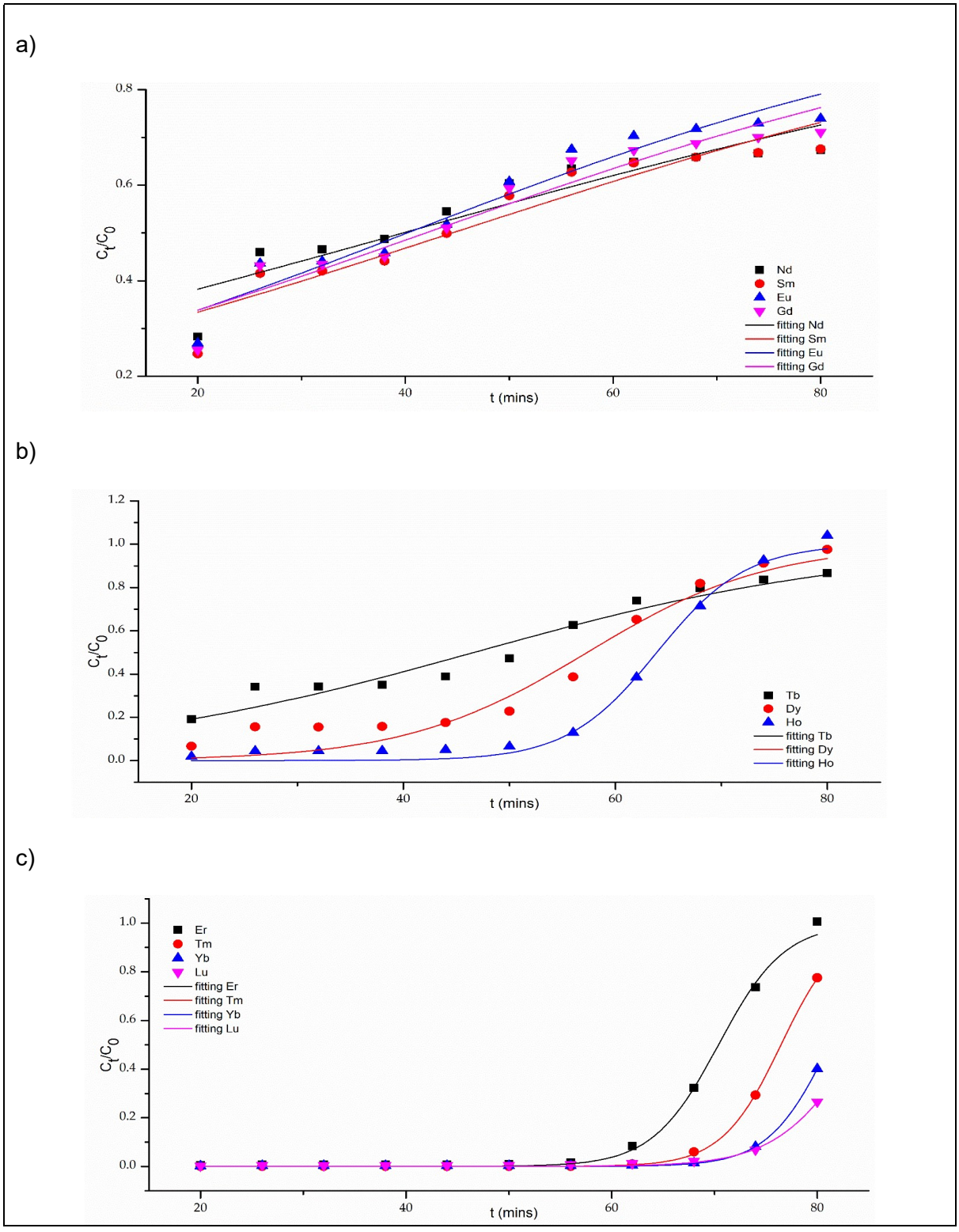

SI Figure 4. Fitting of the Yoon-Nelson model to a) Nd-Gd, b) Tb-Ho and c) Er-Lu

SI.2.3 Thomas model

This model is based on the Langmuir kinetics of adsorption and gives a general analytical description to predict the behaviour of a dynamic adsorption process. The Thomas model assumes that the system has constant flow with no axial dispersion and that the sorption process is governed by mass transfer instead of chemical processes [76]. Equations (S5) and (S6) show the non-linear and linear equations respectively, where k_{Th} (mL·mg^{-1}·min^{-1}) is the Thomas model constant and q_0 (mg·g^{-}) is the predicted adsorption capacity, m (g) is the mass of the absorbent, and Q (mL·min^{-1}) is the influent flow rate [77].

$$\frac{C_t}{C_0} = \frac{1}{1+e^{\left(\frac{k_{Th}q_0m}{Q}\right)-k_{Th}C_0t}} \quad \text{(S5)}$$

$$ln\left(\frac{C_t}{C_0}-1\right) = \left(\frac{k_{Th}q_0m}{Q}\right) - k_{Th}C_0t \quad \text{(S6)}$$

a)

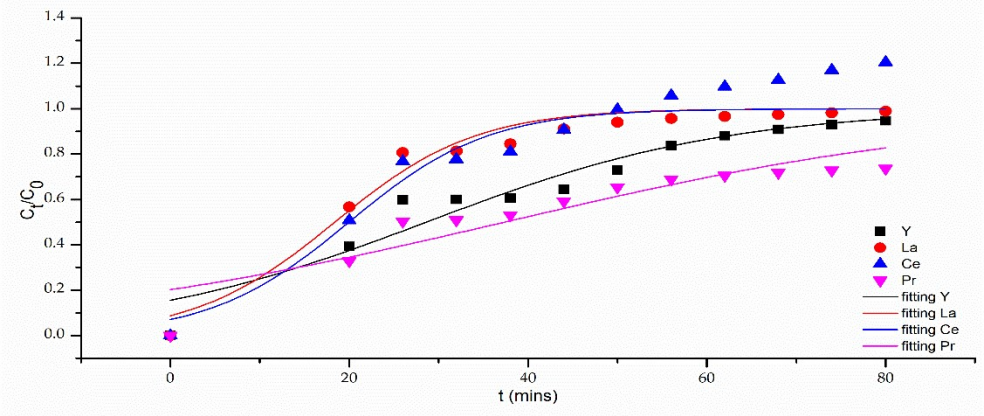

b)

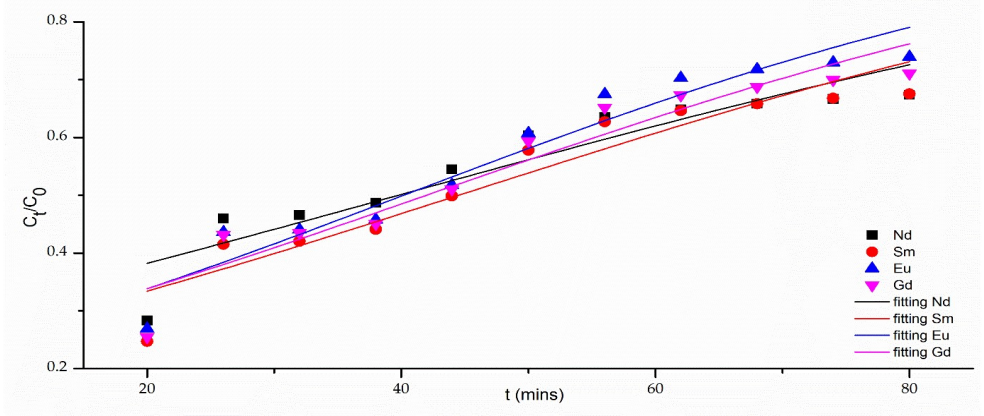

c)

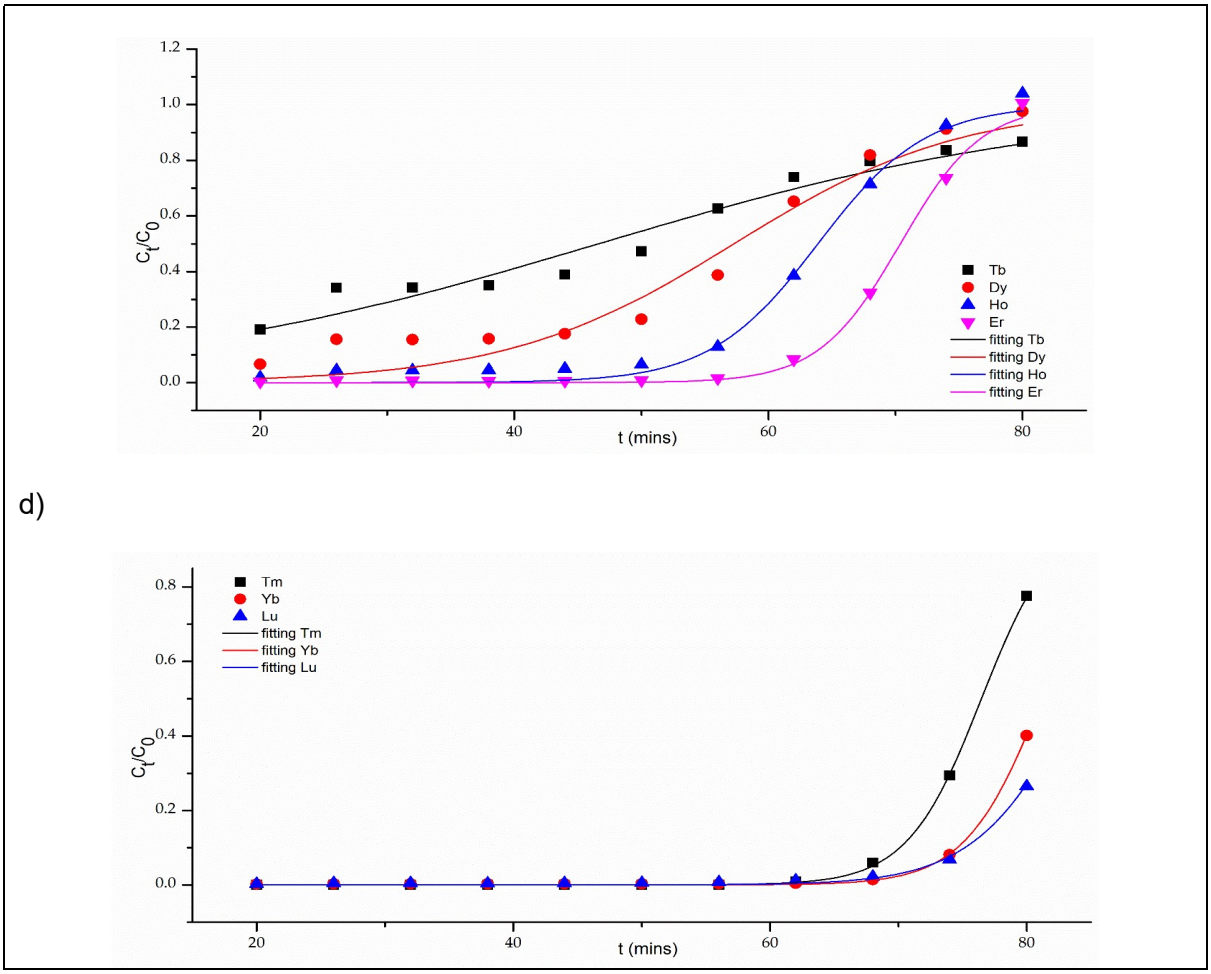

SI Figure 5. Fitting of the Thomas model to a) Y-Pr, b) Nd-Gd, c) Tb-Er and d) Tm-Lu

SI.2.4 Modified Dose Response model

Another simplified model to evaluate the dynamic behaviour of a fixed-bed column is the Modified Dose Response model [78]. The modified dose response model is proposed to minimize the error associated from the Thomas model and describes the adsorption as a function of the concentration of the adsorbate in the bulk fluid phase [79]. The non-linear and linear models can be expressed as equations (S7) and (S8) respectively, where *a* is the MDR constant.

$$\frac{C_t}{C_o} = 1 - \frac{1}{1+\left(\frac{C_o Q t}{q_m m}\right)^a} \quad \text{(S7)}$$

$$ln\left(\frac{C_t}{C_o - C_t}\right) = aln(C_o Q t) - aln(qm) \quad \text{(S8)}$$

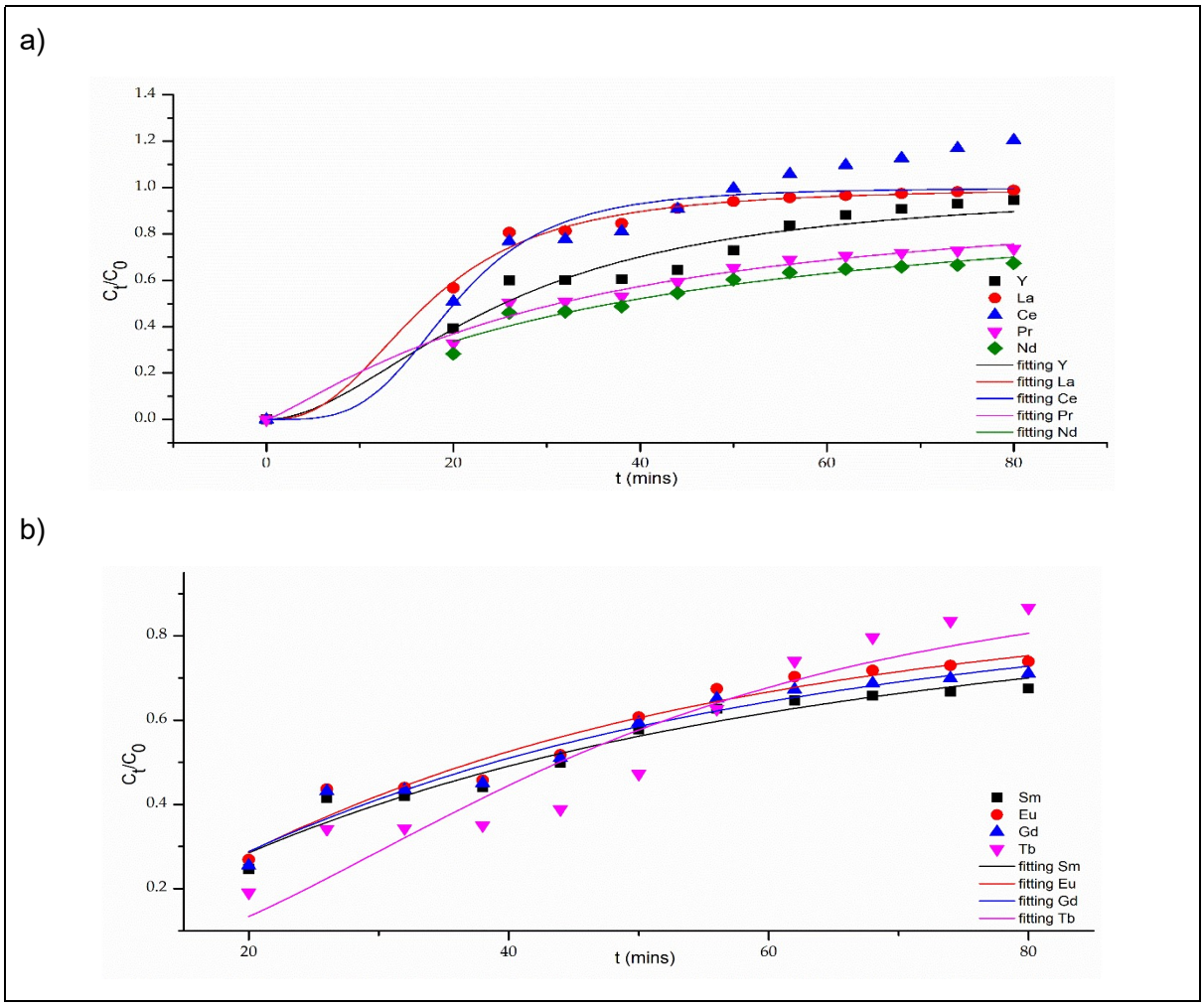

SI Figure 6. Fitting of the MDR model to a) Y-Nd and b) Sm-Tb

SI.3 Experimental Procedures

SI 3.1 General Procedure

All reagents were supplied by Acros, Aldrich, Fisher or Fluorochem chemical suppliers and were used as supplied unless stated otherwise. NMR spectra were recorded using either a Bruker AMX400 or an Advance DFX400 instrument. Deuterated chloroform ($CDCl_3$) or deuterated dimethyl sulfoxide (DMSO-d_6) were used as solvents. Chemical shifts (δ) are reported in parts per million (ppm) with the abbreviations s, d, t, q, dd, dt and m denoting singlet, doublet, triplet, quartet, double doublet, double triplet and unresolved multiplet resonance respectively. All coupling constants (*J*) are recorded in Hertz (Hz). Assignments were made using chemical shift and coupling constant data using DEPT-90, COSY, HSQC and HMBC experiments where required. IR spectra were recorded on a Perkin-Elmer Spectrum One FT-IR spectrometer instrument with peak intensities abbreviated to: w, weak; m, medium; s, strong; br, broad. All melting points were determined on a Stuart SMP10 melting point apparatus. Mass spectra were recorded under conditions of electrospray ionisation (ESI) on a Thermo Scientific LTQ-Orbitrap XL with a Thermo Scientific Accela HPLC. Thermogravimetric (TGA) analyses were performed using a TGA-Q50 thermogravimetric analyser.

SI 3.2 Synthetic Procedures

Synthesis of 5-Bromo-2,9-dimethyl-1,10-phenanthroline

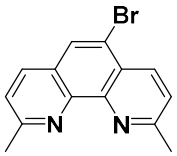

In a round-bottom flask 2,9-dimethyl-1,10-phenanthroline (25.0 g, 120 mmol) was dissolved in oleum ($H_2SO_4.SO_3$, 100 mL). To the stirred solution was added bromine (3.38 mL, 66.0 mmol) and the mixture was heated at 170 °C for 18 hours. The reaction was cooled to room temperature before pouring onto an ice/water mixture (CAUTION). The solution was basified using NaOH before extraction with $CHCl_3$ (3 x 150 mL). The combined organic extracts were washed with brine, dried over $MgSO_4$, filtered and the organic solvent was removed under reduced pressure to give 5-bromo-2,9-dimethyl-1,10-phenanthroline (24.5 g, 85.3 mmol, 71 %) as an off-white solid. M.p. > 300 °C; FT-IR (ATR) ν_{max} / cm^{-1} = 3364m, 3050w, 2916w, 1603m, 1598m, 1547w, 1492m, 1434w, 1373w.

δ_H (400 MHz, $CDCl_3$) = 8.54 (d, J = 8.5 Hz, 1H, Ar*H*), 8.05 (d, J = 4.0 Hz, 1H, Ar*H*), 8.04 (s, 1H, Ar*H*), 7.59 (d, J = 8.4 Hz, 1H, Ar*H*), 7.50 (d, J = 8.2 Hz, 1H, Ar*H*), 2.98 (s, 3H, CH_3), 2.94 (s, 3H, CH_3); ^{13}C NMR (101 MHz, $CDCl_3$): δ_C (ppm) = 160.1, 159.9, 145.7, 144.7, 136.0, 135.3, 128.6, 127.0, 126.0, 124.3, 124.1, 119.6, 25.0 (CH_3), 25.7 (CH_3); ESI-FTMS: calculated $C_{14}H_{12}N_2Br$ $[M+H]^+$: 287.0178; observed: 287.0176;

Synthesis of 5-(4-hydroxyphenyl) Neocuproine

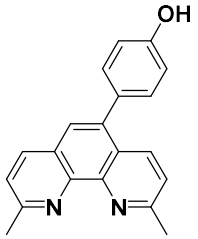

5-Bromoneocuproine (0.53 g, 1.85 mmol) was dissolved in EtOH (40 mL), H_2O (40 mL) and toluene (200 mL). K_2CO_3 (0.75 g, mmol), tetrakis triphenylphosphine palladium (0) (0.062 g, mmol) and 4-hydroxyphenylboronic acid (0.32 g, mmol) were added and the mixture was heated at 90 °C overnight. The reaction was allowed to cool before the solvent was evaporated *in vacuo*. The solid was diluted with H_2O (75 mL) and $CHCl_3$ (100mL), the organic phase was separated and dried over $MgSO_4$ and the solvent was removed *in vacuo* to afford 2,9-dimethyl-5-(4-hydroxyphenyl)-1,10-phenanthroline as a yellow solid (0.43 g, 75%). M.p. >300 °C; FT-IR (ATR) ν_{max} / cm^{-1} = 2923w, 2951w, 2161w, 1981, 1837, 1683m, 1653m, 1634m,1516w, 1406m, 1372m, 1275w, 1228w, 1007m, 981w, 884w, 831w.

δ_H (400 MHz, DMSO) = 8.37 (d, J = 8.5 Hz, 1H, ArH), 8.29 (d, J = 8.2 Hz, 1H, ArH), 7.65 (s, 1H, ArH), 7.56 (dd, J = 8.4 Hz, 2.6 Hz, 2H, ArH), 7.11 (d, J = 8.4 Hz, 2H, ArH), 6.57 (d, J = 8.3 Hz, 2H, ArH), 2.77 (s, 6H, CH3); δ_C (101 MHz, DMSO) = 162.7, 157.6, 157.5, 145.1, 143.4, 138.0, 136.1, 134.6, 131.6, 130.7, 126.3, 125.8, 124.9, 124.4, 123.4, 122.3, 116.7, 25.0 (CH_3), 24.8 (CH_3); ESI-FTMS: calculated $C_{20}H_{16}ON_2$ $[M+Na]^+$: 323.1155, observed: 323.1150;

Synthesis of Neocuproine-functionalised SiO_2 Gel

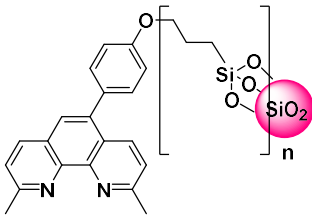

Sodium hydride (60% dispersion in mineral oil, (0.118 g, 3.3 mmol, 1.8 eq) was added to a suspension of 4-(hydroxyphenyl)-neocuproine (0.65 g, 1.95 mmol) in DMF (150 mL) at 120 °C and the mixture stirred for 30 minutes. Chloropropyl-functionalised SiO_2 gel (3.2 g) was slowly added, and the suspension was stirred at 120 °C for 18 hours. The resultant neocuproine-functionalised SiO_2 gel was filtered and washed with DMF (100 mL), EtOH (100 mL) deionised water (100 mL) and $CHCl_3$ (100 mL). The neocuproine-functionalised SiO_2 gel (3.2 g) was dried at 120 °C to afford an orange solid. FT-IR (ATR) ν_{max} / cm^{-1} = 3403w, 1054s, 796w;

Chapter 3 – Application of $CyMe_4$-BTPhen Functionalised Silica to the Separation of Rare Earth Elements (REEs)

3.1 Extraction of Actinides Using $CyMe_4$-BTPhen

In one of the later stages of reprocessing spent nuclear fuel, the separation of actinides from REEs must occur in order for the actinides to be recycled back into the nuclear fuel cycle. These minor actinides can be subjected to transmutation into shorter lived elements ($t_{1/2} < 10^1$ years) in high neutron-flux "Generation IV" reactors. This is achieved by irradiating the actinides with an intense neutron source from a high-power fission system using either a thermal reactor, fast reactor or accelerator-driven sub-critical system (ADS) [1]. REEs must be removed from the mixture as they are present in much greater quantities and have a higher ability to absorb neutrons due to their larger neutron cross section (Bohr radius), thus hindering transmutation. The REEs and minor actinides have very similar physical and chemical properties to each other as REE(III) have ionic radii of 98-116 pm [2] Whereas actinides(III) have ionic radii of 95-111 pm [3,4].

$CyMe_4$-BTBP **37** (Figure 3.1) was successfully developed to extract actinides over the REEs by solvent extraction in 1-octanol and 4 M HNO_3 which gave a separation factor ($SF_{Am/Eu}$) of 400 [5]. $CyMe_4$-BTBP **37** bears two adjacent nitrogens on the triazine rings which increases the nucleophilicity of the molecule allowing easier binding to the metal centre due to the "alpha-effect". The alpha-effect stabilizes the electron deficiency in the transition state, via π bonding from the lone pair of the nitrogen at the α-position. The overlap of the α- nitrogen electrons will raise the HOMO of the molecule and therefore increase reactivity. The coordination cavity is 0.1 nm which corresponds to the size of Am(III) and Eu(III). $CyMe_4$-BTBP **37** is able to extract just the actinides over the REEs because of the more diffuse nature of the 5*f* orbitals on the actinides compared to the 4*f* orbitals in REEs [6].

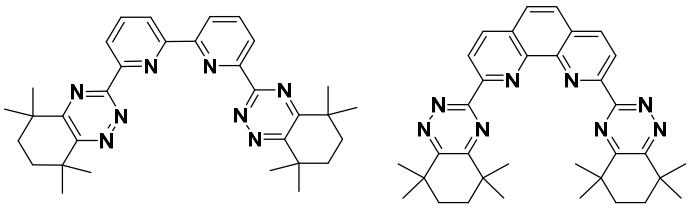

37 38

Figure 3.1. Structures of $CyMe_4$-BTBP (left) and $CyMe_4$-BTPhen (right)

Back extraction with glycolic acid is relatively easy however due to the poor rate of extraction rom **37** $CyMe_4$-BTPhen **38** (Figure 3.1) was developed as a pre-organised molecule locked in the cis position by the phenanthroline ring. The separation factors were very similar to $CyMe_4$-BTBP **37** ($SF_{Am/Eu} \approx 200 – 400$ from a range of 1 – 4 M HNO_3). Metal complexes have been crystalised with Eu(III) as shown in Figure 3.2. The complex holds an orthogonal shape with two tetradentate ligands surrounding the Eu(III) metal centre. As the metal is 10-coordinate a

bidentate nitrate ion is also incorporated into the complex. This complex allows the sufficient room for stripping agents to displace the metal centre once extracted. ^{1}H NMR titration studies have also found that a 2:1 complex is the predominate species in solution, however 1:1 complexes are formed when the concentration of metal ions is above 0.3 equivalents [7].

Whitehead *et al.* characterised a 1:1 complex of tetradentate 4,7-dimethyl CyMe$_4$-BTPhen – Europium (III) complex (Figure 1.15) with three bidentate nitrate ions, giving a coordination number of 10 on the metal centre [8].

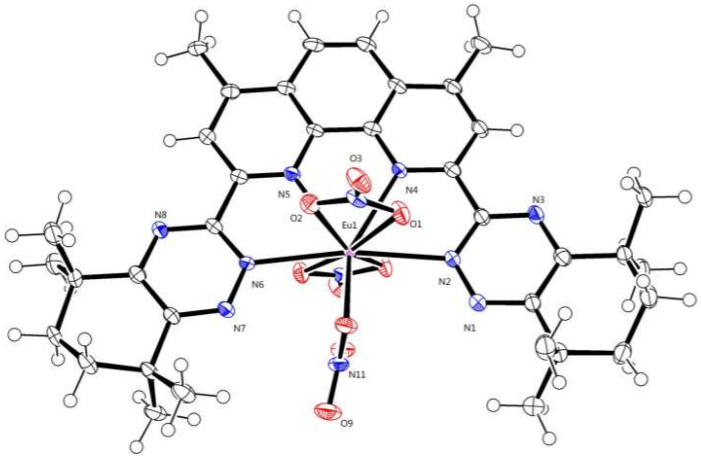

Figure 3.2: X-ray crystallographic structure of 4,7-Me-CyMe$_4$-BTPhen–Eu(NO$_3$)$_3$ complex (additional solvent molecules omitted for clarity) [8]

3.2 Synthesis of CyMe$_4$-BTPhen

The original four step synthetic route of CyMe$_4$-BTPhen **38** involved oxidizing neocuproine **27** with selenium dioxide to afford a bis-aldehyde **39** before being converted in a one pot reaction into a *bis*-nitrile **40**. Hydrazine and ethanol when added to the *bis*-nitrile produced the *bis*-aminohydrazide **41** which underwent standard condensation with CyMe$_4$ diketone **42** to generate the CyMe$_4$-BTPhen ligand **38** (Scheme 3.1). The CyMe$_4$ diketone **42** was developed to omit any alpha protons, thus increasing radiolytic stability in the harsh conditions of the spent nuclear fuel reprocessing steps. This route provided adequate yields, however large quantities of toxic selenium was produced as a by-product. This lead to the current synthetic route which negates the use of selenium but requires more steps as shown in scheme 1.4 [9].

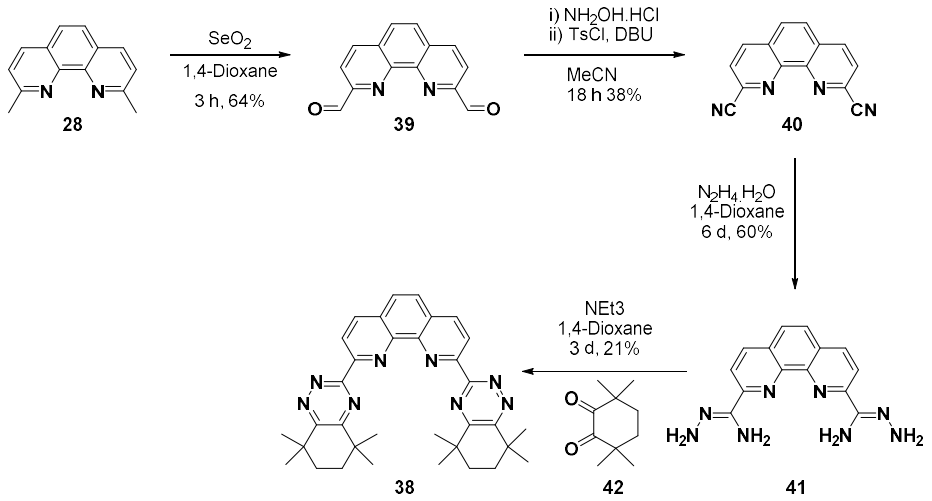

Scheme 3.1: Original synthetic route for the synthesis of $CyMe_4$-BTPhen **38**

A second synthetic route to synthesize $CyMe_4$-BTPhen **38** (Scheme 3.2) was developed to omit the use of SeO_2, it consists of six adequately yielding steps. This procedure was adapted from a protocol reported by Ulven in 2011 and adapted by Harwood *et al* [10–13]. The first step begins with a benzylic chlorination of neocuproine **28** with recrystallized *N*-chlorosuccnimide, using *m*-CPBA as a radical initiator which undergoes a Wohl-Zielger reaction, as proposed by Goldfinger, to produce the 2,9-*bis*-(tri-chloro methyl)phenanthroline **40**. Subsequently, the tri-chloromethyl groups were converted to amides **45** via the corresponding methyl esters **44** using sulfuric acid and methanol. $POCl_3$ was then added to dehydrate the *bis*-amide **45** to a *bis*-nitrile **40** before hydrazine in DMSO was added to form the *bis*-aminohydrazide **41**. A standard condensation reaction was then carried out with the $CyMe_4$ diketone **42** to afford $CyMe_4$-BTPhen **38** (Scheme 3.2).

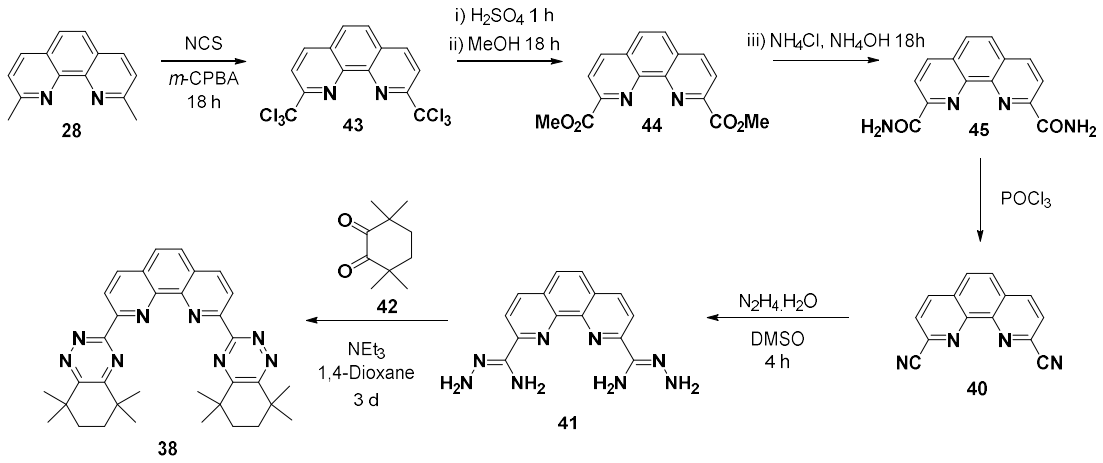

Scheme 3.2: New/current route for the synthesis of $CyMe_4$-BTPhen **38**

5-(4-hydroxyphenyl)-$CyMe_4$-BTPhen **46** was developed to see if the additional 4-hydroxyphenyl group would alter the extraction of actinides [13–16]. The synthesis of 5-(4-hydroxyphenyl)-$CyMe_4$-BTPhen **33** followed a very similar approach to the synthetic route of $CyMe_4$-BTPhen **35**, as depicted in Scheme 3.3. After the mono bromination of neocuproine **27**

to afford bromo neocuproine **32**, the benzylic chlorination of bromo neocuproine **32** with recrystallized *N*-chlorosuccinimide, using *m*-CPBA as a radical initiator which undergoes a Wohl-Zielger reaction, as proposed by Goldfinger, to produce the bromo-2,9-*bis*-(tri-chloro methyl)phenanthroline **44**. Subsequently, the tri-chloromethyl groups were converted to amides **46** via the corresponding methyl esters **45** using sulfuric acid and methanol. $POCl_3$ was then added to dehydrate the *bis*-amide **46** to a *bis*-nitrile **47** before hydrazine in DMSO was added to form the *bis*-aminohydrazide **48**. A standard condensation reaction was then carried out with the $CyMe_4$ diketone **39** to afford bromo $CyMe_4$-BTPhen **46**. A Suzuki-Miyauara reaction was carried out using **49** using a palladium catalyst and (4-hydroxyphenyl)boronic acid to afford 5-(4-hydroxyphenyl)-$CyMe_4$-BTPhen **43** (Scheme 3.3).

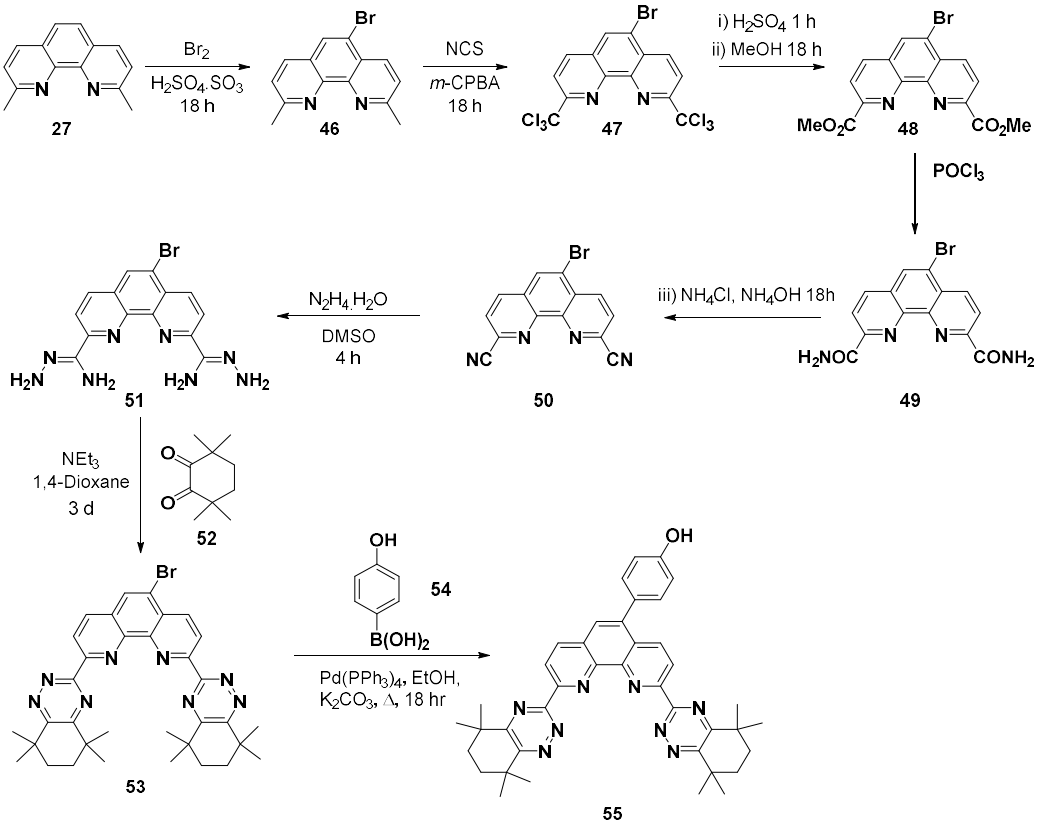

Scheme 3.3: Synthesis of 5-bromo $CyMe_4$-BTPhen **54** and 5-(4-hydroxyphenyl)-$CyMe_4$-BTPhen **55** [16]

5-(4-hydroxyphenyl)-$CyMe_4$-BTPhen **55** was found to still be highly efficient at the extraction of Am (III) but also selective D_{Eu} <1 across most concentrations of HNO_3 with a final separation factor of $SF_{Am/Eu} \approx 680$ in 3 M HNO_3 (Figure 3.3) Interestingly there is a slight difference in selectivity between the REE ions across all concentrations of HNO_3, which sparked the research in this thesis to attempt to separate REE ions into smaller groups.

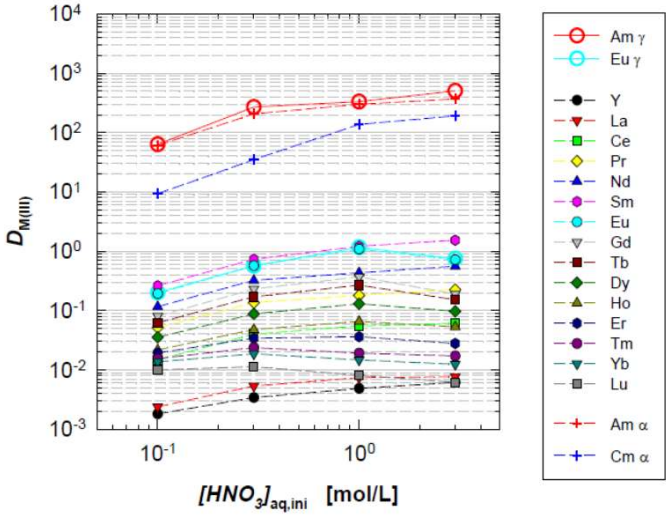

Figure 3.3 Extraction of Am (III), Ln (III) and Y (III) by 5-(4-hydroxyphenyl)-CyMe$_4$-BTPhen **55** in 1-octanol as a function of nitric acid concentration

Similarly to NC-Si **38**, 5-(4-hydroxyphenyl)-CyMe$_4$-BTPhen **55** can be immobilised onto silica gel to form CyMe$_4$-BTPhen functionalised silica gel (BTPhen-Si) **57** as shown in Scheme 3.4. In this work BTPhen-Si **57** is synthesized and characterised. Fixed-bed column studies are carried out to test extraction capabilities. The mechanism of adsorption and desorption is determined and compared to NC-Si.

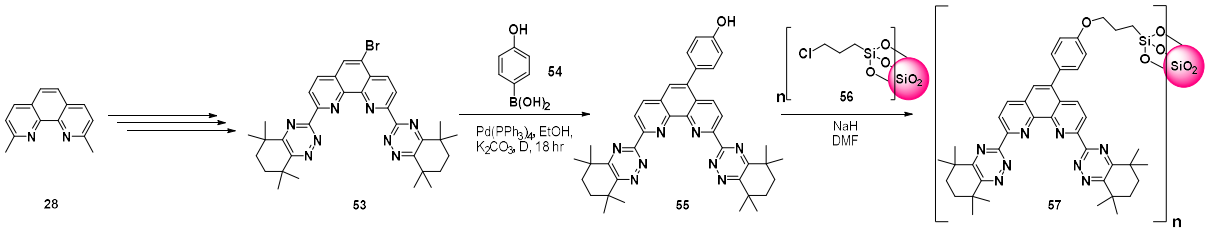

Scheme 3.4. Synthesis of BTPhen-Si **57**

3.3 References

1. Schmidt, H.; Wilden, A.; Modolo, G.; Švehla, J.; Grüner, B.; Ekberg, C. Gamma Radiolytic Stability of $CyMe_4$-BTBP and the Effect of Nitric Acid. *Nukelonika.* **2015**, *60*, 879–884.

2. Hudson, M.J.; Harwood, L.M.; Laventine, D.M.; Lewis, F.W. Use of Soft Heterocyclic N-Donor Ligands to Separate Actinides and Lanthanides. *Inorg. Chem.* **2013**, *52*, 3414–3428.

3. Housecroft, C.E.; Sharpe, A.G. *Inorganic Chemistry*; 4th ed.; Pearson: England, 2012;

4. Lewis, F.W.; Harwood, L.M.; Hudson, M.J.; Drew, M.G.B.; Hubscher-Bruder, V.; Videva, V.; Arnaud-Neu, F.; Stamberg, K.; Vyas, S. BTBPs versus BTPhens: Some Reasons for Their Differences in Properties Concerning the Partitioning of Minor Actinides and the Advantages of BTPhens. *Inorg. Chem.* **2013**, *52*, 4993–5005.

5. Lewis, F.W.; Harwood, L.M.; Hudson, M.J.; Drew, M.G.B.; Desreux, J.F.; Vidick, G.; Bouslimani, N.; Modolo, G.; Wilden, A.; Sypula, M.; et al. Highly Efficient Separation of Actinides from Lanthanides by a Phenanthroline-Derived Bis-Triazine Ligand. *J. Am. Chem. Soc.* **2011**.*133*, 13093-13102.

6. Choppin, G.R. Comparative Solution Chemistry of the 4f and 5f Elements . *J. Alloy. Compd.* **1995**, *223*, 174-179.

7. F. W. Lewis, L. M. Harwood, M. J. Hudson, M. G. B. Drew, V. Hubscher-Bruder, V. Videva, F. Arnaud-Neu, K.S. and S.V. No Title. *Inorg. Chem.* **2013**, *52*, 4993–5005.

8. Edwards, A.C.; Andreas, G.; Mullich, U.; Sharrad, C.A.C.; Pritchard, R.G.; Whitehead, R.C.; Harwood, L.M. Transition Metal-Free, Visible-Light Mediated Synthesis of 1,10-Phenanthroline Derived Ligand Systems†. *Chem. Commun.* **2017**, *53*, 8160–8163.

9. Edwards, A.C.; Wagner, C.; Geist, A.; Burton, N.A.; Sharrad, C.A.; Adams, R.W.; Pritchard, R.G.; Panak, P.J.; Whitehead, R.C.; Harwood, L.M. Exploring Electronic Effects on the Partitioning of Actinides from Lanthanides Using Functionalised Bis-Triazinyl Phenanthroline Ligands. *Dalt. Trans.* **2016**, *45*, 18102–18112.

10. Afsar, A.; Cowell, J.; Distler, P.; Harwood, L.M.; John, J.; Westwood, J. Synthesis of Novel BTPhen-Functionalized Silica-Coated Magnetic Nanoparticles for Separating Trivalent Actinides and Lanthanides. *Synlett.* **2017**, 2795-2799.

11. Ulven, T.; Larsen, A.F. Efficient Synthesis of 4,7-Diamino Substituted 1,10-Phenanthroline2,9-Dicarboxamides. *Org. Lett.* **2011**, *13*, 3546–3548.

12. Afsar, A.; Westwood, J.; Distler, P.; Harwood, L.M.; Mohan, S.; John, J.; Davis, F.J. Separation of Am(III), Cm(III) and Eu(III) by Electro-Spun Polystyrene-Immobilized CyMe4-BTPhen. *Tetrahedron.* **2018**, *74*, 28, 5258–5262.

13. M. Harwood, L.; Afsar, A.; Westwood, J.; J. Hudson, M.; John, J.; Distler, P. Comparing the Extraction of Am(III), Cm(III) and Eu(III) by CyMe4-BTPhen-Functionalized Silica and Zirconia-Coated Magnetic Nanoparticles. *Heterocycles.* **2016**, *93*, 453-464.

14. Afsar, A.; Westwood, J.; Distler, P.; Harwood, L.M.; Mohan, S.; John, J.; Davis, F.J. Separation of Am(III), Cm(III) and Eu(III) by electro-spun polystyrene-immobilized CyMe4-BTPhen. *Tetrahedron.* **2018**, 74, 5258-5262.

15. Afsar, A.; Harwood, L.M.; Hudson, M.J.; Westwood, J.; Geist, A. Effective Separation of the Actinides Am(III) and Cm(III) by Electronic Modulation of Bis-(1,2,4-Triazin-3-Yl)Phenanthrolines. *Chem. Commun.* **2015**, *51*, 5860–5863.

16. Afsar, A.; Laventine, D.M.; Harwood, L.M.; Hudson, M.J.; Geist, A. Utilizing Electronic Effects in the Modulation of BTPhen Ligands with Respect to the Partitioning of Minor Actinides from Lanthanides. *Chem. Commun.* **2013**, *49*, 8534–8536.

Application of a CyMe4-BTPhen Functionalized Silica to the Separation of Rare Earth Elements (REEs)

[1]Zoe Y. Selfe, [1]Laurence M. Harwood, [2]Mark D. Ogden

[1]Department Of Chemistry, University of Reading, Whiteknights, Reading RG6 6AD, UK

[2]Department of Chemical and Biological Engineering, University of Sheffield, Sir Robert Hadfield Building, Sheffield, S1 3JD, United Kingdom

Corresponding author: Zoe.Selfe@pgr.reading.ac.uk

ABSTRACT

Rare Earth Elements (REEs) play a vital role in the manufacturing of high technological products and contribute quite substantially to green technology. This research focuses on implementing methods used in nuclear fuel cycle separations to increase sustainability in today's world by using functionalized silica for the separation of REEs from nitric acid. $CyMe_4$-BTPhen is an extractant of actinides used in the reprocessing of spent nuclear fuel (SNF) with the ability to bind to REEs in the absence of actinides. A fixed-bed column adsorption/desorption process using $CyMe_4$-BTPhen-functionalized silica gel (BTPhen-Si) will be investigated for the partitioning of REEs. The synthesis of BTPhen-Si requires 12 steps where 1 g of starting material neocuproine yields 0.15 g of BTPhen-Si with a molarity of 0.0868 mmol per g of adsorbent. Functionality of the silica gel was determined using thermogravimetric analysis (TGA), infrared spectroscopy (FT-IR) and energy dispersive X-ray analysis to confirm 90% immobilisation of $CyMe_4$-BTPhen onto silica gel. BTPhen-Si had an overall adsorption capacity of 0.048 mg g^{-1} with adsorption capacities ranging from 0.0016 to 0.0038 mg g^{-1} for Y and Sc, respectively. Based on the breakthrough times (t_b) the series could be separated into two groups, mid REE ions (Pr-Eu) (>3 mins) and late REE ions (Gd-Lu) (<1.5 mins), however Sc and Ce would elute with the mid REE ions, whereas Y and La elute with the late REEs. Adams-Bohart, Thomas, Yoon Nelson, Modified Dose Response (MDR) and Lagergren's pseudo first and second order rate kinetics were investigated to describe the mechanism of adsorption. Adams-Bohart and Thomas models were able to describe all ions (Sc, Y and all REEs), however they gave the lowest correlation coefficients at R^2 = ~0.86 and 0.9, respectively. Yoon-Nelson and MDR were not able to describe Sc, Pr, Nd, Sm and Eu. Gibbs free energy was also calculated where all REE ions except Y had a negative ΔG, indicating a spontaneous adsorption process. BTPhen-Si could provide a good material for the extraction of REE ions, however improvements are required to increasing separation and adsorption capacities.

keywords: synthesis, ion exchange, rare earth elements, rare earth separations, functionalized silica

1 INTRODUCTION

Today's world is heavily reliant on Rare Earths Elements (REEs) with uses in all sectors of technology, their addition to products makes them overall stronger and lighter [1]. Contrary to their name "Rare Earth" the metals are actually rather abundant in the Earth's crust. Ce, an early REE, has a concentration of 66 ppm in the Earth's crust, similar to that of Cu (68 ppm) [2]. The later REEs are less abundant with Tm and Lu being the least abundant with concentrations of 0.3 and 0.31 ppm, respectively [2]. The Rare Earth series are a group of seventeen chemical elements (lanthanum (La) to lutetium (Lu)) as well as scandium (Sc) and yttrium (Y). They have useful properties such as strong magnetic fields and the ability to luminesce.

REEs are extremely vital in today's high technological world, having a vast range of applications in industry and consumer products including; catalysts (74%), ceramics and glass (10%), metallurgical applications and alloys (6%), polishes (4%) and others (6%) [3]. REEs are used in medical systems, fluorescent lamps, catalysts and clean energy technologies such as wind turbines and electric cars. Cerium carbonate and cerium oxide are used in catalytic converters in vehicles and neodymium-iron-boron alloys have uses in computer hard drives, electric vehicles, mobile phones and wind turbines as they have strong magnetic fields [4]. Per year, 7,300 tonnes of Nd and 24,000 tonnes of Ce are being produced worldwide and is set to increase as demands are expected to grow by 3 to 7 times between 2021 and 2040 [5–7].

Currently, only 1% of REEs are recycled and, due to their demand, they have remained on the EU critical materials list since 2011. 90% of the world's supply comes from China, coupled with high export prices and high economic values we see these metals as precious [8,9]. A balance between extraction/processing and substitution/recycling is to occur to keep the supply risk low. Supply risk is based upon the concentration of primary supply, global suppliers, and the source countries and is seen as a 'bottleneck' [10].

In 2020 the global consumption of REEs reached 167,000 tonnes and is forecasted to reach 280,000 tonnes by 2030 [11,12]. The United States' electrical vehicle market is set to grow from 1.4 million vehicles in 2020 to 6.9 million in 2025 with each vehicle requiring 1 kg of REE, making up 10% of the global supply of REE [5]. Offshore wind power capacity is expected to reach 86 GW by 2050 in the US requiring over 15 ktonnes of Nd. This rising need for green energy sources coupled with the versatility of said metals, makes recycling these metals a must.

Recycling REEs is paramount in order to keep up with the demands of modern life and rising prices. Large, retired wind turbines and electric vehicle motors are more easily recycled compared to smaller products such as hard disk drives (HDD) and mobile phones. Nissan recovers REEs from its electric motors by subjecting them to iron oxide at 1400 °C to create a molten mixture. Separation of the REE from the iron carbon slag materials is then achieved by the addition of a borate-based flux [13]. For the smaller products, where the concentration of REEs are low, the techniques and infrastructures are unfortunately underdeveloped and costly compared to the low quantities of recoverable materials. In an average HDD there are many different metals (Al, Fe, Cu, Sn, Ni, AG, Au and Pd) but only 2.5-4.6 g of NdFeB which makes separating the REEs from the other metals rather difficult [14]. Traditional hydrometallurgical methods are carried out using H_2SO_4 at room temperature to precipitate out Nd from NdFeB and then converted to NdF_3 or Nd_2O_3 to separate from steel and copper [9,15]. Large amounts of harmful chemicals are required for such reprocessing, deeming hydrometallurgical methods impractical and dangerous. The Ames Laboratory in Iowa have developed and employed a safer method involving dissolution in Cu (II) under 100 °C to recover Nd from NdFeB. Ammonium oxalate is then added to precipitate the REEs, and calcination occurs at 800 °C to afford RE_2O_3 [16].

After obtaining the REEs in their ore form after mining, many processes are used to extract the Rare Earth Oxides (REO). The first step is physical beneficiation to crush the ores and decrease the particle sizes to 0.1 nm. A mixture of fatty acids and water is added to separate the REEs from the materials of low economic value. Chemical beneficiation is also required to remove strontium/calcium carbonates to obtain a REO with a 85-90% purity. After the REO are obtained, the most challenging step is intra-rare earth separation. The REE series all have

very similar chemical and physical properties to each other, all possessing the 3+ oxidation state apart from Ce^{4+}, Yb^{2+}, Sm^{2+} and Eu^{2+} [17,18]. Across the REE series a decrease in ionic radii from La to Lu occurs forming the basis of adjacent REE separation. The valence 4f-orbitals provide little to no shielding as they are rather diffuse and core like in nature. Upon increasing nuclear charge, a pull on the orbitals occurs and the ionic radii decreases across the series, this is known as “Lanthanide Contraction” [19,20]. Techniques used previously for the separation of REEs include fractional distillation, requiring hundreds of dissolution and crystallisation steps of REE nitrates/hydroxides. Some of the REEs can also be separated from others using selective oxidation/reduction reactions [21].

In industry, separation of the REEs is currently carried out using counter current liquid-liquid solvent extraction techniques where the use of an organic ligand in kerosene or aromatic solvent will extract and transport REEs from an aqueous layer to the organic layer. Typical ligands used in this process are di-2-ethyl-hexylphosphoric acid (HDEHP) for RE chlorides/sulfates, and tri-n-butyl phosphate (TBP) for RE nitrates [22]. DEPHA gives an inter-separation factor of $SP_{RE1/RE2}$ = 2.5, which increases between later REEs. Other examples used are 2-ethyl-hexyl-2-ethyl-hexyl-phosphoric acid (HEHEHPA), versatic acid 10 46, versatic acid, Cyanex ® 572 and Aliquat 336 [23]. Most commercial ligands use oxygen donors, however pyridines are able to bind to REEs too as ligands must possess donor atoms such as oxygen, sulfur and nitrogen.

The downsides of solvent-solvent extraction are the need for the large volumes of solvents, degradation of solvents, solubility issues and the formation of large quantities of secondary waste. Chromatography is an alternative technique to solvent-solvent extraction, examples include extraction chromatography, cation-exchange chromatography and displacement chromatography. This separation technology is versatile and reusable and can be used even if the metal concentration is low. The use of strong acid (SA) cation exchange resins are particularly efficient as they have a large surface area and high selectivity for REEs. A large amount of research has been devoted into recovering REEs from acidic solutions for the use in uranium mining waste streams and technological waste streams. An impregnated resin such as Cyanex 272 and 1-hexyl-4-ethyloctyl-isopropylphosphonic acid (HEOPPA) was able to recover REEs in the order of sorption; Lu(III) > Yb(III) > Tm(III) > Er(III) > Y(III) > Ho(III) showing the ability to separate adjacent REEs [24]. N. M. Shokobayev et al studied D72, a gel like resin with sulfuric acid functional groups, where it was observed that the resin had a higher capacity for earlier REEs compared to the later REEs [25].

Pyridine is an N-donor ligand capable of binding to REEs and transition metals. Suzuki. T *et al* studied the REE extraction/separation ability of pyridine functionalized resin materials using 4-vinylpyridine and *m/p*-divinylbenzene embedded in silica beads. A column chromatography technique was employed and the REEs were eluted in reverse order in methanolic nitric acid solution [26]. 1,10-phenanthroline **1**, a precursor of neocuproine **2** (1,10-phenanthroline 2,9 dimethyl), contains two N-donor atoms also capable of binding to REEs (Figure 1). F. Hart and F. Laming were able to isolate 1,10-phenanthroline REE chlorides and 1,10-phenanthroline REE trithiocyanates for all REEs (La-Lu) [27]. 1,10-phenanthroline Nd (III) and Am (III) complexes were measured to have a binding constant ($\log_{10}K_{101}$) of 1.61 ± 0.03 and 3.03 ± 0.09, respectively [28]. The backbone of 1,10-phenanthroline is easily functionalizable with silica and able to bind to transition metals from dilute acid media to provide an effective way to extract metals [29].

Neocuproine **2**, a precursor of $CyMe_4$-BTPhen **3** is similar to 1,10-phenanthroline **1**, however it bears two methyl groups in the 2 and 9 positions. It is a known extractant of copper, iron and cobalt forming 2:1 ligand to metal complexes (Figure 1) [30–33]. Neocuproine can be functionalized onto silica gel (NC-Si) **4** and used to extract REEs from 2% nitric acid where the REE series can be separated into 3 groups; early, mid and late REEs.

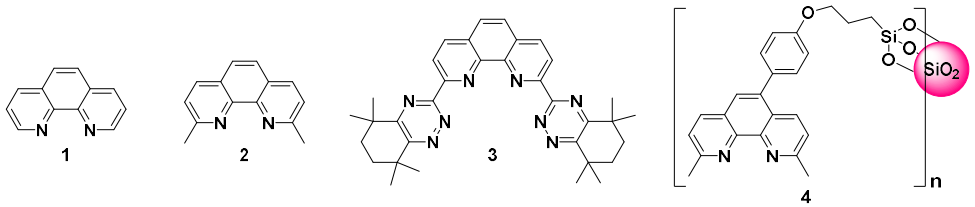

Figure 1. Structures of 1,10-phenanthroline **1,** neocuproine **2**, $CyMe_4$-BTPhen **3** and NC-Si **4**

$CyMe_4$-BTPhen **3** is a heterocyclic ligand previously used in the separation of actinides from REEs in spent nuclear fuel (SNF) raffinate via solvent-solvent extraction in 1-octanol [34]. $CyMe_4$-BTPhen **3** contains the 1,10-phenanthroline **1** moiety as well a 1,2,4-triazine functional group where coordination occurs through 6 nitrogen donor atoms in either a 1:2 or 1:1 metal to ligand complex. Actinides' 5*f*-orbitals are more expanded compared to 4*f*-orbitals in REE ions which in turn forms stronger covalent bonds to the ligand [35–37]. This basis efficiently separates actinides from REEs giving separation factors ($SF_{Am/Eu}$) of ~200-400 in the range of 1-4 M HNO_3 [38]. This theory of *f*-orbital size preference could pave the way for separations between adjacent REEs ions from each other due to the lanthanide contraction phenomenon.

This work investigates $CyMe_4$-BTPhen functionalized silica gel (BTPhen-Si) **5** in a fixed-bed column for the adsorption and desorption of REEs from an aqueous solution of 2% nitric acid. The structure and details of this material is given in Figure 2. BTPhen-Si **5** is a soft donor ligand with the potential to extract. Due to the slight size differences between REEs, intra rare earth partitioning could occur as BTPhen-Si **5** would bind preferentially to some REEs over others depending on the cavity size of $CyMe_4$-BTPhen.

Functionality	**Characteristic**	
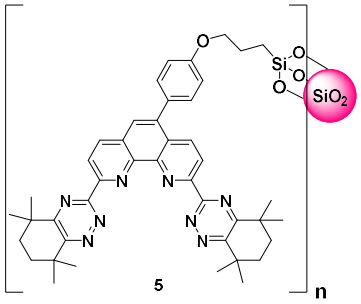	Name:	$CyMe_4$-BTPhen functionalized silica gel **5**
	Acronym:	BTPhen-Si
	Particle size:	40-63 μm*
	Pore size:	60 Å*
	H^+ capacity:	0.628 ± 0.001 mmol·g^{-1}

Figure 2. Functionality and characteristics of $CyMe_4$-BTPhen functionalized silica gel (BTPhen-Si) **5**. *taken from silica gel precursor material [39]

2. MATERIALS AND METHODS

2.1. Materials

All reagents were purchased from AlfarAesar, Fisher, Fluorochem or Sigma-Aldrich. All chemicals were of analytical grade and used as received without further purification. 3-Chloropropyl-functionalized silica gel (CP-Si) (8 in Figure 3) was purchased from Sigma Aldrich with a particle size of 230-400 mesh and a pore size of 60 Å and used as supplied [39]. The extent of chloropropyl labelling of the purchased substrate was ~ 2.5 % loading and the matrix active group was ~ 8 % functionalized.

2.2. Synthesis of BTPhen-Si

The synthesis of BTPhen-Si **5** starts with the mono-bromination of the precursor, neocuproine **2**, using bromine (0.6 equivalents) in the presence of H_2SO_4 (20% SO_3). After 9 subsequent steps, the bromine on the phenanthroline backbone allows a Suzuki-Miyaura reaction using 4-hydroxyphenylboronic acid and a tetrakis(triphenylphosphine)palladium(0) catalyst to form 4-(Hydroxyphenyl)-$CyMe_4$-BTPhen (7 in Figure 3). This phenol functionalized ligand could then be immobilised onto CP-Si **8** using NaH in DMF to afford BTPhen-Si **5**, as shown in Figure 3.

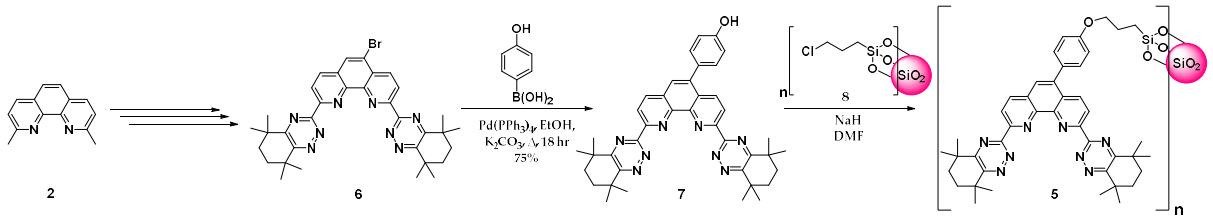

Figure 3. Synthesis of BTPhen-Si solid phase extractant

2.3. Characterization of BTPhen-Si

Confirmation of the synthesis of 4-(hydroxyphenyl) $CyMe_4$-BTPhen **7** was achieved using NMR spectroscopic analysis. The degree of immobilization of these ligands on the silica surface was estimated by elemental analysis using energy dispersive X-ray spectroscopy (EDX) in conjunction with SEM. Thermogravimetric analysis (TGA) was performed to determine the percentage organic content, given in supplemental information.

For adsorption studies, inductively coupled plasma mass spectroscopy analysis (ICP-MS) analysis was carried out using a Thermo-Fisher iCAP Q ICP-MS with Rh as the internal standard. A stock solution of 2% HNO_3 spiked with 5 ppb Rh was prepared using ultra-pure water and HNO_3 (70%, purified by redistillation, ≥ 99.999% trace metals basis). All standard solutions were prepared using a stock solution of 2% HNO_3 spiked with 5 ppb Rh. Standards were prepared using metal mixes purchased from Sigma-Aldrich as TraceCERT (Traceable Certified Reference Materials). Standards used to calibrate the ICP-MS were at concentrations of 5, 10, 25, 50 and 100 ppb. All extraction samples were normalised to 2% HNO_3 and spiked with 5 ppb Rh before testing. Samples (5 mL) were taken before and after extractions to provide true initial and end concentrations. An average of three readings was taken with all samples.

2.4. Adsorption Studies – Dynamic Method

BTPhen-Si **5** (0.1 g) was loaded into a column (D=1.1 cm, H=2.6 cm). A sample of REE solution (containing Sc, Y, La, Ce, Pr, Nd, Sm, Eu, Gd, Tb, Dy, Ho, Er, Tm, Yb, Lu) (~0.12 mg L^{-1}) (4 mL) in 2% nitric acid (HNO_3) was passed through the column with a flow rate of 0.5 mL min^{-1}. The eluate was collected from the column and subjected to ICP-MS analysis. Desorption of the RE (III) ions was performed by passing samples of nitric acid with various concentrations (0.1 M, 0.5 M, 1, M, 1.5 M, 2 M, 2.5 M, 3 M, 3.5 M, 4 M) (1 mL) through the column with a flow rate of 0.5 cm^3 min^{-1}. The effluent solution was collected in 1 mL fractions and subjected to ICP-MS analysis. A graph of C_t/C_0 against time for each individual rare earth ion was plotted to obtain the breakthrough curve where C_0 is the initial REE (III) ion concentration (mg L^{-1}) and C_t is the outlet ion concentration at a particular time (mg L^{-1}). The exact same experiment was also carried out on chloropropyl SiO_2 gel **7**, however no adsorption of rare earth ions were achieved, confirming the $CyMe_4$-BTPhen ligand itself was responsible for the adsorption of rare earth metals.

2.4.1. Column Kinetics

Pseudo first-order (PFO) and pseudo second-order kinetic (PSO) models have been used to understand the characteristics and the mechanism of the adsorption of rare earth ions onto BTPhen-Si (5 in Figure 1). The linear equation for pseudo-first order model, based on Lagregren's model is given in equation (1) and the linear pseudo second-order expression is given in equation (2) [40–42].

$$ln(q_e - q_t) = ln(k_1 q_e) - k_1 t \quad (1)$$

$$\frac{t}{q_t} = \frac{1}{k_2 q_e^2} + \frac{t}{q_e} \quad (2)$$

Where k_1 (min^{-1}) is the pseudo-first order rate constant, k_2 (min^{-1}) is the second-order rate constant, q_e ($mg \cdot g^{-1}$) is the adsorption capacity at equilibrium. q_t (mg g^{-1}) is the adsorption capacity at any time t (min) which is calculated using equation (3) where C_0 is the initial REE (III) ions concentration (mg L^{-1}), C_t is the outlet concentration (mg L^{-1}), W is the mass of the material used and V is the solution volume (L).

$$q_t = (C_0 - C_t)\left(\frac{V}{W}\right) \quad (3)$$

2.3.2. Breakthrough Modelling

Several theoretical adsorption models have been used to predict the adsorption behaviours of the rare earth ions on BTPhen-Si **5**. The shape of the curve is determined by the equilibrium isotherm which is influenced by the individual transport diffusional processes in the column and adsorbent. The four most commonly used mathematical models for continuous adsorption have been applied to the breakthrough curves in this work; Adams-Bohart, Yoon Nelson, Thomas and Modified Dose Response (SI.2) [43–46].

2.3.3. Gibbs Free Energy

Determination of the spontaneity of the adsorption reaction for each separate rare earth ion was measured using the change in Gibbs free energy (∆G°). The expression for change in Gibbs free energy is given in equation 5, where K_c is the equilibrium constant determined by the ratio between the adsorption concentration and elution concentration of a particular ion as shown in equation (4) [43].

$$K_C = \frac{q_e}{c_e} \quad (4)$$

$$\Delta G° = -RTlnK_c \quad (5)$$

Where K_c is the equilibrium constant, q_e is the amount of ion (mg) absorbed onto 5 from 1 L of solution at equilibrium, C_e is the equilibrium concentration (mg L^{-1}) of the ion in the eluted solution, T is the temperature in Kelvin and R is the gas constant (j mol^{-1} K^{-1}) to give ΔG (kJ mol^{-1} K^{-1}) [43].

3 RESULTS

3.1. Characterization of Adsorbent

Full characterization data is given in supplemental information (SI) section. The confirmation of the functionalization of BTPhen-Si **5** onto the surface of the SiO_2 gel was determined by the comparison with commercial chloropropyl-functionalized SiO_2 gel (**7** in Figure 3) using FT-IR. Both show a strong Si-O-Si stretch at 1050 cm^{-1}, but only BTPhen-Si **5** shows a stretch at 1590 cm^{-1} relating to conjugated C=C stretches from the organic content on the ligand (SI.1.1). Elemental analysis using energy dispersive X-ray spectroscopy of BTPhen-Si **5** and chloropropyl-functionalized SiO_2 gel **7** showed an increase in the carbon content after immobilisation of the $CyMe_4$-BTPhen ligand **3** onto the SiO_2, as well as a decrease in Si and Cl content (SI.1.3). There was also a ~90% loss of chlorine, all of which equates to ~90% immobilisation onto the surface of the SiO_2. TGA analysis showed a mass loss around 90°C, corresponding to absorbed water, followed by a mass loss between 100-475 °C relating to decomposition of organic matter, indicating a ~6% w/w of $CyMe_4$-BTPhen content in BTPhen-Si **5** (SI Figure 2). This 6% of organic matter relates to the amount of 4-hydroxypropyl-BTPhen which gives a molarity of 0.0868 mmol per 1 g of BTPhen-Si **5**. The metal to ligand ratio using the average molecular weight of REEs (excluding Pm), Y and Sc gives a molar ratio of 1:250.

3.2. Adsorption Studies – Dynamic Method

Analysis of the breakthrough curves obtained by fixed-bed dynamic adsorption study of rare earth ions onto BTPhen-Si **5** allows the performance of the fixed-bed column to be measured based on breakthrough time [47,48]. Three key characteristics are measured; breakthrough time (t_b) (C_t/C_0 = 0.05), exhaustion time (t_s) (C_t/C_0 = 0.95), as well as the time it takes for half of the ions to elute (τ) (C_t/C_0 = 0.5) [47]. The breakthrough curves, $C_t/C_0 = f(t)$, for the rare earth metals (III) (La-Lu) and Sc (III) and Y(III) are displayed in Figure 4.

a)

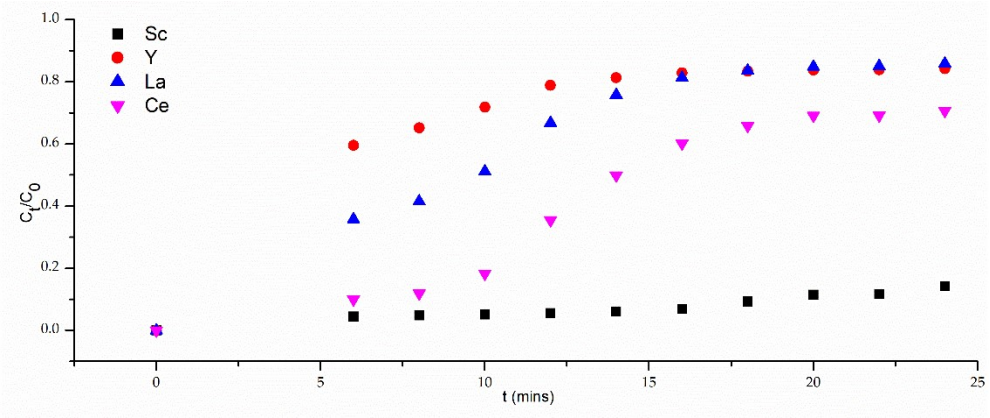
Sc
Y
La
Ce
C_t/C_0
t (mins)

b)

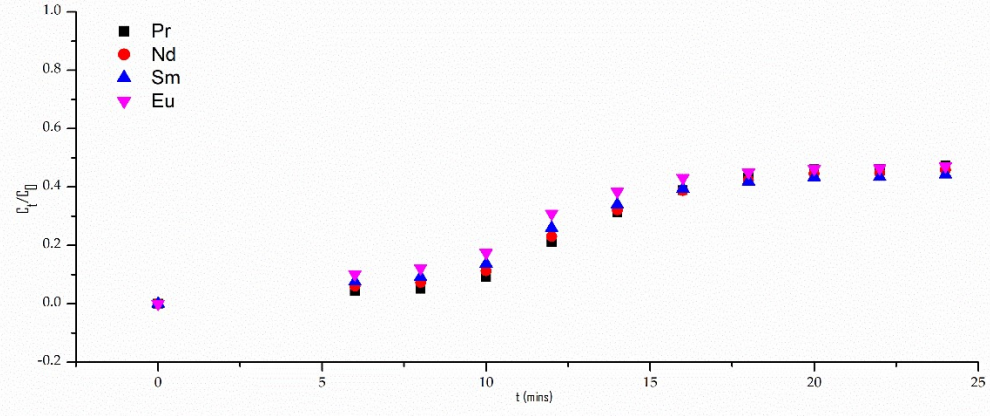
Pr
Nd
Sm
Eu
t (mins)

c)

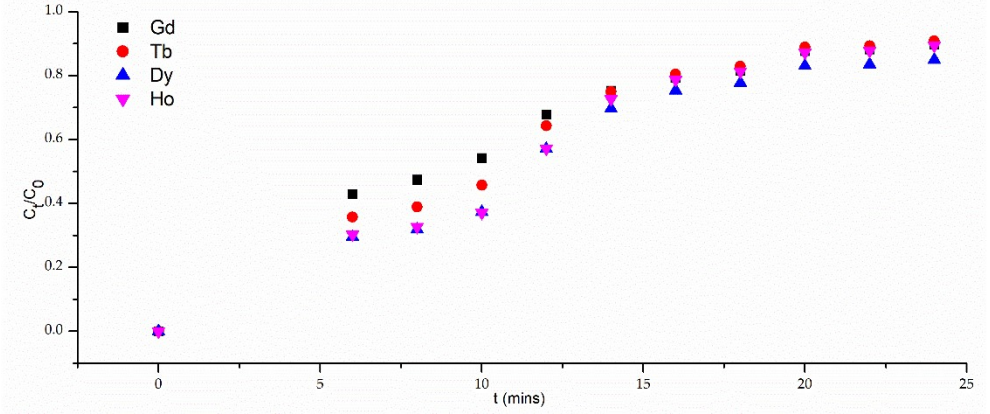
Gd
Tb
Dy
Ho
C_t/C_0
t (mins)

d)

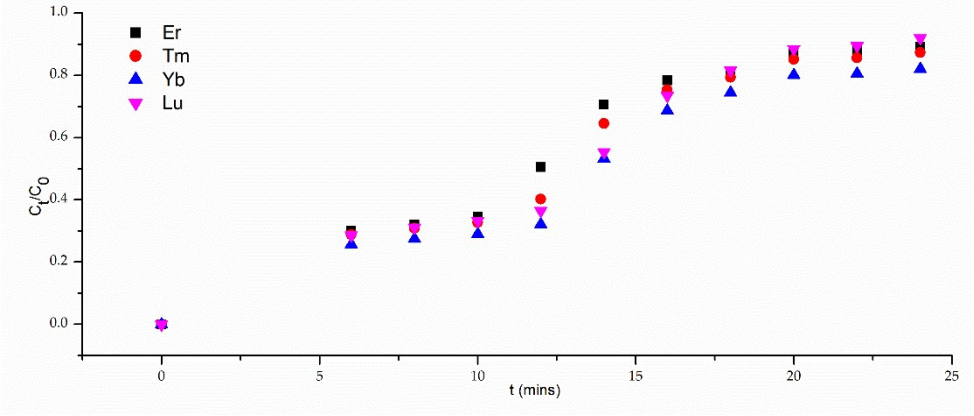
Er
Tm
Yb
Lu
C_t/C_0
t (mins)

Figure 4. Breakthrough curves for the adsorption of first quarter of the REE series (a), second quarter of the REE series (b), third quarter of the REE series (c) and the last quarter of the REE series (d) REEs by BTPhen-Si **5** in 2 M nitric acid. Subsequentially increasing nitric acid concentration 0 – 4 M, flow rate 0.5 mL/min, pH; 5, temperature; 24°C.

The results of this study indicate that the breakthrough curves for each rare earth ion (III) vary between each species but most follow the characteristic S-shaped profile (Figure 4). Based on the breakthrough times (t_b) the series could be separated into two groups; mid REE ions (Pr-Eu) and late REE ions (Gd-Lu), where Sc and Ce would elute with the mid REE ions, whereas Y and La would elute with the late REEs. It appears that BTPhen-Si **5** has a preference for Ce-Eu and Sc as these ions took longer to elute from the column. Only Y-Ce and the later REEs (Gd-Lu) were able to achieve τ where 50% of their initial concentration is eluted from the column. For earlier REEs (Pr and Eu) and Sc, the majority remain on the column (Table 1). Figure 5 shows the relationship between the z/r and the breakthrough times; t_b and τ. It appears there is no trend in the breakthrough times of the earlier REEs (La-Sm) (Figure 5 a)), but a gradual increase is observed in proportion to z/r for the later REEs (Gd-Lu). Eu shows some anomalies as it has similar z/r ratios to Y and Gd but it takes a lot longer to elute from the column, possibly creating stronger bonds to the ligand. Figure 5 b) shows a direct correlation between the z/r and the time it took for 50% of the ion to be eluted for the later REE ions (Gd-Lu) as the τ increased across these ions. Sc and La-Eu however did not reach 50% elution and higher concentrations of nitric acid and/or more bed volumes would be required to elute these ions.

Table 1. Column parameters determined for breakthrough behavior upon increasing nitric acid concentration 0.01 – 4 M. Flow rate; 0.5 mL min^{-1}, pH; 5, temperature; 24°C.

REE	Breakthrough (t_b)		Exhaustion		50% Capacity (τ)	
	conc. (units)	time (mins)	conc. (units)	time (mins)	conc. (units)	time (mins)
Sc	0.0038	8.2				
Y	0.0016	1.3			0.0008	5.0
La	0.0026	0.8	0.000129	15.6	0.0013	9.8
Ce	0.0036	3.0			0.0018	14.0
Pr	0.0038	7.3				
Nd	0.0038	4.9				
Sm	0.0037	4.0				
Eu	0.0036	3.0				
Gd	0.0023	0.7	0.000114	18.2	0.0011	8.8
Tb	0.0026	0.8	0.000128	15.9	0.0013	10.5
Dy	0.0028	1.0	0.000141	18.3	0.0014	11.3
Ho	0.0028	1.0	0.000139	16.1	0.0014	11.3
Er	0.0028	1.0	0.000139	18.2	0.0014	11.9
Tm	0.0028	1.0	0.000142	16.1	0.0014	12.8
Yb	0.0030	1.2	0.000148	17.5	0.0015	13.7
Lu	0.0029	1.0	0.000143	19.1	0.0014	13.4

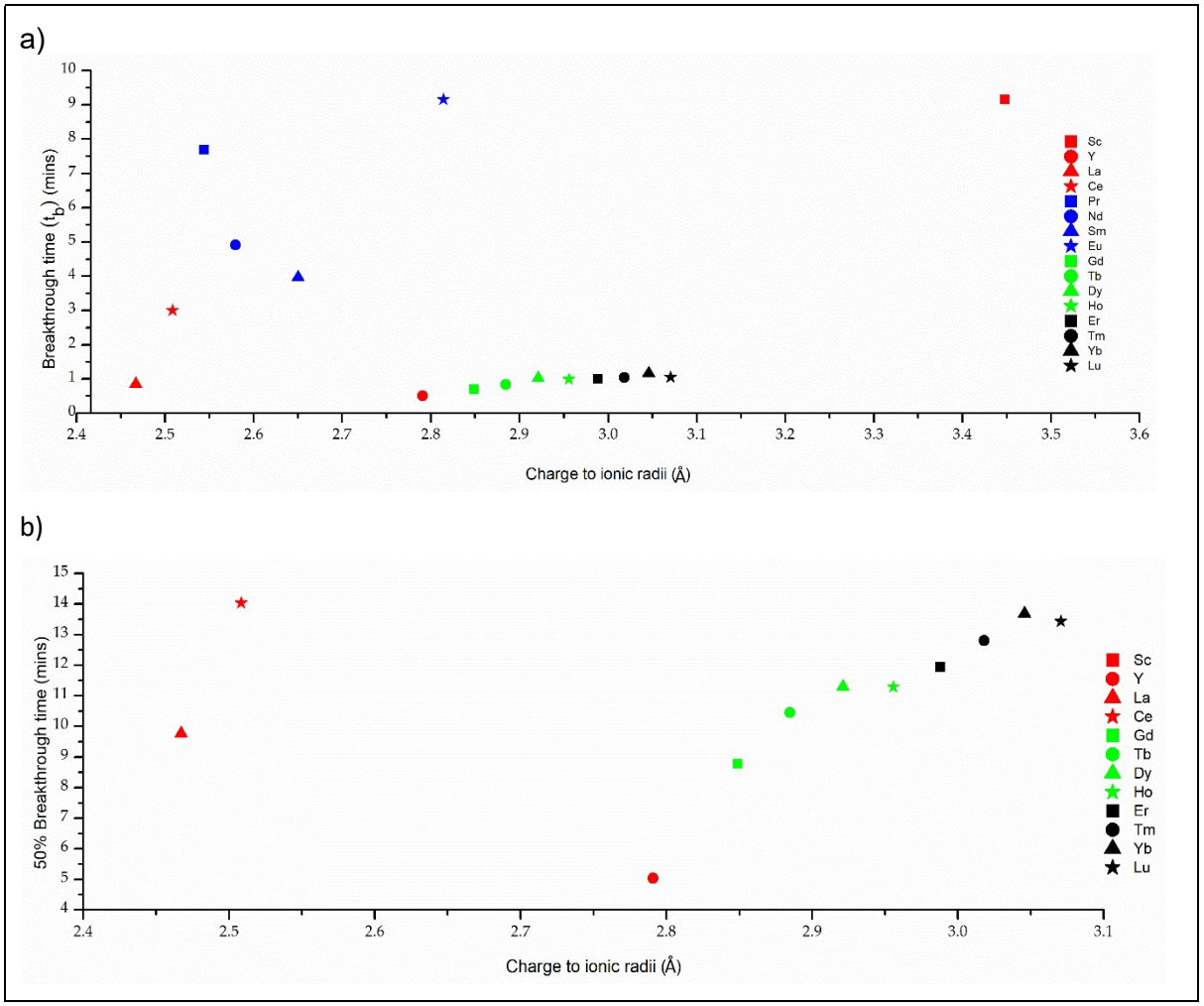

Figure 5. Breakthrough times; (a) t_b and (b) τ

3.2.1 Column Kinetics

A graph of $\ln(q_e - q_t)$ was plotted against t using Lagregren's expression (9) where linear regression was applied to find the pseudo first-order rate constant (k_1) from the slope and q_e was found from the intercept for each of the rare earth ions (Table 2). Similarly, the pseudo-second order kinetic constant (k_2) and q_e for each of the rare earth ions was found from the slope and intercept (respectively) from the graph of t/q_t against t and displayed in table 2 [49].

The Lagregren expression explains adsorption processes, however in this study the process is the desorption of ions from BTPhen-Si which gives rise to negative values for the rate constants; k_1 and k_1. Overall, the pseudo-second order rate equation gave higher correlation coefficients (R^2) (>0.804), and therefore gave a better description of desorption for all REE ions compared to the first-order rate (>0.559). The theoretical q_e values for the early REEs are much closer to the experimental q_e values obtained from the second order rate equation (except for Ce), whereas the q_e values obtained from the first order rate equation are much closer to the experimental values for the late REEs (except for Yb). For both first-order and second-order there seems to be no trend in k_1 or k_2 rate constants across the REE series, however as k_1/k_2 is a time scaling factor, the higher the value of this parameter the quicker the system reaches equilibrium conditions.

Table 2. REE uptake by BTPhen-Si **5** in 2 M nitric acid subsequentially increasing nitric acid concentration 0.01 – 1 M. Flow rate; 0.5 mL min^{-1}, pH; 5, temperature; 24°C.

REE	Experimental	PFO			PSO		
	q_e (mg g^{-1}) (x 10^{-3})	q_e (mg g^{-1})	k_1 (min^{-1})	R^2	q_e (mg g^{-1}) (x 10^{-3})	k_2 (min^{-1})	R^2
Sc	0.00383	0.00042	-0.133	0.975	0.00342	-824	0.998
Y	0.00162	0.00585	-0.071	0.559	0.00060	-1455	0.992
La	0.00257	0.00469	-0.110	0.620	0.00053	-882	0.961
Ce	0.00361	0.00147	-0.180	0.652	0.00111	-444	0.961
Pr	0.00382	0.00072	-0.201	0.646	0.00201	-389	0.986
Nd	0.00375	0.00089	-0.184	0.648	0.00208	-417	0.989
Sm	0.00369	0.00126	-0.161	0.627	0.00214	-473	0.993
Eu	0.00359	0.00166	-0.147	0.605	0.00203	-511	0.993
Gd	0.00228	0.00310	-0.124	0.694	0.00041	-872	0.889
Tb	0.00256	0.00231	-0.149	0.648	0.00037	-916	0.880
Dy	0.00281	0.00173	-0.166	0.637	0.00058	-685	0.929
Ho	0.00278	0.00155	-0.175	0.654	0.00042	-812	0.889
Er	0.00279	0.00108	-0.194	0.689	0.00042	-795	0.887
Tm	0.00284	0.00082	-0.208	0.753	0.00050	-691	0.894
Yb	0.00297	0.00056	-0.226	0.793	0.00069	-541	0.913
Lu	0.00285	0.00078	-0.211	0.826	0.00034	-829	0.804

3.3. Adsorption Modelling

Several mathematical models have been proposed for predicting the efficiency of laboratory scale column studies for industrial applications. In this present study, Adams-Bohart, Yoon Nelson, Thomas and MDR models were employed to find the best fitting model to predict the behavior of the dynamic column. Comparisons between the rate constants and the charge to ionic radii ratio (z/r) where made and displayed in Table 3 and Figure 6. Across the REE series (La to Lu) the z/r increases due to lanthanide contraction, however Sc and Y both have a much larger z/r ratio compared to their position in the series, Sc having a larger ratio than the rest of the REEs and Y has a similar z/r to that of Eu. The fittings for all models are provided in the supplementary information (SI Figures 3-6).

The values of $\ln(C_0/C_t)$ were plotted against t and the slope (k_{AB}) and intercept (N_0) were calculated using Adams-Bohart equation (S1) as a linear relationship. The values of k_{AB} and N_0 are represented in Table 3 along with the correlation coefficients (R^2) (0.618 to 0.937) for each REE. The R^2 value increases with increasing z/r ratio suggesting the Adams-Bohart model describes the later ions better than the earlier ones (Figure 6 a)). BTPhen-Si **5** has the highest saturation capacities (N_0) for Sc, Ce, Pr, Nd and Sm indicating a preference for these ions, which agrees with the slow breakthrough times seen in Table 1. There doesn't appear to be a trend between k_{AB} and z/r ratio for the smaller REEs (Y-Eu), however as the z/r ratio increases for the larger REEs (Gd-Sc) the k_{AB} also increases, showing that size isn't the only contributing factor determining rate of adsorption/desorption.

The values of τ and k_{YN} are obtained from a graph of C_t/C_0 against t by plotting a non-linear curve fit using the Yoon-Nelson equation (S3), these constants and correlation coefficients for all rare earth ions (III) are represented in Table 3. The K_{YN} is the rate constant that explains the diffusion characteristics of the mass transfer zone. The Yoon-Nelson model gave accurate values for τ in comparison to the experimental data when data from comparing Tables 3 and 1. The Yoon-Nelson model could not be fit for Sc and Pr-Eu as 50% breakthrough (τ) was not achieved. Good R^2 values (0.788 to 0.969) were calculated for the REEs that could be described by the Yoon-Nelson model. For the later REEs, as the charge to ionic radii increases from Gd to Lu (2.85-3.09), the rate constant also increases, showing a correlation with the size of the ion and the method of desorption. La and Ce doesn't follow suit indicating that other factors aside from the size of the ion are contributing to adsorption/desorption characteristics (Figure 6 b)).

Overall, the Thomas model provided a good fit to every rare earth ion with R^2 values ranging from 0.80 to 0.97, with a slightly better fit for the late REEs. A linear regression curve using equation S6 was applied to the graph of $\ln((C_0/C_t)-1)$ against t to find the k_{Th} and q_0 values from the slope and intercept respectively (Table 3). As the z/r increases from 2.5 to 2.8 for REEs elements; Ce to Y, the K_{Th} decreases. Similarly to the Yoon-Nelson model, as the z/r increases above 2.82 Å (Eu to Sc) the K_{Th} starts to increase again. There appears to be no direct correlation between the size and rate constant, indicating there are other factors affecting adsorption/desorption (Figure 6 c)).

Table 3. Breakthrough modelling parameters for REE on BTPhen-Si

	Adams-Bohart			***Yoon-Nelson***		
REE	k_{AB} (L mg^{-1} min^{-1})	N_0 (mg L^{-1})	R^2	k_{YN} (min^{-1})	τ (min)	R^2
Sc	27.950	0.0255	0.768			
Y	9.782	0.0117	0.618	0.196	6.385	0.788
La	15.662	0.0122	0.846	0.207	9.602	0.946
Ce	28.790	0.0143	0.883	0.188	15.757	0.925
Pr	35.142	0.0161	0.874			
Nd	30.754	0.0167	0.887			
Sm	27.530	0.0172	0.878			
Eu	24.572	0.0171	0.868			
Gd	14.622	0.0119	0.846	0.197	8.970	0.946
Tb	17.115	0.0119	0.882	0.222	9.943	0.969
Dy	18.826	0.0127	0.890	0.201	11.381	0.957
Ho	19.227	0.0123	0.896	0.228	11.004	0.969
Er	19.843	0.0124	0.906	0.227	11.391	0.967
Tm	20.637	0.0128	0.917	0.216	12.204	0.960
Yb	21.803	0.0136	0.925	0.198	13.606	0.953
Lu	21.593	0.0127	0.937	0.229	12.484	0.962
	Thomas			***Dose-Response***		
REE	k_{Th} (L mg^{-1} min^{-1})	q_0 (mg g^{-1})	R^2	q_m (mg g^{-1})	a	R^2
Sc	0.074	0.2169	0.947			
Y	0.070	0.0465	0.797			
La	0.144	0.0127	0.887	0.165	3.494	0.964
Ce	0.191	0.0522	0.890	0.253	4.468	0.991
Pr	0.184	0.0765	0.855			
Nd	0.157	0.0791	0.855			
Sm	0.136	0.0813	0.831			
Eu	0.123	0.0771	0.817			
Gd	0.147	0.0088	0.970	0.154	2.935	0.954
Tb	0.177	0.0168	0.956	0.173	3.706	0.929
Dy	0.163	0.0257	0.925	0.194	3.820	0.951
Ho	0.187	0.0236	0.942	0.193	4.257	0.925
Er	0.191	0.0256	0.941	0.200	4.300	0.912
Tm	0.187	0.0298	0.933	0.214	4.225	0.903
Yb	0.174	0.0374	0.922	0.237	4.148	0.913
Lu	0.216	0.0302	0.947	0.223	4.442	0.864

The values of q_m and a are obtained by plotting a non-linear curve using the MDR equation (S7) on a graph of C_t/C_0 against t to determine whether the MDR model gave a good description of the mechanics of the adsorption of the rare earth ions (III). The model was only able to be fit to the later REE ions (Gd-Lu) and La and Ce with high correlation coefficients (0.864 to 0.991) (Table 3). The MDR rate constant (q_m) showed a slight increase across the rare earth series, corresponding to the slight increase in elution time across the series from Gd to Lu, showing a slight preference for the later REE ions.

a)

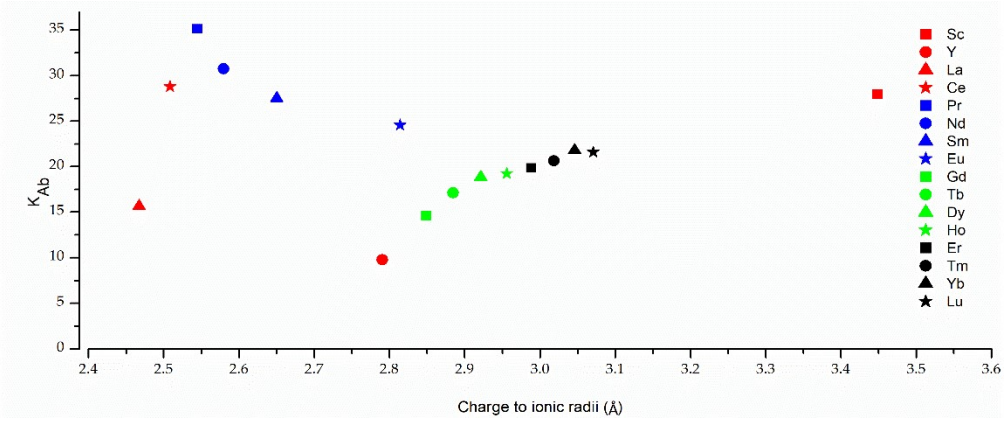

b)

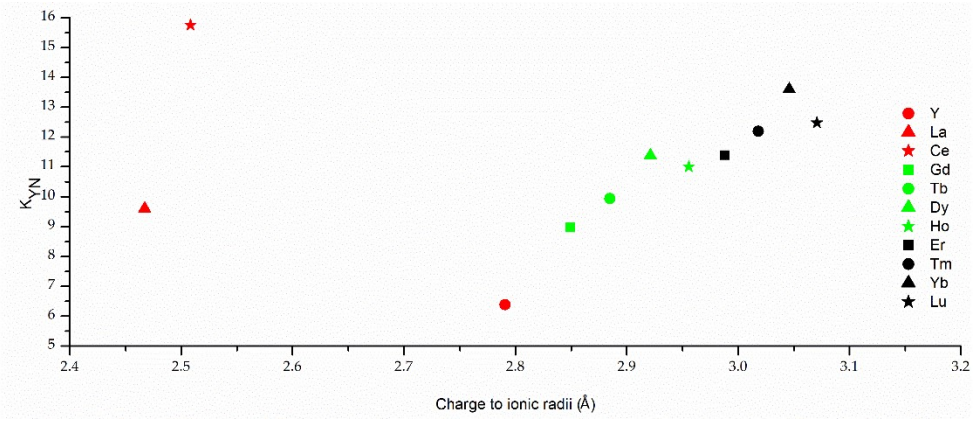

c)

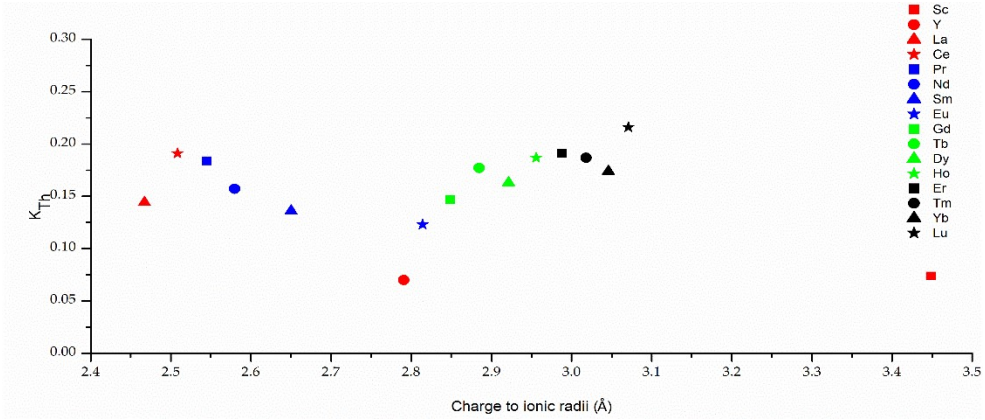

d)

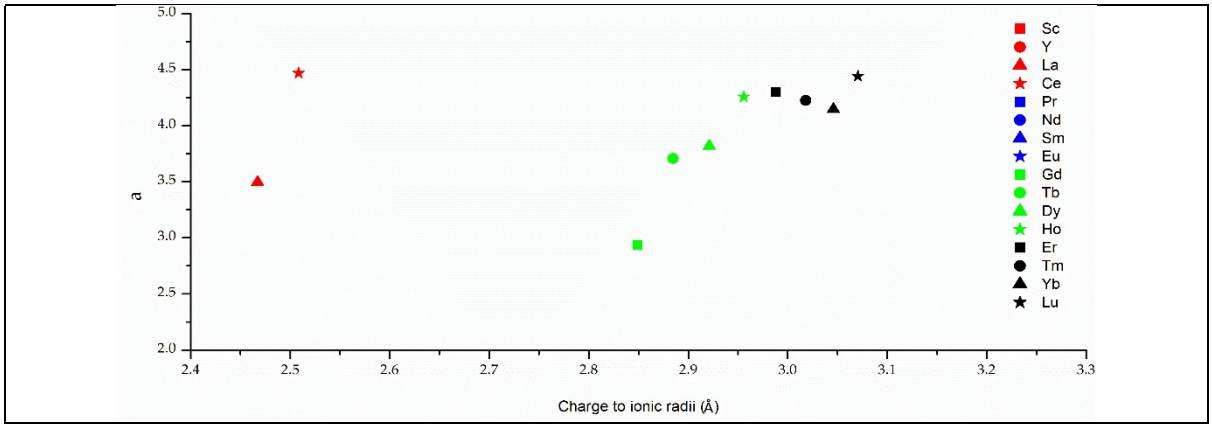

Figure 6. Model parameters for breakthrough models plotted versus charge density indicator (Z/IR) of REE – a) Adams-Bohart constant (k_{AB}), b) Yoon-Nelson constant (k_{YN}), c) Thomas constant f(k_{Th}) and d) MDR constant (a). Upon increasing nitric acid concentration 0.01 – 4 M. Flow rate; 0.5 mL min^{-1}, pH; 5, temperature; 24°C.

Overall, the Thomas and Adams-Bohart models described the adsorption mechanism of all REE ions, however the R^2 values for Adams-Bohart were the lowest compared to Yoon-Nelson, Thomas and MDR. The early and mid REEs were best described by the Thomas model, whereas the later REEs were best described by Yoon-Nelson.

3.4 Gibbs Free Energy

The Gibbs free energy (ΔG°) was calculated for each of the rare earth ions to understand how favourable adsorption is onto BTPhen-Si **5** at room temperature. Figure 7 shows the calculated values for ΔG° for all rare earth ions. Sc and Pr have the lowest ΔG° values compared to the other ions, indicating a more spontaneous adsorption process. Y is the only ion to have a positive ΔG° showing adsorption is not a spontaneous process and more energy input is required to increase spontaneity and produce a more favourable adsorption process [50]. Overall, the larger REEs (Ce-Sm) have a much more negative ΔG° values than the smaller REEs (Gd-Sc). Interestingly, Y and Eu have similar z/r ratios of 2.78 and 2.81 Å respectively, however, their ΔG° values are very different. Y has a positive ΔG° (0.94 kJK^{-1}mol^{-1}) and Eu has a negative ΔG° (-5.36 kJK^{-1}mol^{-1}) indicating that the size of the ion is not the only contributing factor to the ΔG°.

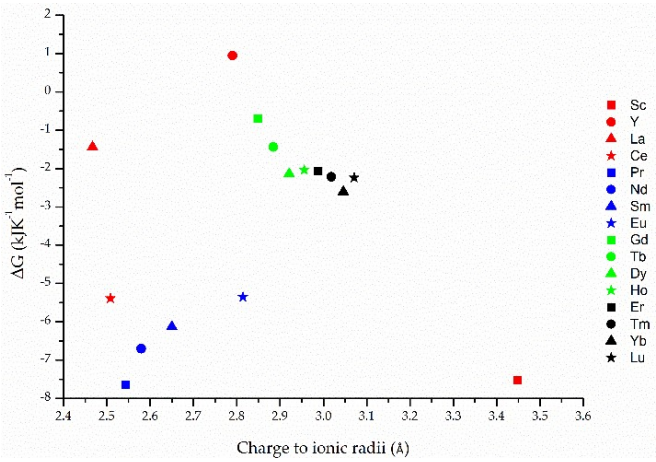

Figure 7. Gibbs free energy change (ΔG°) for the adsorption of rare earth ions onto BTPhen-Si

4. DISCUSSION

This method described shows BTPhen-Si has a preference for Sc, Pr-Eu, as they have longer elution times than the rest. This provides a promising method to selectively separate these ions from the rest of the REE series. Interestingly, Pr-Eu have very similar charge to ion ratios (2.53-2.81 Å) however Sc has a much higher z/r indicating other factors are affecting the extraction of REEs.

The fitting of data to both isothermal and kinetic models provides a valuable technique for evaluating adsorbent capabilities. Specifically, this method enables the quantification of adsorption capacities, rates, breakthrough times, and competitive ion behaviour, in addition to facilitating comparisons between different absorbents. However, it is important to note that the model parameters obtained may not be applicable to "real-life" REE waste sludges due to the presence of varying concentrations and other components. The data obtained from this study provides an initial insight into the absorption behaviour of BTPhen-Si and the successful fittings are given in supplementary information.

All REE ions can be described by the Adams-Bohart model and the Thomas model with average R^2 values of 0.863 and 0.901, respectively. Both models assume that the adsorption process takes place in two stages. There is an initial rapid adsorption stage followed by a slower stage as the adsorbent reaches saturation point. Both of the models consider the effects of the flow rate and the initial concentration. The Thomas model is slightly different as it takes into account the bulk fluid phase, whereas the Adams-Bohart does not.

The Yoon-Nelson and MDR models are both capable of describing La-Ce and Gd-Lu, however MDR could not describe Y. Yoon-Nelson describes the process as a single step adsorption process whilst considering pore diffusion and equilibrium. Whereas the MDR model assumes that the adsorption is a function of the concentration of the adsorbate in the bulk fluid phase.

4.1. Comparison with NC-Si

The synthesis and immobilization of neocuproine **2** onto silica to form NC-Si **4** involves 3 steps, whereas the synthesis and immobilization of $CyMe_4$-BTPhen onto silica to form BTPhen-Si **5** involves 12 steps (Table 4). Having a synthetic procedure of 9 steps fewer would be economically and environmentally preferential when scaling up for industry as fewer chemicals are required and less waste products formed. If 1 g of neocuproine **2** starting material was used in the synthesis of BTPhen-Si **5** and for NC-Si **4**, we would see a 3.8-fold increase in the mass of NC-Si produced compared to a 6.7-fold decrease in the mass of BTPhen-Si produced. A debate between cost effectiveness and efficiency would be required in order to choose which adsorption material provides the best outcome.

This work follows very similar experimental procedures to the ones described in [Chapter 2] for NC-Si **4** for use in fixed-bed adsorption techniques. NC-Si **4** has a lower overall adsorption capacity than BTPhen-Si **5** at 0.015 mg g^{-1} compared to 0.048 mg g^{-1}, however the degree of immobilization of neocuproine onto silica is 63% lower than BTPhen-Si (Table 4). If the degree of immobilization were to increase, then the adsorption capacity could also have the potential to increase. BTPhen-Si prefers the mid REEs which reflects the larger cavity size on the $CyMe_4$-BTPhen **3** ligand compared to neocuproine **2** which prefers the slightly smaller late REEs. This knowledge could allow more efficient partitioning of REEs if BTPhen-Si and NC-Si were used simultaneously or in succession. Both BTPhen-Si **5** and NC-Si **4** follow the same pseudo-second order rate expression for the desorption of REEs from the column and both can be described by Yoon-Nelson isotherm model for the adsorption of late REEs.

Table 4. Comparison between BTPhen-Si **5** and NC-Si **4**

Feature	BTPhen-Si	NC-Si
1 g of neocuproine to yield	0.15 g	3.84 g
Immobilisation %	~90%	~57%
w/w % of ligand weight	~6%	~5%
% of ions extracted	76%	80%
Overall adsorption capacity	0.048 mg g^{-1}	0.015 mg g^{-1}
Preferences	Ce-Eu (mid) and Sc	Late
Average R^2 for 1st order	0.689	0.882
Average R^2 for 2nd order	0.934	0.988
Closeness to q_e 1st order	Early	All
Closeness to q_e 2nd order	Late	n/a
Description of early	Thomas	Adams-Bohart
Description of mid	Adams-Bohart	MDR
Description of late	Yoon-Nelson	Yoon-Nelson
Separation of REEs into groups	Mid (including Sc and Ce), Late including (Y and La)	Early, mid, late
Metal:ligand molar ratio	1:250	1:1334

4.2. Comparison with literature

The extraction and recycling of REE ions is a widely researched topic with lots of different adsorbents being developed and tested for the extraction of REE ions. Table 4 presents a comparison of the adsorption capacities of different solid supports for multi-element mixtures of REEs. Among the solid supports investigated, phosphinic acid, sulfonic acid, diglycolamides, and carbon-based materials have been the most extensively studied. The adsorption capacities of diglycolamides and hydroxamic acids have been found to be the highest, with values exceeding 15 and 190 mg g^{-1}, respectively. Sulfonic acid resins, on the other hand, exhibit a relatively lower adsorption capacity of around 10 mg g^{-1} for all REE ions, with no variation across the series. Silica-supported poly-diglycolamide has been observed to provide the best separation among the materials studied, as it exhibits the greatest difference in adsorption capacities between early and late REEs. In general, an increase in the z/r ratio leads to an increase in the adsorption capacity of the solid supports, with a few exceptions. Kenaf cellulose-based poly(hydroxamic acid) ligand, graphene oxide-corn zein composites, and poly(acrylamino phosphonic dithiocarbamate) fibers show a decrease in adsorption capacity upon increasing the z/r ratio which could be used in conjunction with other supports to provide a more complementary separation. In comparison to the other solid supports mentioned in table 5, BTPhen has low adsorption capacities. However, this could be increased upon increasing ligand concentration on the silica support.

Table 5. Comparison of solid supports for the extraction of REE ions

Solid support	Functional Group	Analyte	Adsorption Capacity ($mg\ g^{-1}$)	Ref.
Modified Activated Carbon with 0.01 mol^{-1} $KMnO_4$	-	Y, Sc, La, Yb, Lu, Eu,	0.048, 0.051, 0.05, 0.06, 0.051, 0.051	[69]
Fe_3O_4@$mSiO_2$–DODGA	Diglycolamide	Y, Sc, Nd, Sm, Eu, Ho, Yb, Lu,	16.29, 14.28, 60.80, 27.54, 36.86, 17.16, 34.36, 42.15,	[70]
Silica gel modified with diglycol amic acid	Diglycolamide	La, Ce, Pr, Nd, Sm, Eu, Gd, Tb, Dy, Ho, Er, Tm, Yb and Lu	10.3, 14.7, 12.8, 16.2, 18.9, 20.9, 21.6, 22.8, 25.9, 27.2, 28.0, 28.6, 25.7, 21.2	[71]
Silica-supported poly-diglycolamide	Diglycolamide	La, Ce, Pr, Nd, Sm, Ey, Gd, Tb, Yd, Ho, Er, Tm, Yb, Lu	29, 32, 33, 35, 39, 42,51, 48, 51, 52, 50, 48, 49	[66]
Fluorinated b-diketone group on solid support styrene divinyl benzene	Diketone	La, Ce, Nd, Sm, Eu, Gd, Dy, Er, Yb, Lu	9.91, 9.82, 8.37, 9.20, 8.49, 9.95, 10.53, 9.18, 9.33, 9.63	[72]
Alkyl phosphinic acid resin (APAR)	Phosphinic acid	Y, La, Ce, Pr, Nd, Sm, Eu, Gd, Tb, Dy, Ho, Er, Tm, Yb, Lu	1.40,1.99, 1.96, 1.98, 2.03, 2.14, 2.14, 2.18, 2.18, 2.22, 2.21, 2.22, 2.26, 2.32, 2.36	[73]
Kenaf cellulose-based poly(hydroxamic acid) ligand	Hydroxamic acid	La, Ce, Pr, Gd, Nd, Eu, Sm	260, 245, 235, 220, 210, 195, 192	[64]
Graphene oxide-corn zein composites	-	Y, La, Er, Yb, Nd	14.2, 17.3, 11.7, 10.1, 9.7	[67]
DOWEX 50WX8	Sulfonic acid	Y, La, Ce, Nd, Dy, Gd	11.2, 25.4, 23.3, 21.2, 16.9, 17.7	[65]
Lewatit MDS 200H	Sulfonic acid	Y, La, Ce, Nd, Dy, Gd	10.6, 26.8, 24.9, 20.9, 16.2, 17.9	[65]
Purolite C160	Sulfonic acid	Y, La, Ce, Nd, Dy, Gd	10.0, 28.7, 26.4, 25.5, 13.0, 13.8	[65]
Poly(acrylamino phosphonic dithiocarbamate) fibres	Phosphonic acid	Y, La, Ce, Pr, Nd, Sm, Eu, Gd, Tb, Dy, Ho, Er, Tm, Yb, and Lu	62.59, 28.60, 30.29, 30.95, 31.70, 32.68, 32.68, 31.79, 32.16, 31.51, 31.36, 30.32, 30.98, 31.69, 31.15	[68]

NC-Si **4**	Phenanthroline	Y, Sc, La, Ce, Pr, Nd, Sm, Eu, Gd, Tb, Dy, Ho, Er, Tm, Yb, Lu	0.0016, 0.0038, 0.0026, 0.0036, 0.0038, 0.0038, 0.0037, 0.0036, 0.0023, 0.0026, 0.0028, 0.0028, 0.0028, 0.0028, 0.003, 0.0029	Chapter 2
BTPhen-Si **5**	Phenanthroline and triazine	Y, Sc, La, Ce, Pr, Nd, Sm, Eu, Gd, Tb, Dy, Ho, Er, Tm, Yb, Lu	0.0026, 0.0036, 0.0038, 0.0038, 0.0037, 0.0016, 0.0036, 0.0023, 0.0026, 0.0028, 0.0028, 0.0028, 0.0028, 0.0030, 0.0029, 0.0038	This study

5. CONCLUSIONS

The REE adsorption performance of BTPhen-Si **5** was evaluated through a continuous-flow fixed-bed adsorption experiment. The Adams-Bohart and Thomas models could be used to describe adsorption of all REE ions, however their R^2 values were relatively low compared to Yoon-Nelson and MDR, at 0.86 and 0.90, respectively. Yoon-Nelson and MDR models had high R_2 values and were able to describe all of the late REE ions and some of the earlier/mid REE ions, except for Sc, Pr, Nd, Sm and Eu, however MDR was not able to describe Y. There doesn't seem to be a clear connection between the z/r ratio and rate constants (K_{AB}, K_{Th}, K_{YN} and a). Experimental data had a better fit to Lagergren's pseudo second-order reaction kinetics compared to pseudo first-order kinetics. First-order kinetics gave closer theoretical q_e values to the experimental values for the late REEs, whereas pseudo second-order gave closer q_e values for the early REEs. Gibbs free energy change (ΔG) showed the adsorption of REEs onto **3** was a spontaneous process, with the earlier REEs (Sc, Ce-Eu) having more negative ΔG values compared to the Y, La and late rate earths ions. A comparison between BTPhen-Si **5** and NC-Si **4** has been made where NC-Si **4** is able to partition the REEs much more effectively than BTPhen-Si **5** into more delineated groups, however BTPhen had a higher overall adsorption capacity. In order to increase the adsorption capacities, further studies would be required to optimise conditions; including pH, acid type, temperature. An increase in the concentration of BTPhen on the silica could also be developed to see if improvements in adsorption capacities could occur.

6. REFERENCES

1. Klinger, J.M. Rare Earth Elements: Development, Sustainability and Policy Issues. *Extr. Ind. Soc.* **2018**, *5*, 1–7, doi:10.1016/j.exis.2017.12.016.
2. Rudnick, R.L.; Gao, S. Rudnick_Gao_Treatise. *Treatise on geochemistry* **2003**, *3*, 1–64, doi:10.1016/j.apcatb.2004.01.017.
3. *Mineral Commodity Summaries 2021*; Reston, VA, 2021;
4. Xu, L.; Guo, G.; Uy, D.; O'Neill, A.E.; Weber, W.H.; Rokosz, M.J.; McCabe, R.W. Cerium Phosphate in Automotive Exhaust Catalyst Poisoning. *Appl. Catal. B Environ.* **2004**, *50*, 113–125.
5. Fujita, Y.; McCall, S.K.; Ginosar, D. Recycling Rare Earths: Perspectives and Recent Advances. *MRS Bull.* **2022**, *47*, 283–288, *47*, 283–288, doi:10.1557/s43577-022-00301-w.
6. Kingsnorth, D. Meeting the Challenges of Supply This Decade. *Present. to Environ. Energy Study …* **2011**.
7. Humphries, M. Rare Earth Elements: The Global Supply Chain. *Rare Earth Miner. Policies Issues* **2011**, 1–20.
8. European Commission *Tackling the Challenges in Commodity Markets and on Raw*

Materials; Brussels, 2012;

9. Binnemans, K.; Jones, P.T.; Blanpain, B.; Van Gerven, T.; Yang, Y.; Walton, A.; Buchert, M. Recycling of Rare Earths: A Critical Review. *J. Clean. Prod.* **2013**, *51*, 1–22, doi:10.1016/j.jclepro.2012.12.037.
10. European Commission Methodology for Establishing the EU List of Critical Raw Materials. *Publ. Off. Eur. Union.* **2017**, 1-5, doi:10.2873/769526.
11. Wang, J.; Guo, M.; Liu, M.; Wei, X. Long-Term Outlook for Global Rare Earth Production. *Resour. Policy* **2020**, *65*, 101569-101577, doi:10.1016/j.resourpol.2019.101569.
12. Watari, T.; Nansai, K.; Nakajima, K. Review of Critical Metal Dynamics to 2050 for 48 Elements. *Resour. Conserv. Recycl.* **2020**, *155*, 104669-104686. , doi:10.1016/j.resconrec.2019.104669.
13. Nissan and Waseda University in Japan Testing Jointly Developed Recycling Process for Electrified Vehicle Motors Available online: https://global.nissannews.com/en/releases/nissan-waseda-university-in-japan-testing-jointly-developed-recycling-process-for-ev-motors (accessed Jan 2023).
14. Nguyen, R.T.; Diaz, L.A.; Imholte, D.D.; Lister, T.E. Economic Assessment for Recycling Critical Metals From Hard Disk Drives Using a Comprehensive Recovery Process. *Jom* **2017**, *69*, 1546–1552, 1546–1552, doi:10.1007/s11837-017-2399-2.
15. J.W. Lyman; G.R. Palmer Recycling of Rare Earths and Iron from NdFeB Magnet Scrap. *High Temp. Mater. Process. (London, U. K.)* **1993**, *11*, 175–188, doi:10.1515/HTMP.1993.11.1-4.175.
16. Mudring, A.-V.; Prodius, D.; Nlebedium, C.I. Dissolution and Separation of Rare Earth Metals 2020.
17. Nash, K.L.; Jensen, M.P. Analytical-Scale Separations Of The Lanthanides: A Review Of Techniques And Fundamentals. *Sep. Sci. Technol.* **1999**, *36*, 1257–1282.
18. Cotton, S. Lanthanide and Actinide Chemistry. *Lanthan. Actin. Chem.* 2006, 1–263.
19. Choppin, G.R. Comparative Solution Chemistry of the 4f and 5f Elements. *J. Alloy. Compd.* **1995**, *223*, 174–179, doi:10.1016/0925-8388(94)09002-5.
20. Cotton, S.A.; Raithby, P.R. Systematics and Surprises in Lanthanide Coordination Chemistry. *Coord. Chem. Rev.* **2017**, *340*, 220–231, doi:10.1016/j.ccr.2017.01.011
21. Gupta, C.K.; Krishnamurthy, N. Extractive Metallurgy of Rare Earths. *Int. Mater. Rev.* **1992**, *37*, 197–248, doi:10.1179/imr.1992.37.1.197.
22. Xie, F.; Zhang, T.A.; Dreisinger, D.; Doyle, F. A Critical Review on Solvent Extraction of Rare Earths from Aqueous Solutions. *Miner. Eng.* **2014**, *56*, 10–28, doi:10.1016/j.mineng.2013.10.021.
23. Talens Peiró, L.; Villalba Méndez, G. Material and Energy Requirement for Rare Earth Production. *Jom* **2013**, *65*, 1327–1340, doi:10.1007/s11837-013-0719-8.
24. Wang, Z.H.; Ma, G.X.; Lu, J.; Liao, W.P.; Li, D.Q. Separation of Heavy Rare Earth Elements with Extraction Resin Containing 1-Hexyl-4-Ethyloctyl Isopropylphosphonic Acid. *Hydrometallurgy* **2002**, *66*, 95–99, doi:10.1016/S0304-386X(02)00109-3.
25. Shokobayev, N.M.; Bouffier, C.; Dauletbakov, T.S. Rare Earth Metals Sorption Recovery from Uranium in Situ Leaching Process Solutions. *Rare Met.* **2015**, *34*, 195–201, doi:10.1007/s12598-014-0237-z.
26. Suzuki, T.; Itoh, K.; Ikeda, A.; Aida, M.; Ozawa, M.; Fujii, Y. Separation of Rare Earth Elements by Tertiary Pyridine Type Resin. *J. Alloys Compd.* **2006**, *408–412*, 1013–1016, doi:10.1016/j.jallcom.2004.12.130.
27. Hart, F.A.; Laming, F.P. Complexes of 1,10-Phenanthroline with Lanthanide Chlorides and Thiocyanates. *J. Inorg. Nucl. Chem.* **1964**, *26*, 579–585, doi:10.1016/0022-

1902(64)80291-8.

28. Ogden, M.D.; Hoch, C.L.; Sinkov, S.I.; Meier, G.P.; Lumetta, G.J.; Nash, K.L. Complexation Studies of Bidentate Heterocyclic N-Donor Ligands with Nd(III) and Am(III). *J. Solution Chem.* **2011**, *40*, 1874–1888, doi:10.1007/s10953-011-9762-7.

29. Simonzadeh, N.; Schilt, A.A. Chelation Properties of Silica-Bound 1,10-Phenanthroline. *J. Coord. Chem.* **1989**, *20*, 117–120, doi:10.1080/00958978909408856.

30. Frederick Smith, G.; McCurdy, W.H. 2,9-Dimethyl-1,10-Phenanthroline, New Specific in Spectrophotometric Determination of Copper. *Anal. Chem.* **1952**, *24*, 371–373.

31. O'Reilly, E.J.; Plowman, R.A. Coordination Compounds of Substituted 1, 10-Phenanthrolines and Related Dipyridyls: I. Synthesis of 2, 9-Dimethpl-1, 10-Phenanthroline. *Aust. J. Chem.* **1960**, *13*, 145–149, doi:10.1071/CH9600145.

32. Lalia-Kantouri, M.; Gdaniec, M.; Czapik, A.; Chrissafis, K.; Ferenc, W.; Sarzynski, J.; Papadopoulos, C.D. Neocuproine as a Redox-Active Ligand Platform on Iron and Cobalt. *J. Therm. Anal. Calorim.* **2012**, *109*, 131–139, doi:10.1007/s10973-011-1692-5.

33. Jesse, K.A.; Filatov, A.S.; Xie, J.; Anderson, J.S. Neocuproine as a Redox-Active Ligand Platform on Iron and Cobalt. *Inorg. Chem.* **2019**, *58*, 9057–9066, doi:10.1021/acs.inorgchem.9b00531.

34. Geist, A.; Hill, C.; Modolo, G.; Foreman, M.R.S.J.; Weigj, M.; Gompper, K.; Hudson, M.J.; Madic, C. 6,6'-Bis(5,5,8,8-Tetramethyl-5,6, 7,8-Tetrahydro-Benzo[1,2,4)Triazin-3yl)[2,2']Bipyridine, an Effective Extracting Agent for the Separation of Americium(LII) and Curium(III) from the Lanthanides. *Solvent Extr.Ion Exch.* **2006**, *24*, 463–483, doi:10.1080/07366290600761936.

35. Adam, C.; Kaden, P.; Beele, B.B.; Müllich, U.; Trumm, S.; Geist, A.; Panak, P.J.; Denecke, M.A. Evidence for Covalence in a N-Donor Complex of Americium(Iii). *Dalt. Trans.* **2013**, *42*, 14068–14074, doi:10.1039/c3dt50953b.

36. Vitova, T.; Pidchenko, I.; Fellhauer, D.; Bagus, P.S.; Joly, Y.; Pruessmann, T.; Bahl, S.; Gonzalez-Robles, E.; Rothe, J.; Altmaier, M.; et al. The Role of the 5f Valence Orbitals of Early Actinides in Chemical Bonding. *Nat. Commun.* **2017**, *8*, 1–9, doi:10.1038/ncomms16053.

37. Kaltsoyannis, N. Does Covalency Increase or Decrease across the Actinide Series? Implications for Minor Actinide Partitioning. *Inorg. Chem.* **2013**, *52*, 3407–3413, doi:10.1021/ic3006025.

38. Lewis, F.W.; Harwood, L.M.; Hudson, M.J.; Drew, M.G.B.; Desreux, J.F.; Vidick, G.; Bouslimani, N.; Modolo, G.; Wilden, A.; Sypula, M.; et al. Highly Efficient Separation of Actinides from Lanthanides by a Phenanthroline-Derived Bis-Triazine Ligand. *J. Am. Chem. Soc.* **2011**, *133*, 13093–13102, doi:10.1021/ja203378m.

39. Sigma-Aldrich - 3-Chloropropyl-Functionalized Silica Gel Available online: https://www.sigmaaldrich.com/GB/en/product/aldrich/364266 (accessed on 11 January 2023).

40. Qiu, H.; Lv, L.; Pan, B.C.; Zhang, Q.J.; Zhang, W.M.; Zhang, Q.X. Critical Review in Adsorption Kinetic Models. *J. Zhejiang Univ. Sci. A* **2009**, *10*, 716–724, doi:10.1631/jzus.A0820524.

41. Ho, Y.S. Second-Order Kinetic Model for the Sorption of Cadmium onto Tree Fern: A Comparison of Linear and Non-Linear Methods. *Water Res.* **2006**, *40*, 119–125, doi:10.1016/j.watres.2005.10.040.

42. Ho, Y..; McKay, G. Pseudo-Second Order Model for Sorption Processes. *Process Biochem.* **1999**, *34*, 451–465, doi:10.1021/acs.oprd.7b00090.

43. Costa, T.B. da; Silva, M.G.C. da; Vieira, M.G.A. Recovery of Rare-Earth Metals from

Aqueous Solutions by Bio/Adsorption Using Non-Conventional Materials: A Review with Recent Studies and Promising Approaches in Column Applications. *J. Rare Earths* **2020**, *38*, 339–355, doi:10.1016/j.jre.2019.06.001.

44. Lakshmipathy, R.; Sarada, N.C. A Fixed Bed Column Study for the Removal of Pb2+ Ions by Watermelon Rind. *Environ. Sci. Water Res. Technol.* **2015**, *1*, 244–250, doi:10.1039/c4ew00027g.

45. Park, D.; Yun, Y.S.; Park, J.M. The Past, Present, and Future Trends of Biosorption. *Biotechnol. Bioprocess Eng.* **2010**, *15*, 86–102, doi:10.1007/s12257-009-0199-4.

46. Solgi, M.; Tabil, L.G.; Wilson, L.D. Modified Biopolymer Adsorbents for Column Treatment of Sulfate Species in Saline Aquifers. *Materials (Basel).* **2020**, *13*, doi:10.3390/ma13102408.

47. Patel, H. Fixed-Bed Column Adsorption Study: A Comprehensive Review. *Appl. Water Sci.* **2019**, *9*, 1–17, doi:10.1007/s13201-019-0927-7.

48. Dolatyari, L.; Yaftian, M.R.; Rostamnia, S. Fixed-Bed Column Dynamic Studies and Breakthrough Curve Analysis of Eu(III) Ion Adsorption onto Chemically Modified SBA-15 Silica Materials. *Sep. Sci. Technol.* **2017**, *52*, 393–403, doi:10.1080/01496395.2016.1250781.

49. Basuki, R.; Ngatijo; Santosa, S.J.; Rusdiarso, B. Comparison the New Kinetics Equation of Noncompetitive Sorption Cd(II) and Zn(II) onto Green Sorbent Horse Dung Humic Acid (HD-HA). *Bull. Chem. React. Eng. & Catal.* **2018**, *13*, 475–488, doi:10.9767/bcrec.13.3.1774.475-488.

50. Xu, S.; Wang, Z.; Gao, Y.; Zhang, S.; Wu, K. Adsorption of Rare Earths(III) Using an Efficient Sodium Alginate Hydrogel Cross-Linked with Poly-γ-Glutamate. *PLoS One* **2015**, *10*, 1–12, doi:10.1371/journal.pone.0124826.

51. Bohart, G.S.; Adams, E.Q. Some Aspects of the Behavior of Charcoal with Respect to Chlorine. *J. Am. Chem. Soc.* **1920**, *42*, 523–544, doi:10.1021/ja01448a018.

52. Yoon, Y.H.E.E.; Nelson, J.H. Application of Gas Adsorption Kinetics I. A Theoretical Model for Respirator Cartridge Service Life. *Am. Ind. Hyg. Assoc. J.* **1984**, *45*, 509–516, doi:10.1080/15298668491400197.

53. Aksu, Z.; Çağatay, Ş.Ş.; Gönen, F. Continuous Fixed Bed Biosorption of Reactive Dyes by Dried Rhizopus Arrhizus: Determination of Column Capacity. *J. Hazard. Mater.* **2007**, *143*, 362–371, doi:10.1016/j.jhazmat.2006.09.039.

54. Thomas, H.C. Heterogeneous Ion Exchange in a Flowing System. *J. Am. Chem. Soc.* **1944**, *66*, 1664–1666, doi:10.1021/ja01238a017.

55. Thomas, H.C. Chromatography: A Problem in Kinetics. *Ann. N. Y. Acad. Sci.* **1948**, *49*, 161–182, doi:https://doi.org/10.1111/j.1749-6632.1948.tb35248.x.

56. Xu, Z.; Cai, J.G.; Pan, B.C. Mathematically Modeling Fixed-Bed Adsorption in Aqueous Systems. *J. Zhejiang Univ. Sci. A* **2013**, *14*, 155–176, doi:10.1631/jzus.A1300029.

SUPPLEMENTAL INFORMATION

SI.1 Characterisation of BTPhen functionalised silica

SI.1.1 FT-IR Analysis of BTPhen functionalised silica

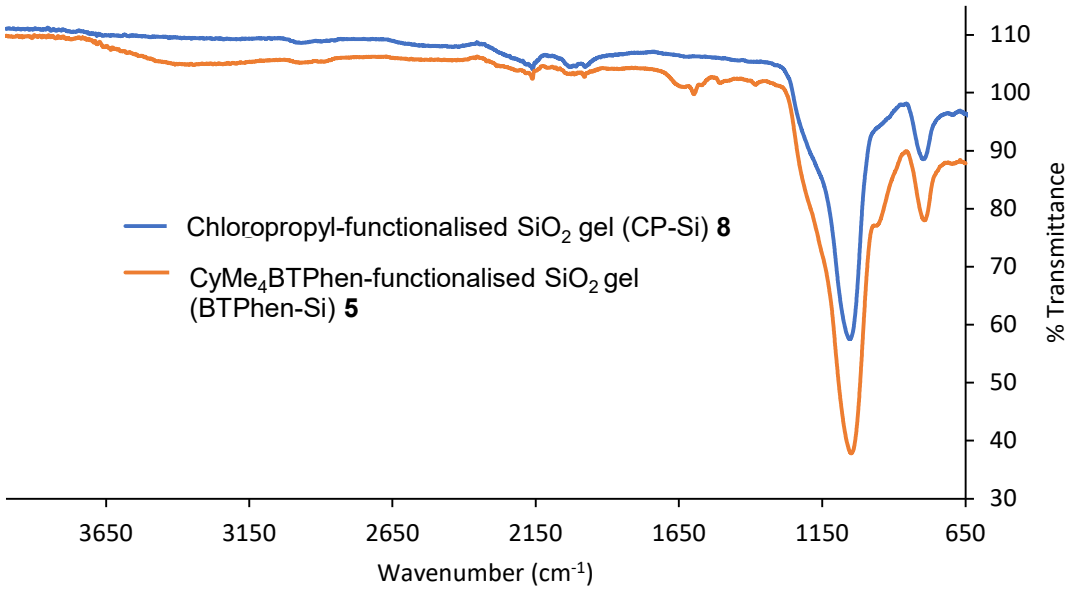

SI Figure 1. FT-IR spectra

SI Table 1. FT-IR assignment

Wavelength (cm^{-1})	Assignment	Reference
1052	Si-O-Si	5, 8
1500-1600	C=C	5
823	C-Cl	5, 8

SI.1.2 EDX Analysis of BTPhen functionalised silica

SI Table SI 2. *FT-IR assignment*

Element	Chloropropyl-functionalised SiO_2 gel 40	$CyMe_4$-BTPhen-functionalised SiO_2 gel 41
Carbon (%)	16.86	22.03
Oxygen (%)	44.11	39.38
Silicon (%)	34.27	31.29
Chlorine (%)	1.04	0.10

SI.1.3. TGA Analysis of BTPhen functionalised silica

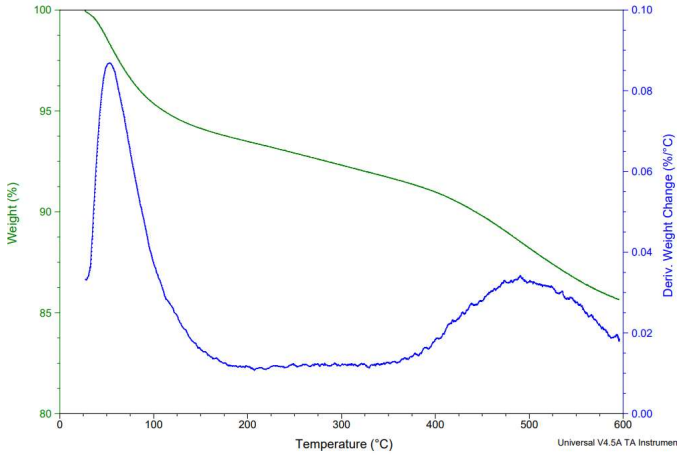

Figure SI 2. TGA analysis of BTPhen-Si

2.3. Adsorption Modelling

2.3.1. Adams-Bohart model

The Adams-Bohart model only clarifies the initial region of the breakthrough curve ($C_t/C_0 < 0.5$). This model also assumes that there is minimal axial dispersion and insignificant mass transfer, therefore the adsorption rate only depends on the capacity of the adsorbent and the concentration of the adsorbed metals [51]. The linear (S1) and non-linear (S2) forms of the equation are written as follows:

$$\frac{C_t}{C_0} = exp(k_{AB}C_0 t - k_{AB} q \frac{H}{v}) \quad \text{(S1)}$$

$$\ln\left(\frac{C_t}{C_0}\right) = k_{AB}C_0 t - k_{AB} q \frac{H}{v} \quad \text{(S2)}$$

Where k_{AB} is the Adams-Bohart rate constant (L mg^{-1} min^{-1}), N_0 is the saturation concentration (mg L), H is the bed depth of the fixed-bed column (cm), v is the linear velocity calculated by dividing the flow rate by the column sectional area (cm min^{-1}) [51].

a)

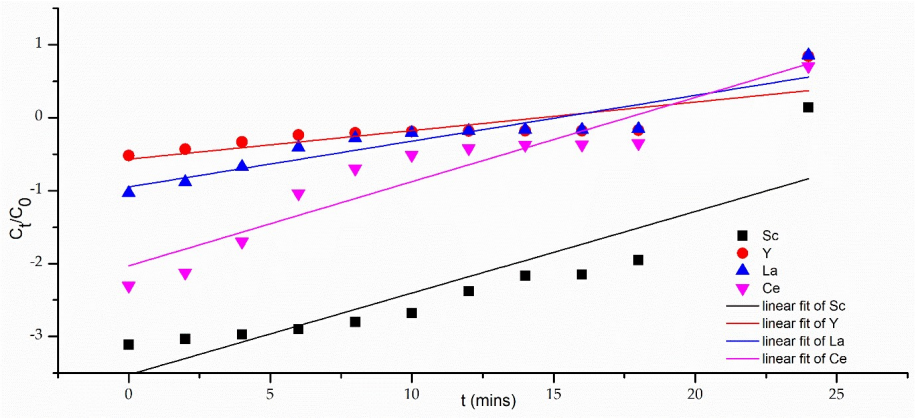

b)

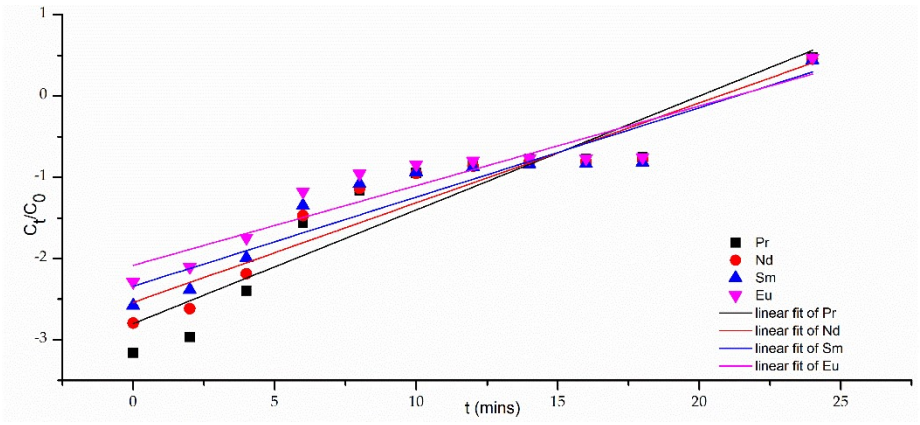

c)

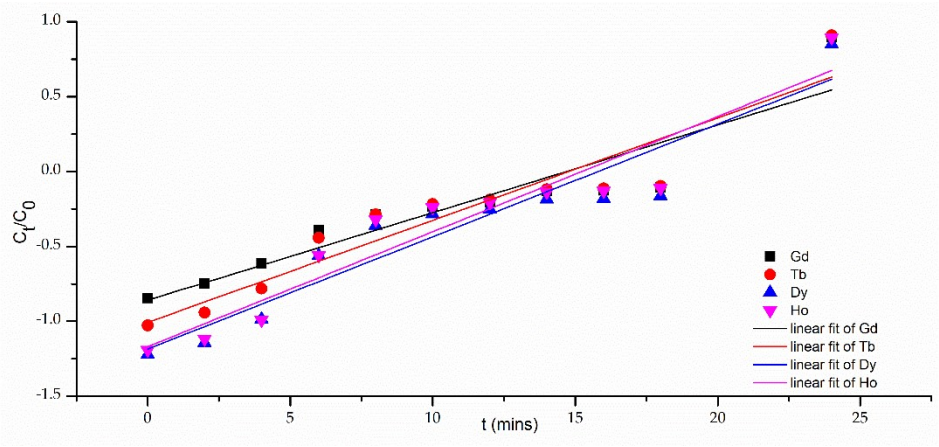

d)

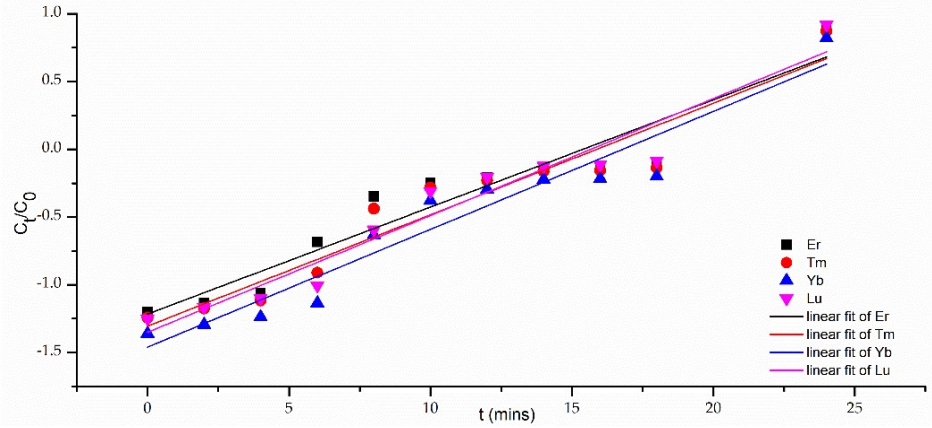

SI Figure 3. Fitting of the Adams-Bohart model to a) Sc-Ce, b) Pr-Eu, c) Gd-Ho and d) Er-Lu

SI.2.2. Yoon-Nelson model

The Yoon-Nelson model is a simple model that doesn't require knowledge on the physical properties of the adsorption bed or the type of adsorbent [52]. The model assumes that the decreasing rate of the probability for each molecule adsorption is favorably related to the probability of adsorbate and the breakthrough within the bed [53]. The Yoon Nelson model provides data on the breakthrough rate and the time it takes for 50% of the ion to elute from the column (τ). The non-linear (S3) and linear (S4) expressions are written as follows:

$$\frac{C_t}{C_0} = \frac{1}{1+(\exp(k_{YN}(\tau - t)))} \quad \text{(S3)}$$

$$\ln\left(\frac{C_t}{C_0 - C_t}\right) = k_{YN}t - k_{YN}\tau \quad \text{(S4)}$$

k_{YN} is the Yoon-Nelson rate constant (min^{-1}) and τ is the time required for 50% adsorbate breakthrough (min).

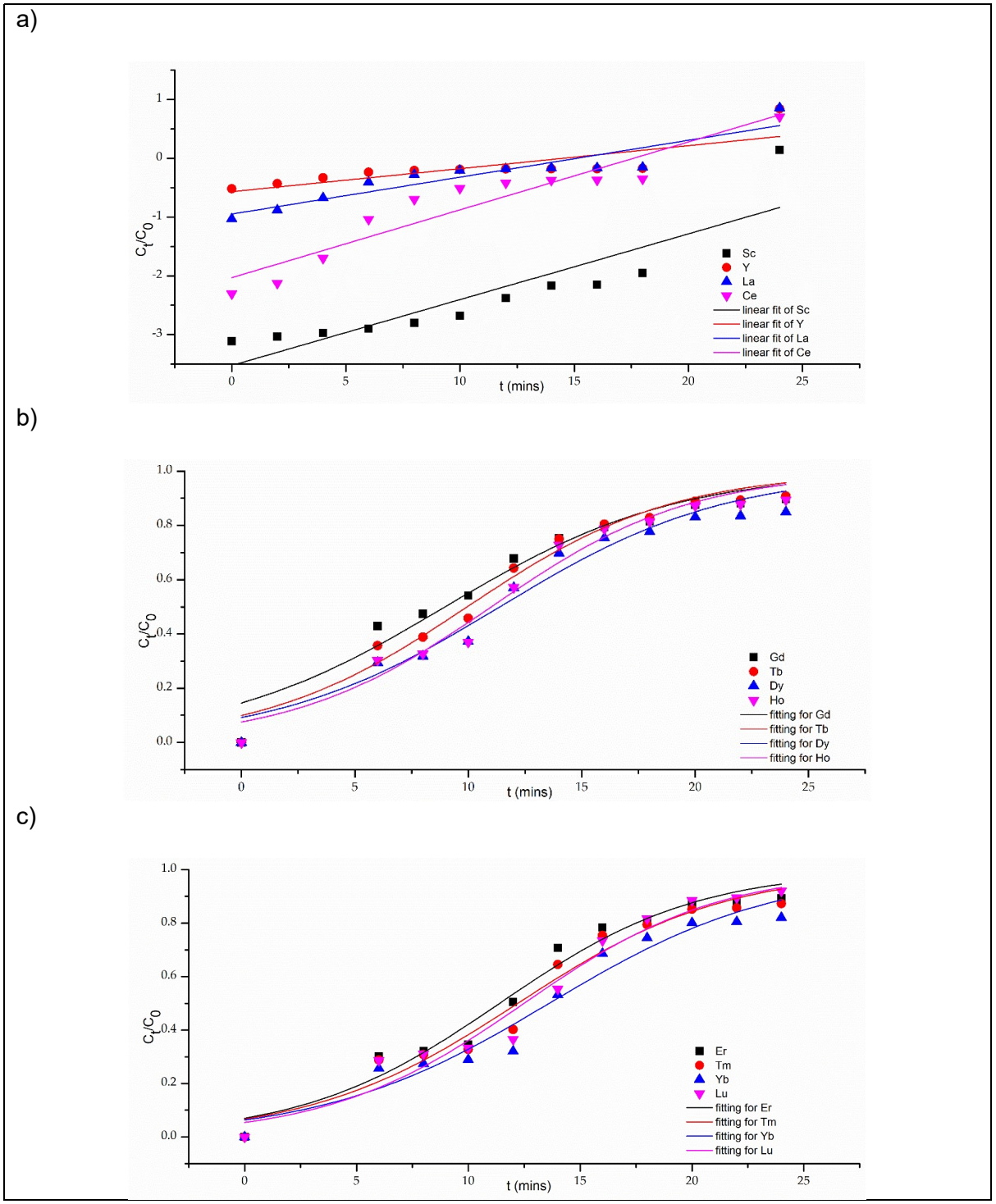

SI Figure 4. Fitting of the Yoon-Nelson model to a) Sc-Ce, b) Gd-Ho and c) Er-Lu

SI.2.3. Thomas model

This model is based on the assumption that the adsorption follows a Langmuir isotherm and pseudo second-order kinetics [54]. The Thomas model assumes that the system has constant flow with no axial dispersion and that the sorption process is governed by mass transfer instead of chemical processes. Equations (S5) and (S6) show the non-linear and linear equations respectively, where k_{Th} (mL mg^{-1} min^{-1}) is the Thomas model constant and q_0 (mg g^{-1}) is the

predicted adsorption capacity, *m* (g) is the mass of the absorbent, and *Q* (mL min^{-1}) is the influent flow rate [55].

$$\frac{C_t}{C_0} = \frac{1}{1+\exp\left[\left(\frac{k_{Th}q_0 m}{Q}\right)-k_{Th}C_0 t\right]} \quad \text{(S5)}$$

$$ln\left(\frac{C_t}{C_0}-1\right) = \left(\frac{k_{Th}q_0 m}{Q}\right) - k_{Th}C_0 t \quad \text{(S6)}$$

a)

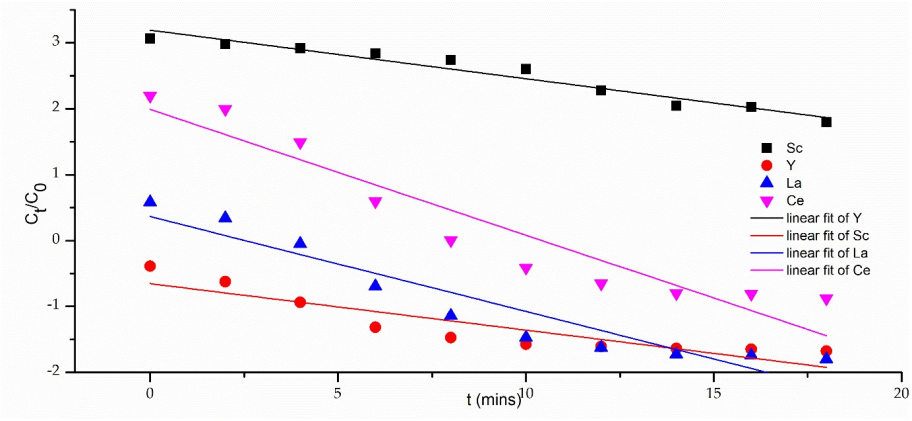

b)

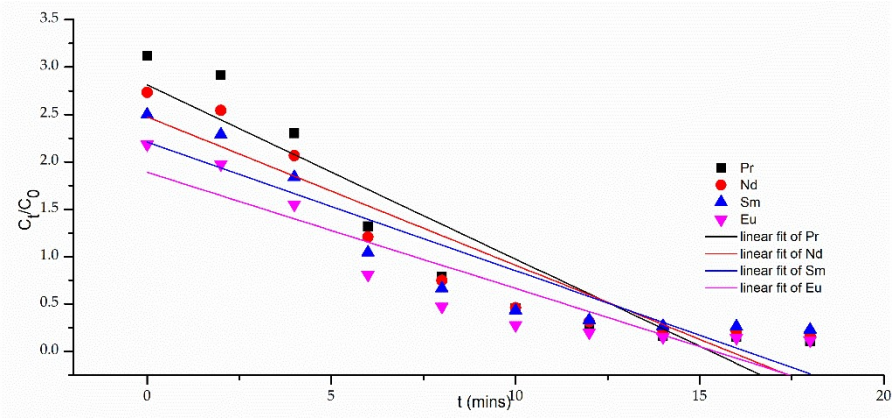

c)

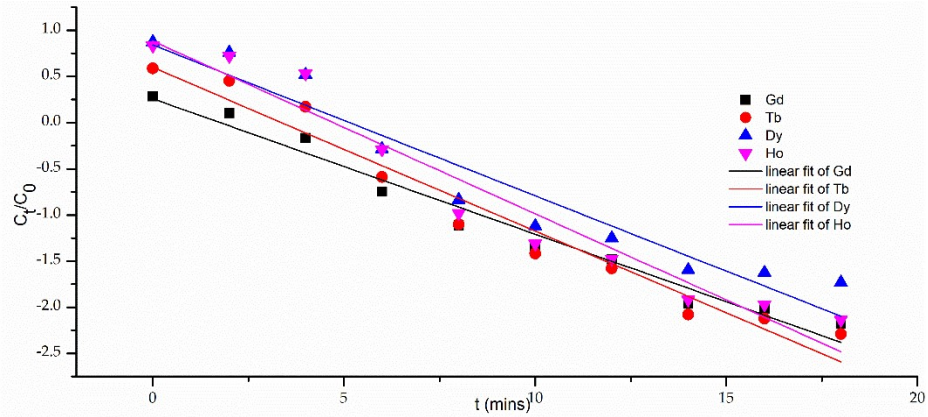

d)

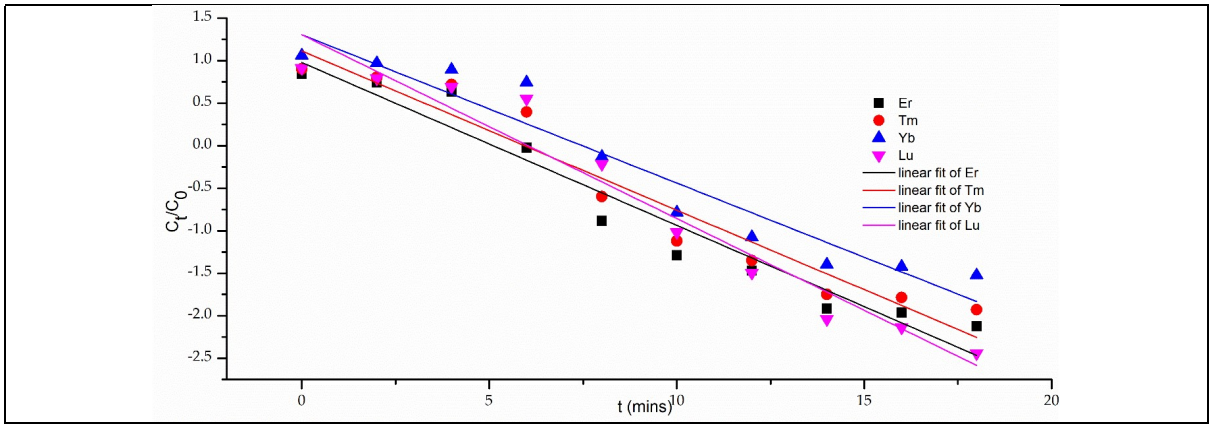

SI Figure 5. Fitting of the Thomas model to a) Sc-Ce, b) Pr-Eu, c) Gd-Ho and d) Er-Lu

SI.2.4. Modified Dose Response model

Another simplified model to evaluate the dynamic behavior of a fixed-bed column is the Modified Dose Response model. This model lowers any errors that may arise from the Thomas model at higher or lower time periods of the breakthrough curve [56]. The non-linear and linear models can be expressed as equations (S7) and (S8) respectively, where ***a*** is the MDR constant and q_m is the adsorption capacity (mg L^{-1}).

$$\frac{C_t}{C_o} = 1 - \frac{1}{1+\left(\frac{C_o Q t}{q_m m}\right)^a} \quad \text{(S7)}$$

$$ln\left(\frac{C_t}{C_o - C_t}\right) = a ln C_o Q t - a ln q m \quad \text{(S8)}$$

a)

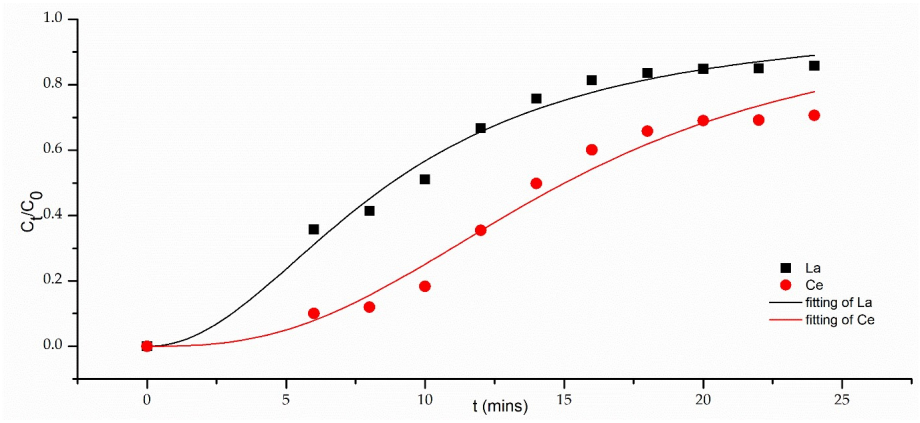

b)

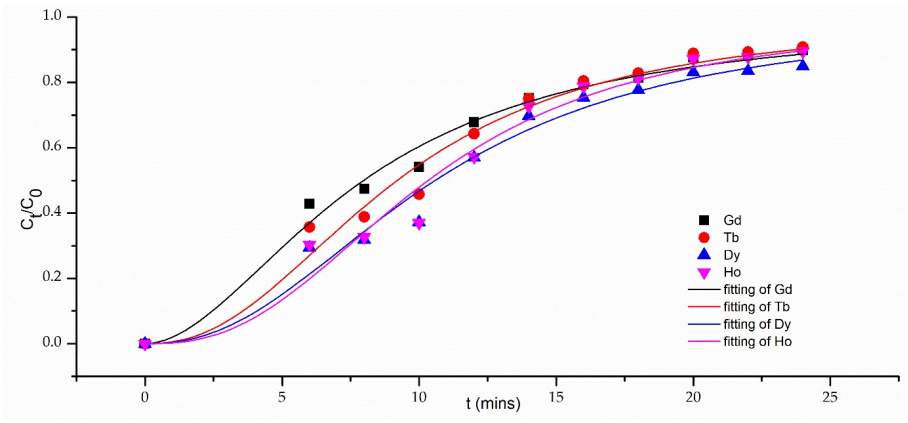

c)

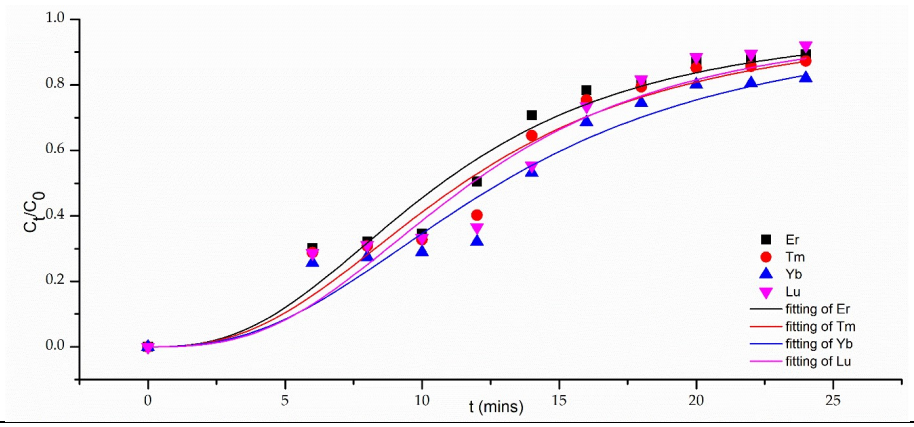

SI Figure 6. Fitting of the MDR model to a) La-Ce, b) Gd-Ho and c) Er-Lu

SI.3 Experimental Procedures

SI 3.1 General Procedure

All reagents were supplied by Acros, Aldrich, Fisher or Fluorochem chemical suppliers and were used as supplied unless stated otherwise. NMR spectra were recorded using either a Bruker AMX400 or an Advance DFX400 instrument. Deuterated chloroform ($CDCl_3$) or deuterated dimethyl sulfoxide (DMSO-d_6) were used as solvents. Chemical shifts (δ) are reported in parts per million (ppm) with the abbreviations s, d, t, q, dd, dt and m denoting singlet, doublet, triplet, quartet, double doublet, double triplet and unresolved multiplet resonance respectively. All coupling constants (*J*) are recorded in Hertz (Hz). Assignments were made using chemical shift and coupling constant data using DEPT-90, COSY, HSQC and HMBC experiments where required. IR spectra were recorded on a Perkin-Elmer Spectrum One FT-IR spectrometer instrument with peak intensities abbreviated to: w, weak; m, medium; s, strong; br, broad. All melting points were determined on a Stuart SMP10 melting point apparatus. Mass spectra were recorded under conditions of electrospray ionisation (ESI) on a Thermo Scientific LTQ-Orbitrap XL with a Thermo Scientific Accela HPLC. Thermogravimetric (TGA) analyses were performed using a TGA-Q50 thermogravimetric analyser.

SI 3.2 Synthetic Procedures

Synthesis of BTPhen-Si

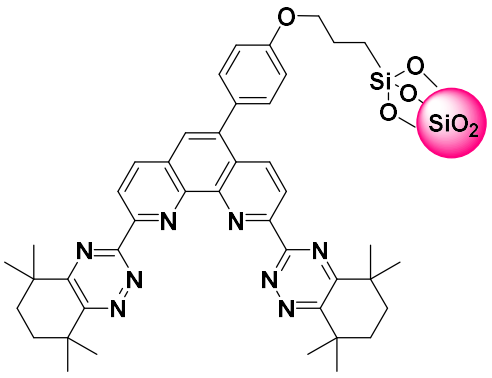

41

Sodium hydride (60% dispersion in mineral oil) (0.039 g, 1.1 mmol, 1.8 eq) was added to a suspension of 4-(hydroxyphenyl)-$CyMe_4$-BTPhen **33** (0.4 g, 0.62 mmol) in DMF (55 mL) at 120 °C and the mixture stirred for 30 minutes. Chloropropyl-functionalised SiO_2 gel **40** (0.25 g) was slowly added in small additions over 15 minutes and the suspension was stirred at 120 °C for 18 hours. The reaction was cooled, filtered and washed with DMF (100 mL), EtOH (100 mL), deionised water (100 mL) and $CHCl_3$ (100 mL). The $CyMe_4$-BTPhen-functionalised SiO_2 gel **41** (0.37 g) was dried at 120 °C to afford a dark orange solid. FT-IR (ATR) ν_{max} / cm^{-1} = 2988w, 1599w, 1393w, 1050s, 795w, 440s;

Chapter 4 – Application of Phenanthroline-based Functionalized silica to the Separation of Rare Earth Elements (REEs)

Chapter 3 investigated the use of CyMe4-BTPhen functionalized silica gel (BTPhen-Si) (Figure 3.4) in a fixed-bed column to extract and recover REEs from a 2% nitric acid solution. Although effective, the synthesis of BTPhen-Si is costly due to the requirement of palladium for the Suzuki reaction. Therefore, for large-scale industrial use, cost-effective alternatives are required. This study explores the use of alternative ligands, including a benzimidazole-fused neocuproine functionalized silica gel (BNC-Si) **51**, an epoxy functionalized neocuproine which can form hydroxyaminopropylneocuproine-functionalized silica gel (HANC-Si) **52**, and tetra(4-hydroxyphenyl)BTPhen-functionalized silica gel (TBTPhen-Si) **53** (Figure 4.1). The objective is to determine their potential for REE extraction and recovery in a fixed-bed column.

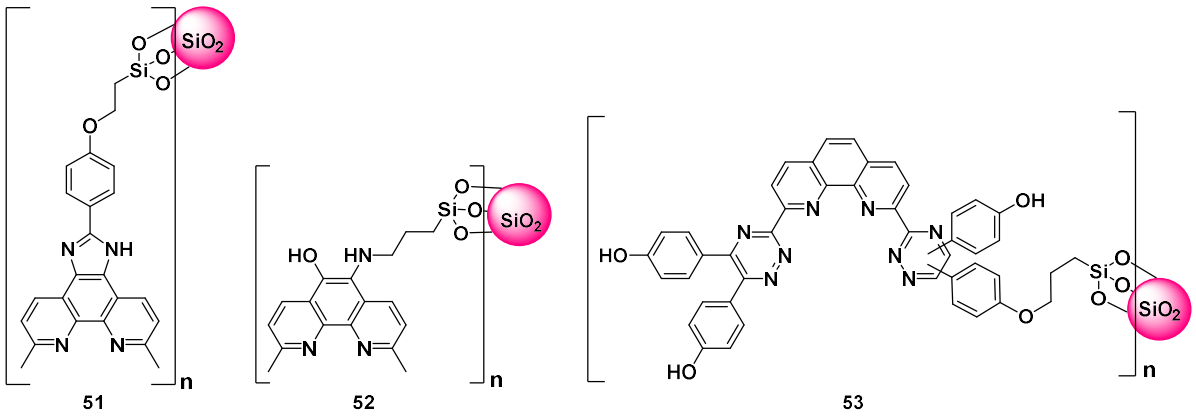

Figure 4.1. Structures of BNC-Si **51** (left), HANC-Si **52** (middle) and TBTPhen-Si **53** (right)

As well as alternatives to the Suzuki reaction, the linkage between silica and the ligand is studied to see if the change in electronics of the system affects the extraction and partitioning of REEs. The synthesis of NC-Si and BTPhen-Si both require 4-hydroxyphenylboronic acid to synthesize (4-hydroxyphenyl)-CyMe$_4$BTPhen and (4-hydroxyphenyl)-neocuproine to allow an ether linkage with chloropropyl silica gel (Figure 4.2). In this work neocuproine will undergo a Suzuki reaction with 4-boronobenzoic acid and an amide linkage with aminopropyl silica gel with be formed to produce aminopropyl neocuproine functionalised silica gel (ANC-Si) **54**. Dynamic fixed-bed column studies are carried out to determine adsorption capacity.

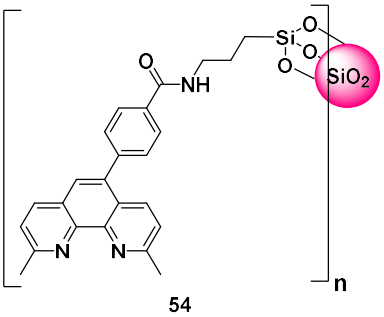

Figure 4.2. Structure of ANC-Si **54**

The Suzuki-Miyaura reaction is a palladium-catalyzed cross-coupling reaction between an aryl halide or triflate and an organoboron compound providing a way to couple two sp^2 carbons together [1,2].

4.1 Suzuki-Miyaura Reaction Mechanism

The mechanism of the Suzuki-Miyaura reaction involves several steps as depicted in Scheme 4.1. First, the palladium catalyst, usually $Pd(PPh_3)_4$ or $Pd_2(dba)_3$, undergoes oxidative addition with the aryl halide or triflate, generating a Pd(II) intermediate. This Pd(II) intermediate coordinates with a boronic acid or ester forming a Pd(II) boronate complex [3]. The coordination of the organoboron compound is usually facilitated by the presence of a base, such as triethylamine or potassium carbonate. The next step is transmetallation, where the Pd(II) boronate complex is transformed into a Pd(II) aryl complex. This process involves the transfer of the aryl group from the boron atom to the palladium atom, resulting in the formation of a new carbon-carbon bond. Finally, the reaction is completed by reductive elimination, which regenerates the Pd(0) catalyst and releases the desired cross-coupled product. The reductive elimination step involves the transfer of the aryl group from the palladium atom to the adjacent carbon atom, resulting in the formation of the new carbon-carbon bond and the release of the desired product.

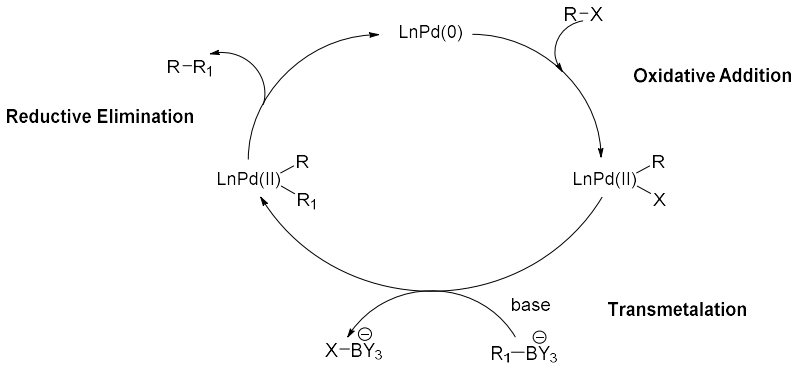

Scheme 4.1. Suzuki-Miyaura coupling mechanism

4.2 References

1. Barder, T.E.; Walker, S.D.; Martinelli, J.R.; Buchwald, S.L. Catalysts for Suzuki-Miyaura Coupling Processes: Scope and Studies of the Effect of Ligand Structure. *J. Am. Chem. Soc.* **2005**, *127*, 4685–4696.
2. Suzuki, A. Organoboron Compounds in New Synthetic Reactions. *Pure Appl. Chem.* **1985**, *57*, 1749–1758.
3. Miyaura, N.; Suzuki, A. Palladium-Catalyzed Cross-Coupling Reactions of Organoboron Compounds. *Chem. Rev.* **1995**, *95*, 2457–2483.

Application of Phenanthroline-Based Functionalized Silica to the Separation of Rare Earth Elements (REEs)

[1]Zoe Y. Selfe, [1]Laurence M. Harwood, [2]Mark D. Ogden

[1]Department Of Chemistry, University of Reading, Whiteknights, Reading RG6 6AD, UK

[2]Department of Chemical and Biological Engineering, University of Sheffield, Sir Robert Hadfield Building, Sheffield, S1 3JD, United Kingdom

Corresponding author: Zoe.Selfe@pgr.reading.ac.uk

ABSTRACT

Rare Earth Elements (REEs) play a crucial role in the production of a wide range of high-end technical products, resulting in a strong dependence on REEs. Only 1% of all REEs are recycled from end-of-life products, which is becoming increasingly concerning as demand is set to rise. Fortunately, China is able to keep up with demands as 99% of REEs currently come from China [1,2]. Adsorption using ligands immobilised onto solid supports provides an effective method for the extraction of REEs from solutions of low concentrations. In this paper, four *N*-donor ligands bearing the 1,10-phenanthroline moiety have been synthesized and immobilized onto silica gel. These four ligands had different linkages to silica gel; ANC-Si featured an amide group, BNC-Si possessed an benzimidazole linker while HANC-Si attaches to the silica through a secondary amine. All three systems were attached to the silica through the bridge of the neocuproine however TBTPhen-Si attaches to the silica gel on the 1 and 10 positions of the phenanthroline molecule through benzoyl groups. BNC-Si had the highest w/w% of ligand on the silica, with HANC-Si the least (14 and 4 w/w%, respectively). Extraction studies using separate fixed-bed dynamic columns have been carried out to determine the adsorption capacities of each of the four ligand-immobilized silica systems on the extraction and potential separation of REEs from acidic media. Simple models described breakthrough curves (i.e., Adams-Bohart, Thomas, Yoon Nelson, Modified Dose Response (MDR)). All ligand systems, except for HANC-Si, were able to be described by at least two models. These four new systems were found to have adsorption capacities: 0.00484, 0.0101, 0.0106 and 0.0157 mg g^{-1} for BNC-Si, HANC-Si, ANC-Si and TBTPhen-Si, respectively. Cost analysis was calculated giving figures between £26.5k and £9.2k per gram of material synthesized (TBTPhen-Si and HANC-Si, respectively). Their adsorption capacities, costs and yields were measured and compared to previous phenanthroline-derived silica gel systems, NC-Si and BTPhen-Si. TBTPhen-Si had a higher adsorption capacity than NC-Si, however BTPhen-Si had the highest overall adsorption capacity (0.0484 mg g^{-1}) out of the six.

keywords: synthesis, ion exchange, rare earth elements, rare earth separations, functionalized silica

1 INTRODUCTION

Rare earth elements (REEs) are used in all areas of technology, as they make products stronger and lighter [3]. Despite the name "Rare Earth," these metals are actually relatively abundant in the Earth's crust. For example, cerium (Ce) has a concentration of 66 parts per million (ppm) in the Earth's crust, which is similar to that of copper (Cu) at 68 ppm [4]. However, the later REEs are less abundant, with thulium (Tm) and lutetium (Lu) being the least abundant elements, with concentrations of 0.3 and 0.31 ppm, respectively [4]. The rare earth series includes 17 chemical elements, including lanthanum (La) to lutetium (Lu), as well as scandium (Sc) and yttrium (Y), which have useful applications such as being used in strong permanent magnets.

These elements play a crucial role in various industrial and consumer products. They are used in catalysts (74%), ceramics and glass (10%), in alloys (6%), polishes (4%), and other areas (6%) [5]. They are also used in medical equipment, fluorescent lamps and clean energy technologies such as wind turbines and electric cars. Cerium carbonate and cerium oxide are used in catalytic converters in vehicles, and neodymium-iron-boron alloys are used in computer hard drives, electric vehicles, mobile phones, and wind turbines because they can generate strong magnetic fields [6]. The production of these elements is on the rise with 7,300 tonnes of neodymium (Nd) and 24,000 tonnes of cerium (Ce) being produced worldwide each year. This trend is expected to continue as the demand for these elements is predicted to increase by 3 to 7 times between 2021 and 2040 [7–9].

However, little of the REEs used are recycled (*ca.* 1%) and therefore REEs have been on the EU critical list since 2011 [1,2]. As the demand is set to grow, a supply risk is imminent [10]. Offshore wind power is expected to reach 86 GW by 2050, with each wind turbine requiring Nd (28.5%), Dy (4.4%), B (1%) and Fe (66%), with a combined weight of 4 tonnes [11]. These large wind turbines, when retired, can more easily be recycled compared to smaller products such as hard disc drives (HDD) and mobiles phones as the concentration of REEs is much higher in relation to the rest of the composition. There are currently no industrial recycling plants to recycle the REEs in wind turbine magnets, but hydrometallurgical methods on a laboratory scale are being investigated. A process described by Kumari *et al.* involved a roasting step where REEs and iron are converted to their respective oxides at 1123 K with the addition of 0.5 M HCl [12]. Research is currently being carried out to avoid the use of high temperatures as this requires a high energy input [13].

Obtaining Rare Earth Oxides (REO) from their ores requires multiple steps. Crushing the ores into fine powders, referred to as physical beneficiation, makes it easier to dissolve the unwanted solids in fatty acids and water. Chemical beneficiation removes strontium/calcium carbonates to obtain REOs with a purity of 85-90%. The most difficult step in the process is the separation of REEs from each other as they all have very similar chemical properties, with all possessing the 3+ oxidation state [14,15]. However, there is a slight decrease in the ionic radius across the REE series, known as the “lanthanide contraction”, due to the increased nuclear charge causing a pull on the outer 4*f* valance orbitals that have decreased shielding from the nucleus [16,17].

Liquid-liquid solvent extraction separation is currently the most widely used separation technique in industry. Other methods, including ion exchange, fractional precipitation, and magnetic separation are also being developed and researched as alternatives to solvent extraction, but solvent extraction is still the most used method for separating REEs due to its efficiency and reliability. Typical ligands involved in liquid-liquid solvent extraction contain oxygen, sulfur or nitrogen donors. Examples of these ligands are; di-2-ethyl-hexylphosphoric acid (HDEHP) for RE chlorides/sulfates, and tri-n-butyl phosphate (TBP) for RE nitrates as well as 2-ethyl-hexyl-2-ethyl-hexyl-phosphoric acid (HEHEHPA), versatic acid 10 46, versatic acid, Cyanex® 572 and Aliquat® 336 [18].

Liquid-liquid solvent extraction techniques are usually efficient, but they do have drawbacks - particularly the use of large quantities of organic solvents. Degradation of the ligands and solvents can also occur, which will affect extraction efficiency as well as leading to third phase formation [19]. Chromatography involving a solid phase can be used as an alternative where a ligand is attached to a solid support, allowing the extraction from an aqueous medium.

Examples include extraction chromatography, cation-exchange chromatography and displacement chromatography and such approaches can extract REEs from very low aqueous concentrations. The use of strong acid (SA) cation exchange resins is currently the most efficient in the separation of REEs and these resins have been used in many different waste streams. as Cyanex® 272 and 1-hexyl-4-ethyloctyl-isopropylphosphonic acid (HEOPPA) were able to recover REEs in the order of sorption; Lu(III) > Yb(III) > Tm(III) > Er(III) > Y(III) > Ho(III) showing the ability to separate adjacent REEs [20].

The study by Suzuki *et al*. examined the ability of pyridine-functionalized resin materials, consisting of 4-vinylpyridine and *m*/*p*-divinylbenzene co-polymers embedded on silica beads, to extract and separate REEs by column chromatography. The adsorbed REEs could be eluted in reverse order using methanolic nitric acid solution [21].1,10-phenanthroline, a precursor of neocuproine, contains two nitrogen donor atoms that can bind to REEs, as demonstrated by Hart and Laming, who were able to extract 1,10-phenanthroline REE chlorides and 1,10-phenanthroline REE trithiocyanates for all REEs (La-Lu) from an aqueous solution [22]. The binding constant ($log_{10}K_{101}$) of the 1,10-phenanthroline Nd(III) complex was found to be 1.61 ± 0.03 [23]. 1,10-Phenanthroline can be readily immobilized onto silica providing a solid support and an effective method for metal extraction [24]. Additionally, 1,10-phenanthroline can also be functionalized with Merrifield resin to form complexes with Nd, Sm, Eu, Gd, Tb, Er and Yb [25].

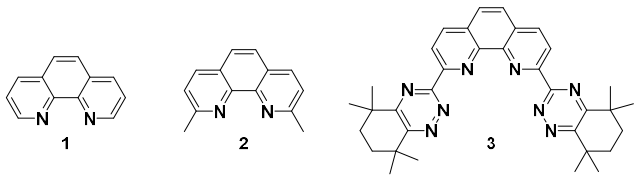

Figure 1. Structures of 1,10-phenanthroline **1,** neocuproine **2** and $CyMe_4$-BTPhen **3**

Neocuproine **2** contains the 1,10-phenathroline **1** moiety which can bind to Cu, Fe and Co in a 2:1 ligand to metal fashion (Figure 1) [26–29]. In previous work, 4-(hydroxyphenol)-neocuproine had been synthesized and attached to silica via an ether linkage to form neocuproine functionalized silica gel (NC-Si) **4** which was able to extract REEs from 2% nitric acid. NC-Si was able to partition the REE series into three groups; early, mid and late REEs. In this work neocuproine will be attached to silica gel via an amide linkage to form aminopropyl neocuproine silica gel (ANC-Si) **5** (Figure 2). The electronics are altered according to the linkage, where 4-(hydroxyphenyl) donates electrons into the phenanthroline rings and 4-(amidophenyl) withdraws electrons from the rings, changing the ability to extract and partition REEs. The ability of ANC-Si **5** to extract REEs from an acidic solution will be studied using a fixed-bed column technique.

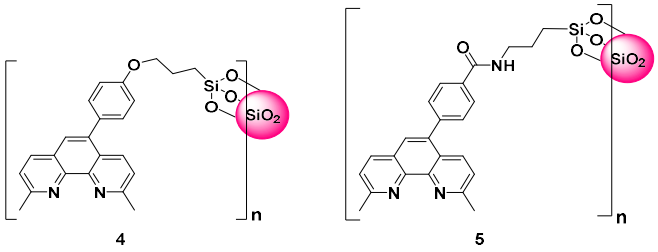

Figure 2. structures of NC-Si **4** and ANC-Si **5**

The $CyMe_4$-BTPhen **3** ligand has been utilized in the past to separate actinides from REEs in spent nuclear fuel using a technique known as solvent-solvent extraction with 1-octanol as the organic phase [30]. This heterocyclic ligand is composed of a 1,10-phenanthroline **1** moiety and a 1,2,4-triazine functional group, which coordinates to the metal through four nitrogen atoms in either a 1:2 or 1:1 ratio of metal to ligand (depending on the concentration of the metal). The expanded 5*f*-orbitals of actinides have a greater degree of covalency with the ligand compared to the 4*f*-orbitals of REEs, resulting in An/Ln separation factors of 200-400 in 1-4 M HNO_3 [31–35]. This concept of *f*-orbital size preference may also lead to the separation of adjacent rare earth ions from each other due to the lanthanide contraction phenomenon.

$CyMe_4$-BTPhen **3** can be modified with silica gel to create $CyMe_4$-BTPhen functionalized silica gel (BTPhen-Si) **6** as an alternative to liquid-liquid extraction (Figure 3). The immobilization process of $CyMe_4$-BTPhen with silica gel involves the synthesis of 5-(4-hydroxyphenyl)$CyMe_4$-BTPhen **8**, which allows for a substitution reaction to occur with chloropropyl silica gel **9** to form BTPhen-Si. The synthesis of **8** involves 11 steps, all with good yields and relatively inexpensive reagents, except for the final step where a Suzuki-Miyaura reaction is required to add a 4-hydroxyphenyl group to the phenanthroline backbone.

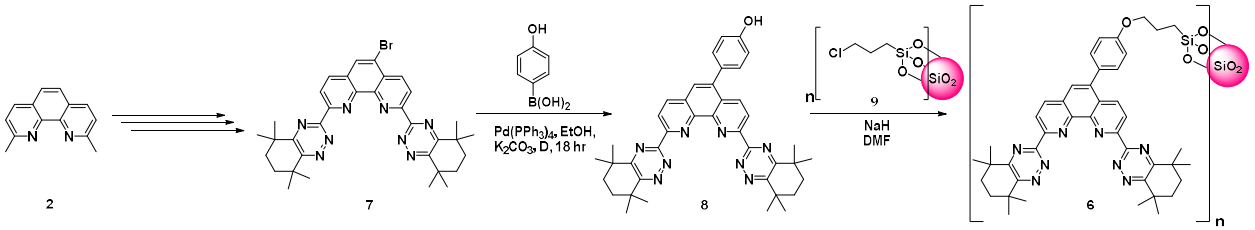

Figure 3. Synthesis of BTPhen-Si **6**

Previous work investigated $CyMe_4$-BTPhen functionalized silica gel (BTPhen-Si) **6** in a fixed-bed column for the adsorption and desorption of REEs from an aqueous solution of 2% nitric acid. The extraction of REEs was efficient; however the synthesis of BTPhen-Si is relatively long and involves the use of an expensive palladium catalyst for the Suzuki-Miyaura reaction step. If these ligands were to be scaled up and adopted in industry, a cheaper method must be found. In this work, alternative ligands are explored to see if the Suzuki-Miyaura reaction can be omitted. These include the study of a benzimidazole-fused neocuproine-functionalized silica gel (BNC-Si) **10**, as well as an epoxy-functionalised neocuproine, which can be ring-opened by a nucleophilc functionality to form hydroxyaminopropylneocuproine-functionalized silica gel (HANC-Si) **11**. Tetra(4-hydroxyphenyl)BTPhen-functionalized silica gel (TBTPhen-Si) **12** has also been synthesized and all have been assessed in a fixed-bed column technique, their structures are displayed in table 1.

Table 1. Functionality and characteristics of ANC-Si **5**, BNC-Si **10**, HANC-Si **11** and TBTPhen-Si **12**. *taken from silica gel precursor material [36]

Structure	Name	Acronym	Particle Size
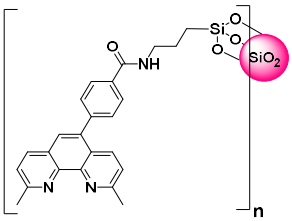 5	5-(4-aminopropyl)neocuproine functionalized silica gel	ANC-Si	
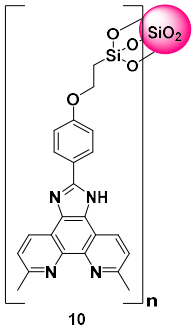 10	benzimidazole-fused neocuproine functionalized silica gel	BNS-Si	40-63 µm*
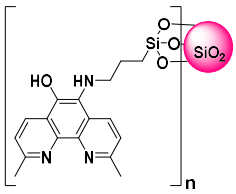 11	hydroxyaminopropylneocuproine-functionalized silica gel	HANC-Si	40-63 µm*
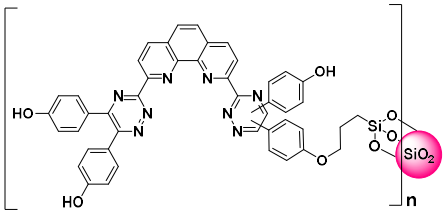 12	Tetra(4-hydroxyphenyl)BTPhen-functionalized silica gel	TBTPhen-Si	40-63 µm*

2. MATERIALS AND METHODS

2.1 Materials

All reagents were purchased from AlfarAesar, Fisher, Fluorochem or Sigma-Aldrich. All chemicals were of analytical grade and used as received without further purification. 3-Chloropropyl-functionalized silica gel **9** with a particle size of 230-400 mesh and a pore size of 60 Å was purchased from Sigma-Aldrich and used as supplied [36]. The extent of chloropropyl labelling of the purchased substrate was ~ 2.5 % loading and the matrix-active group was ~8% functionalized.

2.2 Synthesis

2.2.1 Synthesis of ANC-Si

In order to introduce functionality onto the phenanthroline backbone of neocuproine **2**, mono-bromination at the 5-position was carried out using bromine (0.6 equivalents) in the presence of H_2SO_4 (20% SO_3). A Suzuki-Miyaura coupling reaction using 4-(ethoxycarbonyl)phenyl)boronic acid **14** and Bromo-neocuproine followed to form 5-(4-hydroxycarbonylpheny)neocuproine **15** which permits amide coupling with aminopropyl-functionalized silica gel **16** to from 5-(4-aminopropyl)neocuproine silica gel (ANC-Si) **5** (Figure 4).

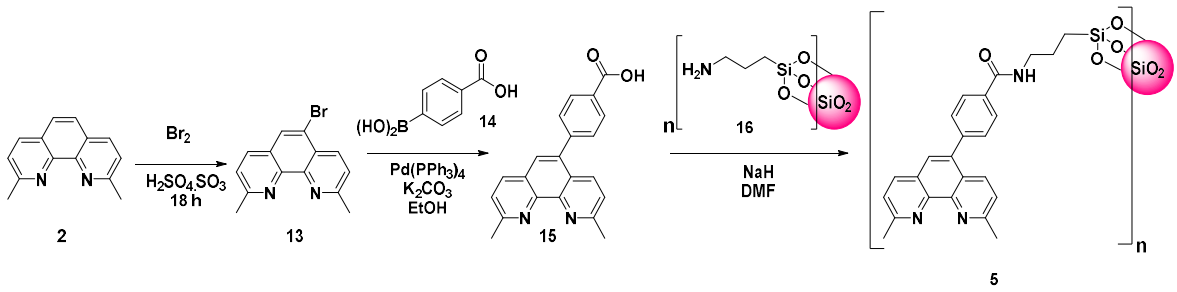

Figure 4. Synthesis of ANC-Si **5** solid phase extractant

2.2 Synthesis of BNC-Si

Benzimidazole-fused neocuproine-functionalised silica gel **10** was synthesized as a means of providing a possible alternative way to attach the neocuproine ligand onto chloropropyl-functionalized silica gel **9**. This route would provide a way of attachment through the alcohol group on the phenol, similar to 5-(4-hydroxyphenyl)CyMe$_4$-BTPhen (**8** in Figure 3). This method of synthesis by-passes the Suzuki-Miyaura coupling step. The formation of a neocuproine diketone **17** would see a means to functionalise imidazole with a phenol group using 4-hydroxybenzaldehyde (Figure 5).

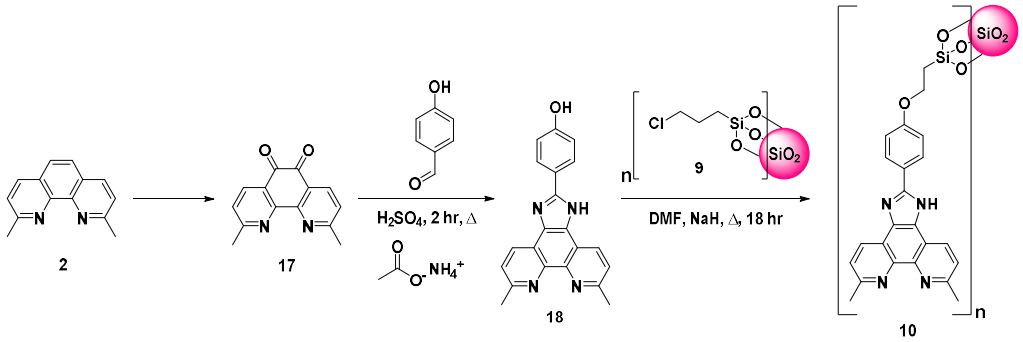

Figure 5. Synthesis of BNC-Si solid phase extractant

2.2.3 Synthesis of HANC-Si

Another method to omit the need for a Suzuki-Miyaura coupling reaction is the formation of an epoxy-group on the neocuproine backbone. Neocuproine **2**, at a pH of 8.6, can undergo epoxidation on the phenanthroline backbone to form epoxyneocuproine **19** as depicted in Figure 6 [37]. Subsequent ring opening of the three-membered epoxy-ring using the amine located on aminopropyl-functionalized silica gel **16** can provide a way of attaching the phenanthroline backbone directly onto the silica gel. The backbone epoxy-derivative of neocuproine was synthesized using sodium hypochlorite in dichloromethane with tetrabutylammonium hydrogen sulfate as a phase transfer catalyst. Reaction with aminopropyl-functionalized silica gel **16** leads to ring opening of the epoxide to attach directly onto the neocuproine to form aminopropylhydroxyneocuproine-functionalized silica gel **10**. The crude product was subjected to washings with multiple solvents to remove any unreacted 6-epoxyneocuproine **19**.

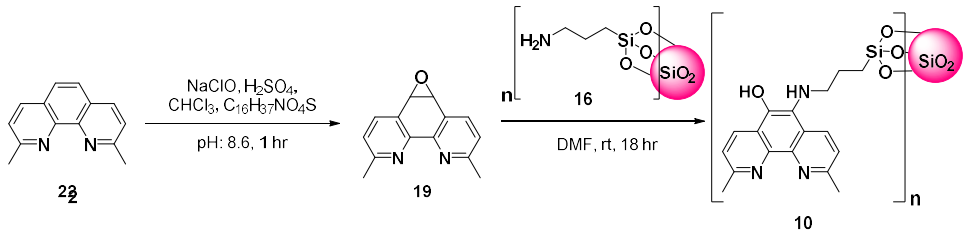

Figure 6. Synthesis of HANC-Si **10** solid phase extractant

2.2.4 Synthesis of TBTPhen-Si

The synthesis of tetra(4-hydroxyphenyl)BTPhen **20** is very similar to that of CyMe$_4$-BTPhen **3** where a hydrazonamide functional group is added to neocuproine to form 1,10-phenanthroline-2,9-dicarbohydrazonamide, as reported by Afsar *et al.* [38,39]. This allows the addition of 4,4'-

dihydroxybenzil to form tetra(4-hydroxyphenyl)BTPhen **20** followed by a substitution reaction with chloropropyl-functionalized silica gel **9** to form TBTPhen-Si **12** (Figure 7)

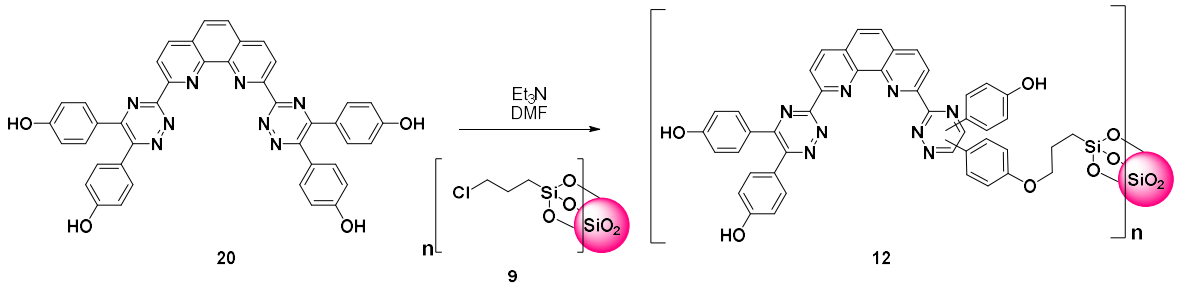

Figure 7. Synthesis of BTPhen-Si solid phase extractant

2.3 Characterization of ANC-Si, BNC-Si, HANC-Si and TBTPhen-Si

Confirmation of the synthesis of 5-(4-hydroxycarbonylpheny)neocuproine **15**, neocuproine-5,6-dione **17**, neocuproine-5,6-diimine **18**, epoxy-neocuproine **19** and tetra(4-hydroxyphenyl)BTPhen **20** was achieved using NMR spectroscopic analysis. The degree of immobilization of these ligands on the silica surface was estimated by elemental analysis using energy dispersive X-ray spectroscopy (EDX) in conjunction with SEM. Thermogravimetric analysis (TGA) was performed to determine the percentage organic content.

For adsorption studies ICP-MS analysis was carried out with Rh as the internal standard. A stock solution of 2% HNO_3 spiked with 5 ppb Rh was prepared using ultra-pure water and 70% ultra-pure HNO_3 (≥ 99.999% trace metals basis). All standard solutions were prepared using a stock solution of 2% HNO_3 spiked with 5 ppb Rh. Standards were prepared using metal mixes purchased from Sigma-Aldrich as TraceCERT (Traceable Certified Reference Materials). Standards used to calibrate the ICP-MS were at concentrations of 5, 10, 25, 50 and 100 ppb. All extraction samples were normalised to 2% HNO_3 and spiked with 5 ppb Rh before testing. Samples (5 mL) were taken before and after extractions to provide true initial and end concentrations. An average of three readings was taken with all samples.

2.4 Adsorption Studies – Dynamic Method

2.4.1 Adsorption Studies on ANC-Si

ANC-Si **5** (0.1 g) was loaded into a column (D=1.1 cm, H=2.6 cm). A sample of REE solution (containing Sc, Y, La, Ce, Pr, Nd, Sm, Eu, Gd, Tb, Dy, Ho, Er, Tm, Yb, Lu) (~0.12 mg L^{-1}) (1 mL) in 2% nitric acid (HNO_3) was passed through with a flow rate of 0.5 mL min^{-1}. The eluate was collected and subjected to inductively-coupled plasma mass spectroscopic analysis (ICP-MS). Desorption of the REE (III) ions was performed by passing samples of nitric acid concentrations (0 M – 2 M (in 0.2 M increments)) (1 mL) through the column with a flow rate of 0.5 cm^3 min^{-1}. The effluent solution was collected in 1 mL fractions and subjected to ICP-MS analysis. A graph of C_t/C_0 against time for each individual rare earth ion was plotted to obtain the breakthrough curves for each system, where C_0 is the initial REE (III) ion concentration (mg L^{-1}) and C_t is the outlet ion concentration at a particular time (mg L^{-1}). The same procedure was also carried out on both aminopropyl-functionalized silica gel and chloropropyl-functionalized silica gel; however no adsorption of REEs occurred, confirming the ligands themselves were responsible for the adsorption of rare earth metals this was also seen for **10**, **11** and **12**.

2.4.2 Adsorption Studies on BNC-Si and HANC-Si

BNC-Si **10** and HANC-Si **11** (0.1 g) were loaded into separate columns (D=1.1 cm, H=2.6 cm). A sample of REE solution (containing Sc, Y, La, Ce, Pr, Nd, Sm, Eu, Gd, Tb, Dy, Ho, Er, Tm, Yb, Lu) (~0.12 mg L^{-1}) (1 mL) in 2% nitric acid (HNO_3) was passed through each column with a flow rate of 0.5 mL min^{-1}. The eluate was collected and subjected to ICP-MS analysis. Desorption of the REE (III) ions was performed by passing samples of nitric acid concentrations (0 M – 2 M (in 0.1 M increments)) (1 mL) through the column with a flow rate of 0.5 cm^3 min^{-1}. The effluent solution was collected in 1 mL fractions and subjected to ICP-MS analysis. A graph of C_t/C_0 against time for each individual rare earth ion was plotted to obtain the

breakthrough curves for each system, where C_0 is the initial REE (III) ion concentration (mg L^{-1}) and C_t is the outlet ion concentration at a particular time (mg L^{-1}).

2.4.3 Adsorption Studies on TBTPhen-Si

TBTPhen-Si **12** (1 g) was loaded into a column (D=1.4 cm, H=4.1 cm). A sample of REE solution (containing Sc, Y, La, Ce, Pr, Nd, Sm, Eu, Gd, Tb, Dy, Ho, Er, Tm, Yb, Lu) (~0.12 mg L^{-1}) (10 mL) in 2% nitric acid (HNO_3) was passed through with a flow rate of 0.5 mL min^{-1}. The eluate was collected and subjected to ICP-MS analysis. Desorption of the REE (III) ions was performed by passing samples of nitric acid concentrations (0 M – 2 M (in 0.1 M increments)) (2 mL) through the column with a flow rate of 0.5 cm^3 min^{-1}. The effluent solution was collected in 2 mL fractions and subjected to ICP-MS analysis. A graph of C_t/C_0 against time for each individual rare earth ion was plotted to obtain the breakthrough curves for each system, where C_0 is the initial REE (III) ion concentration (mg L^{-1}) and C_t is the outlet ion concentration at a particular time (mg L^{-1}).

2.5 Adsorption Capacity– Dynamic Method

The adsorption q (mg·g^{-1}) capacity provides a way of quantifying the efficiency of a material. It can be calculated either at equilibrium or at any given time t (mins). The adsorption capacity is given in equation (1) where C_0 is the initial REE (III) ion concentration (mg L^{-1}) and C_t is the outlet ion concentration at a particular time (mg L^{-1}).

$$q = (C_0 - C_t)\left(\frac{V}{W}\right) \quad (1)$$

2.6 Breakthrough Modelling

In order to compare the adsorption capabilities of NC-Si **5** between the rare earth elements, a breakthrough curve was plotted. The variation of C_t/C_0 as a function of time for the adsorption of rare earth metals allows models to be applied to the data to find predicted uptake capacity and model suitability. Several mathematical models have been developed to predict the dynamic behaviour of the column. The following models were used to determine the breakthrough performance as well as to calculate the rate constants and adsorption capacities. In this study; Adams-Bohart, Yoon Nelson, Thomas and Modified Dose Response models were applied to the data obtained from the adsorption study [40–43]. All of the models used to fit the breakthrough data are given in SI.2.

3 RESULTS

3.1.1 Characterization of ANC-Si

The confirmation of the functionalization **15** onto the surface of the silica gel was determined by the comparison with commercial aminopropyl-functionalized silica **15** using FT-IR. Both show a strong Si-O-Si stretch at 1045 cm^{-1} but only ANC-Si **5** shows a C=O stretch at 1655 cm^{-1} and aromatic stretches at 1380 cm^{-1}, confirming immobilization of the ligand onto the silica gel. Elemental analysis and TGA were used to determine the degree of immobilization of the organic ligand onto the surface of the silica gel. Elemental analysis showed that the carbon and nitrogen content had increased by 27.92% and 1.59%, respectively, upon the introduction of the ligand. TGA analysis showed a mass loss at 100 °C due to residual absorbed water, followed by a second mass loss from 100 °C to 300 °C, presumed to correspond to the organic material decomposing. This ~5.5% weight loss is presumed to equate to the amount of immobilized 5-(4-hydroxycarbonylpheny)neocuproine **15** onto the functionalized silica gel.

3.1.2 Characterization of BNC-Si

Confirmation of the functionalization of BNC-Si **5** onto the surface of the silica gel was determined by the comparison with commercial chloropropyl-functionalized silica gel **9** using FT-IR analysis that indicated introduction of the ligand onto the silica gel as shown by absorptions at 1612 cm^{-1} and 1372 cm^{-1} corresponding to C=C and C-H stretches, respectively, whilst also demonstrating the presence of the Si-O-Si bond, as confirmed by an absorption at 1055 cm^{-1}. Elemental analysis showed an increase in C and N content in the BNC-Si **10** as well as an 80% decrease in the amount of Cl content, which indicates 80% immobilization of BNC onto the silica gel. TGA analysis showed that at 100 °C there was an initial mass loss

equating to loss of the residual absorbed water in the sample. Between 300 and 550 °C there was a 14% derease in mass lost relating to ~14% w/w loading.

3.1.3 Characterization of HANC-Si

Proton NMR and FT-IR spectroscopic analysis of epoxy neocuproine **19** confirmed the presence of the epoxy functional group, as well as the immobilization onto the aminopropyl-functionalised silica gel **16**. The proton NMR spectrum of epoxy neocuproine **19** confirmed the formation of the three membered epoxy ring on the phenanthroline by the disappearance of two aromatic protons and the appearance of two aliphatic protons at δ 4.6. The FT-IR spectrum of HANC-Si **11** showed aromatic C-H stretches at 1628 cm^{-1}, confirming the incorporation of the phenanthroline ligand onto the aminopropyl-functionalized silica gel. The presence of the Si-O-Si bonds are shown as a stretching absorption at 1055 cm^{-1}, all indicating successful immobilization of neocuproine onto silica gel via the opening of the epoxide ring. Elemental and TGA analysis both confirmed the immobilization of neocuproine onto aminopropyl-functionalised silica gel **16**. Elemental analysis of HANC-Si **11**, carried out by SEM, was compared to that of aminopropyl-functionalized silica gel **16**. The carbon content for HANC-Si **11** was 22%, compared to that of aminopropyl-functionalised silica gel **16**; 16.81 %, giving a 131% increase, along with an increase in nitrogen content, proving immobilization of the ligand onto silica gel had been successful. The degree of immobilization was also estimated from TGA analysis (Figure 3.8), where a 2% loss of mass at 100 °C was attributed to the loss of residual absorbed water and a subsequent 4% mass loss from 200 – 400 °C could be attributed to an immobilization of 4% from neocuproine and aminopropyl onto the silica gel.

3.1.4 Characterization of TBTPhen-Si

The degree of incorporation of tetra(4-hydroxyphenyl)BTPhen **12** onto the surface of the functionalized silica was measured using FT-IR and elemental analysis. FT-IR analysis allowed the comparison between chloropropyl-functionalized silica gel **9** with TBTPhen-Si **12**. Both show a strong Si-O-Si stretch at 1058 cm^{-1}; whereas TBTPhen-Si **12** was the only one to show organic aromatic stretches at 1606 cm^{-1}, 1487 cm^{-1} and 1383 cm^{-1} corresponding to C=C, C-C and C-H stretches respectively, confirming immobilization onto the silica gel. Energy dispersive X-Ray spectroscopy (EDX) allowed comparison between chloropropyl-functionalized silica gel **9** and tetra(4-hydroxyphenyl)BTPhen-functionalized silica gel **12**. The increase in carbon content (~319%) as well as the decrease in Cl content (~98.4%) showed that 98% of the chloropropyl groups had been substituted. The loss of Si content also showed immobilization of tetra(4-hydroxyphenyl)BTPhen **20** onto the available sites on the silica gel has occurred. TGA analysis showed a mass loss at 0-100°C attributed to the loss of absorbed water. A 7% mass loss between 300 and 700°C relates to a 7% w/w of organic content, presumed to correspond mainly to tetra(4-hydroxyphenyl)BTPhen immobilized on the silica gel.

3.5. Adsorption Studies on ANC-Si, BNC-Si, HANC-Si and TBTPhen – Dynamic Method

Analysis of the breakthrough curves obtained by fixed-bed dynamic adsorption study of rare earth ions onto ANC-Si **5**, BNC-Si **10**, HANC-Si **11** and TBTPhen-Si **12** allowed the performance of the fixed-bed column to be measured based on breakthrough times [44,45]. The breakthrough curves, $C_t/C_0 = f(t)$, for the rare earth metals (III) (La-Lu) and Sc (III) and Y(III) are displayed in Figure 8 where C_t is the concentration of the eluate at time t (mins) and C_0 is the concentration of the eluate when $t = 0$. The breakthrough time is when $C_t/C_0 = 0.05$ which gives a good indication of the speed at which elution starts to occur.

3.5.1 Adsorption Studies on ANC-Si

The breakthrough cuve for the desorption of REE ions from a dynamic fixed-bed column of ANC-Si **5** shows the classic “S” shaped breakthrough curves for every ion (Figure 8). Back extraction from the column appears to be rather difficult for all ions, except Gd, requiring a larger quantity of nitric acid and/or higher concentrations for complete elution of ions from the column. Gd seems to elute first before all of the other REE ions showing a way of separating Gd from the rest of the REEs. Overall, it appears that the earlier REEs (Sc-Gd) have faster breakthrough times (<5 mins) than the later REE ions (Tb-Lu) (>10 mins).

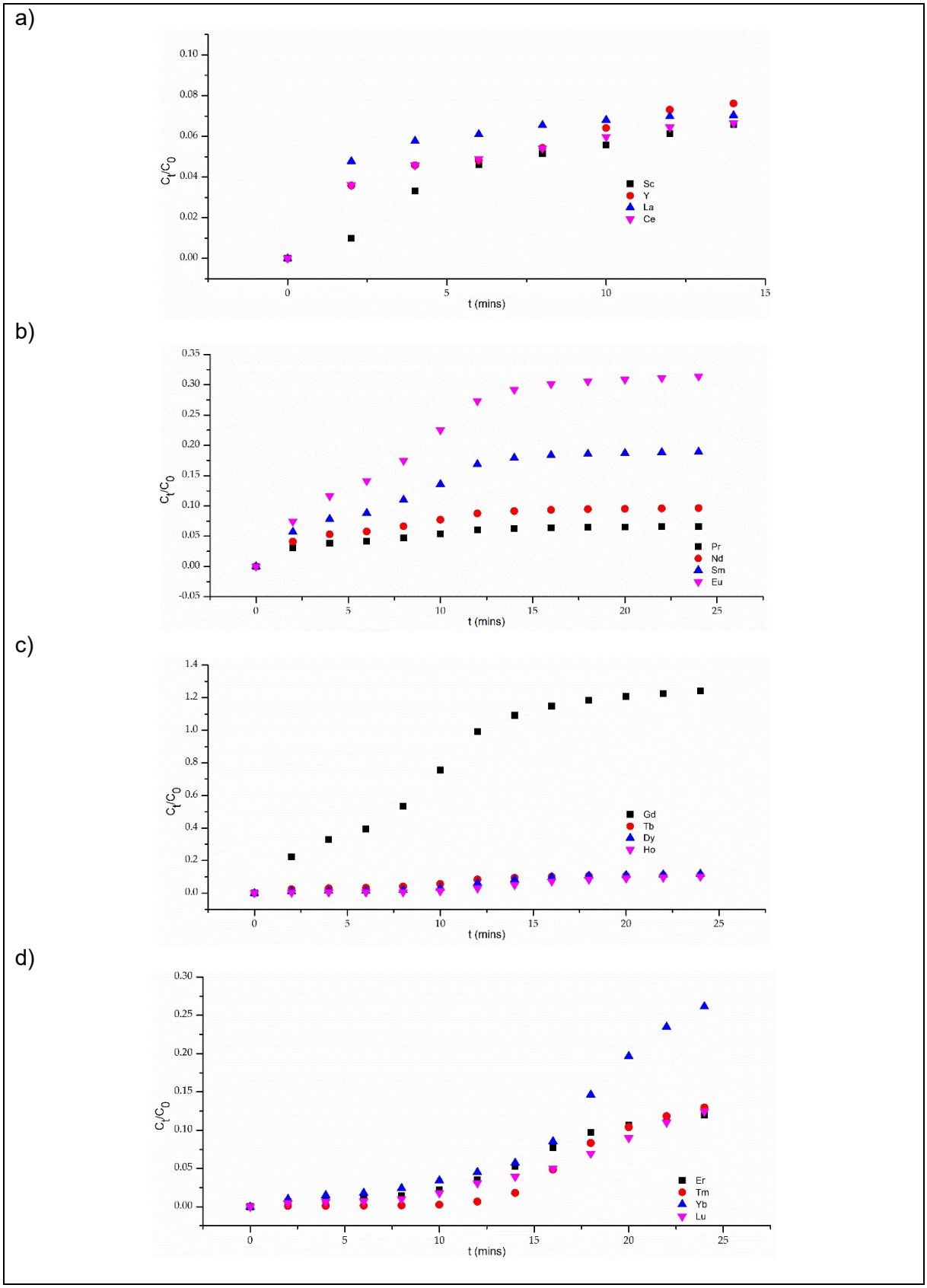

Figure 8. Breakthrough curves for the adsorption of first quarter of the REE series (a), second quarter of the REE series (b), third quarter of the REE series (c) and the last quarter of the REE series (d) rare earth metals by NC-Si flow rate 0.5 mL/min.

The adsorption capacity (q) provides a way of measuring the extraction efficiency of a material. Figure 5 shows the q for each ion calculated using equation (1). The overall q for ANC-Si is 0.010557 $mg \cdot g^{-1}$ where ANC-Si prefers La, Ce and Ho-Lu, as evident from their high q values. As the z/r ratio increases from La to Y (2.467 Å to 2.791 Å, respectively) the q decreases from 0.000773 $mg \cdot g^{-1}$ to 0.000549 $mg \cdot g^{-1}$, after which the q starts to increase again from Eu to Lu.

Gd and Sc are outliers and show noticeably lower adsorption capacities to what we would expect them to have with regard to their z/r ratio. This shows there are other factors affecting adsorption that are not related to ionic radius. The percentage of REE ions remaining on the column after the addition of eluent is a good indication of which ions the material prefers. 80% of all ions, except Eu, Gd and Yb, remain on the column showing that back extraction is rather difficult. For complete elution of all ions a higher concentration of nitric acid or a larger volume would be required to recover all REE ions.

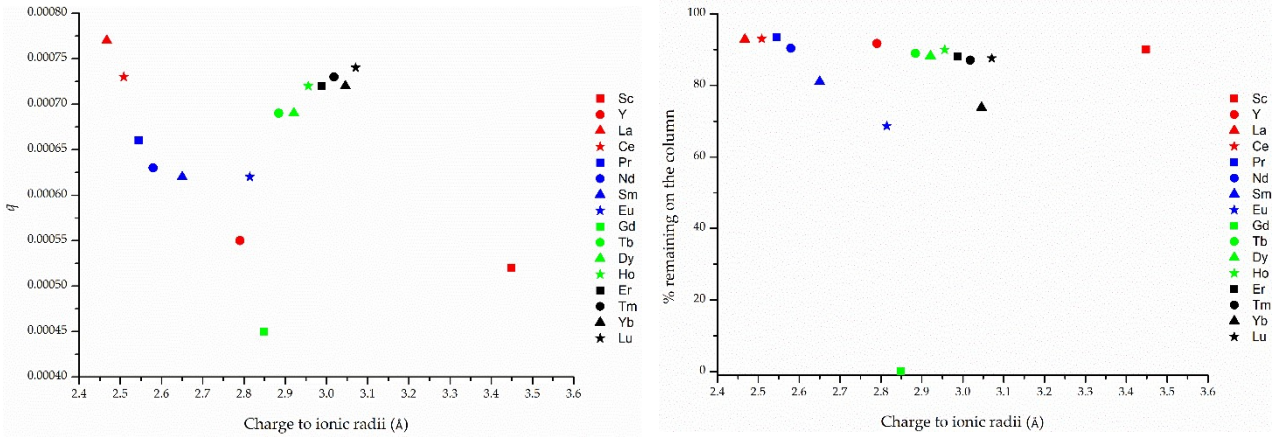

Figure 9. (Left) Graph of adsorption capacities (q) for all REEs in a column of ANC-Si **5** and (Right) Graph of the percentage of REE ions remaining on a column of ANC-Si **5**

3.5.2 Adsorption Modelling on ANC-Si

Adsorption modelling was achieved using Adams-Bohart, Yoon-Nelson, Thomas and MDR models and displayed in Table 2. The equations used to fit the adsorption curves for ANC-Si are S2, S3, S6 and S7 and are given in the supplementary information section.

The Thomas model was able to fit most of the REE ions, except for Sc and La with high R^2 coefficients (>0.827). The overall trend across the REE series shows that K_{Th} and R^2 increases whereas q_0 decreases. The Adams-Bohart model is a similar model to Thomas and therefore was able to describe all ions except for Sc, La and Ce (R^2 >0.797) showing an increase in K_{AB} across the series. Gd had the lowest N_0 value, indicating a lower adsorption capacity with relates to the data in Table 6.

Interestingly all models were able to fit Gd with Yoon-Nelson having the highest R^2 value for it. Gd was the only ion that the models; Yoon-Nelson and MDR was able to describe adsorption for. The Yoon-Nelson model was able to determine τ for Gd as it was the only ion to achieve over 50% elution from the column, coinciding with Figure 8. The other ions would require a higher concentration or volume of nitric acid to elute from the column if the ligand allows for such.

Table 2. Breakthrough modelling parameters for REE on ANC-Si

REE	Adams-Bohart			Yoon-Nelson		
	k_{AB} (L mg^{-1} min^{-1})	N_0 (mg L^{-1})	R^2	k_{YN} (min^{-1})	τ (min)	R^2
Sc						
Y	63.2	0.0103	0.838			
La						
Ce						
Pr	47.9	0.0142	0.815			
Nd	54.7	0.0112	0.799			
Sm	80.0	0.0068	0.797			
Eu						
Gd	133.9	0.0019	0.823	0.432	6.657	0.871
Tb	107.6	0.0070	0.870			
Dy	178.7	0.0053	0.890			
Ho	256.8	0.0048	0.906			
Er	207.2	0.0052	0.956			
Tm	372.6	0.0044	0.938			
Yb	216.5	0.0046	0.990			
Lu	216.2	0.0053	0.978			
REE	**Thomas**			**Dose-Response**		
	k_{Th} (L mg^{-1} min^{-1})	q_0 (mg g^{-1})	R^2	q_m (mg g^{-1})	a	R^2
Sc						
Y	0.037	0.421	0.870			
La						
Ce	0.027	0.571	0.827			
Pr	0.034	0.492	0.849			
Nd	0.038	0.391	0.837			
Sm	0.058	0.221	0.835			
Eu	0.072	0.151	0.833			
Gd	0.853	0.022	0.806	0.025	3.86	0.825
Tb	0.078	0.234	0.883			
Dy	0.126	0.183	0.890			
Ho	0.183	0.165	0.900			
Er	0.150	0.174	0.959			
Tm	0.266	0.148	0.921			
Yb	0.163	0.150	0.982			
Lu	0.160	0.175	0.974			

3.5.3 Adsorption Studies on BNC-Si

BNC-Si **10** does not seem to have very good extraction capabilities for REE ions and breakthrough seems to occur rather quickly (<5 mins) for all ions (Figure 10). There appears to be a slight preference for the smaller ions such as Sc and Er-Lu as these take longer to elute from the column compared to the larger ions.

a)

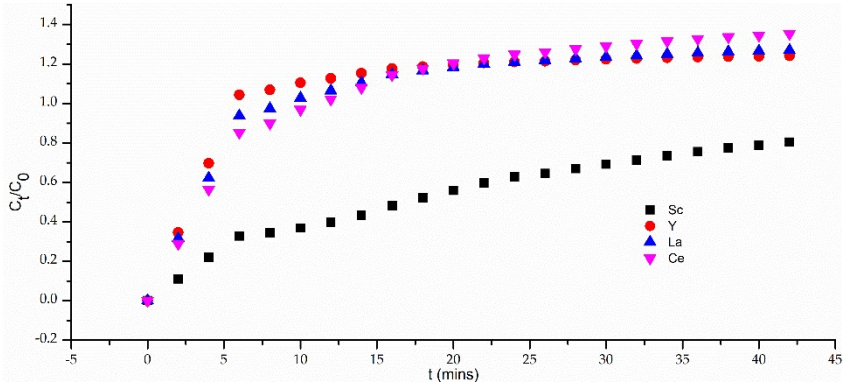

b)

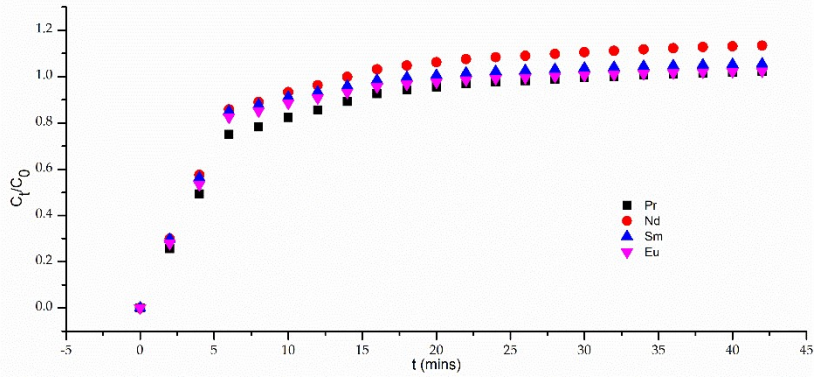

c)

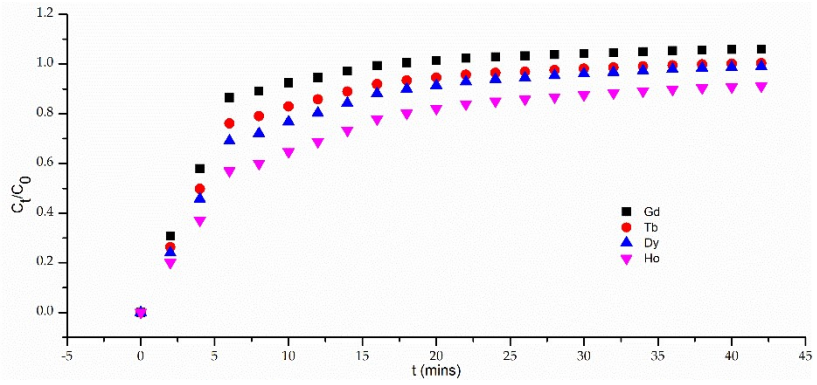

d)

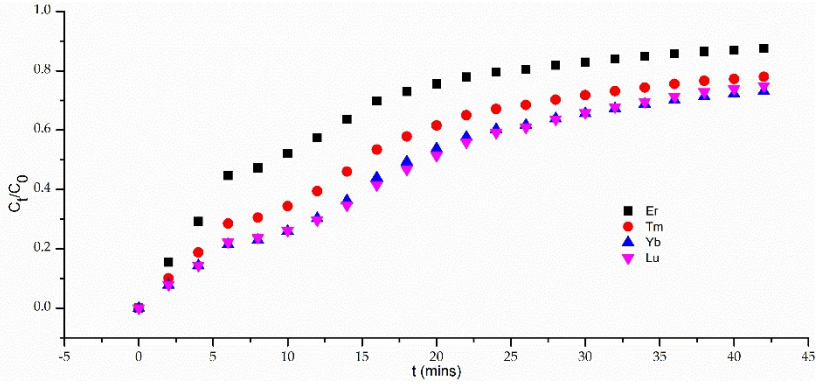

Figure 10. Breakthrough curves for the adsorption of first quarter of the REE series (a), second quarter of the REE series (b), third quarter of the REE series (c) and the last quarter of the REE series (d) rare earth metals by NC-Si flow rate 0.5 mL/min.

The overall adsorption capacity (q) for BNC-Si **10** is 0.00484 mg·g^{-1}, where a preference for the smaller (higher z/r ratio) REE ions (Dy to Lu and Sc) is seen. The overall trend shows an increase in q as the z/r increases, however Gd and Y do not follow the trend, showing other factors are affecting the extraction ability besides the size of the ion. Determination of the percentage of ions remaining on the column after a particular time is a good indicator of back extraction performance as well as measuring selectivity of REEs on a BNC-Si (Figure 11). A fixed-bed column of BNC-Si shows complete desorption of the larger ions (La – Dy) after 45 minutes leaving Ho, Er, Tm, Yb, Lu and Sc left bound to the column. This provides a way of separating the smaller REEs from the larger REEs as well as separating Y and Gd from the rest of the REE ions.

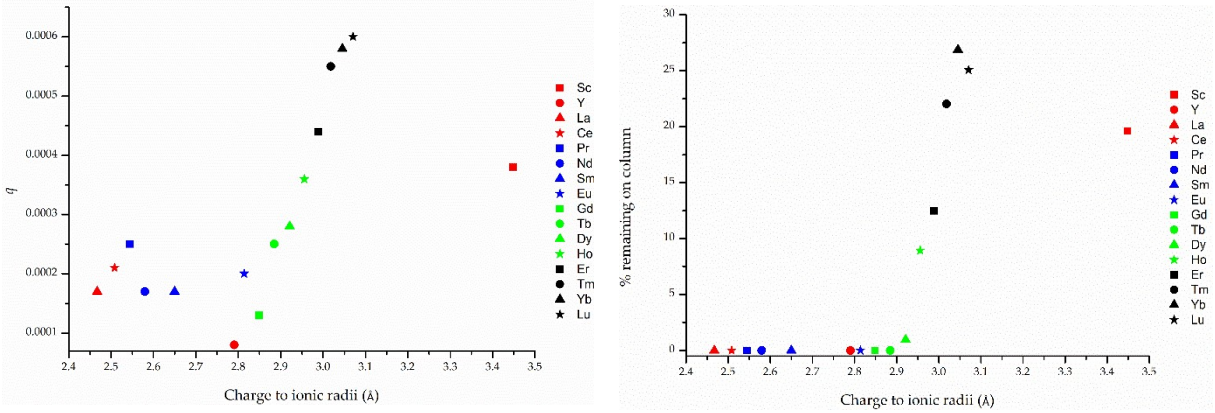

Figure 11. (Left) a graph of adsorption capacities (q) for all REEs in a column of BNC-Si **10** and (Right) a graph of the percentage of REE ions remaining on a column of BNC-Si **10** after 45 minutes

3.5.4 Adsorption Modelling on BNC-Si

The linear fitting of the Adams-Bohart and Thomas models (equations (S2) and (S6)) and the non-linear fitting of the Yoon-Nelson and MDR models (equations (S3) and (S7)) was carried out on the fixed-bed column of BNC-Si. The results from the fitting are displayed in Table 3. Fitting was achieved for Yoon-Nelson, Thomas and MDR, with the Thomas model able to describe all ions except Y. Both the Yoon-Nelson and MDR models are able to extract all ions with a z/r ratio above 2.54 Å (Table 6), except for Y-Ce. Across the REE series the K_{YN} and the K_{Th} decreases indicating a slower rate of adsorption for the later REE ions which is also confirmed with the increased τ time. Adams-Bohart was only able to fit the smaller REE ions, Yb and Lu showing their adsorption mechanism is very different to rest of the series. Y could not be described by any of the models, possibly due to its poor adsorption onto the fixed-bed column, as seen in Table 6.

Table 3. Breakthrough modelling parameters for REE on BNC-Si

REE	Adams-Bohart			Yoon-Nelson		
	k_{AB} (L mg^{-1} min^{-1})	N_0 (mg L^{-1})	R^2	k_{YN} (min^{-1})	τ (min)	R^2
Sc				0.076	18.847	0.932
Y						
La						
Ce						
Pr				0.402	4.528	0.952
Nd				0.672	3.548	0.908
Sm				0.637	3.627	0.970
Eu				0.575	3.868	0.970
Gd				0.671	3.508	0.969
Tb				0.412	4.436	0.945
Dy				0.278	5.371	0.925
Ho				0.135	7.929	0.857
Er				0.106	11.143	0.887
Tm				0.082	18.013	0.907
Yb	61.4	0.0057	0.784	0.078	22.069	0.921
Lu	60.1	0.0059	0.810	0.080	22.242	0.944
REE	**Thomas**			**Dose-Response**		
	k_{Th} (L mg^{-1} min^{-1})	q_0 (mg g^{-1})	R^2	q_m (mg g^{-1})	a	R^2
Sc	0.072	0.085	0.927	0.040	1.15	0.982
Y						
La	0.771	0.005	0.964			
Ce	0.531	0.007	0.974			
Pr	0.187	0.006	0.959	0.013	1.81	0.991
Nd	0.515	0.008	0.877	0.010	2.60	0.905
Sm	0.335	0.006	0.939	0.010	2.28	0.978
Eu	0.219	0.001	0.946	0.011	2.05	0.991
Gd	0.361	0.005	0.931	0.009	2.35	0.974
Tb	0.157	0.001	0.938	0.013	1.73	0.994
Dy	0.117	-0.001	0.945	0.015	1.55	0.995
Ho	0.073	0.010	0.833	0.021	1.20	0.996
Er	0.075	0.040	0.859	0.030	1.22	0.995
Tm	0.074	0.084	0.877	0.053	1.26	0.992
Yb	0.077	0.105	0.896	0.068	1.35	0.990
Lu	0.079	0.105	0.924	0.072	1.39	0.989

3.5.5 Adsorption Studies on HANC-Si

The fixed-bed column for HANC-Si **11** shows good extraction capabilities for all REE ions except for Gd, displayed in Figure 12 showing an effective way of separating Gd from other REE ions. Back extraction seems to be a challenge and therefore a higher concentration of nitric acid and/or larger quantity of eluate would appear to be necessary to elute all REE ions from the column.

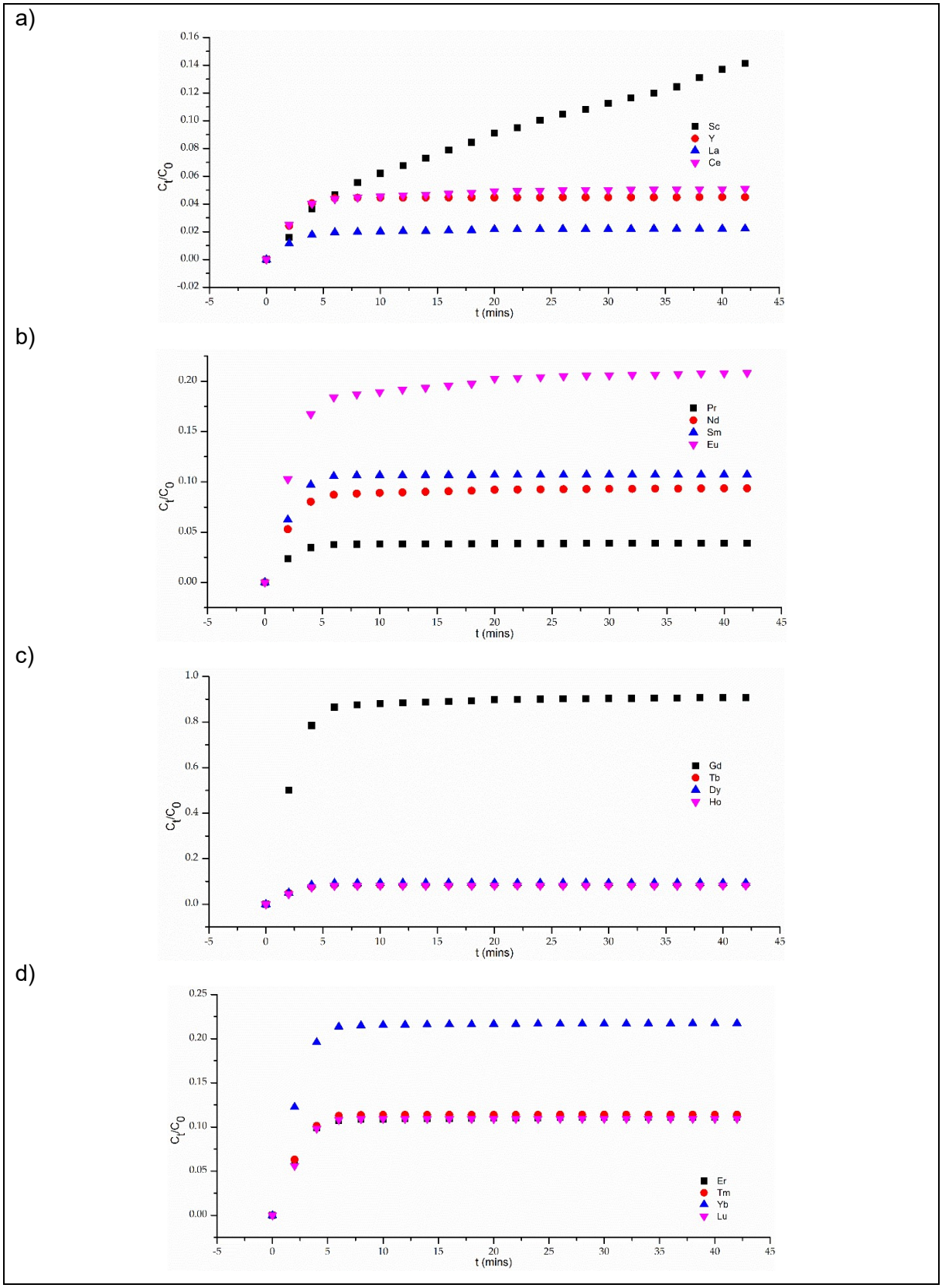

Figure 12. Breakthrough curves for the adsorption of first quarter of the REE series (a), second quarter of the REE series (b), third quarter of the REE series (c) and the last quarter of the REE series (d) rare earth metals by NC-Si flow rate 0.5 mL/min.

HANC-Si **11** shows a very similar trend to ANC-Si **5** where the *q* is the lowest for the mid-range REE ions with a z/r ratio between 2.55 and 2.85 Å (Nd, Sm, Y, Eu and Gd) (Figure 13). The overall adsorption capacity is also very similar with a value of 0.0101 $mg \cdot g^{-1}$ compared to that of ANC-Si **5** which is 0.0106 $mg \cdot g^{-1}$. The percentage of ions left on the column is also very similar to ANC-Si **5** where over 80% of all ions remain on the column after 45 minutes, apart

from Eu, Gd and Yb, even though they have very similar z/r ratios compared to their neighbouring ions.

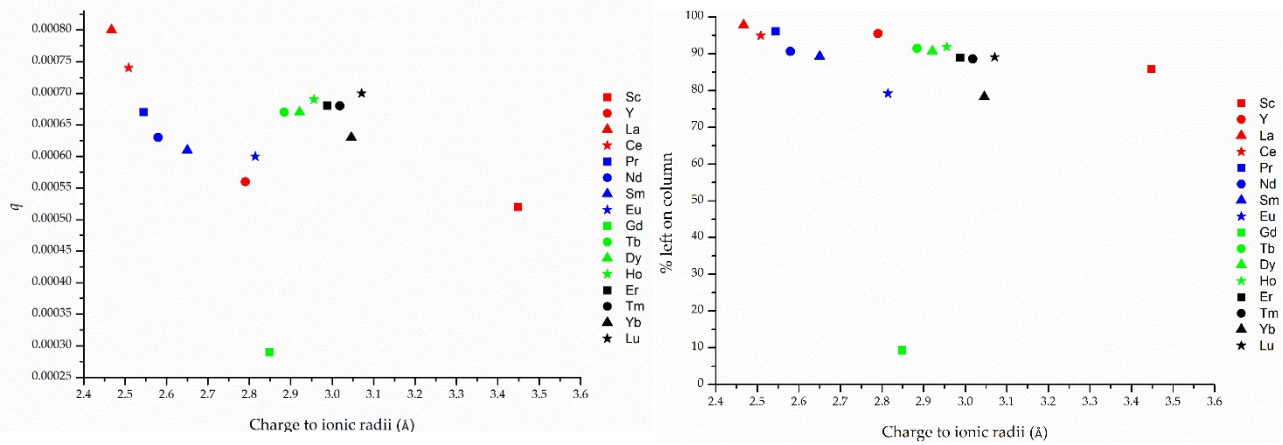

Figure 13. (Left) adsorption capacity (*q*) for REE compared to charge to ionic radii (*z/r*) and (Right) percentage still adsorbed on fixed-bed column of HANC-Si **11**

3.5.6 Adsorption Modelling on HANC-Si

Adsorption modelling was attempted on a fixed-bed column of HANC-Si, however as desorption was not ideal most of the ions could not be described by any of the models (Table 4). As Gd and Sc were able to be eluted from the column they were described by Yoon-Nelson model and Thomas model, respectively. The Yoon-Nelson model was able to give accurate values for τ correlating to figure 12 c).

Table 4. Breakthrough modelling parameters for REE on HANC-Si

REE	***Adams-Bohart***			***Yoon-Nelson***		
	k_{AB} (L mg^{-1} min^{-1})	N_0 (mg L^{-1})	R^2	k_{YN} (min^{-1})	τ (min)	R^2
Sc Y La Ce Pr Nd Sm Eu Gd Tb Dy Ho Er Tm Yb Lu				0.81982	2.38945	0.740
REE	***Thomas***			***Dose-Response***		
	k_{Th} (L mg^{-1} min^{-1})	q_0 (mg g^{-1})	R^2	q_m (mg g^{-1})	a	R^2
Sc Y	0.040	0.398	0.790			

La		
Ce		
Pr		
Nd		
Sm		
Eu		
Gd		
Tb		
Dy		
Ho		
Er		
Tm		
Yb		
Lu		

3.5.7 Adsorption Studies on TBTPhen-Si

Breakthrough studies of TBTPhen-Si **12** doesn't show the classic "S" shaped breakthrough curve. Figure 14 shows that the elution of REE ions is directly proportional to time and therefore volume of the eluate. TBTPhen-Si appears to have a preference for Y and Sc as they take longer to elute from the column compared to the rest of the ions.

a)

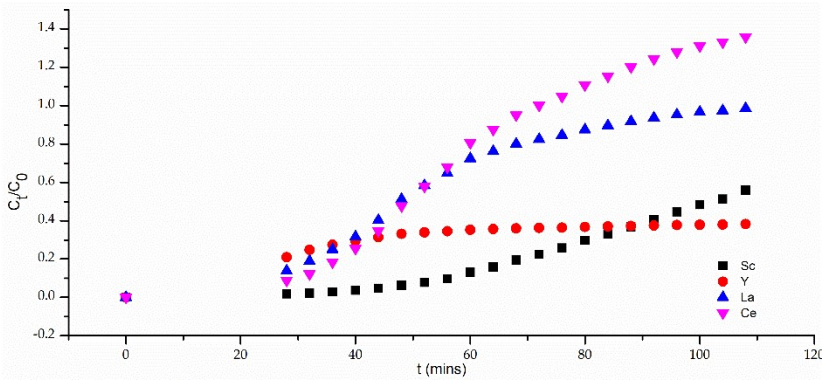

b)

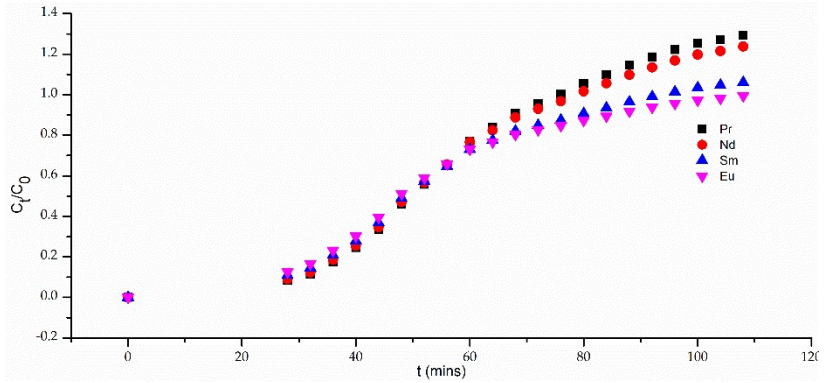

c)

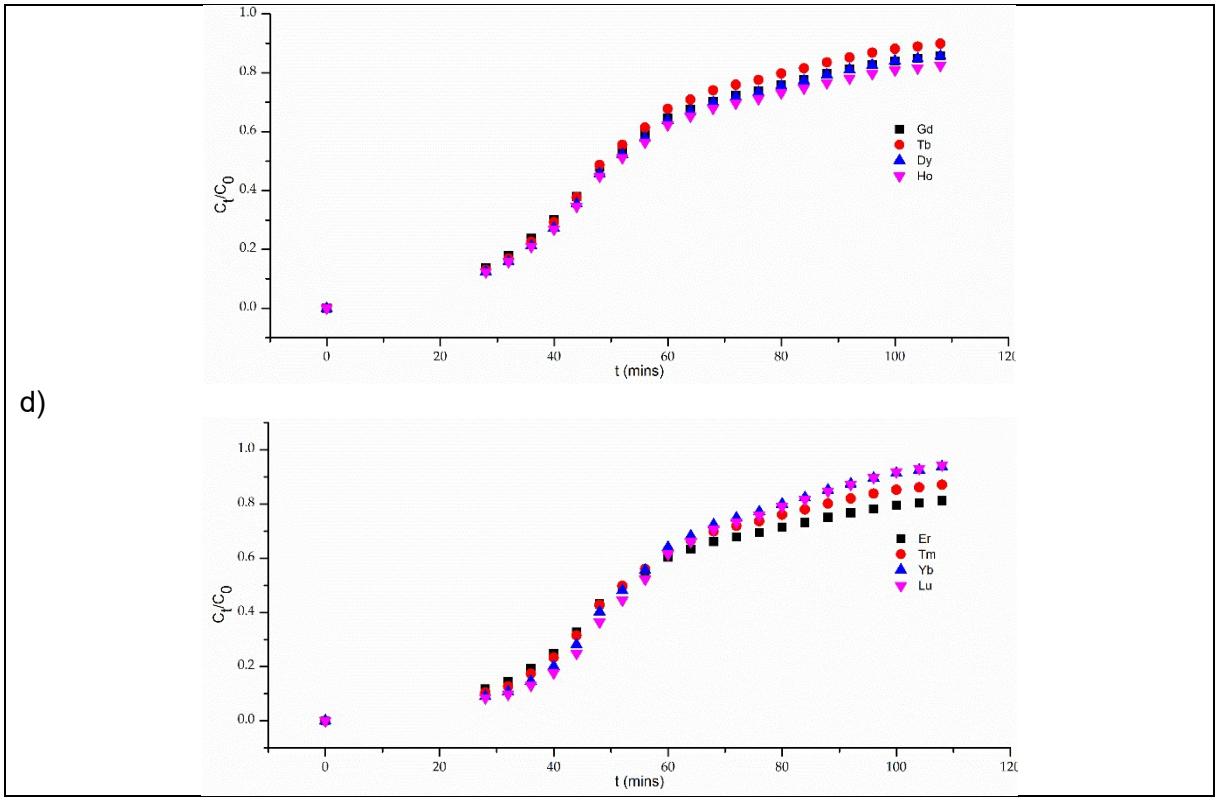

Figure 9. Breakthrough curves for the adsorption of first quarter of the REE series (a), second quarter of the REE series (b), third quarter of the REE series (c) and the last quarter of the REE series (d) rare earth metals by NC-Si flow rate 0.5 mL/min.

Overall, TBTPhen-Si **12** has a preference for the larger REE ions as there is an overall decrease in *q* as the z/r increases (Figure 14). However, as the z/r ratio increases above 3.1 Å, there is an increase in the *q* with a strong preference for Sc even though it has the largest z/r and therefore the smallest radius. Again, Gd does not follow the overall trend and is the least preferred ion as it has the lowest *q*. The larger REE ions are able to be completely desorbed from the column; whereas the mid to smaller ions are still present on the column after elution. Over 40% of Sc and Y remain on the column showing an effective way to separate Sc and Y from the rest of the REE ions.

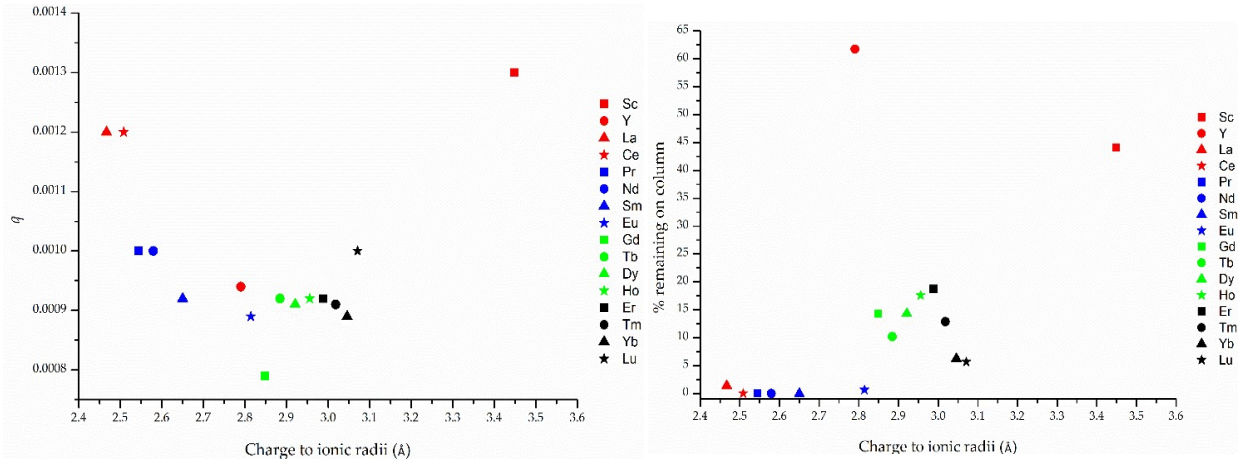

Figure 14. (Left) adsorption capacity (*q*) for REE compared to charge to ionic radii (*z/r*) and (Right) percentage still adsorbed on fixed-bed column of TBTPhen-Si after 45 minutes

3.5.8 Adsorption Modelling on TBTPhen-Si

Model fitting was carried out on a fixed-bed column of TBTPhen-Si using equations (S2), (S3), (S6) and (S7). The Yoon-Nelson model was not able to describe the adsorption mechanism of

any of the REE ions on the column of TBTPhen-Si (Table 5). The linear fitting of Adams-Bohart and Thomas was able to describe all of the ions, with high R^2 coefficients obtained for the Thomas model compared to the Adam-Bohart model. Non-linear fitting of MDR was only able to describe La to Lu, but not Sc and Y. Ce had the highest constant out of every ion showing that it had the most optimum adsorption mechanism out of the REE ions.

Table 5. Breakthrough modelling parameters for REE on TBTPhen-Si

REE	***Adams-Bohart***			***Yoon-Nelson***		
	k_{AB} (L mg^{-1} min^{-1})	N_0 (mg L^{-1})	R^2	k_{YN} (min^{-1})	τ (min)	R^2
Sc	83.7	0.0047	0.957			
Y	9.4	0.0122	0.682			
La	25.6	0.0059	0.763			
Ce	39.8	0.0049	0.799			
Pr	44.2	0.0045	0.796			
Nd	43.3	0.0044	0.789			
Sm	37.3	0.0046	0.766			
Eu	32.8	0.0048	0.747			
Gd	33.5	0.0045	0.752			
Tb	28.8	0.0054	0.745			
Dy	29.5	0.0055	0.752			
Ho	28.0	0.0058	0.749			
Er	29.1	0.0058	0.754			
Tm	32.0	0.0056	0.755			
Yb	36.9	0.0054	0.770			
Lu	38.0	0.0055	0.790			
REE	***Thomas***			***Dose-Response***		
	k_{Th} (L mg^{-1} min^{-1})	q_0 (mg g^{-1})	R^2	q_m (mg g^{-1})	a	R^2
Sc	0.054	0.049	0.985			
Y	0.008	0.077	0.711			
La	0.069	0.025	0.988	0.0001	0.07	0.998
Ce	0.126	0.024	0.986	0.0008	2.25	0.854
Pr	0.120	0.025	0.992	0.0006	1.63	0.896
Nd	0.115	0.025	0.995	0.0005	1.15	0.927
Sm	0.091	0.025	0.974	0.0002	0.23	0.990
Eu	0.075	0.025	0.975	0.0001	0.09	0.998
Gd	0.043	0.028	0.913	0.0002	0.09	0.991
Tb	0.049	0.027	0.927	0.0002	0.10	0.993
Dy	0.045	0.029	0.911	0.0002	0.10	0.989
Ho	0.042	0.030	0.893	0.0003	0.11	0.984
Er	0.042	0.031	0.892	0.0003	0.11	0.983
Tm	0.049	0.030	0.917	0.0002	0.11	0.990
Yb	0.061	0.029	0.959	0.0001	0.10	0.996
Lu	0.064	0.030	0.969	0.0001	0.10	0.996

4 DISCUSSION

4.1 Comparison between ANC-Si, BNC-Si, HANC-Si, TBTPhen, NS-Si and BTPhen-Si

Comparing adsorbents will help determine which material is best to use in an industrial setting. Many factors are involved in deciding which adsorbent is favourable including; adsorption capacity, ability to partition REEs, cost and environmental factors. The ligands; NC-Si **4** and BTPhen-Si **6** have been previously studied and their adsorption capacities measured using very similar experiments. Based on the breakthrough times (t_b) BTPhen-Si **6** could separate the REEs into two groups; mid REE ions (Pr-Eu) (>3 mins) and late REE ions (Gd-Lu) (<1.5 mins), however Sc and Ce elute with the mid REE ions, and Y and La would elute with the late REEs. NC-Si **4** is able to separate REEs into three groups; early, mid and late REEs. The adsorption capacity provides a quantitative way of comparing which is the most efficient adsorbent for REE uptake. NC-Si **4** and BTPhen-Si **6** had the highest overall adsorption capacities; 0.0153 and 0.0484 mg g^{-1}, respectively, with REEs with BNC-Si **10** the least; 0.00484 mg g^{-1} (Figure 16). The *q* for BTPhen-Si **6** shows a four-fold increase in adsorption capability compared to the other materials studied; NC-Si **4**, ANC-Si **5**, BNC-Si **10**, HANC-Si **11** and TBTPhen-Si **12** (Table 6). Out of all materials NC-Si **4** has the best partitioning capability and it proved possible to elute fractions of individual REEs. ANC-Si **5** and HANC-Si **11** had very similar extraction properties with a preference for the later REE and Ce and La; however both systems had poor desorption. BNC-Si **10** had a good partitioning potential as it preferred the later REEs (Tb-Lu and Sc) and eluted the later REEs last and had a preference for Y and Sc.

Interestingly, even though ANC-Si and NC-Si have very similar structures, only differing with their connecting groups to silica (ether and amide, respectively), their adsorption capacities and adsorption mechanisms vary significantly. With electronics playing a part in adsorption, we see the NC-Si more accustomed to the adsorption of REE ions due to the more electron donating effects on the ether linkage, compared to the electron withdrawing amide linkage on ANC-Si.

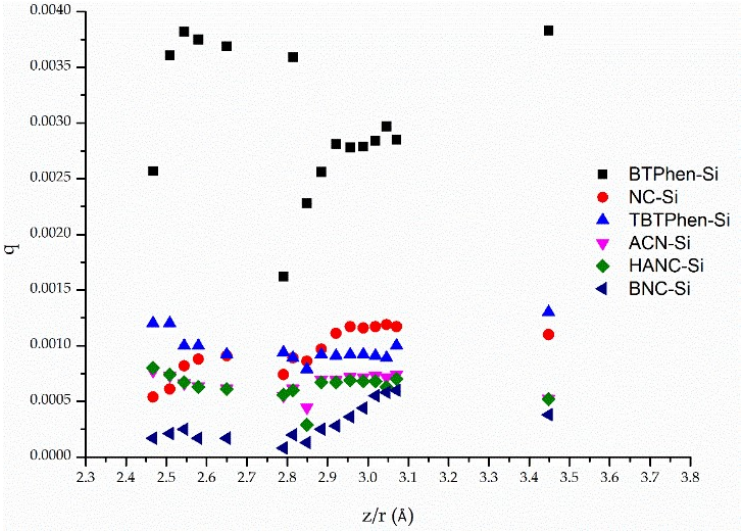

Figure 16. Comparison of *q* for each REE (given as z/r) for each absorbent (ANC-Si **5**, BNC-Si **10**, HANC-Si **11**, TBTPhen **12**, BTPhen-Si **6** and NC-Si **4**)

Table 6 shows the adsorption capacities for every REE in order of charge to ionic radius ratio. Both ANC-Si and HANC-Si had the highest adsorption capacity for La whereas NC-Si had La as the least preferred ion. BNC-Si and TBTPhen-Si had the lowest *q* value for Y; whereas ANC-Si, HANC-Si and TBTPhen-Si had the lowest *q* value for Gd.

Table 6. Adsorption capacities (*q)* for every REE in order of charge to ionic radius ratio for ANC-Si, BNC-Si, HANC-Si, TBTPhen-Si, NC-Si and BTPhen-Si

		Adsorption Capacity, *q*, (units per g)					
REE	**z/r (Å)**	**ANC-Si**	**BNC-Si**	**HANC-Si**	**TBTPhen-Si**	**NC-Si**	**BTPhen-Si**
La	2.46711	0.00077	0.00017	0.0008	0.0012	0.00054	0.00257
Ce	2.50836	0.00073	0.00021	0.00074	0.0012	0.00061	0.00361
Pr	2.54453	0.00066	0.00025	0.00067	0.001	0.00082	0.00382
Nd	2.57954	0.00063	0.00017	0.00063	0.001	0.00088	0.00375
Sm	2.65018	0.00062	0.00017	0.00061	0.00092	0.00091	0.00369
Y	2.7907	0.00055	0.00008	0.00056	0.00094	0.00074	0.00162
Eu	2.81426	0.00062	0.0002	0.0006	0.00089	0.00089	0.00359
Gd	2.849	0.00045	0.00013	0.00029	0.00079	0.00086	0.00228
Tb	2.88462	0.00069	0.00025	0.00067	0.00092	0.00097	0.00256
Dy	2.92113	0.00069	0.00028	0.00067	0.00091	0.00111	0.00281
Ho	2.95567	0.00072	0.00036	0.00069	0.00092	0.00117	0.00278
Er	2.98805	0.00072	0.00044	0.00068	0.00092	0.00116	0.00279
Tm	3.01811	0.00073	0.00055	0.00068	0.00091	0.00117	0.00284
Yb	3.04569	0.00072	0.00058	0.00063	0.00089	0.00119	0.00297
Lu	3.07062	0.00074	0.0006	0.0007	0.001	0.00117	0.00285
Sc	3.44828	0.00052	0.00038	0.00052	0.0013	0.0011	0.00383
Total *q*		**0.0106**	**0.00484**	**0.0101**	**0.0157**	**0.0153**	**0.0484**

4.2 Adsorption modelling

Modelling of breakthrough data provides an effective tool to allow comparison of fixed-bed columns. Allowing a way of quantifying the breakthrough in a universal way that describes the mechanisms involved in the processes. Using the data gathered from these models such as adsorbent capacities, rates and breakthrough times the comparison and optimization can be carried out. All successful fittings are provided in supplementary information.

4.2.1 Adsorption modelling of ANC-Si

Overall, only the Adams-Bohart and Thomas models were able to describe the adsorption processes of all REE ions onto ANC-Si (Table 2). Both models explain the adsorption process of a fixed-bed column of ANC-Si as a two-step process, the first step is an initial rapid adsorption step and the second a much slower step as adsorption reaches saturation point. MDR and Yoon-Nelson models describe adsorption as a single step mechanism which was only true for Gd. Gd had the highest R^2 coefficient for Yoon-Nelson and MDR models and therefore it's adsorption can be thought of as a single step process under isothermal conditions. Gd also had the lowest adsorption capacity out of all REE ions, therefore showing insufficient orbital overlap with the *N* donor atoms on ANC-Si and therefore exhumed from the column straight away.

4.2.2 Adsorption modelling of BNC-Si

The Adams-Bohart model assumes the rate of adsorption is proportional to the concentration of the adsorbing species. None of the REE ions were able to be fit to the Adams-Bohart model, therefore implying other factors are affecting this adsorption process for it to not apply to this system with BNC-Si (Table 3).

Across the REE series the Yoon-Nelson constant (K_{YN}) and Thomas constant (K_{Th}) both decrease, indicating a slower breakthrough of adsorbate and an increase in time it takes to reach maximum adsorption capacity. This slow breakthrough relates to a lower adsorption capacity and/or a slower mass transfer rate. Comparison with experimental data in Table 6 shows that *q* increases across the series, indicating that the slow breakthrough times are related to a slow mass transfer rate for the later REEs and not a low *q*. These lower constants for the later REE ions show that performance is limited, and optimization of the conditions are required to produce a more effective adsorption.

The Thomas model and the MDR models both complement each other both showing that the q_0 and q_m increase across the series, which is confirmed with the experimental data in Table 6.

Y did not manage to meet stereotypical adsorption mechanisms dictated by the four models and therefore other factors are changing the way that Y is adsorbed and desorbed. Y also shows to have the lowest *q* value according to Table 6 showing orbital overlap with BNC-Si is insufficient. Y has similar z/r ratios to Sm and Eu and therefore size is not a factor of the adsorption efficiency in this instance.

4.2.3 Adsorption modelling of HANC-Si

The ability of HANC-Si to adsorb REEs did not comply with any of the models, except for a few exceptions (Table 4). Most ions could not be desorbed from the column, except for Gd and Sc, with the adsorption of Gd being able to be fit to Yoon-Nelson and Sc being able to fit to Thomas model. Both Sc and Gd have similar z/r ratios to other members of the REE series however both carry just one unpaired *d* electron which may lead to some interference with binding to the ligand.

4.2.4 Adsorption modelling of TBTPhen-Si

The Adams-Bohart and Thomas models were both able to effectively describe the adsorption mechanism for the adsorption of all REE ions onto TBTPhen-Si (Table 5). The Thomas model has a higher R_2 value than the Adams-Bohart model, showing the system has a constant flow with no axial dispersion [46]. Out of all the models tested, the MDR model has the highest average R^2 coefficients, describing all ions except for Sc and Y. This model minimizes the error caused by the Thomas model and assumes that adsorption is a function of the concentration of the adsorbate in the bulk fluid phase. Both Sc and Y are not as efficiently extracted compared to the rest of the REE ions, possibly due to the lack of 4*f* orbitals.

4.2 Cost Comparison

Cost is a very important factor when scaling up for use in an industrial situation. A balance has to be made to determine whether the use of expensive materials is worth the value of the outcomes. REEs are a finite resource and are invaluable in today's modern climate. If the adsorbent material can be recycled and used with little to no effect on the performance then the implementation of that material is worth the synthetic effort in the long run for the recovery of REEs. Table 7 shows the cost of synthesizing 1 kg of material with and without the use of chloroform in the synthetic route. If the chloroform can be recycled, purified and re-used, then costs could be significantly lowered. The synthesis of BTPhen-Si and TBTPhen-Si consists of a 13-step synthetic route and an 8-step synthesis, respectively; whereas the synthesis of ANC-Si **5**, BNC-Si **10** and NC-Si **4** consist of 3 steps and HANC-Si **11** just 2 steps. Fewer steps lower the cost of synthesis dramatically (The prices of reagents have been obtained from catalogues of Sigma Aldrich, Fisher Scientific and Tokyo Chemical Industry in Jan 2023 [47–49]).

Table 7. Comparison between ANC-Si **5**, BNC-Si **10**, HANC-Si **11**, TBTPhen-Si **12**, BTPhen-Si **6** and NC-Si **4**. *Not possible to obtain data.

Characteristic	ANC-Si	BNC-Si	HANC-Si	TBTPhen -Si	BTPhen-Si	NC-Si
1 g of neocuproine to yield (g)	2.7	0.76	3	2.97	0.15	3.84
Cost per kg (with $CHCl_3$) (£)	60,013.4	271,936	52,610.5	35,624.1	858,081.8	30,613.4
Cost per kg (without $CHCl_3$) (£)	35,649.7	39,051.1	9,180.8	26,548.7	632,042.2	15,523.1
Number of Synthetic Steps	3	3	2	8	13	3
Overall adsorption capacity (mg g^{-1})	0.0106	0.00484	0.0101	0.0157	0.0484	0.0153
Lowest adsorption capacity (mg g^{-1})	Gd	Y	Gd	Gd	La	Y
Highest adsorption capacity (mg g^{-1})	La	Lu	La	Sc	Yb	Sc
% of ions extracted from inlet (%)	96	79	93	89	76	80
Percentage immobilisation (%)	*	80	*	98	90	57
w/w % of ligand weight (%)	5.5	14	4	7	6	5
Models able to describe adsorption	AB, T	YN, T, MDR	n/a	AB, T, MDR	All	All
Model with highest average R^2	AB, T	MDR	n/a	MDR	YN	YN
Molarity per g of adsorbent (mmol g^{-1})	0.1495	0.3815	0.1429	0.0939	0.0868	0.1466
Metal:ligand molar ratio	1:1963	1:10974	1:1969	1:832	1:250	1:1334

5. CONCLUSIONS

In this study, the adsorbents; ANC-Si **15**, BNC-Si **18**, HANC-Si **19** and TBTPhen **20** were synthesized to evaluate the adsorption effectiveness of REE (III) ions in fixed-bed column studies. Infrared spectroscopy, TGA, EDX and SEM analyses confirmed the successful modification of silica surface with **15, 18, 19** and **20**. The adsorption and desorption performance of REE ions were determined using fixed-bed column systems. Fitting of the mathematical models; Adams-Bohart, Yoon-Nelson, Thomas and MDR to the breakthrough curves found the most effective way to describe the adsorption process of ions onto each of the ligand systems. Adams-Bohart and Thomas described **15** and MDR described both **18** and **20** with the highest average R^2 values. **19** had poor desorption performance and was only able to elute Sc and Gd in a way that could be described as Thomas and Yoon-Nelson, respectively.

The adsorption effectiveness of ANC-Si, BNC-Si, HANC-Si and TBTPhen-Si for the uptake of REEs were compared to NC-Si and BTPhen-Si to determine the most suitable adsorbent for the partitioning of REE ions. All six adsorbents have adsorption capacities (q) above 0.00484 mg g^{-1} with BTPhen-Si having the highest q at 0.0484 mg g^{-1}. NC-Si shows the greatest potential to partition REE as it has a preference for the later REE ions, therefore eluting them last. The performance of these columns will require further experiments to optimize conditions, such as pH, temperature, percentage immobilisation and concentration. As well as reusability of the column.

5. REFERENCES

1. European Commission *Tackling the Challenges in Commodity Markets and on Raw Materials*; Brussels, 2012;
2. Binnemans, K.; Jones, P.T.; Blanpain, B.; Van Gerven, T.; Yang, Y.; Walton, A.; Buchert, M. Recycling of Rare Earths: A Critical Review. *J. Clean. Prod.* **2013**, *51*, 1–22, doi:10.1016/j.jclepro.2012.12.037.
3. Klinger, J.M. Rare Earth Elements: Development, Sustainability and Policy Issues. *Extr. Ind. Soc.* **2018**, *5*, 1–7, doi:10.1016/j.exis.2017.12.016.
4. Rudnick, R.L.; Gao, S. Rudnick_Gao_Treatise. *Treatise on geochemistry* **2003**, *3*, 1–64.
5. *Mineral Commodity Summaries 2021*; Reston, VA, 2021;
6. Xu, L.; Guo, G.; Uy, D.; O'Neill, A.E.; Weber, W.H.; Rokosz, M.J.; McCabe, R.W. Cerium Phosphate in Automotive Exhaust Catalyst Poisoning. *Appl. Catal. B Environ.* **2004**, *50*, 113–125, doi:10.1016/j.apcatb.2004.01.017.
7. Fujita, Y.; McCall, S.K.; Ginosar, D. Recycling Rare Earths: Perspectives and Recent Advances. *MRS Bull.* **2022**, *47*, 283–288, doi:10.1557/s43577-022-00301-w.
8. Kingsnorth, D. Meeting the Challenges of Supply This Decade. *Present. to Environ. Energy Study …* **2011**.
9. Humphries, M. Rare Earth Elements: The Global Supply Chain. *Rare Earth Miner. Policies Issues* **2011**, 1–20.
10. European Commission Methodology for Establishing the EU List of Critical Raw Materials. *Publ. Off. Eur. Union* **2017**, 1–25, doi:10.2873/769526.
11. Rabe, W.; Kostka, G.; Smith Stegen, K. China's Supply of Critical Raw Materials: Risks for Europe's Solar and Wind Industries? *Energy Policy* **2017**, *101*, 692–699, doi:10.1016/j.enpol.2016.09.019.
12. Kumari, A.; Sinha, M.K.; Pramanik, S.; Sahu, S.K. Recovery of Rare Earths from Spent NdFeB Magnets of Wind Turbine: Leaching and Kinetic Aspects. *Waste Manag.* **2018**, *75*, 486–498, doi:10.1016/j.wasman.2018.01.033.
13. Pietrantonio, M.; Pucciarmati, S.; Sebastianelli, L.; Forte, F.; Fontana, D. Materials Recovery from End-of-Life Wind Turbine Magnets. *Int. J. Environ. Sci. Technol.* **2022**, *19*, 8019–8026, doi:10.1007/s13762-021-03546-1.
14. Nash, K.L.; Jensen, M.P. Analytical-Scale Separations Of The Lanthanides: A Review Of Techniques And Fundamentals. *Sep. Sci. Technol.* **1999**, *36*, 1257–1282.
15. Cotton, S. Lanthanide and Actinide Chemistry. *Lanthan. Actin. Chem.* 2006, 1–263.
16. Choppin, G.R. Comparative Solution Chemistry of the 4f and 5f Elements. *J. Alloy. Compd.* **1995**, *223*, 174–179, doi:10.1016/0925-8388(94)09002-5.
17. Cotton, S.A.; Raithby, P.R. Systematics and Surprises in Lanthanide Coordination Chemistry. *Coord. Chem. Rev.* **2017**, *340*, 220–231, doi:10.1016/j.ccr.2017.01.011.
18. Talens Peiró, L.; Villalba Méndez, G. Material and Energy Requirement for Rare Earth Production. *Jom* **2013**, *65*, 1327–1340, doi:10.1007/s11837-013-0719-8.
19. Chiarizia, R.; Jensen, M.P.; Borkowski, M.; Ferraro, J.R.; Thiyagarajan, P.; Littrell, K.C. Third Phase Formation Revisited: The U(VI), HNO3-TBP, n-Dodecane System. *Solvent Extr. Ion Exch.* **2003**, *21*, 1–27, doi:10.1081/SEI-120017545.
20. Wang, Z.H.; Ma, G.X.; Lu, J.; Liao, W.P.; Li, D.Q. Separation of Heavy Rare Earth Elements with Extraction Resin Containing 1-Hexyl-4-Ethyloctyl Isopropylphosphonic Acid. *Hydrometallurgy* **2002**, *66*, 95–99, doi:10.1016/S0304-386X(02)00109-3.
21. Suzuki, T.; Itoh, K.; Ikeda, A.; Aida, M.; Ozawa, M.; Fujii, Y. Separation of Rare Earth Elements by Tertiary Pyridine Type Resin. *J. Alloys Compd.* **2006**, *408–412*, 1013–

1016, doi:10.1016/j.jallcom.2004.12.130.

22. Hart, F.A.; Laming, F.P. Complexes of 1,10-Phenanthroline with Lanthanide Chlorides and Thiocyanates. *J. Inorg. Nucl. Chem.* **1964**, *26*, 579–585, doi:10.1016/0022-1902(64)80291-8.

23. Ogden, M.D.; Hoch, C.L.; Sinkov, S.I.; Meier, G.P.; Lumetta, G.J.; Nash, K.L. Complexation Studies of Bidentate Heterocyclic N-Donor Ligands with Nd(III) and Am(III). *J. Solution Chem.* **2011**, *40*, 1874–1888, doi:10.1007/s10953-011-9762-7.

24. Simonzadeh, N.; Schilt, A.A. Chelation Properties of Silica-Bound 1,10-Phenanthroline. *J. Coord. Chem.* **1989**, *20*, 117–120, doi:10.1080/00958978909408856.

25. Lenaerts, P.; Driesen, K.; Van Deun, R.; Binnemans, K. Covalent Coupling of Luminescent Tris(2-Thenoyltrifluoroacetonato) Lanthanide(III) Complexes on a Merrifield Resin. *Chem. Mater.* **2005**, *17*, 2148–2154, doi:10.1021/cm0486868.

26. Frederick Smith, G.; McCurdy, W.H. 2,9-Dimethyl-1,10-Phenanthroline, New Specific in Spectrophotometric Determination of Copper. *Anal. Chem.* **1952**, *24*, 371–373.

27. O'Reilly, E.J.; Plowman, R.A. Coordination Compounds of Substituted 1, 10-Phenanthrolines and Related Dipyridyls: I. Synthesis of 2, 9-Dimethpl-1, 10-Phenanthroline. *Aust. J. Chem.* **1960**, *13*, 145–149, doi:10.1071/CH9600145.

28. Lalia-Kantouri, M.; Gdaniec, M.; Czapik, A.; Chrissafis, K.; Ferenc, W.; Sarzynski, J.; Papadopoulos, C.D. Neocuproine as a Redox-Active Ligand Platform on Iron and Cobalt. *J. Therm. Anal. Calorim.* **2012**, *109*, 131–139, doi:10.1007/s10973-011-1692-5.

29. Jesse, K.A.; Filatov, A.S.; Xie, J.; Anderson, J.S. Neocuproine as a Redox-Active Ligand Platform on Iron and Cobalt. *Inorg. Chem.* **2019**, *58*, 9057–9066, doi:10.1021/acs.inorgchem.9b00531.

30. Geist, A.; Hill, C.; Modolo, G.; Foreman, M.R.S.J.; Weigj, M.; Gompper, K.; Hudson, M.J.; Madic, C. 6,6'-Bis(5,5,8,8-Tetramethyl-5,6, 7,8-Tetrahydro-Benzo[1,2,4)Triazin-3yl)[2,2']Bipyridine, an Effective Extracting Agent for the Separation of Americium(LII) and Curium(III) from the Lanthanides. *Solvent Extr.Ion Exch.* **2006**, *24*, 463–483, doi:10.1080/07366290600761936.

31. Adam, C.; Kaden, P.; Beele, B.B.; Müllich, U.; Trumm, S.; Geist, A.; Panak, P.J.; Denecke, M.A. Evidence for Covalence in a N-Donor Complex of Americium(Iii). *Dalt. Trans.* **2013**, *42*, 14068–14074, doi:10.1039/c3dt50953b.

32. Vitova, T.; Pidchenko, I.; Fellhauer, D.; Bagus, P.S.; Joly, Y.; Pruessmann, T.; Bahl, S.; Gonzalez-Robles, E.; Rothe, J.; Altmaier, M.; et al. The Role of the 5f Valence Orbitals of Early Actinides in Chemical Bonding. *Nat. Commun.* **2017**, *8*, 1–9, doi:10.1038/ncomms16053.

33. Kaltsoyannis, N. Does Covalency Increase or Decrease across the Actinide Series? Implications for Minor Actinide Partitioning. *Inorg. Chem.* **2013**, *52*, 3407–3413, doi:10.1021/ic3006025.

34. Ligand, P.B.; Lewis, F.W.; Harwood, L.M.; Hudson, M.J.; Drew, M.G.B.; Desreux, J.F.; Bouslimani, N.; Modolo, G.; Wilden, A.; Sypula, M.; et al. Highly Efficient Separation of Actinides from Lanthanides by A. **2011**, 13093–13102, doi:10.1021/ja203378m.

35. Choppin, G.R. Covalency in F-Element Bonds. *J. Alloys Compd.* **2002**, *344*, 55–59, doi:10.1016/S0925-8388(02)00305-5.

36. Sigma-Aldrich - 3-Chloropropyl-Functionalized Silica Gel Available online: https://www.sigmaaldrich.com/GB/en/product/aldrich/364266 (accessed on 11 January 2023).

37. Kohler, L.; Hayes, D.; Hong, J.; Carter, T.J.; Shelby, M.L.; Fransted, K.A.; Chen, L.X.; Mulfort, K.L. Synthesis{,} Structure{,} Ultrafast Kinetics{,} and Light-Induced Dynamics of CuHETPHEN Chromophores. *Dalt. Trans.* **2016**, *45*, 9871–9883, doi:10.1039/C6DT00324A.

38. Afsar, A.; Babra, J.S.; Distler, P.; Harwood, L.M.; Hopkins, I.; John, J.; Westwood, J.; Selfe, Z.Y. Extraction Properties of 4-Tetra(Hydroxyphenyl)BTphen in Liquid-Liquid Extraction Systems with Cyclohexanone/Octanol or in a Solid-Phase Extraction System. *Heterocycles* **2020**, *101*, 209–222, doi:10.3987/COM-19-S(F)14.

39. Afsar, A.; Cowell, J.; Distler, P.; Harwood, L.M.; John, J.; Westwood, J. Synthesis of Novel BTPhen-Functionalized Silica-Coated Magnetic Nanoparticles for Separating Trivalent Actinides and Lanthanides. *Synlett* **2017**, doi:10.1055/s-0036-1590865.

40. Costa, T.B. da; Silva, M.G.C. da; Vieira, M.G.A. Recovery of Rare-Earth Metals from Aqueous Solutions by Bio/Adsorption Using Non-Conventional Materials: A Review with Recent Studies and Promising Approaches in Column Applications. *J. Rare Earths* **2020**, *38*, 339–355, doi:10.1016/j.jre.2019.06.001.

41. Lakshmipathy, R.; Sarada, N.C. A Fixed-bed Column Study for the Removal of Pb2+ Ions by Watermelon Rind. *Environ. Sci. Water Res. Technol.* **2015**, *1*, 244–250, doi:10.1039/c4ew00027g.

42. Park, D.; Yun, Y.S.; Park, J.M. The Past, Present, and Future Trends of Biosorption. *Biotechnol. Bioprocess Eng.* **2010**, *15*, 86–102, doi:10.1007/s12257-009-0199-4.

43. Solgi, M.; Tabil, L.G.; Wilson, L.D. Modified Biopolymer Adsorbents for Column Treatment of Sulfate Species in Saline Aquifers. *Materials (Basel).* **2020**, *13*, doi:10.3390/ma13102408.

44. Patel, H. Fixed-Bed Column Adsorption Study: A Comprehensive Review. *Appl. Water Sci.* **2019**, *9*, 1–17, doi:10.1007/s13201-019-0927-7.

45. Dolatyari, L.; Yaftian, M.R.; Rostamnia, S. Fixed-Bed Column Dynamic Studies and Breakthrough Curve Analysis of Eu(III) Ion Adsorption onto Chemically Modified SBA-15 Silica Materials. *Sep. Sci. Technol.* **2017**, *52*, 393–403, doi:10.1080/01496395.2016.1250781.

46. Thomas, H.C. Heterogeneous Ion Exchange in a Flowing System. *J. Am. Chem. Soc.* **1944**, *66*, 1664–1666, doi:10.1021/ja01238a017.

47. Sigma Aldrich Catalogue Available online: https://www.sigmaaldrich.com/GB/en (accessed on 1 February 2023).

48. Fisher Scientific Catalogue Available online: https://www.fishersci.co.uk/gb/en/home.html (accessed on 1 February 2023).

49. TCI Chemicals Catalogue Available online: https://www.tcichemicals.com/GB/en/ (accessed on 1 February 2023).

50. Bohart, G.S.; Adams, E.Q. Some Aspects of the Behavior of Charcoal with Respect to Chlorine. *J. Am. Chem. Soc.* **1920**, *42*, 523–544, doi:10.1021/ja01448a018.

51. Yoon, Y.H.E.E.; Nelson, J.H. Application of Gas Adsorption Kinetics I. A Theoretical Model for Respirator Cartridge Service Life. *Am. Ind. Hyg. Assoc. J.* **1984**, *45*, 509–516, doi:10.1080/15298668491400197.

52. Thomas, H.C. Chromatography: A Problem In Kinetics. *Ann. N. Y. Acad. Sci.* **1948**, *49*, 161–182, doi:https://doi.org/10.1111/j.1749-6632.1948.tb35248.x.

Supplementary Information

SI.1 Characterisation of ANC-Si

SI.1.1. FT-IR analysis of ANC-Si

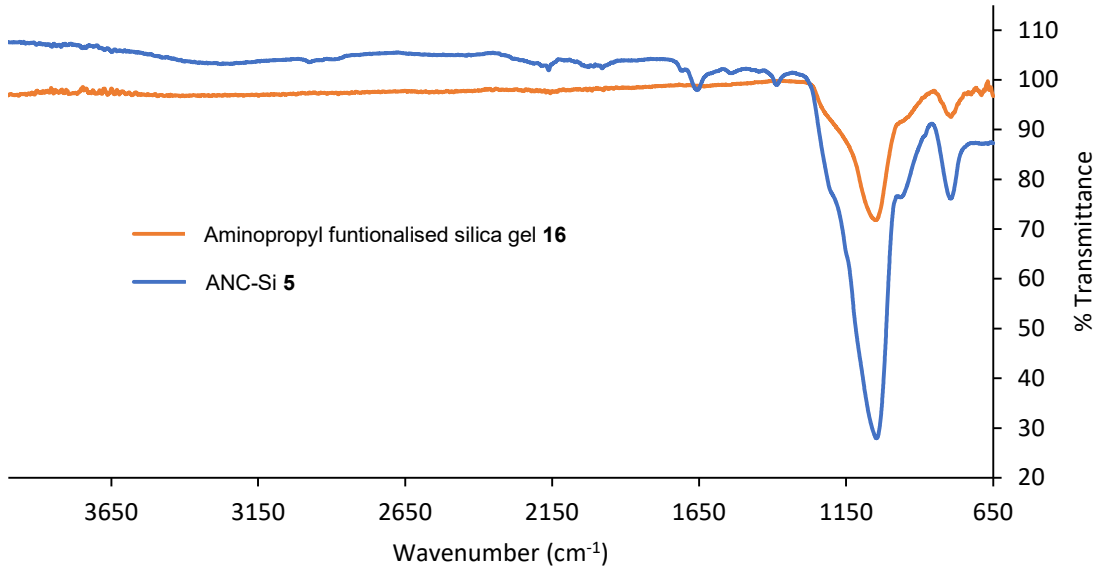

SI Figure 1. FT-IR spectra

SI Table 1. FT-IR assignment

Wavelength (cm^{-1})	Assignment	Reference
1045	Si-O-Si	5, 16
795	Si-O	5, 16
1655	C=O	5
1380	C=C (aromatic)	5

SI.1.2 EDX Analysis of ANC-Si

SI Table 2. EDX analysis of ANC-Si

Element	CP-Si **9**	ANC-Si **5**
Carbon (%)	16.81	22.02
Oxygen (%)	55.33	46.44
Silicon (%)	28.34	28.19
Nitrogen (%)	1.32	2.51

SI 1.3 TGA Analysis of ANC-Si

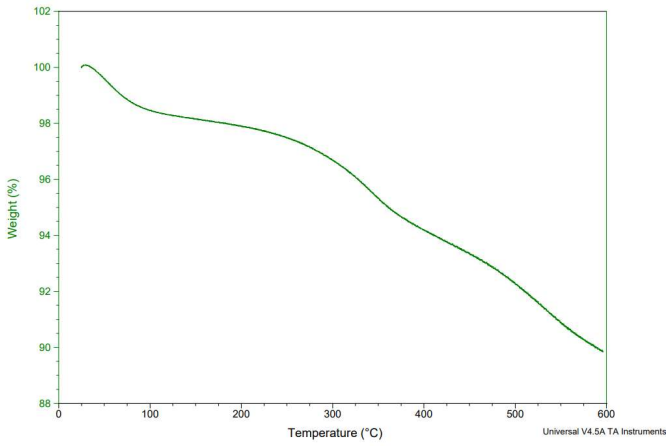

SI Figure 2. TGA analysis of ANC-Si

SI.2 Characterisation of BNC-Si

SI.2.1. FT-IR analysis of BNC-Si

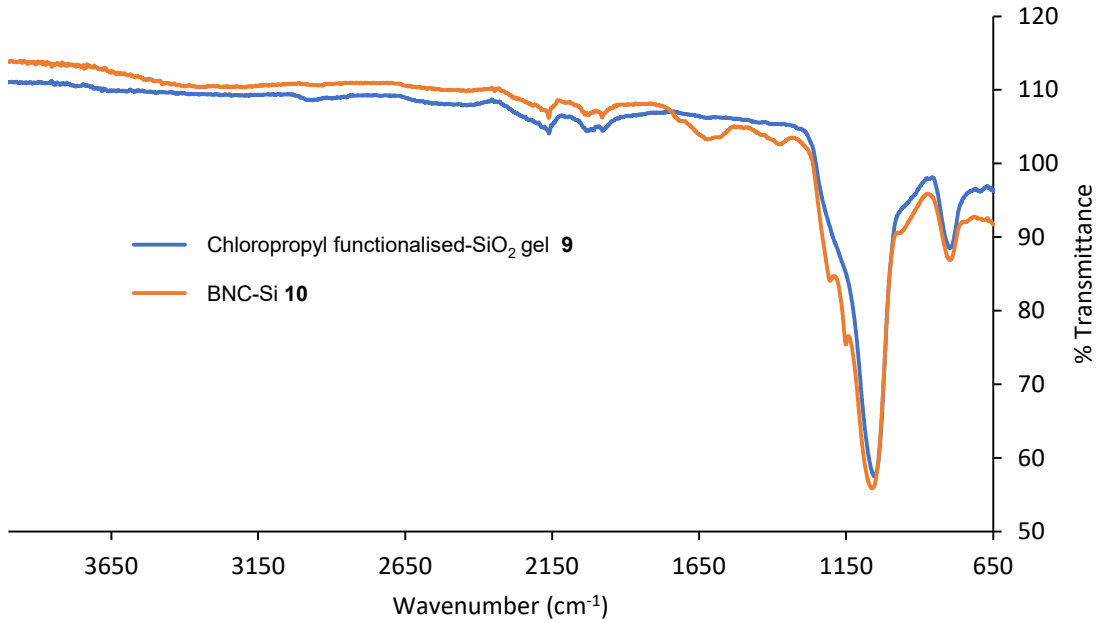

SI Figure 3. FT-IR spectra

SI Table 3. FT-IR assignment

Wavelength (cm^{-1})	Assignment	Reference
1055	Si-O-Si	9, 10
795	Si-O	9, 10
1612	C=C	10
1372	C=H	10

SI.2.2 EDX Analysis of BNC-Si

SI Table 4. EDX analysis of BNC-Si

Element	CP-Si **9**	BNC-Si **10**
Carbon (%)	16.86	39.35
Oxygen (%)	44.11	36.37
Silicon (%)	34.27	16.59
Nitrogen (%)	3.54	5.27
Chlorine (%)	1.04	0.21

SI 2.3 TGA Analysis of BNC-Si

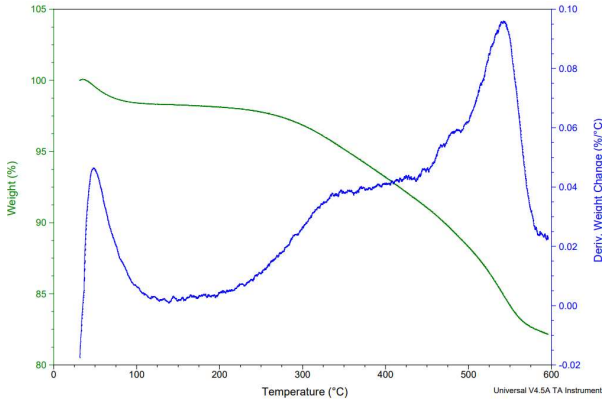

SI Figure 4. TGA analysis of BNC-Si

SI.3 Characterisation of HANC-Si

SI.3.1. FT-IR analysis of HANC-Si

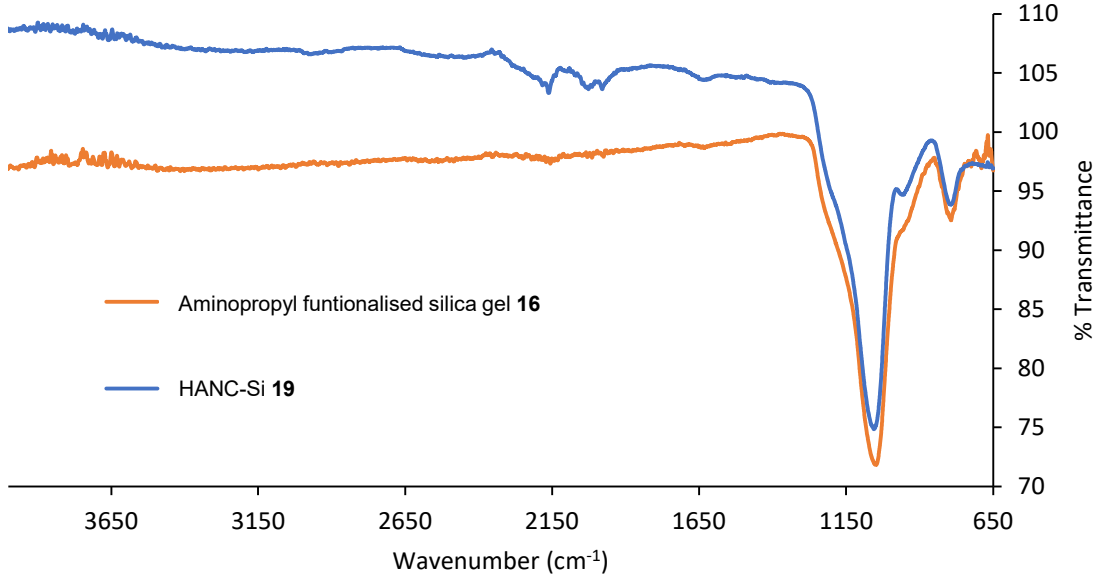

SI Figure 5. FT-IR spectra

SI Table 5. FT-IR assignment

Wavelength (cm^{-1})	Assignment	Reference
1055	Si-O-Si	16, 19
795	Si-O	16, 19
1628	C-H	19

SI.3.2 EDX Analysis of HANC-Si

SI Table 6. EDX analysis of HANC-Si

Element	Aminopropyl SiO_2 **16**	HANC-Si **11**
Carbon (%)	16.81	22.02
Oxygen (%)	55.33	46.44
Silicon (%)	28.34	28.19
Nitrogen (%)	1.32	2.51

SI 3.3 TGA Analysis of HANC-Si

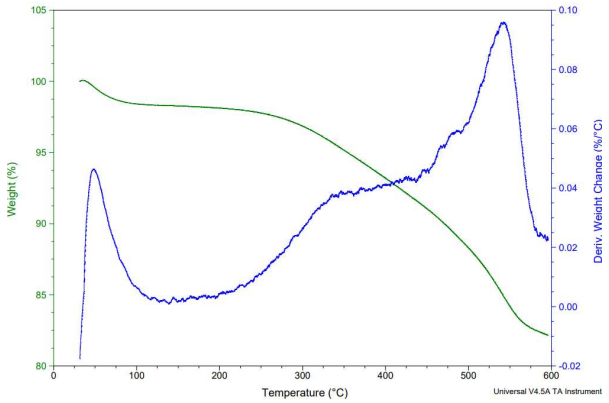

SI Figure 6. TGA analysis of HANC-Si

SI.4 Characterisation of TBTPhen-Si

SI.4.1. FT-IR analysis of TBTPhen-Si

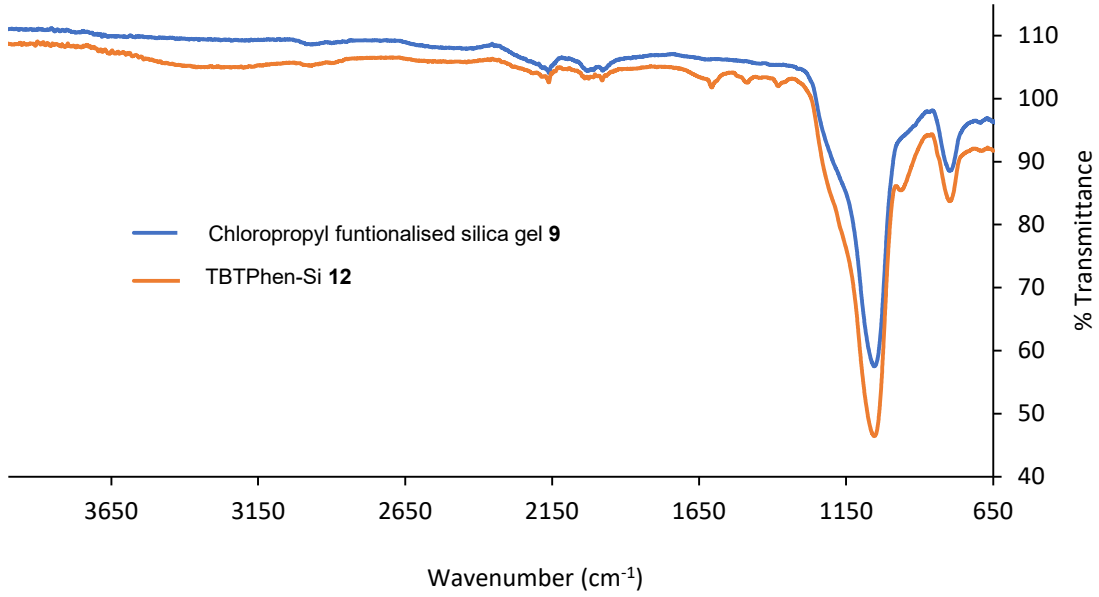

SI Figure 7. FT-IR spectra

SI Table 7. FT-IR assignment

Wavelength (cm^{-1})	Assignment	Reference
1025-1055	Si-O-Si	9, 12
795	Si-O	9, 12
1606	C=C	12
1487	C-C	12
1383	C-H	12

SI.4.2 EDX Analysis of HANC-Si

SI Table 8. EDX analysis of TBTPhen -Si

Element	CP-Si **9**	TBTPhen -Si **12**
Carbon (%)	16.86	53.73
Oxygen (%)	44.11	35.80
Silicon (%)	34.27	10.12
Chlorine (%)	1.04	0.17

SI 4.3 TGA Analysis of TBTPhen -Si

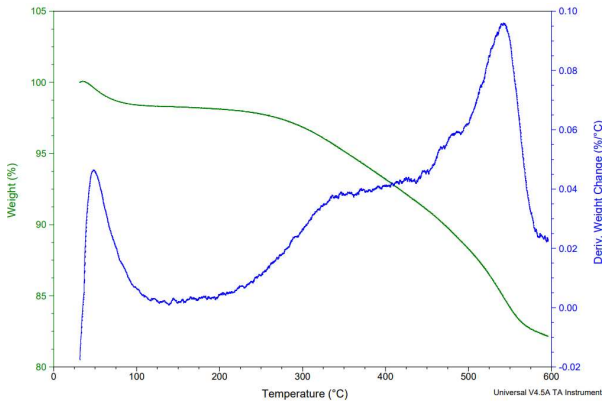

SI Figure 8. TGA analysis of TBTPhen-Si

SI.5 Breakthrough Modelling of REE Column Behaviour of ANC-SI

SI.5.1. Adams-Bohart Model

The Adams-Bohart model is a predictive tool for breakthrough curves assuming that the rate of adsorption is proportional to the concentration of the adsorbing species and the residual capacity of the adsorbent. This model describes the initial part of the process and can assume a two-stage process is taking part [50]. The nonlinear and linear equations are shown in (S1) and (S2), respectively.

$$\frac{C_t}{C_0} = exp(k_{AB}C_0t - k_{AB}q\frac{H}{v}) \quad \text{(S1)}$$

$$\ln\left(\frac{C_t}{C_0}\right) = k_{AB}C_0t - k_{AB}q\frac{H}{v} \quad \text{(S2)}$$

Where C_0 is the initial concentration of REE (III) ions (mg L^{-1}), C_t is the outlet concentration (mg L^{-1}), k_{AB} is the Adams-Bohart rate constant (L mg^{-1} min^{-1}), q is the adsorption capacity (mg L), H is the bed depth of the fixed-bed column (cm), v is the linear velocity calculated by dividing the flow rate by the column sectional area (cm min^{-1}).

a)

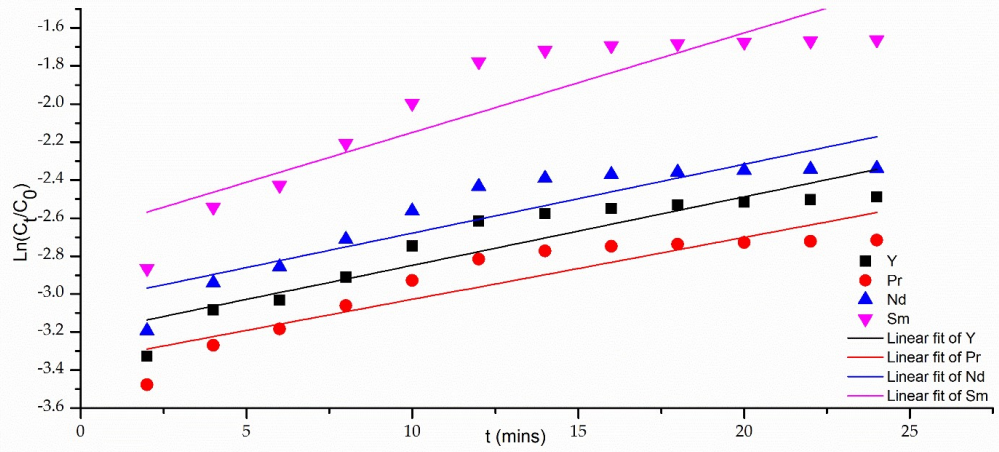

b)

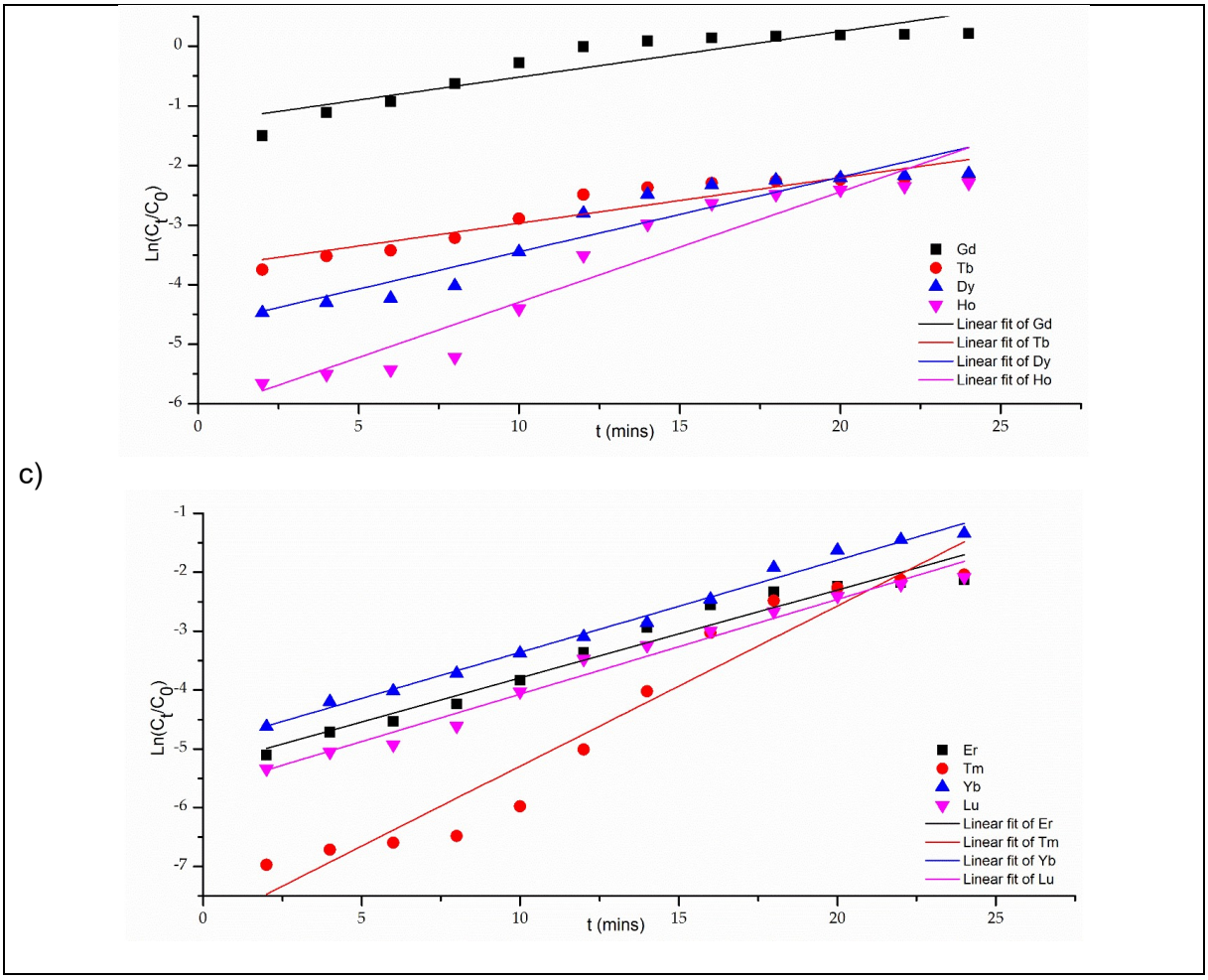

SI Figure 9. Fitting of the Adams-Bohart model to a) Y, Pr-Nd, b) Pr-Eu, c) Gd-Ho and d) Er-Lu

SI.5.2. Yoon-Nelson Model

This model is rather straightforward compared to other models and assumes that the probability of adsorption is proportional to the probability of sorbate sorption and the probability of sorbate breakthrough on the sorbent. No information is required regarding the characteristic of the system, such as the physical properties of the adsorption bed or the type of adsorbent [51]. Equations (S3) and (S4) represent the non-linear and linear forms of the Yoon-Nelson model, respectively. Where k_{YN} is the Yoon-Nelson rate constant (min^{-1}) and τ is the time required for 50% adsorbate breakthrough (min).

$$\frac{C_t}{C_0} = \frac{1}{1+e^{k_{YN}(\tau - t)}} \quad \text{(S3)}$$

$$\ln\left(\frac{C_t}{C_0 - C_t}\right) = k_{YN}t - k_{YN}\tau \quad \text{(S4)}$$

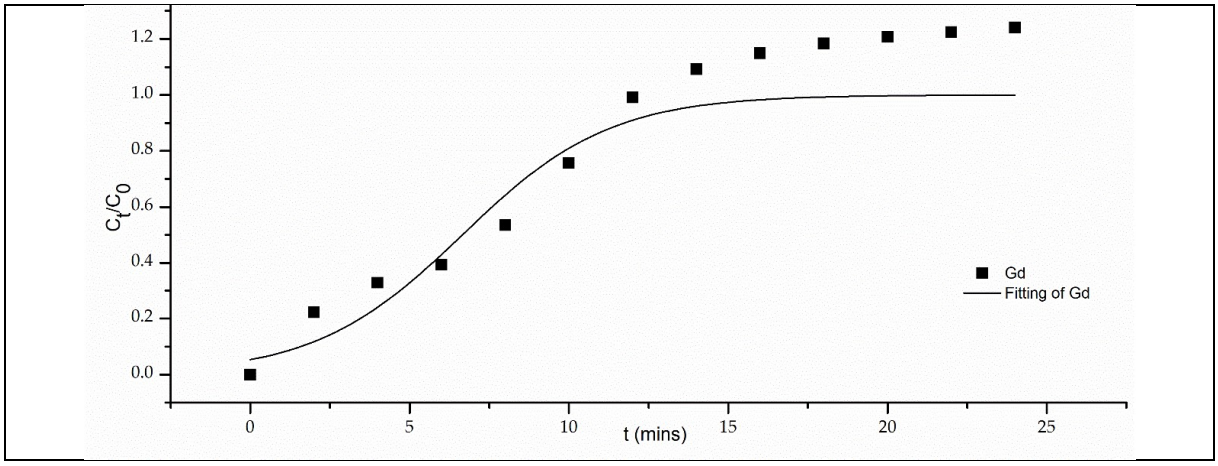

SI Figure 10. Fitting of the Yoon-Nelson model to Gd

SI.5.3. Thomas Model

The Thomas model, much like the Adams-Bohart model, describes the adsorption process in two stages. Both take into account the flow rate and the initial concentration. In addition, the Thomas model also takes into account the bulk fluid phase and is based on the Langmuir isotherm [46]. Equations (S5) and (S6) show the non-linear and linear equations, respectively, where k_{Th} (mL mg^{-1} min^{-1}) is the Thomas model constant and q_0 (mg g^{-1}) is the predicted adsorption capacity, m (g) is the mass of the absorbent, and Q (mL min^{-1}) is the influent flow rate [52].

$$\frac{C_t}{C_0} = \frac{1}{1+\exp\left[\left(\frac{k_{Th}q_0m}{Q}\right)-k_{Th}C_0t\right]} \quad \text{(S5)}$$

$$ln\left(\frac{C_t}{C_0}-1\right) = \left(\frac{k_{Th}q_0m}{Q}\right) - k_{Th}C_0t \quad \text{(S6)}$$

a)

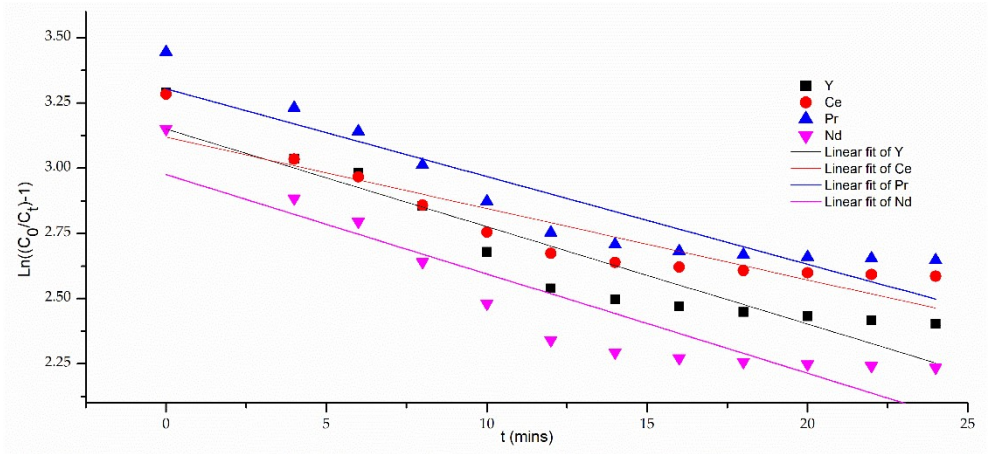

b)

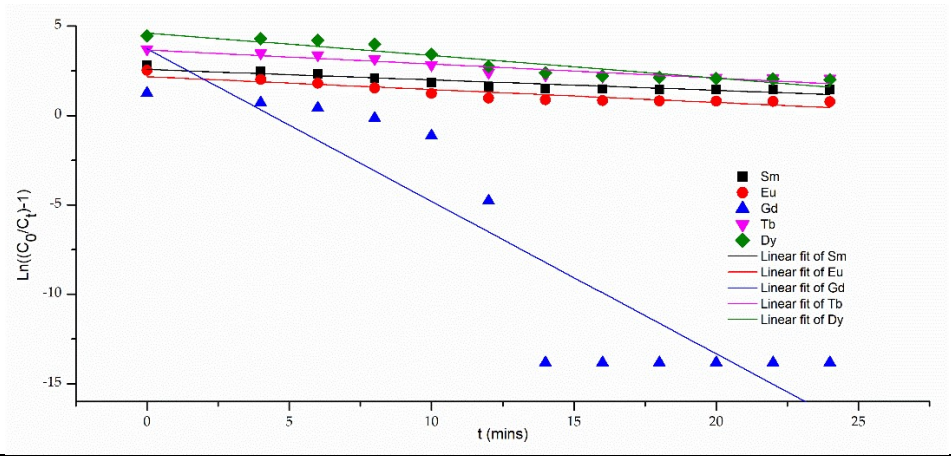

c)

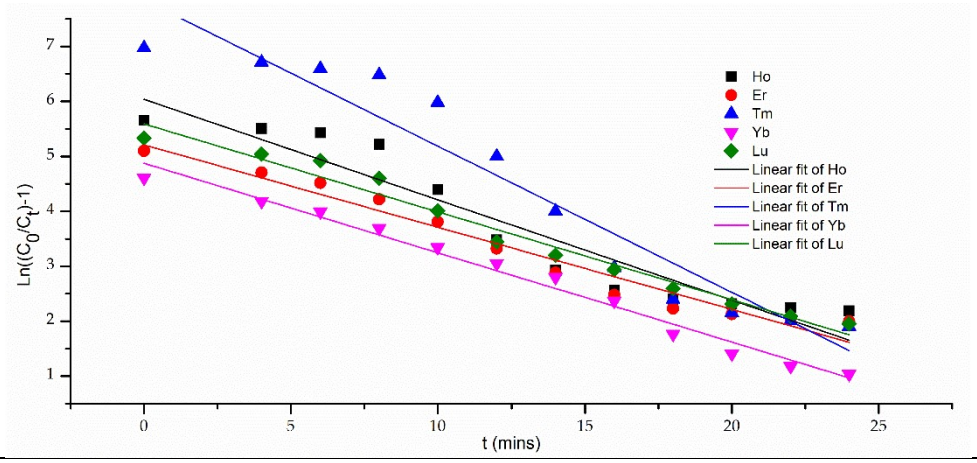

SI Figure 11. Fitting of the Thomas model to a) Y, Ce and Pr-Nd, b) Nd-Gd, b) Sm-Dy and c) Ho-Lu

SI.5.4. MDR Model

The modified dose response model (MDR) is a simplified model to describe the adsorption process of a fixed-bed column. It takes into account the flow rate, initial concentration of the adsorbate and negates any errors that the Thomas equation might produce. The non-linear and linear models can be expressed as equations (S7) and (S8) respectively, where *a* is the MDR constant and q_m is the adsorption capacity (mg L^{-1}).

$$\frac{C_t}{C_o} = 1 - \frac{1}{1+\left(\frac{C_o Q t}{q_m m}\right)^a} \quad \text{(S7)}$$

$$ln\left(\frac{C_t}{C_o - C_t}\right) = aln C_o Q t - alnqm \quad \text{(S8)}$$

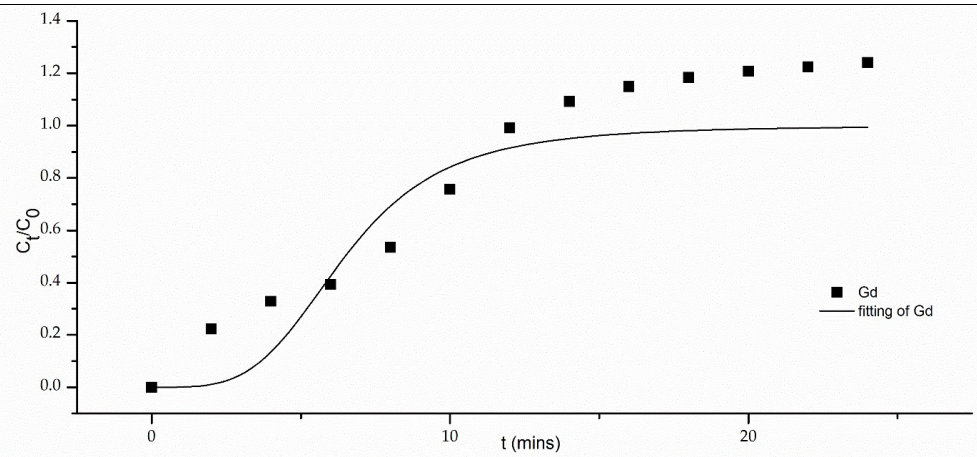

SI Figure 12. Fitting of the MDR model to Gd

SI.6 Breakthrough Modelling of REE Column Behaviour of BNC-SI

SI.6.1. Adams-Bohart Model

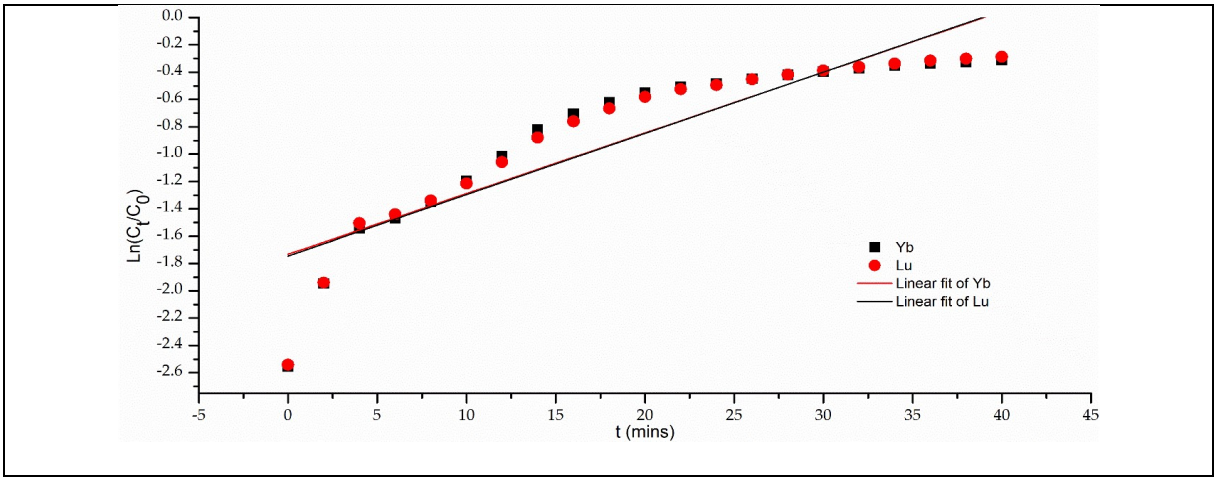

SI Figure 13. Fitting of the Adams-Bohart model to Yb and Lu

SI.6.2. Yoon-Nelson Model

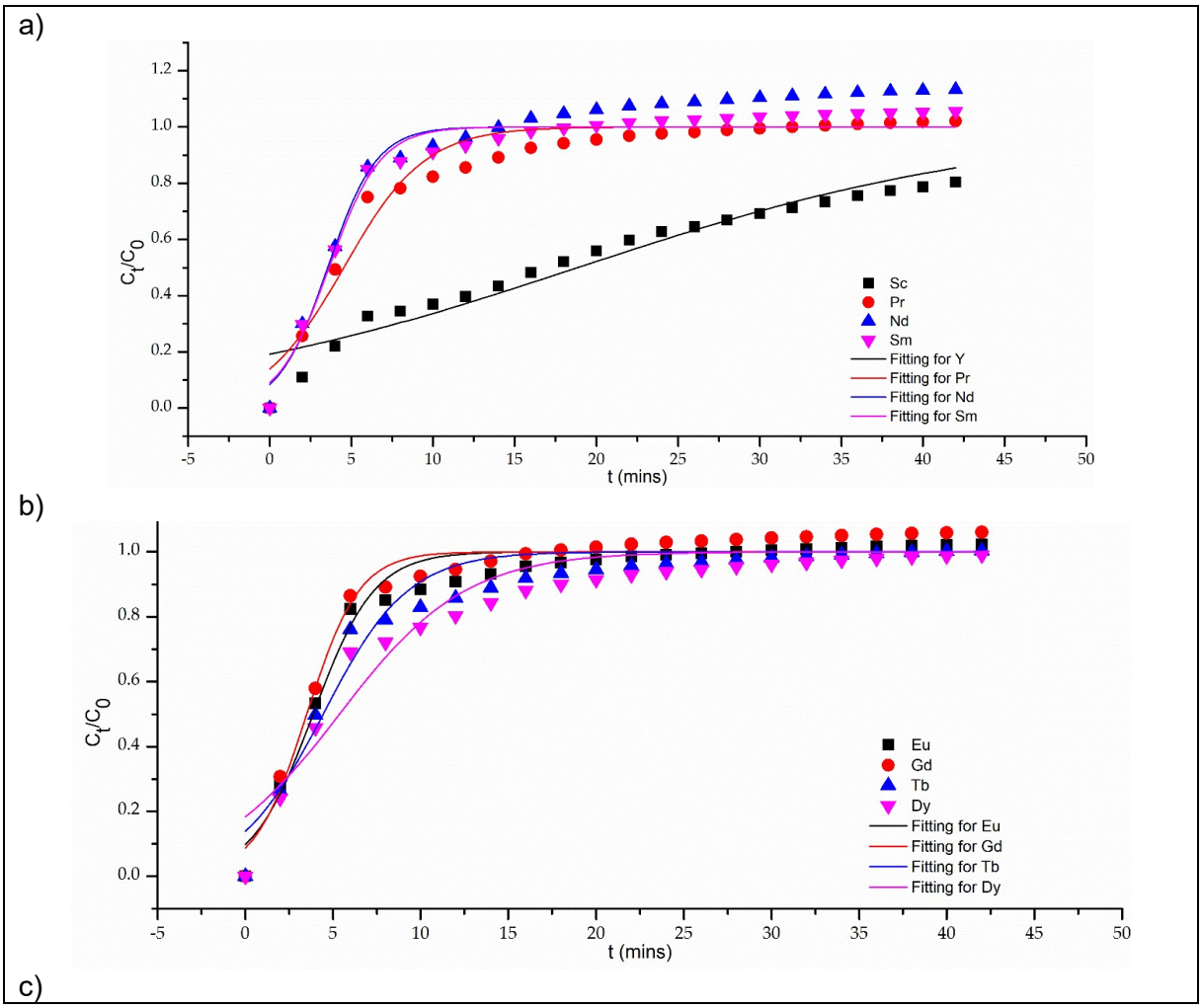

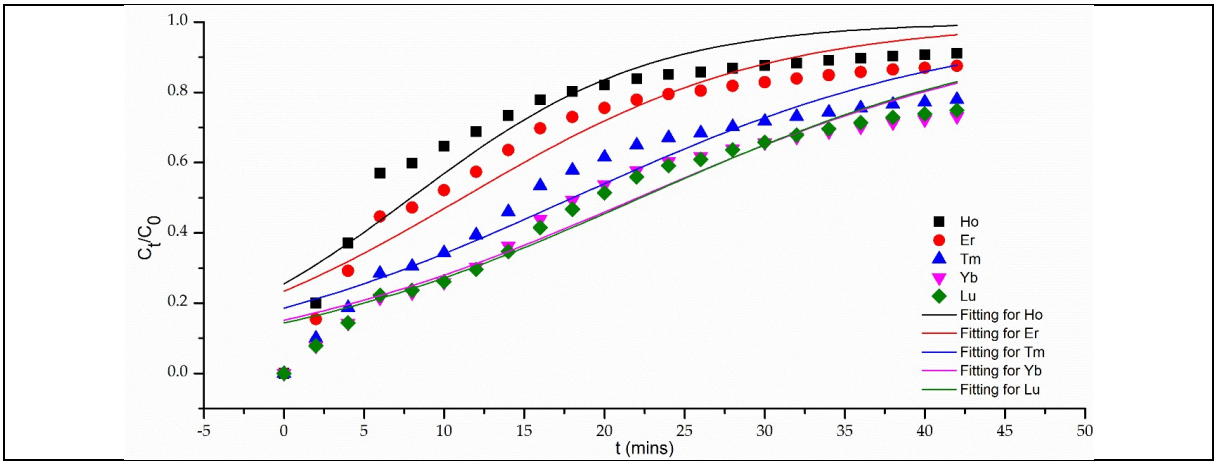

SI Figure 14. Fitting of the Yoon-Nelson model to a) Y, Pr-Sm, b) Eu-Dy, c) Ho-Lu

SI.6.3. Thomas Model

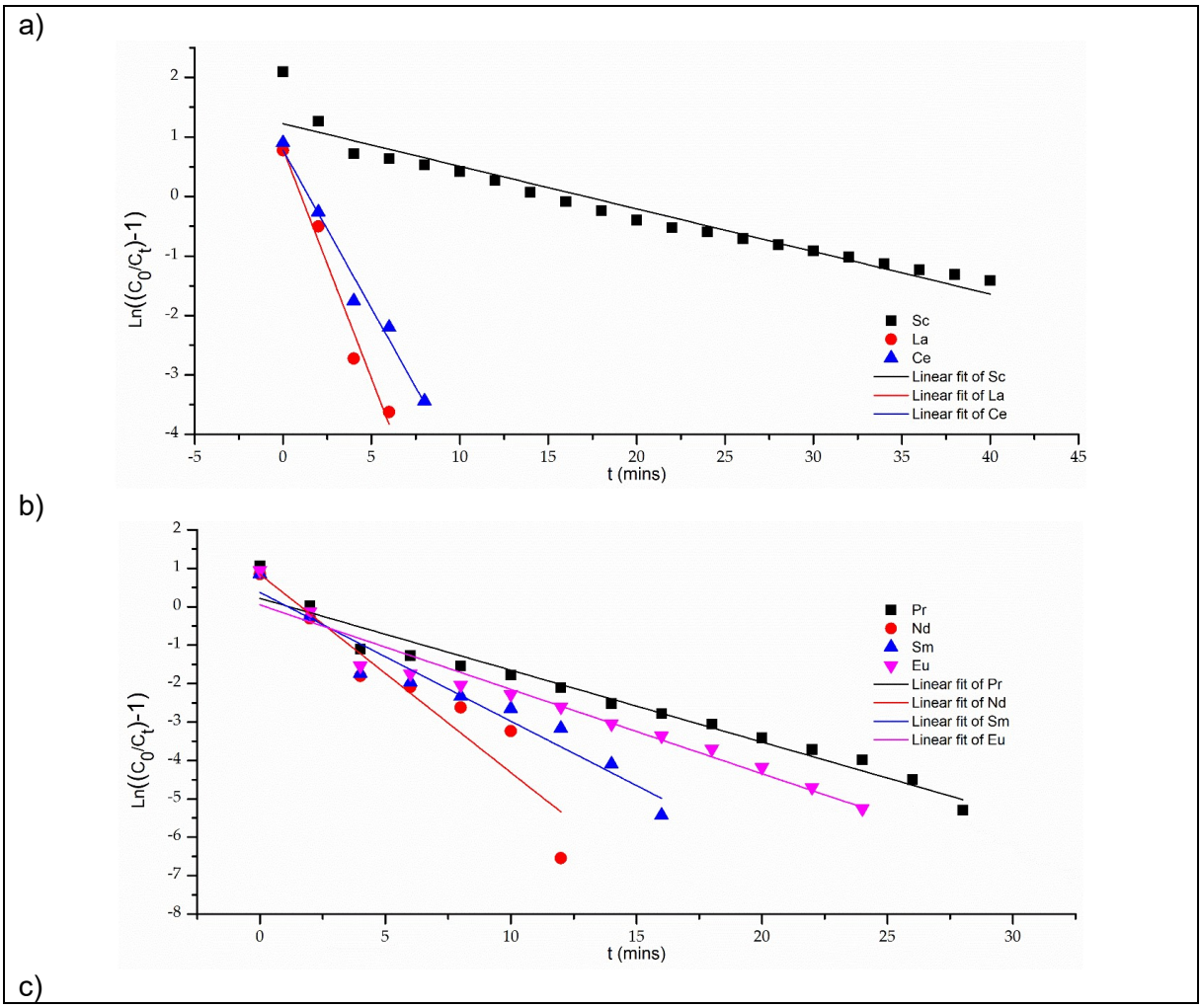

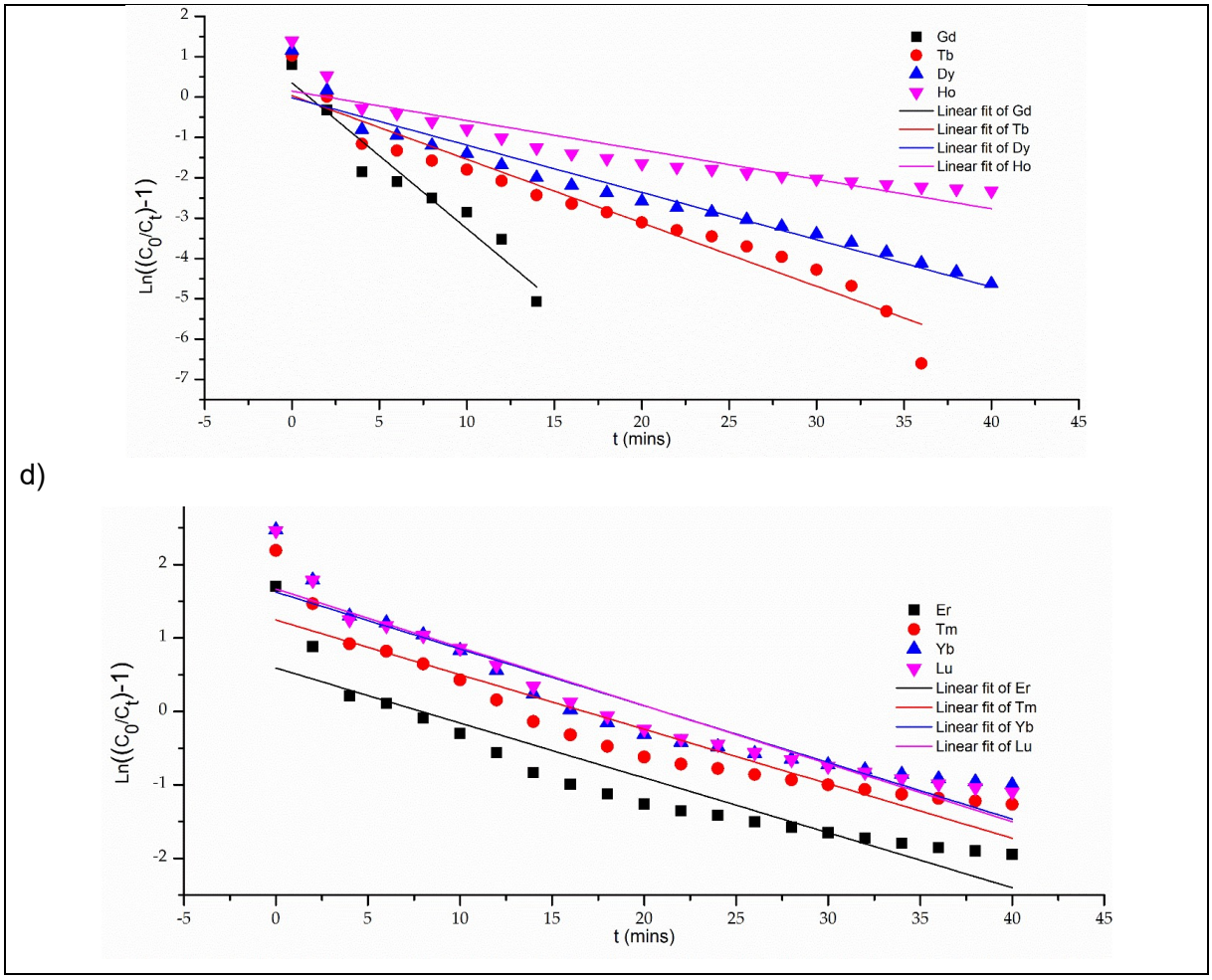

SI Figure 15. Fitting of the Thomas model to a) Sc-Ce, b) Pr-Eu c) Gd-Hoand d) Er-Lu

SI.6.4. MDR Model

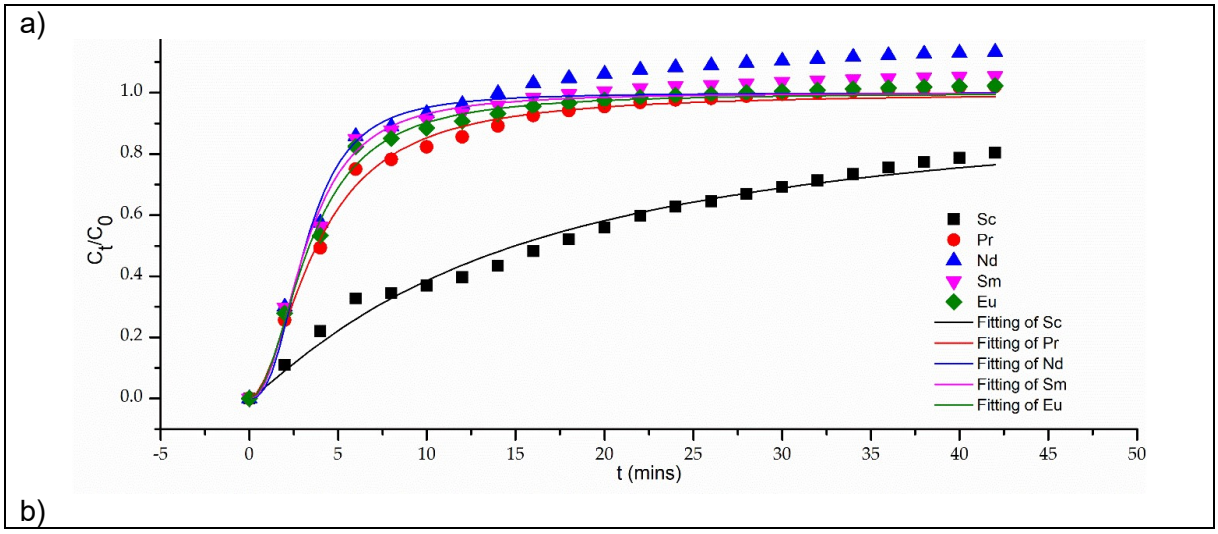

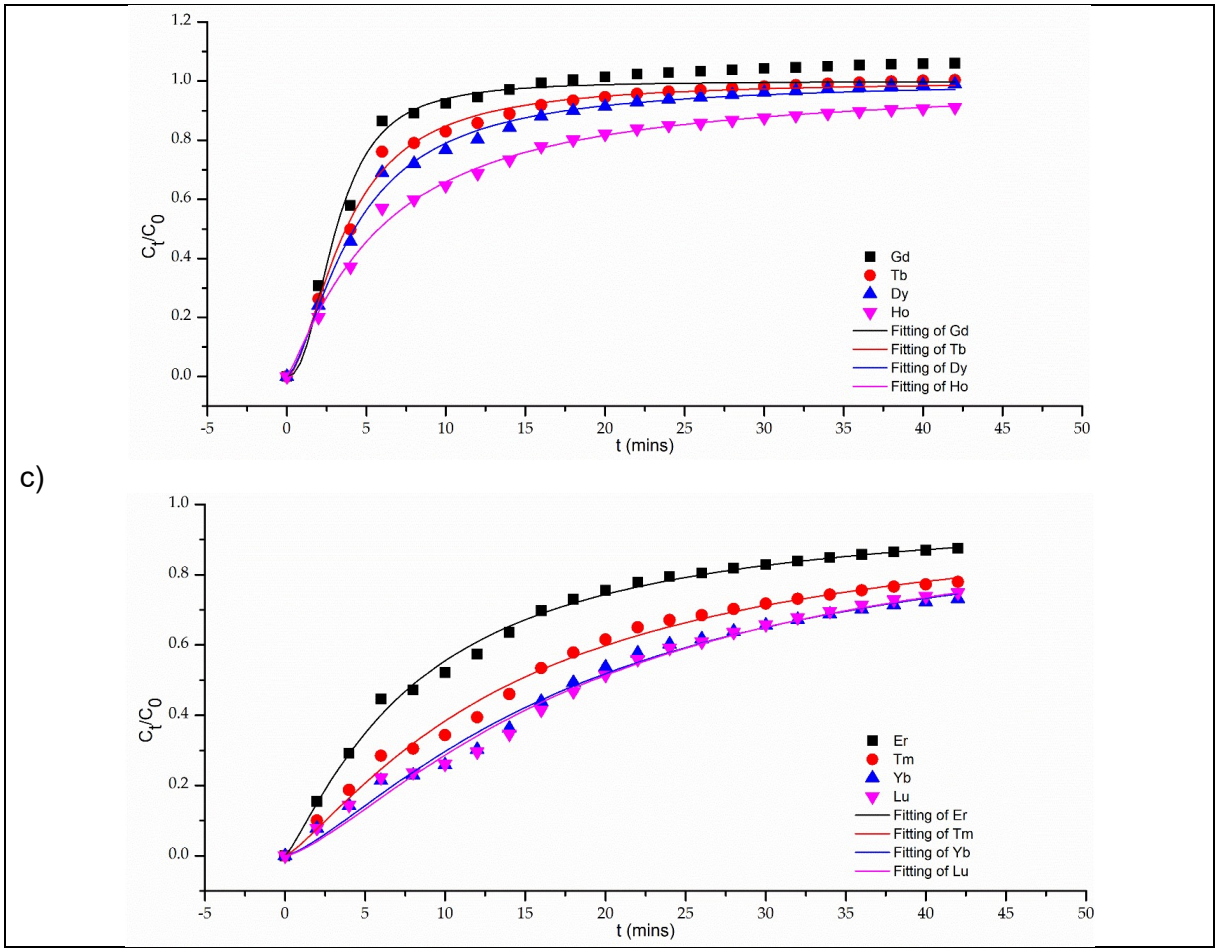

SI Figure 16. Fitting of the MDR model to a) Sc, Pr-Eu, b) Gd-Ho and c) Er-Lu

SI.7 Breakthrough Modelling of REE Column Behaviour of HANC-SI

SI.7.2. Yoon-Nelson Model

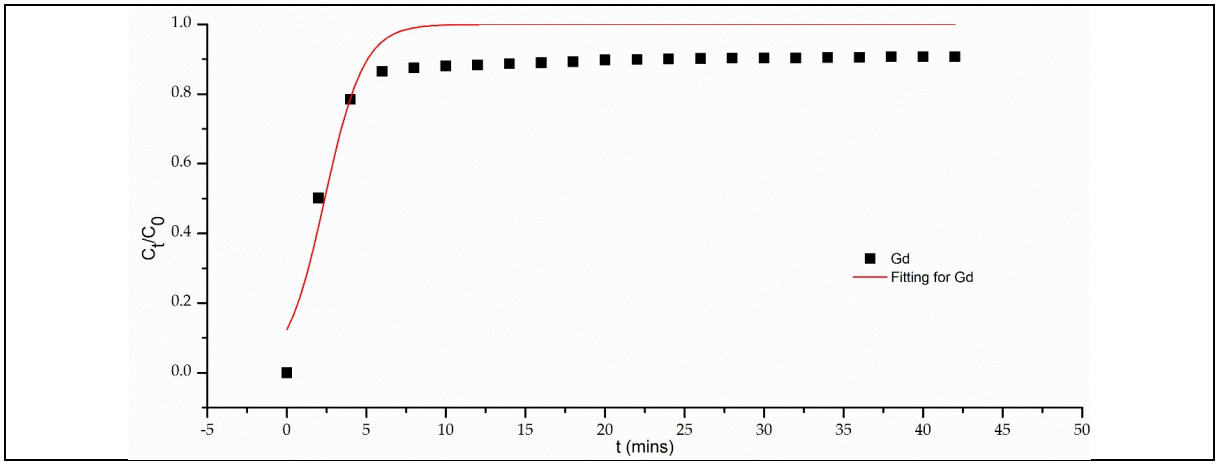

SI Figure 17. Fitting of the Yoon-Nelson model to Gd

SI.7.3. Thomas Model

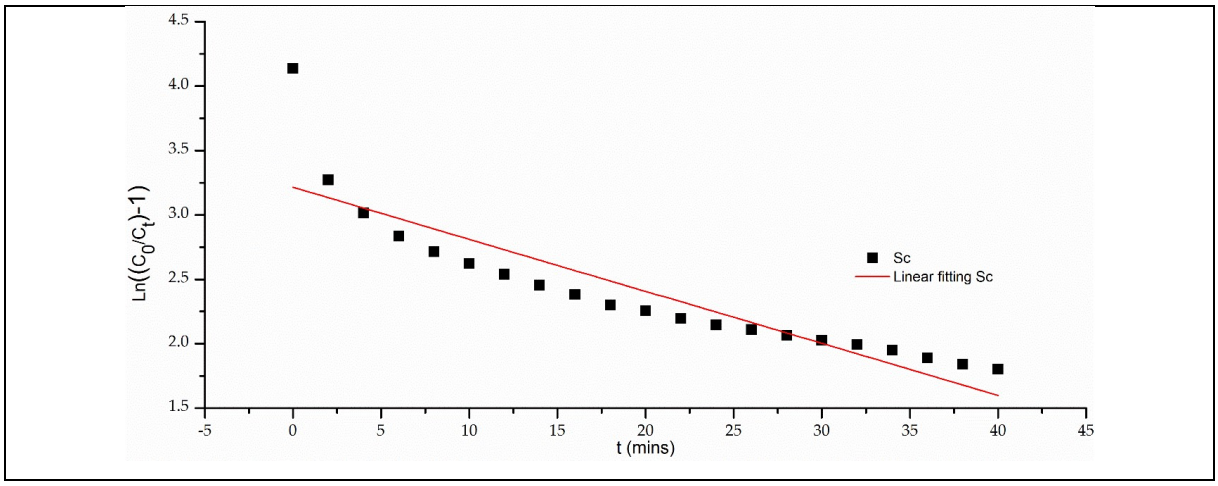

SI Figure 18. Fitting of the Thomas model to Gd

SI.8 Breakthrough Modelling of REE Column Behaviour of TBTPhen-Si

SI.8.1. Adams-Bohart Model

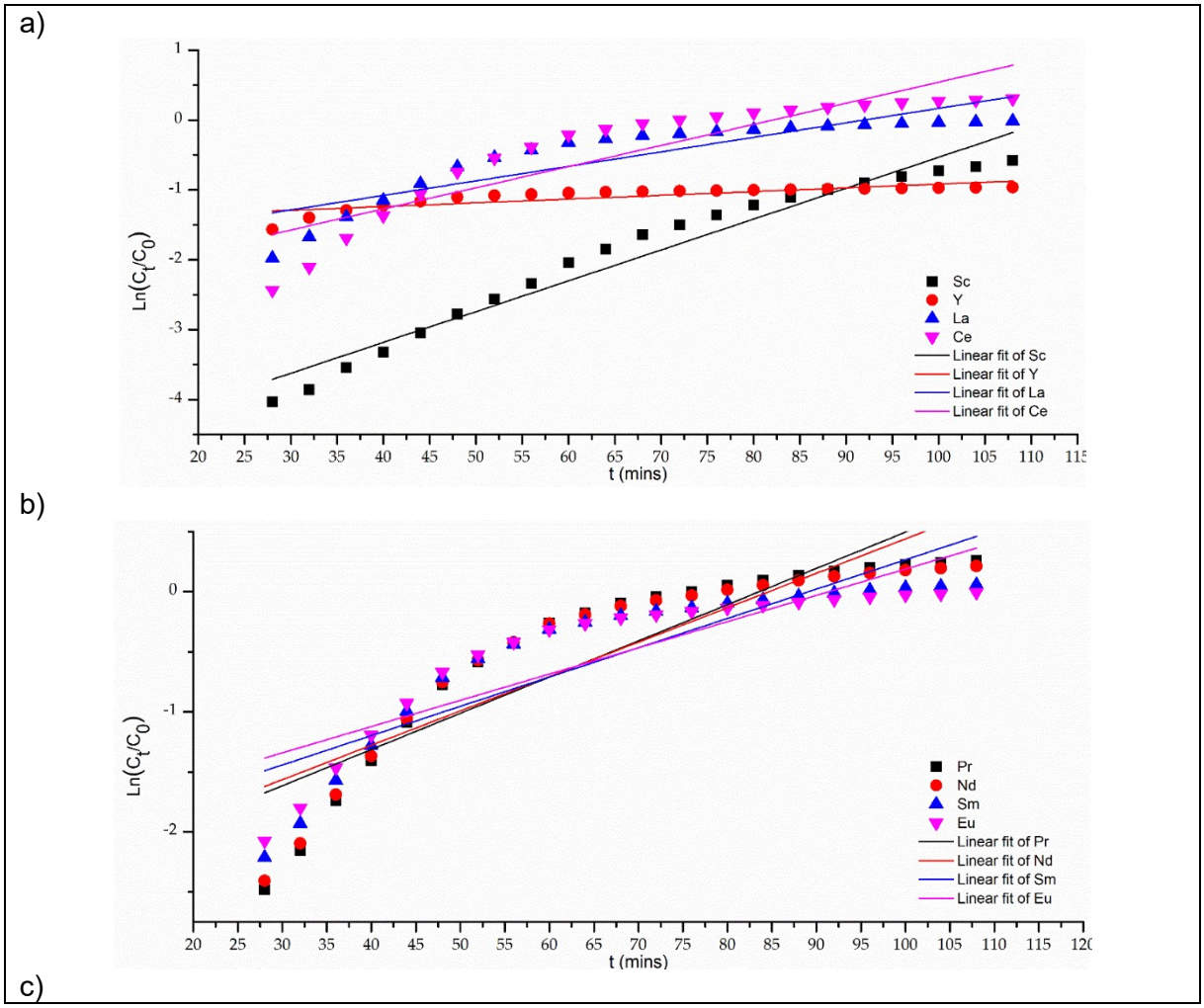

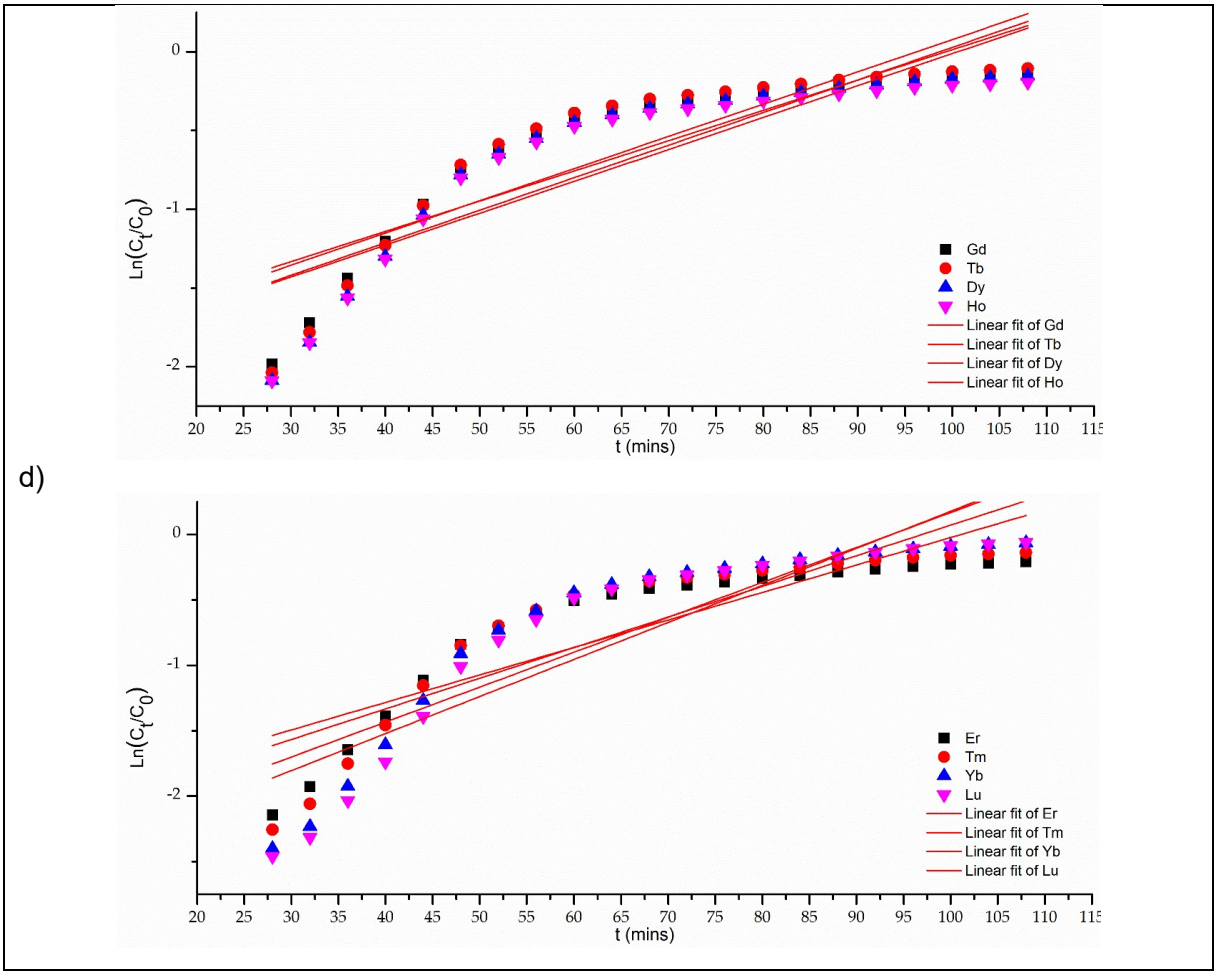

SI Figure 19. Fitting of the Adams-Bohart model to a) Sc-Ce, b) Pr-Eu, c) Gd-Ho and d) Er-Lu

SI.8.3. Thomas Model

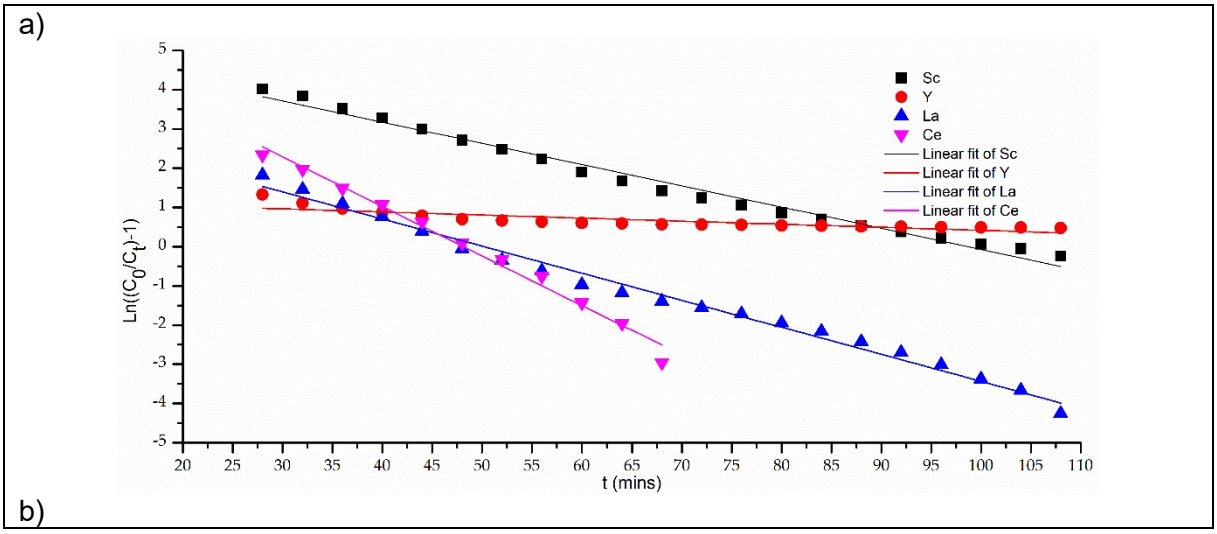

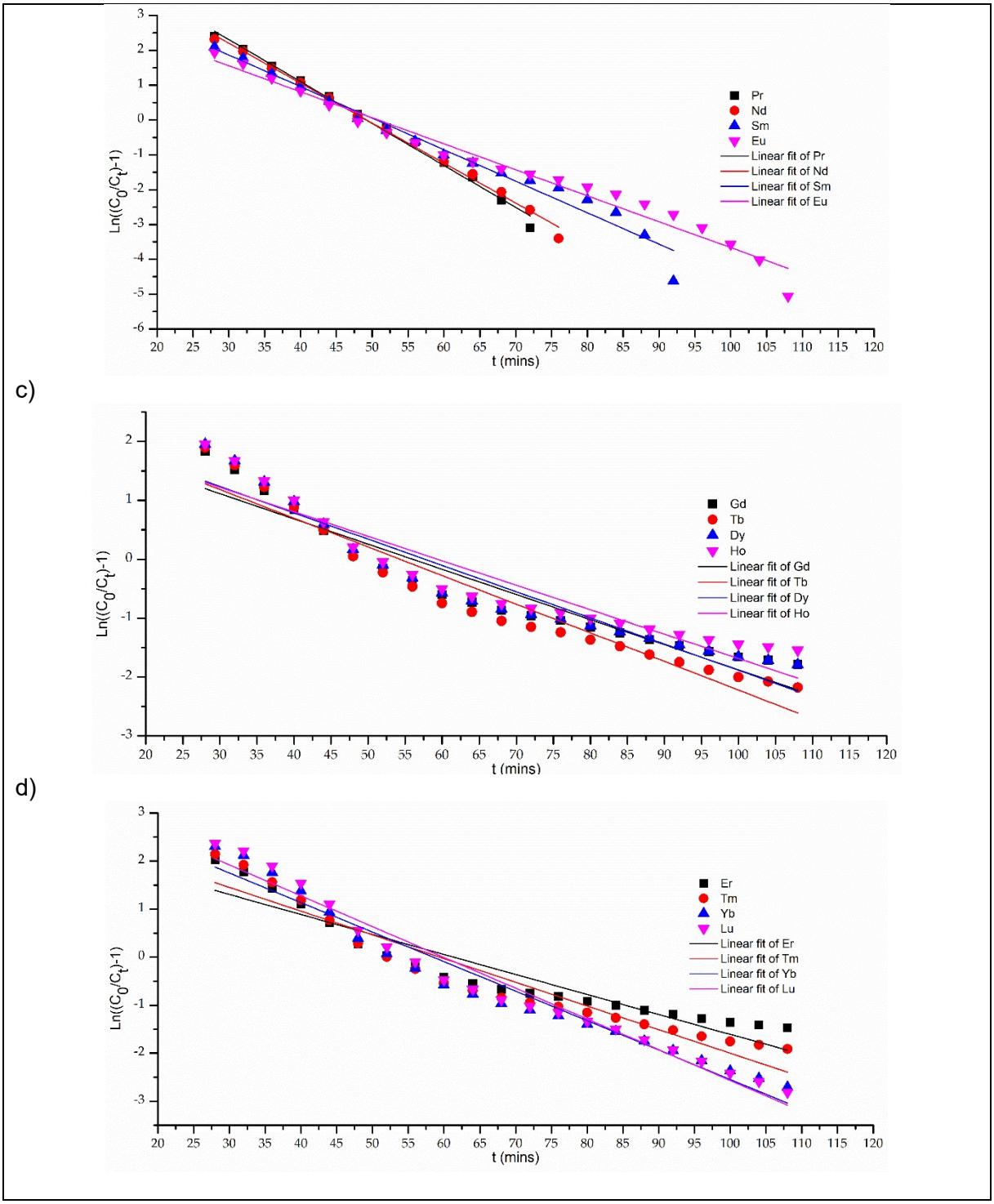

SI Figure 20. Fitting of the Thomas model to a) Y-Pr, b) Nd-Gd, c) Tb-Er and d) Tm-Lu

SI.8.4. MDR Model

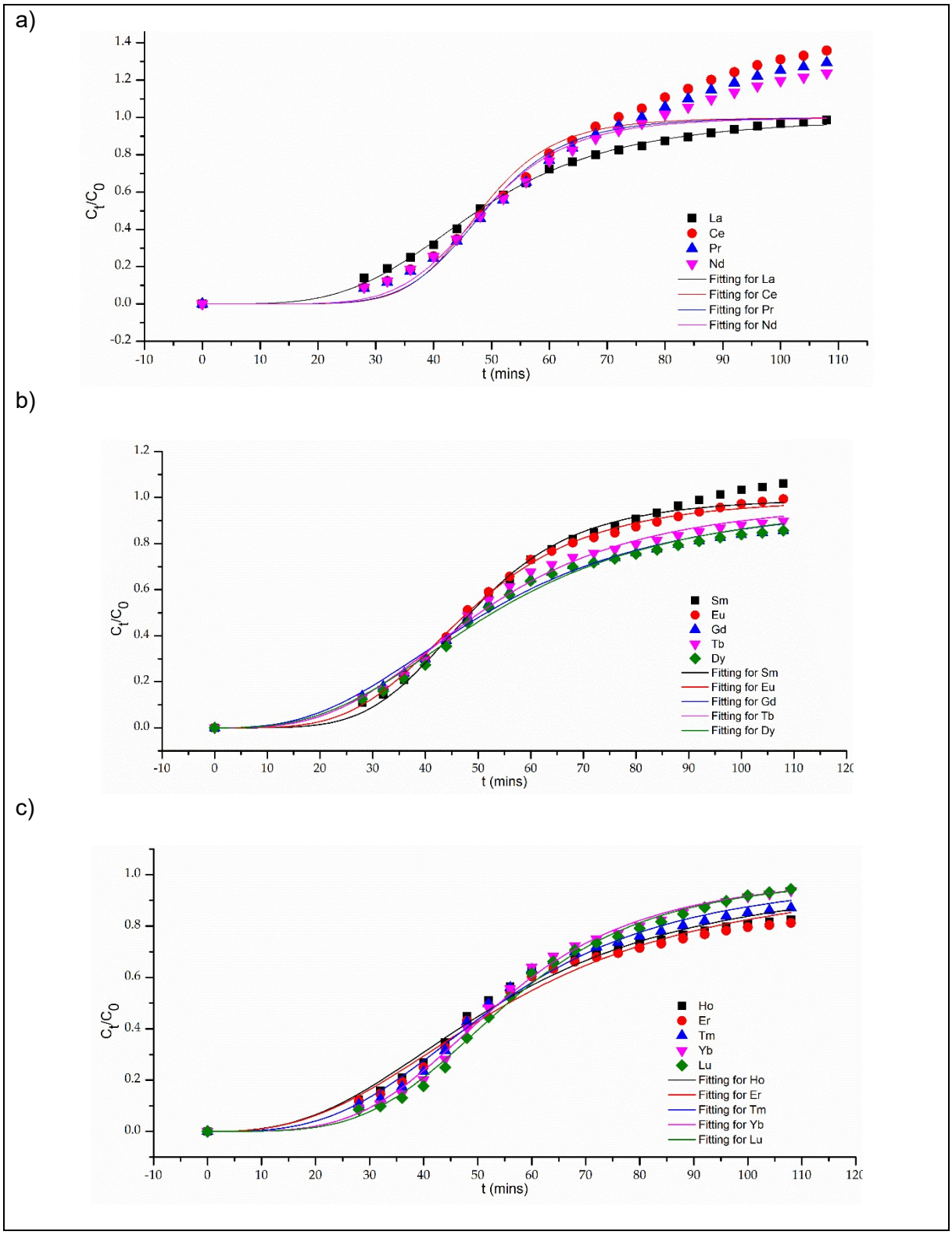

SI Figure 21. Fitting of the MDR model to a) La-Nd, b) Sm-Dy and c) Ho-Lu

SI.6 Experimental Procedure

SI 6.1 General Procedure

All reagents were supplied by Acros, Aldrich, Fisher or Fluorochem chemical suppliers and were used as supplied unless stated otherwise. NMR spectra were recorded using either a Bruker AMX400 or an Advance DFX400 instrument. Deuterated chloroform ($CDCl_3$) or deuterated dimethyl sulfoxide (DMSO-d_6) were used as solvents. Chemical shifts (δ) are reported in parts per million (ppm) with the abbreviations s, d, t, q, dd, dt and m denoting

singlet, doublet, triplet, quartet, double doublet, double triplet and unresolved multiplet resonance respectively. All coupling constants (*J*) are recorded in Hertz (Hz). Assignments were made using chemical shift and coupling constant data using DEPT-90, COSY, HSQC and HMBC experiments where required. IR spectra were recorded on a Perkin-Elmer Spectrum One FT-IR spectrometer instrument with peak intensities abbreviated to: w, weak; m, medium; s, strong; br, broad. All melting points were determined on a Stuart SMP10 melting point apparatus. Mass spectra were recorded under conditions of electrospray ionisation (ESI) on a Thermo Scientific LTQ-Orbitrap XL with a Thermo Scientific Accela HPLC. Thermogravimetric (TGA) analyses were performed using a TGA-Q50 thermogravimetric analyser.

SI 6.2 Synthetic Procedures

Synthesis of 4-(2,9-dimethyl-1,10-phenanthrolin-5-yl)benzoic acid

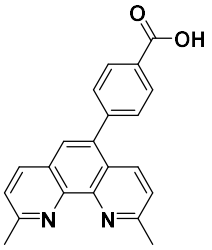

5-Bromoneocuproine (0.050 g, 0.17 mmol) was dissolved in EtOH (2 mL), H_2O (1 mL) and toluene (2 mL). K_2CO_3 (0.072 g, 5.2 mmol), tetrakis triphenylphosphine palladium (0) (0.01 g, 0.0087 mmol) and 4-boronobenzoic acid (0.042 g, 0.25 mmol) were added and the mixture was heated at 90 °C overnight under an inert atmosphere. The reaction was allowed to cool before the solvent was evaporated *in vacuo* to afford 4-(2,9-dimethyl-1,10-phenanthrolin-5-yl)benzoic acid **15** as a yellow solid (0.43 g, 77%). M.p. >300 °C; FT-IR (ATR) ν_{max} / cm^{-1} 3247br, 2968m, 1595s;

δ_H (400 MHz, DMSO) = 8.38 (d, J = 8.2 Hz, 1H), 8.16 (d, J = 8.5 Hz, 1H), 8.00 (d, J = 7.8 Hz, 2H), 7.83 (s, 1H), 7.65 (d, J = 8.2 Hz, 1H), 7.59 (d, J = 8.5 Hz, 1H), 7.41 (d, J = 7.8 Hz, 2H), 2.81 (d, J = 5.5 Hz, 6H); δ_C (101 MHz, DMSO) = 168.4, 158.6, 158.4, 145.5, 144.6, 142.0, 138.6, 137.9, 136.9, 134.7, 129.6, 129.0, 126.6, 125.8, 124.1, 123.7, 79.7, 56.5, 25.6, 25.4, 19.0; ESI-FTMS: calculated $C_{21}H_{17}O_2N_2$ $[M+Na]^+$: 329.1285, observed: 329.1276

Synthesis of Aminopropylneocuproine-functionalised SiO_2

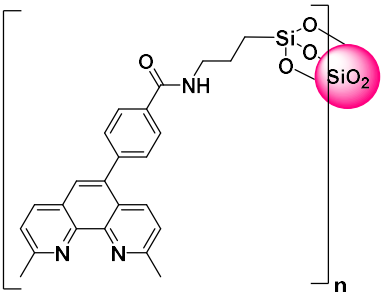

Excess thionyl chloride (2 mL, 27.6 mmol) was added to 4-(2,9-dimethyl-1,10-phenanthrolin-5-yl)benzoic acid (0.05 g, 0.15 mmol) and the mixture heated to reflux for 2 hours. The excess thionyl chloride was removed *in vacuo* to afford 4-(2,9-dimethyl-1,10-phenanthrolin-5-yl)benzoyl chloride (0.052 g, 0.15 mmol) (confirmed by FT-IR, see below). DMF (20 mL) was added to the flask and the mixture stirred at 120 °C for 30 minutes. Aminopropyl-functionalised SiO_2 gel (0.144 g) was added slowly and the reaction was heated under reflux for 18 hours and the reaction was then allowed the cool to room temperature. The aminopropylneocuproine-functionalised SiO_2 gel was filtered and washed with DMF (20 mL), EtOH (20 mL) deionised water (20 mL) and $CHCl_3$ (20 mL). ANC-Si (0.162 g) was dried at 120 °C.

4-(2,9-Dimethyl-1,10-phenanthrolin-5-yl)benzoyl chloride: FT-IR (ATR) ν_{max} / cm^{-1} = 3207m, 2920m, 2850m, 1691m, 1604w, 1562w, 1406m, 1376m, 1196m, 1119m, 1078w, 1053w, 1017m;

Aminopropylneocuproine-functionalised SiO_2 FT-IR (ATR) ν_{max} / cm^{-1} = 3276w, 1654w, 1051s, 796m, 618m, 444s, 417s;Synthesis of 1,10-phenanthroline-5,6-dione[109] (67)

Synthesis of 1,10-phenanthroline-5,6-dione

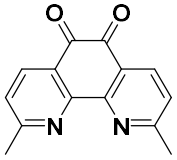

H_2SO_4 (6 mL) was added to a mixture of neocuproine (0.335 g, 1.6 mmol) and KBr (1.9 g, 16.1 mmol, 12 eq) before concentrated HNO_3 (3 mL) was added dropwise, and then the reaction was heated to 100 °C for 2 hours. After cooling to room temperature, the reaction was poured slowly onto ice water (CAUTION) and neutralised with sat. aq. sodium bicarbonate and the product was extracted with $CHCl_3$ (2 x 75 mL). The combined organic extracts were concentrated *in vacuo* to afford the title compound as an orange solid (0.12 g, 31%). M.p. >300 °C; FT-IR (ATR) ν_{max} / cm^{-1} = 2988w, 1676s, 1574s, 1426w, 1363s, 1302s, 1251s.

δ_H (400 MHz, $CDCl_3$) = 8.37 (d, J = 8.0 Hz, 2H, Ar*H*), 7.43 (d, J = 8.0 Hz, 2H, Ar*H*), 2.85 (s, 6H).δ_C (101 MHz, $CDCl_3$) = 179.0, 167.0, 152.5, 137.4, 126.0, 125.5, 15.9; (FTMS + p ESI) cald $C_{14}H_{12}O_2N_2$ $[M+H]^+$: 208.0995; observed: 208.0995;

Synthesis of Benzimidazole-fused Neocuproine

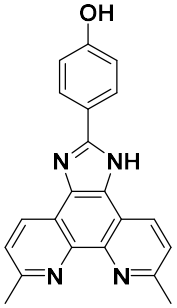

1,10-phenanthroline-5,6-dione (0.1 g, 0.42 mmol) and ammonium acetate (0.054 g, 0.7 mmol) were dissolved in glacial acetic acid (10 mL) and 4-hydroxybenzoic acid (0.054 g, 0.39 mmol) in glacial acetic acid (10 mL) was added dropwise. The reaction was stirred at 90 °C for three hours, then water (50 mL) was added and the reaction was neutralised with ammonia. Chloroform (100 mL) was added and the separated organic extract was concentrated *in vacuo.* The solid residue was triturated with Et_2O (20 mL) and filtered to afford the title compound as a yellow solid (0.053 g, 0.16 mmol, 38%). M.p. >300 °C; FT-IR (ATR) ν_{max} / cm^{-1} = 3287 br, 2488b, 1687w, 1578w, 1374w, 1000br.

δ_H (400 MHz, $CDCl_3$) = 13.36 (s, 1H, N*H*), 9.94 (s, 1H, O*H*), 8.76 (d, J = 8.2 Hz, 2H, Ar*H*), 8.10 (d, J = 8.4 Hz, 2H, Ar*H*), 7.67 (dd, J = 16.4, 8.1 Hz, 2H, Ar*H*), 6.97 (d, J = 8.4 Hz, 2H, Ar*H*), 2.79 (s, 6H); δ_C (101 MHz, $CDCl_3$) = Insufficiently soluble to obtain a meaningful spectrum. ESI-FTMS: calculated $C_{21}H_{17}ON_4$ $[M+Na]^+$: 341.1391, observed: 341.1397;

Synthesis of Benzimidazole-fused Neocuproine-functionalised SiO_2 (BNC-Si)

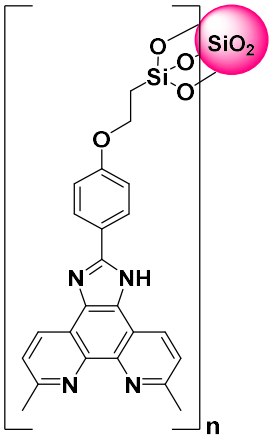

NaH (0.08 g, 0.245 mmol, 1.6 eq) was added to a solution of benzimidazole-fused neocuproine (0.05 g, 0.15 mmol) in DMF (11 mL) . The reaction was allowed to stir at reflux for 30 minutes before chloropropyl-functionalised SiO_2 gel (0.22 g) was added in small portions over 15 minutes and the reaction allowed to proceed for 18 hours. The reaction was cooled to room temperature, filtered and the residue washed with DMF (20 mL), EtOH (20 mL), deionised water (20 mL) and $CHCl_3$ (20 mL). The BNC-Si was dried at 120 °C and obtained as a yellow solid (0.2 g). FT-IR (ATR) vmax / cm^{-1} = 2987w, 1625w, 1393w, 1057s, 801w.

Synthesis of 1,10-dimethylphenanthroline-5,6-epoxide

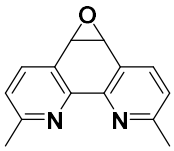

A solution of sodium hypochlorite (25 mL) and distilled water (25 mL) was adjusted to a pH of 8.9 using sulfuric acid (1 mL). To this solution, neocuproine (0.5 g, 2.4 mmol) and tetra *n*-butyl ammonium hydrogensulfate (0.39 g) in $CHCl_3$ (20 mL) as was added whilst stirring vigorously. The reaction was allowed to stir at room temperature for 2 hours, then DCM (100 mL) was added, and the organic phase washed with sat. aq. $NaHCO_3$, water and brine. The organic phase was dried with Na_2SO_4, filtered and concentrated *in vacuo* to afford the epoxide as a yellow solid (0.12 g, 0.5 mmol, 21%). M.p. 35 °C.

δ_H (400 MHz, $CDCl_3$) = 7.90 (d, J = 7.8 Hz, 2H, Ar*H*), 7.27 (d, J = 7.8, 2.7 Hz, 2H, Ar*H*), 4.62 (d, J = 8.0 Hz, 2H, Ar*H*), 2.76 (s, 6H, C*H*$_3$); ^{13}C NMR (400 MHz, $CDCl_3$) δ = 159.9, 148.7, 138.4, 126.6, 123.6, 55.2 (C-O), 14.8; ESI-FTMS: calculated $C_{14}H_{12}N_2O$ $[M+H]^+$: 225.1020 observed: 225.2022;

Synthesis of Aminopropylneocuproine-functionalised SiO_2 (HANC-Si)

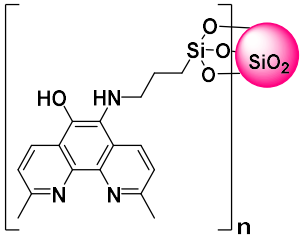

Sodium hydride (60% dispersion in mineral oil, 0.096 g, 4 mmol, 2 eq) was added to a solution 1,10-phenanthroline-5,6-epoxide (0.456 g, 2 mmol) in DMF (40 mL). The reaction was allowed to stir at 120 °C for 30 minutes before chloropropyl-functionalised SiO_2 gel (1.78 g) was added in small portions over 15 minutes. The reaction was allowed to proceed for 18 hours, then cooled to room temperature. The mixture was filtered and the residue washed with MeOH (200 mL), EtOH (200 mL), water (200 mL) and $CHCl_3$ (200 mL) to afford the title compound as a yellow solid (1.6 g). FT-IR (ATR) ν_{max} / cm^{-1} = 1650w, 1049s, 795w.

Synthesis of Tetra(4-hydroxyphenyl)BTPhen Functionalised SiO_2 (TBTPhen-Si)

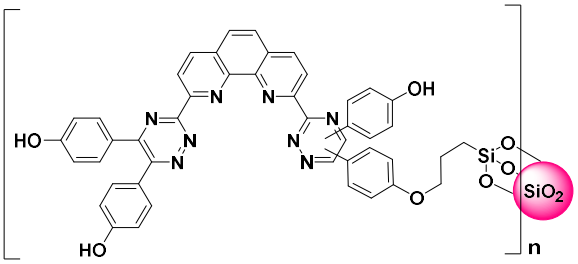

Sodium hydride (60% dispersion in mineral oil, 0.096 g, 4 mmol, 2 eq) was added to a solution of tetra(4-hydroxyphenyl) BTPhen (0.85 g, 0.12 mmol) in DMF (40 mL) at 120 °C and the mixture stirred for 30 minutes. Chloropropyl-functionalised SiO_2 gel (1.62 g, ~ 2.5 mmol g^{-1} loading) was slowly added, and the reaction mixture was stirred at 120 °C overnight. The tetra(4-hydroxyphenyl) BTPhen-functionalised SiO_2 gel was collected by filtration and was thoroughly washed with water (1×100 mL) and ethanol (1×100 mL). Finally, the product (6.8 g) was allowed to dry at 120 °C for 2 days. FT-IR (ATR) ν_{max} / cm^{-1} = 3240br, 2929w, 1606w, 1487w, 1361w, 1051s, 795s.

Chapter 5 – Conclusions

5.1 Introduction

The rare earth elements (REEs) have become an integral part of modern life due to their magnetic and conductive properties, making them a crucial part in consumer products and high technological industries. Fields such as catalysts, ceramics, glass, metallurgy and polishing are the main fields that require REEs. The ever-growing demand for REEs and the difficulty in obtaining and recycling these precious metals, we see these metals on the EU critical materials list since 2011 [1,2]. To overcome the challenges faced with supply problems, the development of materials to recycle and separate these metals from each other is crucial. Retired wind turbines and electric vehicle motors provide a source of recyclable REE, however the infrastructure for recycling smaller components, such as HDD, mobile phones are underdeveloped and costly.

The separation of REEs from each other is a challenging feat due to their similar chemical and physical properties. Current separation techniques involve counter-current liquid-liquid solvent extraction and chromatography. Chromatography has become more of an effective method for the separation of REEs as the use of an adsorbent negates the need for large quantities of solvent waste and storage, as well as the complications that arise from third phase formations. Various ligands with functional groups including; sulfonic acid, diglycolamides and phosphonic acids have demonstrated excellent extraction of REE metals. Pyridine and phenanthroline based ligands have also been seen to bind to REE metals through their *N*-donor atoms. Functionalisation of the 1,10-phenanthroline backbone with silica provides excellent solid-state materials for the extraction of REEs.

5.2 Key Findings

The work outlined in this thesis tackles two main aims: firstly, to partition the REE series into smaller groups or individual elements using phenanthroline based derivatives. Secondly, to investigate alternative ligands and synthetic routes that negate the use of a costly palladium catalyst.

5.2.1 Application of a phenanthroline functionalized silica to the separation of rare earth elements (REEs)

The synthesis and characterization of NC-Si was explored and high yields were obtained for the synthesis of NC-Si. The performance of NC-Si in adsorbing REEs was assessed using a fixed-bed continuous flow experiment. The pseudo first order (PFO) and pseudo second order (PSO) rate constants were determined using Lagergren's rate equations. It was found that pseudo second order reaction kinetics posed a better fit for the adsorption and desorption of REEs on NC-Si compared to PFO. The models; Adams-Bohart, Thomas, Yoon-Nelson and Modified Dose Response (MDR) were fit to the breakthrough data. Although the Adams-Bohart

model was suitable for the description of the adsorption of all REE, it had the lowest overall R^2 value compared to Thomas, Yoon-Nelson and Modified Dose Response (MDR). NC-Si makes a suitable material for the partitioning of REEs as it can separate REE ions into three groups; early (Y, La – Pr), mid (Sc, Nd - Dy) and late (Ho – Lu).

5.2.2 Application of a $CyMe_4$-BTPhen functionalized silica to the separation of rare earth elements (REEs)

The work described in this paper is very similar to "Application of a phenanthroline functionalized silica to the separation of rare earth elements (REEs)" (Chapter 2), however the focus of this paper is on the investigation of BTPhen-Si for the separation of REEs. The synthesis and extraction capabilities of REEs were explored and the adsorption performance of BTPhen-Si was evaluated through a continuous fixed-bed experiment. Overall, BTPhen-Si had a higher adsorption capacity (4-fold) compared to NC-Si, however the partitioning of REEs was not as capable. The models; Adams-Bohart, Yoon-Nelson, Thomas and MDR were also applied to attempt to determine the mechanism of adsorption. The Adams-Bohart and Thomas models were used to describe the adsorption of all REE ions, but their R^2 values were relatively low compared to the Yoon-Nelson and MDR models. Yoon-Nelson and MDR had high R^2 values and were able to describe the late ions and some of the earlier/mid REE ions, except for Sc, Pr, Nd, Sm, and Eu. Experimental data showed pseudo first order (PFO) theoretical q_e values were closer to the experimental values for the late REEs, whereas second first order (PSO) gave closer q_e values for the early REEs. Gibbs free energy change (ΔG) showed that the adsorption of REEs onto BTPhen-Si was a spontaneous process, with the earlier REEs (Sc, Ce-Eu) having more negative ΔG values compared to Y, La, and late REEs. A comparison between BTPhen-Si and NC-Si was made.

5.2.3 Application of phenanthroline-based functionalized silica to the separation of rare earth elements (REEs)

It has been confirmed that phenanthroline-based silica supported structures such as NC-Si and BTPhen-Si can effectively extract REEs using a fixed-bed column technique. ANC-Si, BNC-Si, HANC-Si and TBTPhen-Si were synthesized as alternative ligand-Si systems and subjected to fixed-bed column experiments to compare with NC-Si and BTPhen-Si. ANC-Si and NC-Si have very similar chemical structures, however NC-Si bares a ether linkage from neocuproine to silica, whereas ANC-Si bares a amide linkage. ANC-Si has a slightly lower adsorption capacity compared to NC-Si due to the electron withdrawing amide group. Back extraction of all ions, except Gd, was difficult and there was no preference for any of the REE ions.

NC-Si, BTPhen-Si and ANC-Si all require a Suzuki-Miyaura to form either an amide or a phenol group to allow attachment to silica. The Suzuki-Miyaura reaction involves use of a palladium catalyst, which is expensive and unsustainable. The driving force behind this work was to find

synthetic methods that omit the use of the Suzuki-Miyaura reaction step, whilst keeping the total number of synthetic steps to a minimum. BNC-Si, HANC-Si and TBTPhen-Si where synthesized without carrying out a Suzuki-Miyaura reaction step. Although they had lower adsorption capacities than BTPhen-Si they still managed to achieve some level of REE extraction. The models; Adams-Bohart, Yoon-Nelson, Thomas and MDR were applied to all ligands in this paper, including ANC-Si. Table 5 shows the comparison between all silica supported ligands synthesized in this thesis in order to find the most suitable ligand for the separation of REEs. Many different factors were taken into account when choosing a suitable ligand for scaling for industry, such as cost, number of synthetic steps and adsorption capacities. A colour coding system is given in the table to indicate the relative performance of each ligand system in each category. Ligands that perform the best are represented by the colour green, while the second-best performing ligands are depicted with the colour orange, and ligands that perform the worst are shown in red.

Table 5. Comparison between ANC-Si, BNC-Si, HANC-Si, TBTPhen-Si, BTPhen-Si and NC-Si [3]

Characteristic	ANC-Si	BNC-Si	HANC-Si	TBTPhen-Si	BTPhen-Si	NC-Si
Structure	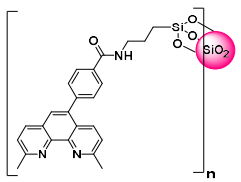	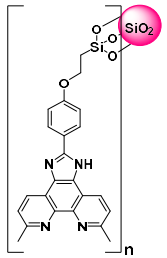	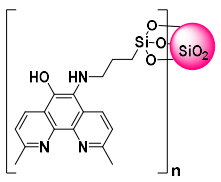	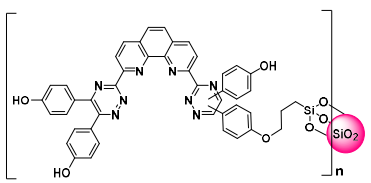	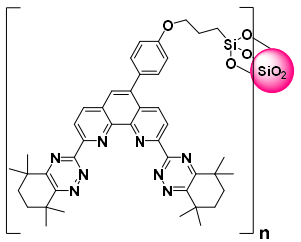	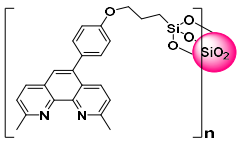
1 g of neocuproine to yield (g)	2.7	0.76	3	2.97	0.15	3.84
Cost per kg (with $CHCl_3$) (£)	60,013	271,936	52,610	35,624	858,082	30,613
Cost per kg (without $CHCl_3$) (£)	35,650	39,051	9,181	26,549	632,042	15,523
Number of Synthetic Steps	3	3	2	8	13	3
Overall Adsorption Capacity (mg g^{-1})	0.0106	0.00484	0.0101	0.0157	0.0484	0.0153
Lowest Adsorption Capacity (mg g^{-1})	Gd	Y	Gd	Gd	La	Y
Highest Adsorption Capacity (mg g^{-1})	La	Lu	La	Sc	Yb	Sc
% of ions extracted from inlet (%)	96	79	93	89	76	80
Immobilisation (%)	n/a	80	n/a	98	90	57
w/w % of ligand weight (%)	5.5	14	4	7	6	5

Models able to describe adsorption	AB, T	YN, T, MDR	n/a	AB, T, MDR	All	All
Model with highest R^2 value for early ions (Sc – Eu)	T	T	n/a	T	T	MDR
Model with highest R^2 value for late ions (Gd – La)	AB	MDR	n/a	MDR	YN	YN
Preferences (based on charge density)	Late (Tb – Sc)	Late (Tb – Sc)	Late (Tb – Sc)	Early (La-Gd)	Early (La-Gd)	Late (Tb – Sc)
Preferences (position in periodic table)	Late (Gd – Lu)	Late (Gd – Lu)	Early (Sc – Eu)	Early (Sc – Eu)	Early (Sc – Eu)	Late (Gd – Lu)
Metal to ligand molar ratio	1:1963	1:10974	1:1969	1:832	1:250	1:1334
Molarity per g of adsorbent	0.1495	0.3815	0.1429	0.0939	0.0868	0.1466
Average predicted pKa of N in positions 1 and 10*	4.75	4.5	6	3.2	4.25	4.75
Predicted pKas on other atoms*	13.5	10, 4.5	O = 6.4 N = 13.5	2.4, 3.2	2.9	n/a
LogP *	5.2	5.7	3.9	12.31	9.6	5.9
Surface Binding Constant (*K*) (mg L^{-1})	4034445	14188	439217	138001	5805	698

5.3 Discussion

The cost of synthesis and the number of steps are two of the most important factors to consider when scaling up for use in an industrial setting. If chemical and production costs are too high then major considerations must be made to decide if employing said system is profitable. The cost of the synthesis of the ligands are calculated from the prices of reagents obtained from the online catalogues of Sigma Aldrich, Fisher Scientific and Tokyo Chemical Industry in January 2023 (Table 5) [4–6]. NC-Si is the cheapest solid supported material out of the six ligands to synthesize (>£36k) when considering the quantity of chloroform required (Table 5). It takes three steps to synthesize, making it a rather straightforward molecule to synthesize and scale up. When comparing the ratio between starting material and product, NC-Si also has the highest ratio, where 1 g of neocuproine will produce 3.84 g of final product compared to just 0.76 g of BNC-Si and 0.15 g of BTPhen-Si. This shows that less starting material is required and therefore making it more sustainable. NC-Si and HANC-Si also involve fewer synthetic steps compared to the rest of the solid supports.

Interestingly, even though all ligand-Si supports contain a phenanthroline functional group, they all had different preferences for different REEs. The linkage to silica alters the electronics of the phenanthroline ring and therefore will have different affinities for REE ions. Tailoring the functional groups will allow preferences for certain REE ions over others facilitating in the partitioning process. With a pKa of 6, HANC-Si has the highest pKa out of all ligands in this work, indicating a higher electron density on both nitrogens in positions 1 and 10 (Table 5). The amide group donates electron density to the nitrogens, allowing more donation to occur to ions with a higher charge density (late REE ions). TBTPhen-Si has the lowest predicted pKa value (pKa = 3.2). It contains four phenol groups which when protonated in acidic media, will withdraw electron density from the phenanthroline ring and nitrogen atoms [3]. This withdrawal of the electron density increases the affinity for REE ions with lower charge densities, such as the earlier ions. BTPhen-Si has the second lowest pKa value of 4.25 which is also seen to have a preference for the earlier REE ions. NC-Si and BNC-Si both contain N-donor groups which donate electron density into the phenanthroline ring and show to have preferences for the later REE ions with higher charge densities. The more electron dense the phenanthroline ring the more able it is to bind to ions with higher charge densities. Table 5 shows that ligands with pKa values of <4.25 will have a preference for the earlier REEs as these ligands are more acidic and prefer ions with higher charge densities.

LogP is the partition coefficient and is determined by the ratio between the concentration of a compound in the organic solvent and the concentration of that compound in the aqueous solvent. The higher the logP value the more hydrophobic the molecule is and therefore is more likely to repel water molecules and bind to non-polar ions. For all ligands in this work, the logP values have been predicted using an online prediction tool [3]. Table 5 shows there is no

correlation between the hydrophobicity of the ligand and the adsorption coefficient in this work. However, the lower the pKa the higher the logP value is for each of the ligands.

The surface binding constant (*K*) was measured for each of the ligand systems in this thesis using the Langmuir isotherm equation shown in equation (1) below. A graph of C_e/q against C_e was plot where C_e is the concentration of ions in the eluate (mg L^{-1}), q is the adsorption capacity (mg g^{-1}) and q_m is the maximum adsorption capacity (mg g^{-1}) [7]. A linear regression was applied, and the intercept was found to calculate K (mg L^{-1}). The surface binding constant gives an indication of the strength of the bond between the REE ions and the ligand itself and shows the equilibrium between a free ion and a bound ion. ANC-Si, HANC-Si and TBTPhen have the highest K constants (Table 5) indicating a high affinity for the ions. This is evident in the absence of τ (the time it takes for 50% of the ions to elute (C_t/C_0 = 0.5)) as fewer than half of the concentration of ions could not be eluted from the column. A high K value shows the equilibrium of REE ions lie heavily towards being bound to the ligand.

$$\frac{C_e}{q} = \frac{1}{Kq_m} + \frac{C_e}{q_m} \quad (1)$$

In order to increase the separation of REE ions, the system needs to be selective and be able to differentiate between REE ions and have little to no affinity for other non-REE ions, as these will introduce competition for the available ligand sites. Many different factors have to be taken into account in order to increase q. If ion exchange is the method of extraction, then the choice of counterion and eluent will have to be considered based upon the composition of REE ions present in the system, as well as the pH of the solution. Temperature will also be a considerable factor as this will affect the rate of adsorption and desorption. The composition of the ligand-Si system itself is one of the most important factors. Having a large maximum functionalization of the ligand onto the silica will increase the maximum adsorption capacity as more ligand will be available for the extraction of the ions, thus allowing the ability to extract from a higher concentration of REE solution. TBTPhen-Si has the highest immobilisation of 98% and the highest adsorption capacity. NC-Si has the lowest immobilisation at 57% and by increasing the immobilisation percentage the adsorption capacity may increase too.

Most importantly, BTPhen-Si and TBTPhen-Si showed the highest adsorption capacities for REEs compared to other four ligands tested. Their separation and selectively for REEs were not as efficient as NC-Si. NC-Si was able to obtain fractions of individual REE ions as the order of elution occurred from large ions to small ions with easy back extraction. Overall, considering cost, separation performance and ease of synthesis NC-Si would be the preferred ligand for the partitioning of REEs. After fine tuning the conditions of a fixed-bed column of NC-Si, as discussed below in Future Work, the performance could be enhanced. This improved performance could lead to producing pure fractions of individual REE ions from the waste streams of end-of-life products and/or processing REEs from their ores. This is beneficial as REE are a finite resource and their supply is at risk due to economic and political issues.

Table 5 shows differences in the mechanisms of adsorption/desorption for early and late REE ions. The majority of ligand-Si systems in this work adsorb early REE ions via a mechanism described by the Thomas model, except for NC-Si, which adsorbs similarly to the MDR model whereas HANC-Si couldn't be described by any model. The Thomas model states that the rate-determining step is governed by the mass transfer of ions from the eluent to the surface of a homogeneous monolayer material with no intraparticle diffusion [8]. The Thomas model follows Langmuir equilibrium, where axial dispersion is negated, and adsorption capacity is directly proportional to the solute concentration [8]. The MDR model is a simplified version of the Thomas model, negating errors at the beginning and end of breakthrough curves, but it takes into account bed height and does not assume the absence of intraparticle diffusion [10].

Interestingly, the Thomas model could not be applied to the adsorption process of late REE ions for any of the ligand systems in this thesis. NC-Si and BTPhen-Si both describe the adsorption mechanism for late REE ions using the Yoon-Nelson model, where the rate-determining step is the mass transfer between the solvent and the porous structure of the adsorbent [11]. This model also assumes that adsorption capacity is not directly proportional to solute concentration and that other effects are occurring. BNC-Si and TBTPhen-Si show a higher R^2 value for the MDR model in the case of late REE ions, while ANC-Si follows the Adams-Bohart model. The Adams-Bohart model states that the rate of adsorption is proportional to the concentration of the adsorbing species and the residual capacity of the adsorbent [11].

NC-Si can be compared to Dowex 50WX8, a strong acid cation exchanger formed of sulfonic acid groups on a styrene divinylbenzene gel. Dowex 50WX8 was able to extract Y, La, Ce, Nd, Gd and Dy from acid mine water with a pH of 2.4. Dowex 50WX8 had a preference for REE ions in the order of La > Ce = Nd > Gd > Dy > Y with adsorption capacities of 25.5, 20.7, 21.5, 22.5, 16.7 and 11.2 mg g^{-1}, respectively. This shows that Dowex 50WX8 prefers the earlier REEs, where the opposite is true for NC-Si preferring the later REEs. The total adsorption capacity for Dowex 50WX8 in pH 2.4 is 118.1 mg g^{-1} which is considerably higher than NC-Si with a maximum adsorption capacity of 0.0153 mg g^{-1} for all ions [13]. Purolite C160 is another microporous polystyrene resin crosslinked with divinylbenzene with sulfonic acid functional groups. It is able to withstand high temperatures and high mechanical stress and is typically used for softening water and for the removal of metals from radioactive waste. It can also be used in the Quentin process to treat sugar solutions at 70°C [14]. Purolite had a preference for REE ions in the order of La > Nd > Gd > Ce > Dy > Y with adsorption capacities of 30.6, 22.8, 22.2, 21.7, 14.5 and 10.3 mg g^{-1}, respectively. An overall adsorption capacity of 101.8 mg g^{-1} was observed for all ions, which is noticeably greater than NC-Si. Sulfonic groups are highly acidic and REE ions are highly charged, which allows stronger ionic bonds to be formed compared to the bonds between nitrogen and REE ions leading to a higher extraction capability of Purolite and Dowex.

The work in this thesis contributes to the existing literature introducing novel approaches to today's current problem of recovering and recycling REE metals. Previous studies have focused on functionalising neocuproine and phenanthroline with various groups such as tritthiocyanates, β-diketonate, carboxamides and (triethoxysilyl)propyl isocyanate groups [15–18]. A study demonstrated that silica gel can be functionalised directly onto the phenanthroline bridge of phenanthroline to extract Cd(III) using a fixed-bed column technique [18]. In this work the phenol group was introduced as a way of easily attaching silica to neocuproine to produce NC-Si, providing a novel material to add to the existing literature. Modified versions of the neocuproine moiety was functionalised in various ways to form more novel compounds, including the addition of benzamides, alcohols, amines, and imidazole groups to the phenanthroline bridge of neocuproine. These compounds were also successfully immobilised onto silica. The application of these materials for the extraction and partitioning of REEs in a fixed-bed column technique was also novel, demonstrating these ligand-Si systems can extract low concentrations of REE ions from acidic aqueous media. With this knowledge, models have been applied to the breakthrough curves of these systems to determine the mechanism of adsorption of each REE ion, giving an in depth estimate of the characteristics of these ligand-Si systems.

$CyMe_4$-BTPhen is an existing molecule used in the separation of actinides from REEs and has also immobilised onto silica through the addition of a phenol group on the phenanthroline backbone. A fixed-bed column technique for the extraction and partitioning of REEs was carried out, adding to the current known abilities of this ligand. A modified version of $CyMe_4$-BTPhen was also synthesized to produce TBTPhen-Si where two 1,2-bis(4-hydroxyphenyl)ethane-1,2-dione groups were added across both aminohydrazines to give a molecule with 9 cyclic rings. This was also immobilised onto silica and REE extraction capabilities were measured.

Out of all six ligand-Si systems synthesized in this work, NC-Si was able to partition the REE ions the most effectively and thus supports and confirms the initial hypothesis of ***"whether REEs can be recovered using sustainable nitrogen donor functionalized silica solid phase extractants."*** The data and analysis provide evidence that the six phenanthroline-based silica supported ligands discussed throughout this thesis can extract REEs and therefore have the potential to recover REEs from waste and mining streams.

5.4 Future work

The work in this thesis highlights the issues with the supply and demand for REEs and emphasizes the importance of recycling these elements as resources are finite. The current methods for processing REEs from ores, as well as reprocessing REEs from end-of-life products, are discussed. This work focuses on the use of phenanthroline-based ligands immobilized onto silica gel to create a solid support for the partitioning of REEs.

Fixed-bed column techniques were carried out using an eluent of a 100 ppb solution of REEs in nitric acid with a pH of 2, and the flow rate was 0.5 mL min^{-1}. Subsequently, solutions of nitric acid were passed through the column to elute REEs and the concentration of nitric acid increased with each addition. Under these conditions, NC-Si showed the greatest potential for use in industry, demonstrating successful partitioning as NC-Si exhibited the highest affinity for the later REEs, causing them to elute last.

Several conditions have to be considered for optimization of the systems, including pH, type of acid eluent, flow rate, ligand concentration, REE concentration, temperature and exposure duration. Varying the pH of the REE eluent will affect the way the ligand binds to the REE ions, thus influencing adsorption capacities and preferences for particular REE ions. Similar effects would occur if a different acid or a mixture of acids were used, as different ions would be involved in complex formation before elution. Varying the temperature may accelerate the kinetics, reaching equilibrium sooner, however heating the system would require a lot of energy and safety concerns would arise. Decreasing the flow rate or increasing the duration of exposure to the REE eluent system may increase adsorption capacity as the ligand has more time to bind to the metal. However, this may result in less pure fractions of REEs being eluted, affecting resolution. By systematically altering the conditions for each ligand system through multiple experiments, the most efficient results can be achieved.

The solutions from either end-of-life waste products and raffinate from processing ores may not solely contain REEs. The possibility of impurities and other competing ions, such as Na, Ca and K would be quite high. These impurities may negatively impact the performance of a fixed-bed column of NC-Si if these ions were to compete with the available sites on the surface of NC-Si. Competing ion tests will have to be conducted to test for any variations in extraction and separation capabilities.

The dimensions of the fixed-bed column could also be altered, affecting the contents of the eluate. Increasing the column length may enhance resolution, leading to purer fractions of REEs. However, this would increase the elution time and may require higher pressures. Changing the column diameter will impact the sample loading capacity, with a smaller diameter producing purer fractions of REEs but having a lower loading capacity compared to a larger diameter column. Altering the pore/mesh size of the silica would also result in changes in the resolution of REEs in the eluent and the flow dynamics within the column. Smaller particles may improve resolution but may require higher pressures for efficient elution.

Furthermore, investigating the chemical structure of the ligand itself would be beneficial to determine if improvements in adsorption capacities and partitioning can be made while avoiding the use of expensive palladium catalysts. Ligands containing N-donor or O-donor atoms are required for binding to REE metals. Increasing the amount of immobilized ligand onto the silica solid support could reduce the amount of silica needed to achieve similar results.

However, reducing the amount of silica may affect the resolution of REE fractions. Attaching ligands to other solid-phase materials such as polymers, clay, zeolites and other bonded phases could potentially enhance partitioning capabilities. Further functionalisation of the neocuproine molecule with sulfonic acid groups may increase the adsorption capacities of REE ions.

The recyclability of the column material is also crucial as it impacts profits and sustainability. Ideally, the fixed-bed column system should be easily stripped and regenerated without material degradation or loss of performance. As discussed in Chapter 4, the costs of synthesizing 1 kg of all ligand-Si supports were calculated. If the ligand systems cannot be easily regenerated and require synthesis each time they are needed, it would increase costs and reduce sustainability. An assessment must be made to determine the viability of employing this method for the separation of REEs.

5.5 References

1. European Commission *Tackling the Challenges in Commodity Markets and on Raw Materials*; Brussels, 2012;
2. Binnemans, K.; Jones, P.T.; Blanpain, B.; Van Gerven, T.; Yang, Y.; Walton, A.; Buchert, M. Recycling of Rare Earths: A Critical Review. *J. Clean. Prod.* **2013**, *51*, 1–22.
3. Pan, X.; Wang, H.; Li, C.; Zhang, J.Z.H.; Ji, C. MolGpka: A Web Server for Small Molecule PKaPrediction Using a Graph-Convolutional Neural Network. *J. Chem. Inf. Model.* **2021**, 61, 3159–3165.
4. Sigma Aldrich Catalogue Available online: https://www.sigmaaldrich.com/GB/en (accessed Feb 2023).
5. Fisher Scientific Catalogue Available online: https://www.fishersci.co.uk/gb/en/home.html (accessed Feb 2023).
6. TCI Chemicals Catalogue Available online: https://www.tcichemicals.com/GB/en/ (accessed Feb 2023).
6. Azizian, S.; Eris, S. Chapter 6 - *Adsorption Isotherms and Kinetics. In Adsorption: Fundamental Processes and Applications*; Ghaedi, M., Ed.; Interface Science and Technology; Elsevier, 2021; Vol. 33, pp. 445–509.
8. Lakshmipathy, R.; Sarada, N.C. A Fixed-bed Column Study for the Removal of Pb2+ Ions by Watermelon Rind. *Environ. Sci. Water Res. Technol.* **2015**, *1*, 244–250.
9. Chu, K.H. Fixed-bed Sorption: Setting the Record Straight on the Bohart-Adams and Thomas Models. *J. Hazard. Mater.* **2010**, *177*, 1006–1012.
10. Yan, G.; Viraraghavan, T.; Chen, M. A New Model for Heavy Metal Removal in a Biosorption Column. *Adsorpt. Sci. Technol.* **2001**, *19*, 25–43.
11. Aksu, Z.; Çağatay, Ş.Ş.; Gönen, F. Continuous Fixed-bed Biosorption of Reactive Dyes by Dried Rhizopus Arrhizus: Determination of Column Capacity. *J. Hazard. Mater.* **2007**, *143*, 362–371.
12. Bohart, G.S.; Adams, E.Q. Some Aspects of the Behavior of Charcoal with Respect to Chlorine. *J. Am. Chem. Soc.* **1920**, *42*, 523–544.
13. Felipe, E.C.B.; Batista, K.A.; Ladeira, A.C.Q. Recovery of Rare Earth Elements from Acid Mine Drainage by Ion Exchange. *Environ. Technol. (United Kingdom)* **2021**, *42*, 2721–2732.
14. Purolite C160 Data Sheet: https://www.lenntech.com/Data-sheets/Purolite-C160-L.pdf (accessed June 2023).

15. Hart, F.A.; Laming, F.P. Complexes of 1,10-Phenanthroline with Lanthanide Chlorides and Thiocyanates. *J. Inorg. Nucl. Chem.* **1964**, *26*, 579–585.

16. Cabral Campello, M.P.; Palma, E.; Correia, I.; Paulo, P.M.R.; Matos, A.; Rino, J.; Coimbra, J.; Pessoa, J.C.; Gambino, D.; Paulo, A.; et al. Lanthanide Complexes with Phenanthroline-Based Ligands: Insights into Cell Death Mechanisms Obtained by Microscopy Techniques. *Dalt. Trans.* **2019**, *48*, 4611–4624.

17. Simonnet, M.; Suzuki, S.; Miyazaki, Y.; Kobayashi, T.; Yokoyama, K.; Yaita, T. Lanthanide Intra-Series Separation by a 1,10-Phenanthroline Derivative: Counterion Effect. *Solvent Extr. Ion Exch.* **2020**, *38*, 430–440.

18. Simonzadeh, N.; Schilt, A.A. Chelation Properties of Silica-Bound 1,10-Phenanthroline. *J. Coord. Chem.* **1989**, *20*, 117–120.

19. Giron, O.D.; Lirag, R.C.M.; Arco, S.D.; Quirit, L.L. Modification of Silica Gel with 1,10-Phenanthroline for Cd(II) and Pb(II) Adsorption. *Kimika* **2013**, *24*, 18–24.